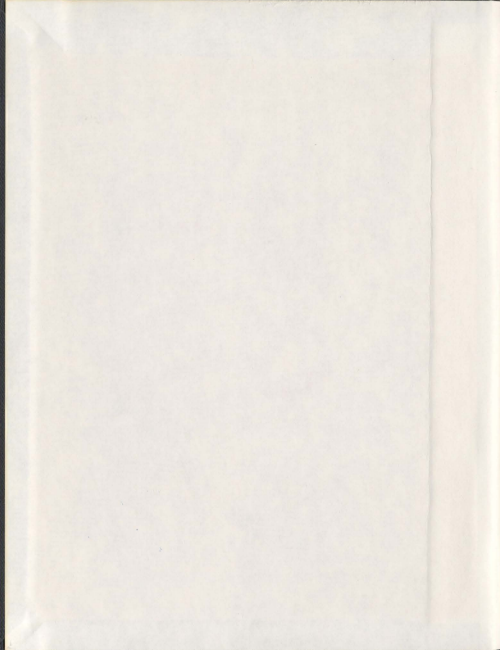


ADAPTIVE POWER TRACKING CONTROL OF
HYDROKINETIC ENERGY CONVERSION SYSTEMS

MOHAMMAD JAHANGIR ALAM KHAN



001311



Adaptive Power Tracking Control of Hydrokinetic Energy Conversion Systems

by

© Mohammad Jahangir Alam Khan, B.Sc., M.Eng.

A thesis submitted to the School of Graduate Studies
in partial fulfillment of the
requirements for the degree of Doctor of Philosophy

**Faculty of Engineering and Applied Science
Memorial University of Newfoundland**

St. John's

Newfoundland

Canada

June 2010

Abstract

Hydrokinetic energy conversion systems (HECS) are electromechanical devices that operate in free-stream water channels in a manner similar to wind turbines. The fundamental process of fluid-mechanic energy conversion using a hydrokinetic turbine is manifested through a nonlinear performance characteristics. The problem of maximum power tracking evolves around this nonlinearity and the underlying control objective is to regulate the turbine's operating conditions such that system efficiency is in the neighborhood of the optimum point. Through this research, it has been identified that a power tracking method that is independent of the turbine's characteristics, which can be implemented without using underwater/mechanical sensors would be of significant interest to the emerging hydrokinetic energy technologies. Further to a comparative analysis of various traditional wind turbine control techniques, an adaptive tracking approach termed as 'extremum seeking control' (ESC) approach has been adopted. Detailed mathematical formulations pertaining to this novel control solution has been provided and relevant parameter tuning and implementation procedures are presented.

In order to provide sufficient insight into the design, operation, and control aspects of a real-life hydrokinetic system, a small-scale vertical axis turbine has been developed in this work. This turbine employs a multi-pole permanent magnet alternator for electromechanical energy conversion. A ac-de-ac power electronic stage interfaces the asynchronous output of the generator to the utility grid through a single-phase connection. Even though a stand-alone test setup is possible, the grid-tied option has been pursued for ease of implementation as well as to explore broader areas of deployment. In addition to modeling and validating all the subsystems in the laboratory, the turbine rotor system has been tested under controlled environment in a tow tank. Associated numerical models have been validated extensively prior to their use in the power tracking control study. In addition, simulation schemes for hydrological flow fields and rotor fluid-dynamic characteristics have been developed as aiding tools to this research.

The extremum seeking controller parameter tuning and implementation method developed in this work, has been found to be capable of successfully regulating the system operating condition at the optimum point. This method requires minimal information on the hydrokinetic device's operational characteristics and can be potentially deployed in wide range of devices. Further work within this research track includes, implementation of the ESC method in mid to large-sized hydrokinetic systems and development of multi-objective control solutions. As a continuation of this research, active efforts are currently being made such that the true potential of the extremum seeking control and other advanced power tracking techniques can be realized in near-future.

Dedicated to my wife Sadia.

Acknowledgments

First and foremost, Dr. Tariq Iqbal and Dr. John Quaiocoe are acknowledged for providing continuous encouragement and timely guidance toward completion of this research. Support from Powertech Labs Inc. (Dr. Gouri Bhuyan and Dr. Ali Moshref) has also contributed heavily during the latter part of this work. Dr. Vlastimil Masek, Dr. Michael Hinchey, Dr. Benjamin Jeyasurya and Dr. Aziz Rahman are also thanked for their Comments, criticisms and suggestions.

Clayton Bear, Vince Ginter, and Justin Boal from New Energy Corp Inc. (NECI) are specially thanked for providing the 4-bladed rotor for test purposes. The author is indebted to Jim Gosse, Dr. Brian Veitch, Paul Bishop, Jerry Smith, and Billy Bidgood from the Memorial University for facilitating design, development, and testing. Also, support from Razzaqul Ahsan (graduate student, Memorial University) in developing the VB interface is acknowledged.

Funding support from the Natural Sciences and Engineering Research Council of Canada (NSERC) and Atlantic Innovation Foundation (AIF) has been instrumental toward conducting this research endeavor.

Table of Contents

Abstract	ii
Acknowledgments	iv
List of Tables	x
List of Figures	xi
List of Symbols	xvii
Chapter 1. Introduction	1
1.1 Research motivation	2
1.2 Research objective	2
1.3 Scope and technical approach	3
1.4 Thesis outline	4
Part I Review of Technology Status and Applied Research	5
Chapter 2. Review of Hydrokinetic Energy Conversion Technologies	7
2.1 Hydrokinetic energy conversion devices	9
2.2 Technology survey	15
2.3 Horizontal and vertical axis turbines	21
2.4 Technical advantages and disadvantages	32
2.5 Summary of technology review	34
Chapter 3. Review of Applied Research in Hydrokinetic System Control	36
3.1 Review of hydrokinetic system control initiatives	36
3.2 Permanent magnet alternator based wind turbine control	38
3.3 Maximum power point tracking control	39
3.4 Summary of applied research review	40

Part II Development and Validation of Simulation Models 41

Chapter 4. Flow Field Representation	43
4.1 Velocity of water	44
4.1.1 Seasonal variation component	48
4.1.2 Turbulence component	50
4.1.3 Wave-current interactions	52
4.2 Density of water	56
4.3 Design and placement related factors	58
4.3.1 Velocity augmentation factor	59
4.3.2 Vertical velocity profile factor	60
4.3.3 Skewed flow factor	62
4.3.4 Yaw misalignment factor	63
4.4 Effective rotor area	64
4.5 Simulation of flow field	64
4.6 Summary of flow field representation methods	68
Chapter 5. Darrieus Rotor Operation and Performance Analysis	69
5.1 General principle	69
5.2 Performance analysis of Darrieus rotors	76
5.2.1 Methods of analysis	76
5.2.2 Single-disk multiple-streamtube analysis	78
5.3 Design considerations	85
5.3.1 Basic dimensioning	86
5.3.2 Blade design	89
5.3.3 Design example	91
5.4 Summary of rotor performance analysis	93
Chapter 6. Dynamic Modeling of Hydrokinetic System Components	94
6.1 System description	96
6.2 Vertical axis rotor	97
6.3 Transmission	100
6.4 Permanent magnet alternator	101
6.4.1 Simplified modeling	103
6.4.2 Parameter Estimation	110

6.5	Power electronic converters	113
6.5.1	Zero-current-switching dc-dc converter	114
6.5.2	Grid-connected dc-ac inverter	117
6.6	System simulation and summary of dynamic modeling	122
Chapter 7. Test Apparatus and Model Validation		123
7.1	Laboratory test apparatus and electrical systems	124
7.1.1	Rectifier coupled permanent magnet alternator	125
7.1.2	Zero-current-switching dc-dc converter	129
7.1.3	Grid-connected dc-ac inverter	133
7.2	Tow-tank test apparatus and turbine rotors	137
7.2.1	Rotor performance evaluation	146
7.2.2	Part-system model validation	159
7.3	Summary of testing and model validation	166
Part III Evaluation of Power Tracking Control Methods		168
Chapter 8. Power Tracking Control Challenges in Hydrokinetic Systems		170
8.1	Control regions	170
8.2	Power tracking control challenges	174
8.3	Possible opportunities	179
8.4	Summary of control requirements	181
Chapter 9. Effects of Efficiency Nonlinearity on Power Tracking Control		182
9.1	Multi-parameter control requirements	184
9.2	Determination of nonlinear efficiency effects	190
9.2.1	Analytical power curve and efficiency curve	191
9.2.2	Efficiency characterization	194
9.3	Case study of hydrokinetic systems	196
9.4	Efficiency characterization of a physical system	198
9.5	Simulation study	200
9.6	Experimental study	204
9.7	Summary of nonlinear efficiency effects	206

Chapter 10. Assessment of Generic Power Tracking Methods	207
10.1 Tip speed ratio (TSR) control	207
10.2 Power signal feedback (PSF) control	208
10.3 Hill climbing search (HCS) control	210
10.4 Simulation based comparison	211
10.5 Summary of controller performance assessment	220
Part IV Synthesis of Extremum Seeking Controllers	222
Chapter 11. Extremum Seeking Control (ESC) Method	224
11.1 Classification of extremum seeking control methods	225
11.2 Extremum seeking control in power tracking applications	228
11.3 Principles of Extremum Seeking Control	228
11.3.1 Extremum seeking control for plants with static nonlinearity	228
11.3.2 Extremum seeking control for plants with nonlinear dynamics	233
11.4 Summary of ESC method attributes	236
Chapter 12. Applicability of ESC in Hydrokinetic Systems	237
12.1 Hydrokinetic systems with static plant model	238
12.1.1 Assessment of dominant nonlinear plant characteristics	238
12.1.2 Assessment of controller parameter variations and disturbance inputs	244
12.2 Hydrokinetic systems with dynamic plant model	249
12.3 Summary of ESC method's applicability in hydrokinetic systems	256
Chapter 13. ESC Synthesis and Implementation in Simulation Model	257
13.1 Internal speed controller design considerations	259
13.1.1 Controller parameter tuning	261
13.1.2 Input dynamics model	262
13.2 ESC parameter selection considerations	264
13.2.1 Parameter sensitivities	264
13.2.2 Output dynamics model and evaluation of system stability	267
13.3 ESC design procedures for hydrokinetic systems	267
13.4 Simulation based test of ESC method	273
13.5 Summary of ESC controller synthesis	281

Chapter 14. Conclusion	282
14.1 Research summary	282
14.2 Contributions	283
14.3 Further work	284
References	287
Appendices	305
Appendix A. List of surveyed technologies	306
Appendix B. Subsystem data	307
Appendix C. Test apparatus	310

List of Tables

4.1	Manning resistance constant	49
4.2	Tidal harmonic components	50
4.3	Bottom roughness parameters	61
4.4	Short simulation of hydrokinetic flow-field	65
5.1	Typical efficiency values	87
5.2	Turbine design example	93
6.1	Major subsystems of the hydrokinetic turbine setup	97
7.1	Permanent magnet alternator model parameters	126
7.2	Converter model parameters	130
7.3	Inverter model parameters	134
7.4	Effects of vertical rotor submersion level on effective rotor height	150
12.1	Case descriptions for ESC dynamic analysis	250
13.1	Parameter sensitivity on ESC performance	265
13.2	ESC design steps for hydrokinetic systems	269
13.3	Comparative performance review	281

List of Figures

2.1	Outline of a hydrokinetic energy converter system	8
2.2	Example of turbine systems: (a)Free-Flow™ (b) Kobold™ (c) Atlantisstrom™ (d) HydroVenturi™ (e) Neo-Aerodynamic™	11
2.3	Example of non-turbine systems: (a) OCPST™ (b) EEL™ (c)VIVACE™ (d) Seasnail™ (e) Tidal Sails™	11
2.4	Conventional hydro versus hydrokinetic energy conversion schemes	12
2.5	Use of ducts and conversion schemes	18
2.6	Use of ducts and applications	19
2.7	System placement and conversion schemes	20
2.8	System placement and applications	21
2.9	General technology status of hydrokinetic turbine technologies (a) relative advancements, and (b) percentage of different conversion schemes	23
2.10	Classification of turbine rotors	24
2.11	Horizontal axis turbines	25
2.12	Vertical axis turbines	26
2.13	Reported consideration for duct augmentation for (a) horizontal axis (b) vertical axis turbines	27
2.14	Augmentation channel classification	28
2.15	Channel shapes (top and side view)	28
2.16	Turbine mounting options	29
2.17	Percentage of turbines considered for various placement arrangements (a) horizontal axis (b) vertical axis	30
4.1	Flow-field elements	44
4.2	Example of annual (year to year) variations of river velocity	46
4.3	Example of monthly (month to month) variation of river velocity	46
4.4	Example of hourly river velocity variation	46
4.5	Example of year round tidal current velocity	47
4.6	Example of daily (day to day) tidal velocity variation	47
4.7	Example of hourly (hour to hour) tidal velocity variation	48

4.8	Examples of (a) river current velocity spectrum (b) tidal current frequency spectrum	49
4.9	River velocity time series measurement (variations in short time scale) . .	51
4.10	Tidal river velocity time series measurement (variations in short time scale)	51
4.11	Kolmogorov's law and river velocity spectrum	52
4.12	Stokes transport phenomena	53
4.13	Water depth versus wave-current interactions	55
4.14	Velocity distribution at various water depths due to wave-current action .	56
4.15	Water density as a function of salinity and temperature	57
4.16	Measurement of salinity and temperature variations	58
4.17	Measurement of salinity and temperature variations	59
4.18	Vertical velocity profile	61
4.19	Velocity skew in relation to the rotor	62
4.20	Yaw misalignment in relation to the rotor	63
4.21	Effects of rotor submersion	64
4.22	Water velocity simulation blocks	67
4.23	Simulation of water velocity variations	68
5.1	Blade-flow interaction	70
5.2	Turbine system components	71
5.3	Pressure and velocity distribution around a turbine	72
5.4	Performance of various rotors	75
5.5	Methods of performance analysis of Darrieus rotor	77
5.6	Flow distribution around a vertical axis turbine	78
5.7	Blade-flow interaction	80
5.8	Gluert's empirical formula	83
5.9	Typical airfoil data (NACA 63-018)	85
5.10	Modified airfoil data (NACA 63-018 with $R_B = 10$, $Re = 2 \times 10^6$)	86
5.11	(a) Water density variations (b) Velocity duration curves and resource classification	88
5.12	Performance of Darrieus rotor at various solidity	91
5.13	Rotor design process	92
6.1	General structure of a hydrokinetic energy conversion system (HECS) . .	96
6.2	Torque components of the hydrokinetic turbine system	98

6.3	Two-mass representation of the drive-train	101
6.4	Radial flux (inner & outer rotor) and axial flux (double & single stator) PM generators	102
6.5	Rectifier-coupled permanent magnet alternator	103
6.6	Per-phase circuit model and waveforms	106
6.7	Power losses in the generator-rectifier system	108
6.8	Inductive load test	111
6.9	Generator dimensions for inertia estimation	112
6.10	Zero-current-switching operation	115
6.11	Grid connected inverter functional blocks	118
6.12	Inverter power control and phasor diagram	120
6.13	Matlab-Simulink™ implementation of the simulation model	121
7.1	Laboratory test rig setup	124
7.2	Outer rotor PMA coupled to turbine shaft	125
7.3	Generator performance in steady state (a) output current and voltage (b) output power and speed	126
7.4	Matlab-Simulink™ model of the PMA	127
7.5	Generator model validation (dynamic simulation)	128
7.6	Converter (dc-dc) stage containing two bricks	129
7.7	Converter steady-state performance (a) output voltage control by trimming/controlling voltage, and (b) output voltage and current relationship	131
7.8	Matlab-Simulink™ implementation of dc-dc converter model	131
7.9	Converter model validation (a) test - output current and voltage (b) simulation - output voltage, and (c) simulation - output current	132
7.10	Inverter (dc-ac) stage containing dump-load circuit	133
7.11	Inverter steady-state performance: input voltage and output power relationship	134
7.12	Matlab-Simulink™ implementation of dc-ac inverter model	135
7.13	Inverter model validation (a) test - output current and voltage (b) simulation - output voltage, and (c) simulation - output current	136
7.14	MUN-OERC tow-tank	138
7.15	Turbine mounting frame	139
7.16	Three bladed turbine design and fabrication at MUN	140
7.17	Three bladed turbine test at MUN OERC tank	140
7.18	Six bladed turbine designed and tested at MUN	141

7.19	Four bladed turbine provided by NECI	142
7.20	Summary of turbine design and performance features	143
7.21	Data acquisition arrangement	144
7.22	Data acquisition and power electronic hardware	145
7.23	Effect of rotor submersion and free surface interactions	149
7.24	Torque ripple in the system output	152
7.25	Start-up behavior	154
7.26	System efficiency at various carriage/water speeds	155
7.27	Turbulence in rotor's flow field	157
7.28	Simplified system structure with a dc end-load	160
7.29	Start-up behavior of the hydrokinetic turbine	161
7.30	Torque ripple behavior of the hydrokinetic turbine	163
7.31	General performance of the hydrokinetic turbine	164
8.1	Control regions of wind and hydrokinetic turbines (fully submerged)	172
8.2	Seaflo TM turbine test data	173
8.3	Example of small vertical axis turbine's (height 0.4 m, diameter 1 m) (a) power and (b) torque curves with water velocity variations from 0–2.5m/s (at 0.25 m/s interval)	175
8.4	Test results on (a) torque ripple, and (b) performance curve	177
8.5	Example of bio-fouling and accumulation of debris (tests on Kobold turbine)	178
8.6	Effects of sub-optimal operation in wind and hydrokinetic turbine	179
9.1	Typical HECS power curve	186
9.2	HECS system optimum operation	187
9.3	Algorithm flow-chart	192
9.4	Exponential curve fitting	195
9.5	Efficiency information for 'System A' and 'System C'	197
9.6	Efficiency characterization of a physical HECS	199
9.7	Simulation based determination of (a) realistic power curves (b) success of power tracking (SOPT) index	201
9.8	Power transfer and tracking success through each of the subsystems	202
9.9	Simulation based evaluation of deviation from optimum point (DFOP) index	203
9.10	Experimental test results (a) power curve (b) efficiency curve	205
10.1	Outline of TSR control in hydrokinetic systems	208

10.2	Outline of PSF control in hydrokinetic systems	209
10.3	Outline of HCS control in hydrokinetic systems	210
10.4	Matlab-Simulink TM implementation of the generic control methods	212
10.5	HECS performance with TSR control - step variations in flow condition	213
10.6	HECS performance with TSR control - stochastic variations in flow condition	214
10.7	HECS performance with PSF control - step variations in flow condition	215
10.8	HECS performance with PSF control - stochastic variations in flow condition	216
10.9	HECS performance with HCS control - step variations in flow condition	217
10.10	HECS performance with HCS control - stochastic variations in flow condition	218
11.1	Classification of various adaptive control systems	226
11.2	Extremum seeking control methods	227
11.3	Extremum seeking control method for plants with static nonlinearity	229
11.4	Decomposition of nonlinear dynamic systems	234
11.5	Extremum seeking controller with dynamic compensator	235
12.1	Extremum seeking control and performance curve	239
12.2	Matlab-Simulink TM simulation blocks for studying performance curve uncertainty	243
12.3	Simulation results for studying performance curve uncertainty	243
12.4	Extremum seeking control with additional system representation	245
12.5	Matlab simulation blocks for studying variations in disturbance input and control parameter	246
12.6	Simulation results for studying variations in disturbance input and control parameter	248
12.7	Variations in gain (solid: smallest and dash: largest) and corresponding influence on tracking capability (left) as well as noise sensitivity (right) for case A	251
12.8	Variations in signal frequency (solid: smallest and dash: largest) and corresponding influence on tracking capability (left) as well as noise sensitivity (right) for case B	252
12.9	Variations in cut-off frequency (solid: smallest and dash: largest) and corresponding influence on tracking capability (left) as well as noise sensitivity (right) for case C	253
12.10	Variations in compensator coefficient (solid: smallest and dash: largest) and corresponding influence on tracking capability (left) as well as noise sensitivity (right) for case D	254

12.11 Variations in phase shift (solid: smallest and dash: largest) and corresponding influence on tracking capability (left) as well as noise sensitivity (right) for case E	255
13.1 Hydrokinetic system power tracking control using extremum seeking method	258
13.2 Internal speed control loop	259
13.3 Determination of simplified input dynamics model	263
13.4 Speed controller tuning (a) root locus (b) step response	270
13.5 Internal speed control loop response (higher order and first order)	271
13.6 Hydrokinetic system tracking capability (left) as well as noise sensitivity (right) with selected controller parameters	272
13.7 Matlab-Simulink™ implementation of the ESC loop	274
13.8 HECS performance with ESC control - step flow velocity variation	276
13.9 HECS performance with ESC control - ramp type flow velocity variation	277
13.10 HECS performance with ESC control - stochastic flow conditions, without step variations	278
13.11 HECS performance with ESC control - step variations in flow condition	279
13.12 HECS performance with ESC control - stochastic variations in flow condition	280
C.1 Thyristor controlled dc power supply for the emulator prime mover	310
C.2 Customized switchable load bank for generator, converter, and turbine testing	311
C.3 Optical speed sensor mounted near the PMA	312
C.4 Optical speed sensor signal conditioning circuit	313
C.5 Customized wattmeter for ac power measurement	314
C.6 Wattmeter signal conditioning circuit	315

List of Symbols

α_K	Kolmogorov's empirical constant (0.48)	[—]
α_{pa}	Power angle (between inverter and utility grid)	[rad]
α_b	Angle of attack on rotor blade	[deg]
α_z	Exponent for vertical velocity correction (0.25 – 0.5)	[—]
\bar{v}_i	Mean velocity during the i^{th} interval	[m/s]
β	Flow skew angle	[deg]
$\Delta\omega_{rot}$	Change in rotor speed	[rad]
ΔE_{co}	Converter (dc-dc) output voltage drop due to regulation	[V]
ΔP_{sys}	Change in turbine system's power output	[watt]
ΔP_{sys}	Difference of actual output power to system output, P_{sys}	[watt]
δ	Yaw misalignment angle	[deg]
η_{con}	Converter (dc-dc) efficiency	[—]
η_{drv}	Drive-train efficiency	[—]
η_{ele}	Electrical system (power electronic converters) efficiency function	[—]
η_{gen}	Generator efficiency	[—]
η_{inv}	Inverter (dc-ac) efficiency	[—]
η_{rec}	Rectifier efficiency	[—]
η_{sys}	Hydrokinetic system overall efficiency	[—]
η	Subsystem efficiency	[—]
η_{aew}	Efficiency contribution of rotor arm, central shaft and walls	[—]
η_{rot}	Rotor efficiency (including arms, shaft, wall and drivetrain)	[—]
N_{rot}	Optimum rotor speed	[rpm, p.u.]
T_{cog}	Generator peak cogging torque	[Nm]
T_{osc}	Peak oscillating rotor torque	[Nm]
θ_z	Estimate of optimum operating point within an ESC loop	[—]
η_{gen}	Peak generator efficiency	[—]
η_{ele}	Electrical system (power electronic converters) peak efficiency	[—]
η_{sys}	Hydrokinetic system peak efficiency	[—]
λ	Optimum tip speed ratio (rotor only)	[—]
λ_{sys}	Optimum tip speed ratio (complete hydrokinetic system)	[—]
C_p	Peak power coefficient (rotor)	[—]
I_e	Optimum electrical system (power electronic converters) output current	[A, p.u.]
I_g	Optimum generator current	[A, p.u.]
κ	von Karman constant (≈ 0.41)	[—]
$\lambda_{d1}^g, \lambda_v^g$	Direct and quadrature axis flux linkage	[—]
λ_m	Generator machine constant	[V.s/rad]
λ	Tip speed ratio (TSR)	[—]

λ_t	Turbine initial tip speed ratio within an ESC loop	[—]
λ_{opt}	Estimate of optimum tip speed ratio within an ESC loop	[—]
ω_i	Frequency of i^{th} water velocity component	rad/s
ω_t	Frequencies of various tidal harmonic elements	rad/s
ω_v	Frequency of velocity variation	rad/s
ω_w	Wave frequency	rad/s
ω_{gre}	Generator's electrical angular velocity	rad/s
ω_z	Modulating / demodulating signal frequency within an ESC loop	rad/s
ω_{gen}	Generator rotational speed	rad/s
ω_{hpf}	High pass filter cut-out frequency within an ESC loop	rad/s
ω_{ps}	Hydrokinetic system's characteristics frequency within an ESC loop	rad/s
ω_{rot}	Rotor rotational speed	rad/s
\bar{v}_s	Mean seasonal velocity	m/s
ϕ_w	Wave velocity potential	J
ψ_z	Output of washout filter within an ESC loop	[—]
ρ_w	Density of water	kg/m ³
σ_t	Standard deviation of water velocity turbulence	[—]
σ_u	Longitudinal mean velocity	cm/s
σ_r	Rotor solidity	[—]
τ_k	Sensor constants: $k = 1 - 4$ for rotor speed, current, voltage, water velocity	s
τ_{out}	Time constant of the wattmeter/power measurement circuits	s
τ_{pa}	Plant-actuator time constant	sec
θ_g	Generator pole angular position	deg
θ_z^*	Input variable at the maxima of f_z within an ESC loop	[—]
θ_{gre}	Generator's electrical angular position	rad
θ_{pf}	Power factor angle	rad
θ_a	Blade azimuth position angle	deg
θ_F	Plant input variable within an ESC loop	[—]
N_{gen}	Speed signal feedback	rpm
ν	Kinematic viscosity of water (1.1×10^{-6})	[—]
ε	Turbulent kinetic energy dissipation rate	cm ² /s ³
φ_i	Uniformly distributed phase angle between $o - 2\pi$	rad
φ_x	Phase difference between mod/demod signals within an ESC loop	rad
$\hat{\psi}_s$	Ambient and measurement noise within an ESC loop	[—]
$\hat{\lambda}$	Error in estimation of optimum tip speed ratio within an ESC loop	[—]
$\hat{\theta}_F$	Estimation error of within an ESC loop	[—]
\hat{Y}_z	Output error within an ESC loop	[—]
ξ_s	Demodulated output signal within an ESC loop	[—]
ξ_{ss}	Small-signal wave perturbation	[—]
$a - c_{g1}$	Coefficients defining generator efficiency curve	[—]
$a - c_{g2}$	Coefficients defining generator efficiency curve	[—]
$a - c_{tj}$	Coefficients defining rotor performance curve	[—]
A_i	Magnitude of i^{th} turbulent velocity component	m/s

A_r	Effective rotor area	$[m^2]$
A_w	Wave amplitude (height between crest and trough)	$[m]$
a_z	Modulating (probing) signal amplitude within an ESC loop	—
a_{e1-2}	Coefficients defining electrical subsystem efficiency curve	—
a_{ind}	Induction factor	—
A_t	Area of each streamtube	$[m^2]$
B	Beta function	—
B_w	Water depth at calm sea	$[m]$
b_z	Demodulating signal amplitude within an ESC loop	—
b_{e1-2}	Coefficients defining electrical subsystem efficiency curve	—
B_{gen}	Generator damping constant (friction and windage losses)	$[Nm.s/rad]$
B_{rot}	Rotor damping constant (representing friction losses)	$[Nm.s/rad]$
C	Blade chord length	$[m]$
C_{TO}^*	First derivative of torque coefficient around the optimum tip speed ratio	—
C_D	Drag coefficient	—
C_L	Lift coefficient	—
C_p	Rotor performance coefficient (including effects of arms, shaft, and walls)	—
C_p^a	Rotor performance coefficient (excluding effects of arms, shaft, and walls)	—
C_T	Rotor torque coefficient (including effects of arms, shaft, and walls)	—
C_t	Amplitudes of various tidal harmonic elements	$[m/s]$
C_T^a	Rotor torque coefficient (excluding effects of arms, shaft, and walls)	—
C_w	Swell velocity	$[m/s]$
$C_z(s)$	Compensator block within an ESC loop	—
C_{zo}	Converter (dc-dc) filter capacitance	$[F]$
C_{fg}	Filter capacitor at the generator's output	$[F]$
C_{norm}	Normal force component	—
C_{betz}^a	Betz limit	—
C_{pi}^{*betz}	Turbine performance coefficient at the initial point	—
C_{tang}	Tangential force coefficient	—
C_{thrust}	Thrust coefficient	—
D	Rotor diameter ($D = 2R$)	$[m]$
d_z	Dynamic compensator zero placement within an ESC loop	—
E_g	Generator open circuit voltage (peak value)	$[V]$
$E_w(s)$	Random white noise (frequency domain) for water velocity simulation	—
E_w	Energy extracted by rotor	$[J]$
e_{a-c}	Generator internal voltage for phase a, b, c, respectively	$[V]$
E_{zo}	Converter (dc-dc) output voltage (before LC filter)	$[V]$
E_{zo}^*	Converter (dc-dc) output voltage (without regulation effect)	$[V]$
E_{inv}	Inverter (dc-ac) internal voltage	$[V]$
f_e	Electrical system (power electronic converters) efficiency	—
f_g	Generator efficiency function	—
f_i	Efficiency function for a given subsystem within a hydrokinetic system	—
f_r	Rotor efficiency i.e., $C_p - \lambda$ function	—

f_t	Summing function of various tidal harmonic elements	[—]
f_z	Nonlinear plant characteristics function within an ESC loop	[—]
f_z^*	Maxima of nonlinear plant characteristics function within an ESC loop	[—]
F_{con}	Converter (dc-dc) efficiency function	[—]
F_{ele}	Switching frequency of electrical system (power electronic converters)	[Hz]
F_{gen}	Generator electrical frequency	[Hz]
f_h	Heaviside step function	[—]
f_{inv}	Inverter (dc-ac) efficiency function	[—]
$F_{ix}(s)$	Input dynamics block within an ESC loop	[—]
$F_{ox}(s)$	Output dynamics block within an ESC loop	[—]
f_{rec}	Rectifier efficiency function	[—]
F_{thrust}	Thrust force	[N]
g	Acceleration due to gravity	[m/s ²]
$G_w(s)$	Speed controller transfer function	[—]
$G_s(s)$	Speed sensor transfer function	[—]
$G_{pm}(s)$	Plant-actuator model transfer function	[—]
H	Absolute rotor height	[m]
h_{eff}	Effective rotor height	[m]
h_{sub}	Height of rotor submersion	[m]
I_c	Converter (dc-dc) output current	[A, p.u.]
i_d^g, i_q^g	Direct and quadrature axis generator current	[A]
I_c	Electrical system (power electronic converters) output current	[A, p.u.]
I_g	Generator output current (peak value)	[A]
I_i	Inverter (dc-ac) output current	[A, p.u.]
I_r	Rectifier output current	[A, p.u.]
I_t	Turbulence intensity	[—]
I_{cgu}	Converter (dc-dc) current in p.u.	[p.u.]
I_c^b	Converter (dc-dc) current base	[A]
I_{dc}	dc current for generator resistance testing	[A]
I_{gl}	Generator current with inductive load	[A]
I_{ggu}	Generator current in p.u.	[p.u.]
I_{gf}	Generator output current through the rectifier-filter terminal	[A]
I_g^b	Generator current base	[A]
I_{gu}^g	Inverter (dc-ac) current in p.u.	[p.u.]
I_i^b	Inverter (dc-ac) current base	[A]
I_{Lco}	Current through converter's (dc-dc) output inductance	[A]
I_{pu}	Subsystem current in p.u.	[p.u.]
I_{rgu}	Rectifier current in p.u.	[p.u.]
I_r^b	Rectifier current base	[A]
J_{con}	Generator cassette/cone inertia	[kg - m ²]
J_{cyl}	Generator rotor/cylinder inertia	[kg - m ²]
J_{disk}	Generator cover/disk inertia	[kg - m ²]
J_{erg}	equivalent rotor-generator system inertia	[kg - m ²]

J_{gen}	Generator inertia	$[kg - m^2]$
J_{rot}	Turbine rotor inertia	$[kg - m^2]$
K_F	Static filter gain (for stochastic water velocity simulation)	
k_w	Wave number	
k_x	Controller gain within an ESC loop	
k_{a-c}	Coefficients associated with R_{nl}	
k_{aug}	Velocity augmentation factor	
k_{cf}	Correction factor for k_{ncc}	
k_{cf}	Correction factor for Non-linear curve constant used in PSF control	
k_{dp}	Rotor design and placement related factors	
k_{econ}	Economical factor	
$k_{i\omega}$	Integral constants for speed controller	
K_{inv}	Inverter (dc-ac) power angle controller parameter (integral)	
k_{ncc}	Non-linear curve constant used in PSF control	
k_{ncc}	PSF non-linear curve constant	
k_{osc}	Empirical oscillating torque constant	
k_{pw}	Proportional constants for speed controller	
k_{pa}	Plant-actuator gain	
k_{phcs}	HCS controller (proportional constant)	
k_{phcs}	HCS controller gain	
k_{phcs}	HCS controller trimming reference gain	
K_{pinv}	Inverter (dc-ac) power angle controller parameter (proportional)	
k_{pspf}	PSF controller (proportional constant)	
k_{pspf}	PSF controller trimming reference gain	
k_{prof}	Vertical velocity profile factor	
k_{ptsr}	TSR controller (proportional constant)	
k_{ptsr}	TSR controller trimming reference gain	
k_{skew}	Skewed flow factor	
k_{spr}	Drive-train spring constant	$[Nm/rad]$
k_{swf}	HCS step weighing factor	
k_{tac}	Torque-speed constant	
k_{yaw}	Yaw misalignment factor	
L	Generator self inductance ($L = L_a = L_b = L_c$)	H
L_{∞}	Deep water depth	m
L_a^d, L_q^d	Direct and quadrature synchronous inductance	H
L_g	Generator synchronous inductance ($L_g = L - M$)	H
L_i	Intermediate water depth	m
L_t	Turbulence scale length	m
L_w	Wave length	m
$L_g(s)$	Transfer function for tracing reference changes within an ESC loop	-
L_{a-c}	Generator self inductance for phase a, b, c, respectively	H
$L_{ab-bc-ca}$	Generator mutual inductance for phase a, b, c, respectively	H
L_{co}	Converter (dc-dc) filter inductance	H

L_{fg}	Equivalent inductance for generator's output filter ($L_{fg} = 2L_g$)	[H]
L_{io}	Inverter (dc-ac) line filter inductance	[H]
M	Generator mutual inductance ($M = L_{ab} = L_{bc} = L_{ca}$)	[H]
m	Number of streamtubes	—
m_w	Water mass	[kg]
$M_z(s)$	Transfer function for determining noise sensitivity within an ESC loop	—
M_{con}	Generator mass	[kg]
M_{cyl}	Generator rotor/cylinder mass	[kg]
M_{disk}	Generator cover/disk mass	[kg]
N_b	Number of rotor blades	—
n_m	Manning resistance constant	[m^{-3}/s]
N_p	Number of generator poles	—
N_v	Number of samples in turbulent velocity component modeling	—
N_{gen}	Generator rotational speed	[rpm]
N_{gen}^*	Generator speed reference	[rpm]
N_{gen}^b	Generator speed base	[rpm]
N_{gpu}	Generator speed in p.u.	[p.u.]
N_{gr}	Gear ratio	—
N_{rot}	Rotor speed	[rpm, p.u.]
O	Symbol implying 'in the neighborhood of...'	—
p	Differential operator (d/dt)	—
p_a, p_b	Water pressure along the rotor cross section at points a, b	[Pa]
p_f	Pressure of fluid/water	[Pa]
P_{cl}	Rectifier coupled generator's copper loss	[watt]
P_{con}	Converter (dc-dc) output power	[watt]
P_{con}^b	Converter (dc-dc) power nominal/base	[watt]
P_{dn}	Downstream water pressure	[Pa]
P_{elec}	Electrical system (power electronic converters) power output	[watt, p.u.]
P_{gen}	Generator output power	[watt]
P_{gen}^b	Generator power nominal/base	[watt]
P_{hyd}	Hydraulic power incident on the rotor system	[watt]
P_{hyd}^b	Rotor hydrodynamic power nominal/base	[watt]
P_{sub}	Subsystem input base power	[watt]
P_{inv}	Inverter (dc-ac) power output (equal to system output P_{sys})	[watt]
P_{inv}^*	Inverter (dc-ac) design settings for power output (power reference)	[watt]
P_{inv}^b	Inverter (dc-ac) power nominal/base	[watt]
P_{in}	System/subsystem input power	[watt]
P_{ll}	Rectifier coupled generator's load loss	[watt]
P_{nll}	Rectifier coupled generator's no load loss	[watt]
P_{out}	System/subsystem output power	[watt]
P_{pu}	Subsystem input power in p.u.	[p.u.]
P_{rec}^b	Rectifier power nominal/base	[watt]
P_{rl}	Rectifier coupled generator's rotational loss	[watt]

P_{rot}	Captured rotor power (low speed shaft).....	[watt]
P_{sft}	High speed shaft power (generator input power)	[watt]
P_{sys}	Hydrokinetic system overall power output	[watt]
p_{0p}	Upstream water pressure	[Pa]
$q_0 - q_5$	Converter (dc-dc) voltage regulation curve-fit coefficients	—
q_c	Characteristics controller gain within an ESC loop	—
R	Rotor radius	[m]
R_B	Blade aspect ratio	—
R_e	Reynold's number	—
R_g	Generator stator resistance	[Ω]
R_m	Hydraulic radius of river channel.....	[m]
R_{a-c}	Generator resistance for phase a, b, c, respectively	[Ω]
R_{con}	Generator radius	[m]
R_{co}	Converter (dc-dc) output resistance	[ω]
R_{cvr}	Converter (dc-dc) voltage regulation	—
R_{cyl}	Generator rotor/cylinder radius	[m]
R_{disk}	Generator cover/disk radius	[kg]
R_{fg}	Equivalent resistance for generator's output filter ($R_{fg} = 2R_g$)	[Ω]
R_{in}	Inverter (dc-ac) line filter resistance	[Ω]
R_{nl}	Equivalent resistance associated with generator's no load loss	[Ω]
R_g^m	Generator armature resistance (at machine temperature)	[Ω]
R_g^r	Generator armature resistance (at room temperature)	[Ω]
S	Salinity of seawater	—
S_m	River channel slope	[m/m]
S_v	Kolmogorov's frequency spectrum	[cm^2/s]
T	Temperature of seawater	[$^{\circ}C$]
T_F	Time constant for water velocity simulation	[s]
T_i	Time period of i^{th} water velocity component	[s]
T_w	Wave period	[s]
T_{cog}	Generator cogging torque	[Nm]
t_{cyl}	Generator rotor/cylinder thickness	[m]
T_{gen}	Generator input torque	[Nm]
T_{load}	Generator electrical load torque	[Nm]
T_{loss}	Generator torque associated with power losses	[Nm]
T_{lax}	Low speed shaft torque	[Nm]
t_{mc}	Machine temperature ($90^{\circ}C$)	[$^{\circ}C$]
T_{mec}	Average mechanical rotor torque	[Nm]
T_{mult}	Torque in multiple streamtube	[Nm]
T_{osc}	Oscillating rotor torque	[Nm]
t_{rm}	Room temperature ($25^{\circ}C$)	[$^{\circ}C$]
T_{rot}	Total rotor torque (oscillating + average).....	[Nm]
T_{si}	Sampling interval for water velocity simulation	[s]
T_{amp}	HCS controller sampling interval	[s]

T_{rot}	Torque in single streamtube	[Nm]
u_s	Shear velocity	[cm/s]
V_{act}^k	Actual value of parameter being sensed	V
V_{sen}^k	Sensor output	V
v_a, v_b	Water velocity along the rotor cross section at points a, b	[m/s]
v_d^g, v_q^g	Direct and quadrature axis generator voltage	V
V_f	Diode forward voltage drop	V
V_g	Generator output voltage (peak value)	V
v_p	Velocity observed at a point near the rotor	[m/s]
v_R	Seasonal river velocity	[m/s]
v_T	Seasonal tidal velocity	[m/s]
v_t	Turbulent water velocity	[m/s]
v_w	Tangential water velocity due to stokes drift	[m/s]
v_z	Velocity at any given height	[m/s]
v_{a-c}	Generator terminal voltage for phase a, b, c, respectively	V
V_{conv}	Converter (dc-dc) nominal output voltage	V
V_{co}	Converter (dc-dc) output voltage	V
V_{dc}	dc voltage for generator resistance testing	V
v_{dn}	Downstream water velocity	[m/s]
v_{eff}	Effective water velocity	[m/s]
V_{gl}	Generator terminal voltage with inductive load	V
V_{grd}	Utility-grid voltage	V
V_{gr}	Generator output voltage at the rectifier-filter terminal	V
V_o^g	Generator output voltage at the rectifier terminal	V
V_{df}	Voltage across inverter (dc-ac) line filter	V
v_{ref}	Velocity at a reference height	[m/s]
v_{rel}	Rotor velocity relative to upstream water velocity	[m/s]
V_{trim}	Trimming/controlling voltage of the converter	V
v_{up}	Upstream water velocity	[m/s]
x	Displacement in tangential direction	m
X_{L0}	Inverter (dc-ac) line filter reactance	Ω
y	Displacement in orthogonal direction	m
z	Displacement in normal direction	m
z_0	Roughness length	[cm]
z_{hub}	Hub height	m
z_{ref}	Reference height	m
z_{surf}	Water surface height	m

Chapter 1

Introduction

River streams, tidal channels, marine currents, and other artificial waterways bear good potential for generating electric power through various hydrokinetic energy conversion technologies. Among a plethora of concepts, hydrokinetic turbines, employing both horizontal and vertical schemes are currently being explored vigorously. Such devices can be deployed in suitable water channels in a modular/array fashion without significantly affecting the natural course of the stream. Turbine performance improvement using flow augmentation channels, and placement methods employing near-surface, floating, or bottom-mounted structures are also being investigated through various research and development initiatives [1, 2].

As the industry is yet to establish a clear trend on what turbine topology will see greatest commercial deployment, vertical axis hydrokinetic energy conversion systems (HECS) have nonetheless gained significant attention [1, 2]. Several favorable attributes of such turbines include omni-directional operation, ease of duct augmentation, simplicity of blade design, and reduced requirement of water-sealed components (gearing, bearing, and generators). On the other hand, weak start-up, torque ripple, effects of unsteady hydrodynamics, and claims of lower efficiency are of concern for vertical axis hydrokinetic systems [3-6]. While the field of horizontal axis turbine design and evaluation benefited from the knowledge of wind turbines and ship propellers, studies on vertical axis hydrokinetic systems have seen comparatively limited exploration. It should also be pointed out that contrary to popular belief, experience of vertical wind turbines cannot be directly

extrapolated to vertical hydrokinetic turbines because of a multitude of reasons. This includes issues such as, complex unsteady hydrodynamic behavior, high solidity rotor design, complex multi-body interactions, and challenging operational conditions [7-9]. In recognition of the need for significant research needs in this area, a small hydrokinetic system (employing permanent magnet alternator and power electronic devices) based on a vertical axis turbine, has been studied in this work. In particular, the problem of maximum power tracking (MPT) for hydrokinetic devices has been thoroughly investigated.

1.1 Research motivation

The general motivation of this research has been to develop a set of basic and applied knowledge that may accelerate the progression of hydrokinetic technologies into a mature field of energy engineering. It is strongly believed that such technologies bear significant potential for generating renewable electric power in a sustainable and environmentally benign manner. In the context of an escalating global energy demand and increasing socio-economic perplexity, hydrokinetic systems may complement other emerging alternative power solutions in near future. While it is understood that significant technological breakthroughs are needed prior to realizing its true potential, this research is also motivated toward instigating necessary discussions, especially in the domains of electrical engineering and control system development.

1.2 Research objective

Considering the current technological needs, exploratory research niche and available academic strength, the primary focus of this research is on studying the power tracking control issues pertaining to hydrokinetic energy conversion systems (HECS). In general, the underlying research objectives have been :

- To identify the current state of hydrokinetic energy conversion technologies in the context of associated control challenges.

- To undertake design, develop, and test activities such that direct knowledge of a turbine's operational characteristics can be developed.
- To identify the power tracking control challenges unique to a class of hydrokinetic energy conversion systems.
- To investigate and collate a set of possible alternative solutions through simulation and qualitative evaluation.
- To formulate an advanced power tracking algorithm that may suit the unique needs within a broader class of hydrokinetic systems.

In order to meet these objectives, this research commenced with a set of comprehensive literature review and multi-disciplinary consultations. While most of these objectives have been achieved, directions toward further continuation is given as part of the concluding remarks.

1.3 Scope and technical approach

This research commences with a review of the general state of hydrokinetic technologies. Based on the current needs of the hydrokinetic energy industry and the gaps identified within the available literature, this research focuses on power tracking control synthesis and analysis. In order to initiate and manage research activities within an academic environment, subsequent focus has been given on a small-scale vertical axis HECS. This allowed consistent and reliable model development, validation, and laboratory scale testing. A multi-pole outer rotor permanent magnet alternator (PMA) is used for electromechanical energy conversion. This machine is coupled to the single-phase utility grid with a power electronic (ac-dc-ac) link. Design and testing of various vertical axis rotors have been carried out in tow-tank environment. Based on the gathered experience, a set of dynamic numerical models has been developed and implemented in Matlab-Simulink™ environment. In addition, modeling and analysis of flow-field variations, rotor performance, and sub-system/part-system validation have been conducted. Subsequent to

an in depth comparative analysis of various conventional methods of power tracking (tip speed ratio (TSR), power signal feedback (PSF), and hill-climbing search (HCS) control), an advanced method namely, the extremum seeking control (ESC) has been investigated. Being an adaptive method, this scheme is deemed highly suitable for a broader class of hydrokinetic systems. Analysis of ESC parameter sensitivity and method of controller synthesis have been developed. Although hardware development and implementation of control methods are viewed as critical steps, various practical limitations (time, resource and logistics) required the reliance on numerical simulation to a great extent.

1.4 Thesis outline

This dissertation is divided into four parts, each focusing on a set of targeted topics. A sequential presentation of research objective, methodology, and results has been generally attempted. Apart from the introductory and concluding chapters, the remainder of the treatise is consolidated into four parts. Each part unfolds with a description of its contents and each chapter ends with a brief summary of the materials presented. In Part I, a high-level technological review of hydrokinetic systems and highlights of contemporary research activities is presented. Various design, development, and test activities are discussed in detail in Part II. Development of steady-state/dynamic models related to hydrokinetic flow-field, turbine rotor, power electronics, and overall system is also presented in this part. These models are used in Part III where the underlying control challenges are identified, effects of efficiency nonlinearity in small-scale hydrokinetic system are evaluated, and a comparative simulation test of various power tracking methods is conducted. In Part IV, the method of extremum seeking control (ESC) is discussed and a novel method of controller synthesis is presented. Also, this model is tested in the simulation environment using the validated numerical models developed as part of this research. Considering the research objectives stated above, and in order to identify the significant contributions derived through this work, attention can be drawn to Chapters 2, 6, 7, 8, 10, and 13 for a succinct overview.

Part I

Review of Technology Status and Applied Research

Review of Technology Status and Applied Research

In order to develop an understanding of the challenges associated with hydrokinetic systems' power tracking control, it is important to put such technologies in the context of current technological developments as well as their future potentials. Also, it is critical to identify the distinctions between hydrokinetic and wind power technologies, while keeping their design and operational synergies in the right perspective. In this part, a high level review of hydrokinetic technologies and recent activities is presented. In absence of sufficient scholarly publications that categorically investigate power tracking control of hydrokinetic devices, a brief review of pertinent literature from wind energy field is conducted.

Chapter 2

Review of Hydrokinetic Energy Conversion Technologies

The process of hydrokinetic energy conversion implies utilization of kinetic energy contained in river streams, tidal currents, or other man-made waterways for generation of electricity. This emerging class of renewable energy technology is being strongly recognized as a unique and unconventional solution that falls within the realms of both inland water resource and marine energy. In contrast to conventional hydroelectric plants, where an artificial water-head is created using dams or penstocks (for large-hydro and micro-hydro, respectively), hydrokinetic converters are constructed without significantly altering the natural pathway of the water stream. With regard to ocean power utilization, these technologies can be arranged in multi-unit array that would extract energy from tidal and marine currents as opposed to tidal barrages where stored potential energy of a basin is harnessed. While modularity and scalability are attractive features, it is also expected that hydrokinetic systems would be more environmentally friendly when compared to conventional hydroelectric and tidal barrages.

In addition to worldwide interest, recent initiatives by North American entities have also seen a greater momentum [10–13]. Resource and technology assessment by EPRI in US [14], BC Hydro/Triton [15] and NRC in Canada [16] have given newer perspectives of North America's tidal current energy potential. While a number of projects are being actively pursued, notable progress has been made in Bay-of-Fundy (Nova Scotia) and in Puget Sound (Washington) [17, 18]. Recently (2003–2007), preliminary in-

vestigations on the use of hydrokinetic technologies for in-land water resources have been conducted by organization such as, US Department of Energy [19], EPRI [20], Idaho National Laboratory [21], and National Hydropower Association [22]. In response to interests from a number of project developers, US Federal Energy Regulatory Commission (FERC) has stated this technology as of tremendous potential [23]. Also, the US congress has endorsed the Energy Independence and Security Act of 2007 (the "EIS-Act" [24]) bringing further encouragement to the development of this technology. At the same time various projects and proposals are in place within a number of jurisdictions in North America (Mississippi [25], Alaska [26], Detroit [27], Ontario [28], and British Columbia [29]).

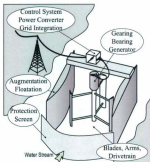


Figure 2.1: Outline of a hydrokinetic energy converter system [30]

While the enthusiasm in this field is obvious, skepticism on technological viability is also prevalent. In addition to several fundamental inquiries (resource availability, definition of technologies, field of application, etc), a number of technology-specific questions (such as, what converter type is best suited, whether duct-augmentation is worth attempting, how to place a turbine in a channel) are continuously being put forward. In this chapter, based on a comprehensive technology survey, the approach of a number

of technology developers as well as research and development (R&D) institutions are analyzed in light of the questions above. Fig. 2.1 illustrates a conceptual outline of a ducted vertical axis hydrokinetic system supplying power to the utility grid. However, any such scheme should be kept in perspective with various real-world constraints such as, availability of suitable grid interconnection points, adverse environmental impacts, as well as relevant cost and economic factors. While a complete converter system may incorporate various important sub-systems (such as, power electronics, anchoring, and environmental monitoring, Fig. 2.1), this review mostly deals with the front-end process of hydrodynamic-to-mechanical power conversion.

2.1 Hydrokinetic energy conversion devices

Being an emerging energy solution, there exists noticeable ambiguity in defining the technology classes, field of applications, and their conversion concepts. This section aims at elaborating on these issues in consultation with the existing literature and present trends.

Conversion schemes

The energy flux contained in a fluid stream is directly dependent on the density of the fluid, cross-sectional area, and fluid velocity cubed. In addition, the conversion efficiency of hydrodynamic, mechanical, or electrical processes reduce the overall output. While turbine systems are conceived as prime choices for such conversion, other non-turbine approaches are also being pursued with keen interest. A brief description of ten (10) interrelated concepts categorized in two broader classes (turbine/non-turbine) is given below:

- **Turbine systems**
 - *Axial (Horizontal)*: Rotational axis of rotor is parallel to the incoming water stream (employing lift or drag type blades) [31].

- *Vertical*: Rotational axis of rotor is vertical to the water surface and also orthogonal to the incoming water stream (employing lift or drag type blades) [9].
 - *Cross-flow*: Rotational axis of rotor is parallel to the water surface but orthogonal to the incoming water stream (employing lift or drag type blades) [32].
 - *Venturi*: Accelerated water resulting from a choke system (that creates pressure gradient) is used to run an in-built or on-shore turbine [33].
 - *Gravitational Vortex*: Artificially induced vortex effect is used in driving a vertical turbine [34].
- **Non-turbine systems**
 - *Flutter Vane*: Systems that are based on the principle of power generation from hydroelastic resonance (flutter) in free-flowing water [35].
 - *Piezoelectric*: Piezo-property of polymers is utilized for electricity generation when a sheet of such material is placed in the water stream [36].
 - *Vortex induced vibration*: Employs vibrations resulting from vortices forming and shedding on the downstream side of a bluff body in a current [37].
 - *Oscillating hydrofoil*: Vertical oscillation of hydrofoils can be utilized in generating pressurized fluids and subsequent turbine operation [38]. A variant of this class includes biomimetic devices for energy harvesting [39].
 - *Sails*: Employs drag motion of linearly/circularly moving sheets of foils placed in a water stream [40].

At present, various turbine concepts and designs are being widely pursued (Fig. 2.2) while the non-turbine systems (Fig. 2.3) are mostly at the proof-of-concept stage (with some exceptions [38]). Therefore, the former type of devices are given due attention as they hold promise for deployment in the near future.



Figure 2.2: Example of turbine systems: (a) Free-Flow™ [31] (b) Kobold™ [9] (c) Atlantisstrom™ [32] (d) HydroVenturi™ [33] (e) Neo-Aerodynamic™ [34]

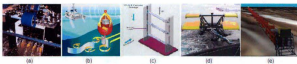


Figure 2.3: Example of non-turbine systems: (a) OCPST™ [35] (b) EEL™ [36] (c) VIVACE™ [37] (d) Seasnail™ [38] (e) Tidal Sails™ [40]

Terminologies for turbine systems

The term 'hydrokinetic turbine' has long been interchangeably used with other synonyms such as, 'water current turbine' (WCT) [28, 41], 'ultra-low-head hydro turbine' [42], 'free flow/stream turbine' (implying use of no dam, reservoir or augmentation) [43], 'zero head hydro turbine' [41, 44], or 'in-stream hydro turbine' [20]. For tidal applications, these converters are often termed as 'tidal in-stream energy converter' (TISEC) [14] or simply 'tidal current turbine'. For rivers or artificial waterways the same technology is generally identified as 'river current turbine (RCT)', 'river current energy conversion system' (RCECS) [30], 'river in-stream energy converter' (RISEC) [20], or in brief, 'river turbine'. Other common but somewhat misleading identifiers include 'watermill', 'water-wheel', or even 'water turbine' [41].

In a 1981 US Department of Energy report [42], this class of technology has been defined as "Low pressure run-of-the-river ultra-low-head turbine that will operate on the equivalent of less than 0.2 m of head". A more recent (2006) assessment by this organization [19] has classified these devices as 'low power/unconventional systems' that may

use hydro resources with less than 8 feet head. As indicated in Fig. 2.4, the USDoE report uses the hydropower potential and working hydraulic head of a potential project as measures of technology classification. This also indicates that the conventional hydroelectric plants use higher head and/or capacity in sharp contrast to the unconventional low-head/hydrokinetic schemes.

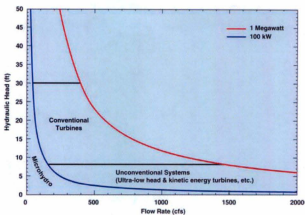


Figure 2.4: Conventional hydro versus hydrokinetic energy conversion schemes [19]

In keeping with the present norms [14, 19–21, 43] and adopting a concise term, the term ‘hydrokinetic energy conversion system’ (HECS) or ‘hydrokinetic turbine’ will be used almost exclusively throughout this dissertation. While other terms may seem suitable for application-specific cases (river, artificial channel, tidal, or marine current), this approach envelopes a broader spectrum where all kinetic energy conversion schemes for use in free-flowing/zero-head hydro streams are considered.

Areas of application

Two main areas where hydrokinetic devices can be used in power generation purposes are, (a) tidal-current, and (b) river-stream. Ocean current represents another potential source of ocean energy where the flow is unidirectional, as opposed to bidirectional tidal variations. In addition to these, other resources include, man-made channels, irrigation canals, and industrial outflows [31,45]. While all hydrokinetic devices operated on the same conversion principles regardless of their areas of application, a set of subtle differences may appear in the forms of design and operational features. These include,

- **Design**

- *Size:* In order to achieve economies of scale, tidal current turbines are currently being designed with larger capacity (several MW). River turbines on the other hand, are being considered in the range of few kW to several hundred kW [14,28].
- *Directionality:* River flow is unidirectional and this eliminates the requirement for rotor yawing. In tidal streams, a turbine may operate during both flood and ebb tides, if such yaw/pitch mechanism is in place.
- *Placement:* Depending on the channel cross-section, a tidal or river current turbine may only be placed at the seafloor/riverbed or in other arrangements (floating or mounted to a near-surface structure). This arises from a multitude of technical (power generation capacity, instrumentation) and non-technical (shipping, fishing, and recreational boating) constraints.

- **Operation**

- *Flow characteristics:* The flow characteristic of a river-stream is significantly different from tidal variations. While the former has strong stochastic variation (seasonal to daily), the latter undergoes fluctuations of dominant periodic nature (diurnal to semidiurnal). In addition, stage of a stream may have diversely varying profile for these two cases.

- *Water Density:* The density of seawater is higher than that of freshwater. This implies, lesser power generation capacity for a tidal turbine unit when placed in a river stream. In addition, depending on the level of salinity and temperature, seawater in different location and time may have varying energy content.
- *Control:* Tidal turbines are candidates for operating under forecasted tide conditions. River turbines may not fall into such paradigms of control and more dynamic control systems may need to be synthesized.
- *Resource prediction:* Tidal conditions can be almost entirely predicted and readily available charts can be used in coordinating the operation of a tidal power plant. For river applications, forecasting the flow conditions is more involved and many geographical locations may not have such arrangements. For a hydrokinetic converter, the level of power output is directly related to flow velocity (and stage). Even though volumetric flow information is available for many locations, water velocity varies from one potential site to the other depending on the cross-sectional area. Therefore, unless a correlation between flow variations and site bathymetry is established, and turbines are operated accordingly, only sub-optimal operation can be achieved.
- **End-use**
 - *Grid-connectivity:* While tidal current systems may see large-scale deployment (analogous to large wind farms), hydrokinetic converters used in river streams may become feasible in powering remote areas or stand-alone loads. Depending on how the technology evolves, this type of alternative schemes may also fall within the distributed generation scenarios in the near future. Bulk power generation through tidal power plants are expected in longer time horizons. It is expected that these technologies will face similar network integration challenges as wind power systems and will take advantage of higher resource predictability [46].

- *Other purposes:* Hydrokinetic turbines can potentially be used in conjunction with an existing large hydroelectric facility, where the tailrace of a stream can be utilized for capacity augmentation (i.e, resource usage maximization) [19, 28]). Direct water pumping for irrigation, desalination of seawater, and space heating are other potential areas of end-use.

2.2 Technology survey

In order to aid the advancement of hydrokinetic conversion technologies and develop suitable solutions to various relevant problems, it is important to identify the current status of this field of engineering and research. A survey that provides insight into the historical perspective and also indicates the industry trends can be very useful in that regard. As part of this research, a comprehensive technology review has been conducted and most of the major schemes reported to date have been considered. This survey essentially overlaps the authors' previous work [30], complements a set of more recent reports published by EPRI [14], Verdant Power [28], and Powertech Labs [29], and identifies subtle advancement in contrast to some previous reviews [42, 47].

Survey methodology

The survey conducted here not only identifies commercial systems, but also accommodates various R&D initiatives undertaken in the academia. As indicated in the Appendix A, total of seventy six different devices and schemes were analyzed. Due to availability of limited information for many devices, mostly the primary conversion hardware and their peripherals (rotors, ducts, placement method in a stream, etc.) are evaluated. The information gathered along the process is organized through the following categories:

- *Application:* In the previous section, various areas of application for hydrokinetic devices have been identified. This discussion is carried forward into the survey by categorizing the potential use of a given device into (a) tidal-current (for tidal and

ocean current resources) (b) river-stream (for free-flowing/zero-head rivers), and (c) multi-application (river, tidal, and other applications). While the information disseminated through the relevant technology developer, research institute, or public-domain document has been the basis of this classification, several ambiguous cases have been considered as 'Multi-application'.

- *Technology type:* In light of the discussion presented earlier, all of the 76 devices or concepts have been attributed to one of the ten (10) conversion schemes. However, further division into 'turbine' or 'non-turbine' systems has not been carried out.
- *Duct:* Ducts are engineered structures that elevate the energy density of a water stream as observed by a hydrokinetic converter. Considerations for these devices is of high significance primarily because of two opposing reasons (a) potential to augment the power capacity and hence reduce the cost of energy (b) lack of confidence as far as their survivability and design/demonstration are concerned. In this survey, attempts were made to identify whether a given scheme is considered for duct augmentation (unknown cases were identified separately) or not.
- *Placement:* The method of placement of a hydrokinetic device, in relation to a channel cross-section, is a very significant component for two basic reasons:
 - The energy flux in the surface of a stream is higher than that of a channel-bottom. In addition, this quantity takes diverse values depending on the distance from the shore and channel-geography. Therefore, water velocity has a highly localized and site-specific 3-dimensional profile and rotor positioning against such variations will dictate the amount of energy that can be effectively extracted.
 - Competing users of the water stream (recreational boats, fishing vessels, bridges & culverts, etc.) would essentially reduce the effective usable area for a turbine installation [28, 29].

In this research, three classes of mounting arrangements are considered: (i) BSM - Bottom Structure Mounted (Fixed) (ii) FSM - Floating Structure Mounted (Buoyant), and (iii) NSM - Near-surface Structure Mounted (Fixed). Each of the devices or schemes has been assigned to one of these methods, whereas unknown systems are identified separately.

In addition to the aspects mentioned above, each of the R&D initiatives is observed for its present status of development and chronology of progression. The summary of these assessments are given in the following section.

Analysis of survey

Although a number of novel concepts have emerged recently, hydrokinetic energy conversion has mostly seen advancements in the domain of axial (horizontal) and vertical axis turbine systems. The significantly higher number of initiatives and several commercial/pre-commercial deployments have brought these systems at the forefront this emerging industry. The commercial systems (existing/discontinued) mostly represent several small-scale river turbines employing inclined [48-51] and floating [52, 53] horizontal axis turbines. These systems were developed for remote powering applications in various countries (Sudan, Peru, etc). However, the current market-status of many these devices is unknown.

One interesting observation derived from the survey is that a great number of technology developers and researchers view their initiatives as solutions for a wide spectrum of applications, beyond river or tidal applications only. Reflecting the lesser level of resource availability, the number of technologies being developed specifically for river applications is less than that of tidal energy systems. The present trend clearly indicates that the area of multiple application (such as, river, tidal, artificial waterways, dam tail-race, and industrial outflows) is of high importance, as these technologies can probably be tailored to suit resource-specific needs.

In addition to realizing various rotor concepts, considerations for incorporating duct augmentation to these systems is a very significant aspect of this technology's overall advancement. As shown in Fig. 2.5, vertical axis systems are given more emphasis for such arrangements, whereas significant portion of axial/horizontal turbines are considered for non-ducted application.

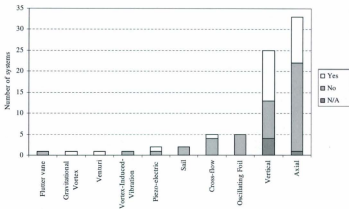


Figure 2.5: Use of ducts and conversion schemes

Regardless of the field of application (river, tidal or others), duct augmentation has naturally seen lesser share of consideration (Fig. 2.6). This arises from the fact that most of the turbine concepts are still at the R&D level, whereas ducts are peripherals to such systems.

Placement of a turbine system, in relation to a given open-channel, is another field of progression where basic design (structural strength, floatation, and anchoring)

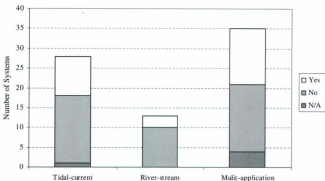


Figure 2.6: Use of ducts and applications

and feasibility studies (survivability, provisions for competing users, etc.) are being investigated. As seen in Fig. 2.7, most vertical axis turbines are being considered for either floating (FSM) or near-surface (NSM) placements. On the contrary, about one-third of the axial turbines are considered for seabed/riverbed installations. Other concepts have indicated early stage plans on their placement methods, which needs to be re-evaluated as these systems attain further advancement.

From applications point of view, river turbines have been designed and developed for either floating or near-surface arrangements. On the contrary, many tidal turbines are being considered for placement at the bottom of the channel. This reflects the constraints imposed by other competing sea users (shipping, fishing, and other usage) as well as design challenges associated with large floating or near-surface-fixed structures, especially in harsh sea conditions.

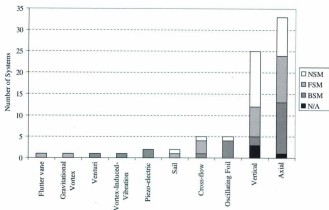


Figure 2.7: System placement and conversion schemes

While both vertical and axial turbines have long been considered as primary choices for hydrokinetic energy conversion, a number of unconventional concepts (such as, vortex induced vibration, and piezoelectric conversion) have appeared recently. Several early river turbine prototypes were deployed and operated from late 70's to late 90's [48, 52] until these were eventually decommissioned. Various non-turbine concepts (namely, oscillating hydrofoil and piezoelectric conversion) had gained good attention in the past [36, 38, 54]. However, their present status of development is unknown. Analyzing the modern day history of hydrokinetic energy conversion, it can be clearly noticed that the present decade has so far seen the greatest level of research and development initiatives. These efforts have enveloped a multitude of technological concepts as well as diverse fields of applications where hydrokinetic technologies may prosper in future.

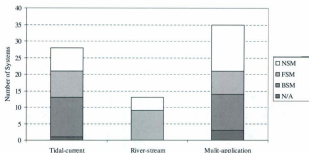


Figure 2.8: System placement and applications

2.3 Horizontal and vertical axis turbines

At the present state of this technology, both horizontal and vertical axis turbines are key contenders for further research, development, and demonstration (RD&D) initiatives [29]. In addition to aiming for specific applications (such as, tidal currents or river streams), a great number of development efforts are directed toward realizing solutions that may serve both of these areas. Duct augmentation is another area, which apparently did not find much success in the wind energy domain. However, it is perceived as a critical element to hydrokinetic conversion concepts.

In this section, an attempt is made to shed light on many of these issues using qualitative and broad observations. This review, however, does not attempt to indicate superiority of one option against the other. Rather, observations of generic nature are provided for the reader and these may appear useful depending on the scope and nature of any RD&D effort in this domain. The following discussions focus on rotor configurations, duct augmentations, and placement schemes, followed by a qualitative discussion on various technical advantages and disadvantages of these options.

Rotor configurations

As discussed in Section 2.2, hydrokinetic energy conversion may employ either rotary turbo machinery or can use non-turbine schemes. While the former class (turbine system) encompasses various classical rotary technologies, the latter group (non-turbine system) is mostly based on various unconventional concepts. Such schemes include, oscillating hydrofoil [38], vortex induced vibration [37], piezo polymer conversion [36], and variable geometry sails [40]. Presently, most of these technologies are either at their proof-of-concept stage or being developed as part-scale models. On the other hand, rotary turbine systems employing horizontal, vertical, or cross flow turbines are occupying most of the discussion. A broad survey of existing and discontinued RD&D initiatives are explored and classified in various maturity groups (from 'concept' to 'commercial') in Fig. 2.9(a). It should be noted that many of the 'commercial' systems, as shown in the figure, employ inclined horizontal axis turbines and probably no longer exist in the market.

In Fig. 2.9(b), percentages of the turbine systems among all the studied RD&D efforts (seventy six systems) are shown. It can be seen that horizontal and vertical axis turbines consist of the greater share (43% and 33%, respectively). Although this result is not surprising, the point of interest is that vertical axis systems are seeing renewed interest, especially when the wind energy industry has effectively discarded this technology.

The choice of turbine rotor configuration requires considerations of a broad array of technical and economical factors. As an emerging field of energy conversion, these issues become even more dominant for hydrokinetic turbines. A general classification of these turbines based on their physical arrangements is given in Fig. 2.10. This list is by no means exhaustive, and many of the concepts are adopted from the wind engineering domain.

Based on the alignment of the rotor axis with respect to water flow, three generic classes could be formed (a) horizontal axis (b) vertical axis, and (c) cross flow turbines.

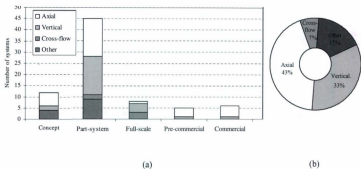


Figure 2.9: General technology status of hydrokinetic turbine technologies (a) relative advancements, and (b) percentage of different conversion schemes

The horizontal axis (alternately called as axial turbines) turbines have axes parallel to the fluid flow and employ propeller type rotors. Various arrangements of axial turbines for use in hydro environment are shown in Fig. 2.11.

Inclined axis turbines have mostly been studied for small river energy converters. Literature on the design and performance analysis could be found in [41, 55, 56]. Information on several commercial products utilizing such topologies is available in [49–51, 57]. Most of these devices were tested in river streams and were commercialized in limited scales. The turbine system reported in [57] was used for water pumping, while the others [49–51] were promoted for remote area electrification. It is however not clear whether these latter devices are still being commercialized.

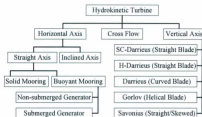


Figure 2.10: Classification of turbine rotors

Horizontal axis turbines are common in tidal energy converters and are very similar to modern day wind turbines from concept and design point of view. Turbines with solid mooring structures require the generator unit to be placed near the riverbed or seafloor. Reports and information on rigidly moored tidal/river turbines are available in [31, 42, 58-62]. Horizontal axis rotors with a buoyant mooring mechanism may allow a non-submerged generator to be placed closer to the water surface. Information on submerged generator systems can be found in [63, 64] and that of non-submerged types are presented in [43, 65].

The cross flow turbines have rotor axes orthogonal to the water flow but parallel to the water surface. These turbines are also known as floating waterwheels. These are mainly drag based devices and inherently less efficient than their lift based counterparts. The large amount of material usage is another problem for such turbines [41, 43, 66]. Darrieus turbines with cross flow arrangements may also fall under this category.

Various arrangements under the vertical axis turbine category are given in Fig. 2.12. In the vertical axis domain, Darrieus turbines are the most prominent options. Although use of H-Darrieus or squirrel-cage Darrieus (straight bladed) turbine is very common, examples of Darrieus turbine (curved or parabolic blades) being used in hydro applications is non-existent. In publications such as, [6, 43, 67-74] a wide array of design, operational

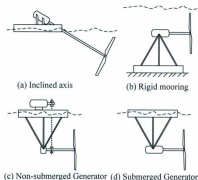


Figure 2.11: Horizontal axis turbines

and performance issues regarding straight bladed Darrius turbines are discussed. The Gorlov turbine is another member of the vertical axis family, where the blades are of helical structure [44, 75, 76]. Savonius turbines are drag type devices, which may consist of straight or skewed blades [69, 70, 77].

Hydrokinetic turbines may also be classified based on their lift/drag properties, orientation to up/down flow, and fixed/variable (active/passive) blade pitching mechanisms. Different types of rotors may also be hybridized (such as, Darrius-Savonius hybrid) in order to achieve certain performance features.

Duct augmentation

Augmentation channels induce a sub-atmospheric pressure within a constrained area and thereby increase the flow velocity. If a turbine is placed in such a channel, the flow velocity around the rotor is higher than that of a free rotor. This increases the possible total power capture significantly. In addition, it may help to regulate the speed

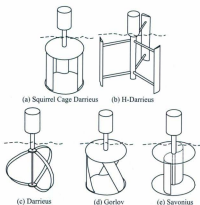


Figure 2.12: Vertical axis turbines

of the rotor and impose lesser system design constraints as the upper ceiling on flow velocity is reduced [78]. Such devices have been widely tested in the wind energy domain. Terms such as, duct, shroud, wind-lens, nozzle, concentrator, diffuser, and augmentation channel are used synonymously for these devices. Discussions on duct augmentation in river/tidal applications can be found in [42, 78-80]. A survey conducted with seventy six hydrokinetic system concepts show that around one-third of the horizontal axis turbines are being considered for such arrangements. On the contrary, vertical axis turbines are being given more attention when it comes to duct augmentation. Almost half of the studied systems consider some form of augmentation scheme to be incorporated with the vertical turbine.

The ducts for horizontal axis turbines mostly take conical shapes (for operation under unidirectional flow) as opposed to vertical turbines where the channels are of rectangular cross-section. This imposes a design asymmetry and subsequent structural vulnerability for the former type. The lesser number of duct augmentation being con-

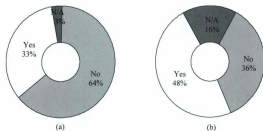


Figure 2.13: Reported consideration for duct augmentation for (a) horizontal axis (b) vertical axis turbines

sidered for horizontal axis turbines can be attributed to this issues. These results only indicate accumulated experience and understanding of duct augmentation options for horizontal and vertical axis turbines, as perceived to date. It is believed that further RD&D on this area will go hand in hand with turbine development.

A simplified classification of various channel designs are given in Fig. 2.14, and Fig. 2.15. A simple channel may consist of a single nozzle, cylinder (or straight path) with brim or diffuser. In a hybrid design, all three options may be incorporated in one unit. Test results on a number of hydrodynamic models can be found in [78, 79] and an example shape is given in Fig. 2.15(a). This work has reported a maximum velocity increase factor of 1.67 (i.e. power coefficient¹ increases 4.63 times). In [80] various hybrid models with rectilinear paths are experimented (Fig. 2.15(b)). Diffusers with multi-unit hydrofoils (Fig. 2.15(c)) are also possible when higher efficiency is required. A straight model with a brim (Fig. 2.15(d)) may have a velocity amplification factor of 1.32. Analytic and test results of various rectilinear diffuser models (Fig. 2.15(e)) can be found

¹A measure of extracted power against the theoretical fluid power considering free-stream/unducted water velocity.

in [81, 82]. It has been found that, a diffuser with an inlet and brim performs the best in this category. Information on various annular ring shaped diffuser models (Fig. 2.15(f)) can be found in [42, 83]. In [42], it has been shown that a power coefficient as high as 1.69 is possible, exceeding the Betz limit of 0.59.

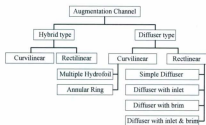


Figure 2.14: Augmentation channel classification

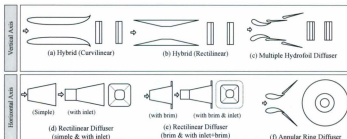


Figure 2.15: Channel shapes (top and side view)

Each of these models come with unique set of performance merits and design limitations. For instance, the hybrid types perform better at the expense of bigger size

(as high as 6 times the rotor diameter). The annular shapes also perform very well when hydrodynamic shapes are optimally designed. Nevertheless, detailed investigation on optimal size, shape and design is still an unsolved problem.

Rotor placement options

While the type of rotor to be deployed and duct augmentation to be incorporated are of paramount importance, placement of the system in a channel also deserves due attention. In general, the placement methods can be divided into three groups as shown in Fig. 2.16. A turbine may incorporate bottom structure mounting (BSM) arrangement where the converter is fixed near the seafloor/riverbed. Also, turbine units may operate under variable elevation if a floating structure mounting (FSM) is devised. The last option is to mount the converter with a structure that is closer to the surface (near-surface structure mounting, NSM).

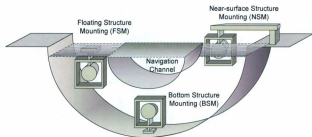


Figure 2.16: Turbine mounting options

The technology survey conducted as part of this research indicates that axial flow turbines are given almost equal consideration for the three options outlined above (Fig 2.16). However, more than half of the vertical axis turbines are being considered for near-surface placement. This probably arises from the fact that this option allows

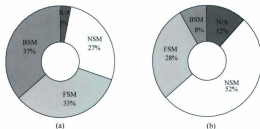


Figure 2.17: Percentage of turbines considered for various placement arrangements (a) horizontal axis (b) vertical axis

the generator and other apparatus to be placed above the water level. However, at the present state of this technology, there is no clear direction on the most attractive option. Several subtle aspects that can be observed in this regard are highlighted below:

- Energy capture:** The energy flux in a river/tidal channel is higher near the surface. This suggests that the FSM option is the best option as long energy extraction is the prime concern. In contrast, the BSM method allows only sub-optimal energy capture. Also, energy capture using the NSM scheme would see fluctuating output subject to variations in river stage or tide height.
- Competing users:** While placing a turbine at the surface of a channel seems attractive, competing users of the water resource may object to such arrangement. Fishing, shipping, recreational boating, and many other activities may leave the BSM or NSM methods as the only option. Floating structures are still possible but these need to be placed closer to the shore where energy resources may appear limited.
- Construction challenge:** Experience of floating structure design for energy harvesting is limited. In contrast, knowledge in civil engineering domain for bottom mounted

structures (e.g. bridges, offshore oil and gas platforms) are quite abundant.

- *Footprint:* Any trenching, piling, or excavation at the riverbed/oceanfloor may become subject to environmental scrutiny. Floating or near-surface structures appear more permissible in this context.
- *Design and operational constraints:* Depending on where a turbine is to be placed various power conversion apparatus (generator, bearing, gearboxes, and power conditioning equipment) would require special design considerations such as, water sealing, lubrication, and protection. Also, variation of water velocity and stage will impose operational constraints. Due attention is also required to address the challenges associated with severe storm conditions, especially for the near surface and floating-type systems.

The areas of application will have specific repercussions on use of duct augmentations devices and corresponding placement schemes. For instance, tidal and marine current turbines work under the natural events of daily tide flow and seasonal ocean current variations, respectively. River turbines operate under the influence of varying volumetric water flow through a river channel subject to various external factors such as, channel cross-section, rainfall, and artificial incidences (such as, transportation, upstream dam opening etc.). River water is less dense than seawater and therefore it has lower energy density. Siting is more stringent in river channels as the usable space is limited and river transportation may further constrain the usability of the sites. There could also be varying types of suspended particles and materials (fish, debris, rock, ice etc.) in river and sea channels depending on the geography of a site. It remains to be seen, how these factors will affect the design, operation, and commercialization of various turbine concepts.

2.4 Technical advantages and disadvantages

It is worthwhile to investigate the opportunities and challenges associated with various hydrokinetic turbine systems, especially when this sector of energy engineering is mostly at the design and development phase. Of particular interest is a review of both horizontal and vertical axis configurations with regard to their technical merits and drawbacks. In this section these two configurations will be studied further.

Vertical axis turbines, especially the straight bladed Darrieus types have gained considerable attention owing to various favorable features such as:

- *Design simplicity:* As an emerging technology, design simplicity and system cost are important factors that may determine the success of hydrokinetic turbine technology. In contrast to horizontal axis turbines where blade design involves delicate machining and manufacturing, use of straight blades make the design potentially simpler and less expensive.
- *Generator coupling:* For hydrokinetic applications, generator coupling with the turbine rotor poses a special challenge. In the horizontal axis turbines, this could be achieved by a right-angled gear coupling, long inclined shaft or underwater placement of the generator. In vertical axis turbines, the generator can be placed in one end of the shaft, allowing the generator to be placed above the water surface. This reduces the need and subsequent cost in arranging water-sealed electric machines.
- *Flotation and augmentation equipment:* The cylindrical shape of the Darrieus turbine allows convenient mounting of various curvilinear or rectilinear ducts. These channels can also be employed for mooring and floating purposes [78]. For axial flow turbines, ducts cannot be easily used for flotation purposes.
- *Noise emission:* Vertical turbines generally emit less noise than the horizontal turbine concepts due to reduced blade tip losses [84]. Subject to further research and investigation, this may prove to be beneficial in preserving the marine-life habitat.

- *Skewed flow:* The vertical profile of water velocity variation in a channel may have significant impact on turbine operation. In a shallow channel, the upper part of a turbine faces higher velocity than the lower section. Vertical turbines, especially the ones with helical/inclined blades are reportedly more suitable for operation under such conditions [85].

The disadvantages associated with vertical axis turbines are: low starting torque, torque ripple, and lower efficiency. Depending on their design, these turbines generally possess poor starting performance. This may require special arrangement for external electrical, mechanical, or electromechanical starting mechanisms. The blades of a vertical turbine unit are subject to cyclic tangential pulls and generate significant torque ripple in the output. Cavitation and fatigue loading due to unsteady hydrodynamics are other concerning issues associated vertical turbines. Axial flow turbines on the other hand, eliminate many of these drawbacks. In addition, various merits of such rotors are:

- *knowledge-base:* Literature on system design and performance information of axial type rotors is abundant. Advancements in wind engineering and marine propellers have significantly contributed to this field. Use of such rotors have been successfully demonstrated for large scale applications (10 – 350 kW), especially for tidal energy conversion [59].
- *Performance:* One key advantage of axial type turbines is that all the blades are designed to have sufficient taper and twist such that lift forces are exerted evenly along the blade. Therefore, these turbines are self-starting. Also, their optimum performance is achieved at higher rotor speeds, and this eases the problem of generator matching, allowing reduced gear coupling.
- *Control:* Various control methods (stall or pitch regulated) of axial type turbines have been studied in great details. Active control by blade pitching allows greater flexibility in over speed protection and efficient operation [59].

- *Annular ring augmentation channels:* Annular ring type augmentation channels provide greater augmentation of fluid velocity as these systems allow concentrated/diffused flow in a three-dimensional manner [42]. The circular shape of the propeller rotor's disc permits the use of this type of duct, which is not possible for vertical axis turbines.

The major technical challenges encountered with axial type rotors are: blade design, underwater generator installation and underwater cabling. While different types of rotors come with unique features, only extensive theoretical understanding, experimental validation, and design expertise would allow selection of an ideal system. As the industry matures, greater insight into various rotor systems will be available.

2.5 Summary of technology review

In this chapter, the state of the hydrokinetic energy conversion technologies has been revisited with an emphasis on indicating the current trends in research and development initiatives. While the initial discussions encompassed various definitions and classifications, the core analysis has been undertaken based on a comprehensive literature survey. The major conclusions that can be derived from the discussions presented earlier are:

- Except for some early commercial systems (small-scale remote power generation from river streams), most of the technologies are at the proof-of-concept or part-system R&D stage.
- A number of novel schemes (such as, piezo-electric, biomimetic and vortex-induced-vibration) have surfaced in recent times, in addition to the continued progress on classical hydrokinetic energy conversion approaches (vertical, axial turbines, etc.).
- In the presence of a wide variety of terminologies attributed to the fundamental process of kinetic energy conversion from water streams, the term 'Hydrokinetic' energy conversion can be used as long as sufficient caveats are given for diverse fields of application such as, rivers, artificial channels, tides, and marine currents.

- In addition to the specific focus on river or tidal current conversion, strong emphasis is given to technologies that may serve both of these areas as well as other potential resources (such as, man-made canals, irrigation channels, and industrial outflows).
- While both axial and vertical axis turbines are being developed for hydrokinetic energy conversion, considerations for duct usage have seen higher preference for the latter class.
- Various options for turbine placement with respect to a channel cross-section (bottom, floating, or near-surface/fixed) are being given almost equal emphasis. However, axial turbines are mostly being considered for placement at the bottom of a channel, whereas vertical turbines are being designed for either floating or near-surface mounting arrangements.
- Recent technological advancement and project-development initiatives clearly indicate a rejuvenated interest in the domain of hydrokinetic energy conversion.

As the hydrokinetic technologies evolve over time, new solutions emerge, and old concepts resurface/disappear, the review presented in here may need to be re-evaluated. However, the major observations made in this section may still appear useful in identifying the technology trend being followed in this field of energy engineering. To conclude this discussion, it can be stated that hydrokinetic energy technologies are emerging as a viable solution for renewable power generation and significant research, development, and deployment initiatives need to be embarked upon before realizing true commercial success in this sector.

Chapter 3

Review of Applied Research in Hydrokinetic System Control

Being a dynamic field of energy engineering, hydrokinetic turbine design, development, and demonstrations activities presented in the preceding section, is evolving very rapidly. A number of investigations aimed at system integration and controller development are also being pursued by various entities. However, availability of public domain information is very insufficient and comprehensive study results are almost non-existent. Nonetheless, the insights gained through these activities can be considered as invaluable and a review of pertinent literature may provide important directions.

3.1 Review of hydrokinetic system control initiatives

With regard to hydrokinetic turbine control, one of the most recent and directly relevant research is conducted by Ginter *et. al.* [86]. The essence of this research is the development and demonstration of a robust gain scheduling controller (H_∞ - linear parameter varying) that can operate throughout the full range of a hydrokinetic system. This work can be undoubtedly termed as a pioneering applied research, where the need for adaptive power tracking capability has been identified as a potential future research. In addition, this research implicitly outlines the immensity of time, effort, and resource requirements, toward commissioning a comprehensive test program. Highlights of relevant real-world deployment initiatives can be found in presentations such as in [87].

On the other hand, one of the first attempts to use an electrical means in hydrokinetic turbines to achieve maximum power extraction can be found in the work reported

by Tuckey *et. al.* [62]. In this project, the maximum power extraction of a small horizontal axis tidal turbine was examined and the tip speed ratio (TSR) of the turbine was directly regulated using a PID type controller. A power coefficient between 20 – 30% was reported and further investigation of blade pitching mechanism was suggested.

Apart from the references cited above, only other references to hydrokinetic control can be found in [88-90]. Most of these works fall short of identifying and addressing power tracking control issues at any detail.

From a mechanical engineering and more specifically, from a fluid-dynamic perspective, the existing knowledge-base on hydrokinetic turbine design and performance is quite rich [3, 7, 91-93]. In sharp contrast, studies with emphasis on control aspects for such systems is very rare. Most of the available literature marginally accommodate active pitch control of tidal turbines employing propeller type rotors [56, 59, 62].

Islam *et. al.* [56] have studied the effects of varying blade pitch and shaft inclination angle for an inclined horizontal axis system and an average mechanical system efficiency of 30% was reported. For vertical axis turbines, most of the control studies also involve a blade pitching mechanism called 'cycloidal pitching'. This is a passive mechanism and as outlined in [94-96], requires sophisticated asymmetrical design of the rotary components.

Considering the knowledge-gap and technological barriers, the emphasis of this work is given toward studying the electrical control schemes for a vertical axis turbine with a view to extracting the maximum amount of power. Realizing the control objectives through electrical means will allow significant simplifications in system design and may permit incorporation of intelligent algorithms utilizing widely available modern embedded electronics.

3.2 Permanent magnet alternator based wind turbine control

While control studies on hydrokinetic turbines is a rarity, wind energy domain is abundant in this regard and may provide important directions toward developing an appropriate control technique for hydrokinetic turbines. Considering the scope of this research, in this review, emphasis is given on fixed-pitch, variable speed wind energy conversion systems (WECS) with permanent magnet alternators (PMA). Also, methods requiring lesser system parameters and reported works with experimental results are given more prominence. Also, in the context of this research, power tracking control methods with true-sensorless (i.e., neither employing mechanical sensors nor realizing their mathematical representations) features are given higher priority.

The PMA based wind turbine presents several unique features such as direct voltage-speed relationship and provision for only speed/torque control. Also, being an asynchronous machine (operating in variable speed/variable frequency mode), use of power electronic converters is indispensable, especially for grid-connected operation. A good number of approaches proposed in the literature have attempted to exploit these observations toward developing novel control methods [97–101]. While these methods have diverse merits, they are unappealing within hydrokinetic systems, for the following reasons:

- Works presented in [97, 99], albeit ‘sensorless,’ require expensive computation, which makes them rather infeasible for real-world scenarios.
- Methods given in [98, 100, 101], are mere reflection of other control methods (such as, tip speed ratio (TSR) or power signal feedback (PSF) control) and heavily rely on system parameters and their interrelationships. Therefore, system modeling and parameter extraction are key requirements for such algorithms.

A large volume of information detailing control methods of WECS can be found in other publications (such as, [86, 102]) and should be consulted in gaining greater understanding of relevant controller synthesis procedures.

3.3 Maximum power point tracking control

Maximum power point tracking is a general term that accommodates various rather ambiguously cited methods found in the literature (hill-climbing search control [103], periodic duty ratio control [104], or directly maximum power point tracking (MPPT)). While strategies proposed in [105-107] are based on the concepts of extremum seeking algorithms, no thorough insight into their implementation and subsequent problems is given. Chang *et. al.* [103,108] and Mutoh *et. al.* [109] have presented several maximum power tracking (MPT) methods that are also based on similar algorithms. In these works, the full range of wind turbine operation is divided into various regions and predetermined system characteristics are incorporated during controller synthesis. Therefore, the very argument that maximum power point tracking controllers require little system information, is violated.

A generic outline of these methods and proposal for a new alternative is given in [110]. This solution estimates a set of parameters and ensure tracking along an optimum point. While this could be useful for WECS control, it is doubtful that it could be suitable for HECS technologies because of the significant computational overhead.

The approaches presented in [111, 112] and [113] outline the fuzzy rule-based steepest ascent maximum power tracking (SA-MPT) control method. Datta, *et. al.* [111] and Koutroulis, *et. al.* [112] present two similar steepest ascent algorithms, in which, variations in power are measured and used to implement the MPT control, while changes in rotor speed are given little considerations. Although, power variation measurement is simple, determination of the weighing factor that determines the tracking reference, is quite difficult and system-dependent. In contrast, in Simoes *et. al.*'s work [113], stepping action of the tracker is generated through a fuzzy rule-base and these rules are tuned through heuristic approaches. Also, three fuzzy logic controllers are used for achieving the desired system performance, making it largely unacceptable, especially when a simple solution is sought. Modified forms of this work can be found in [114,115], which pave the path for a more suitable tracking algorithm.

In addition to employing a hill-climbing MPT method, work presented by Yaoqin *et. al.* [116] provides direction on how to ramp the rotor speed during each stepping action, ensuring lesser mechanical stress. Also, the concept of addition of an offset alongside a generated tracking reference is introduced by Tanaka *et. al.* [117] where only output load is directly controlled to regulate the system's behavior.

A careful review of these publications revealed that controller design activities within the hydrokinetic systems would require greater understanding of the system operation and overall performance. Therefore, subsequent focus is given on identifying the true control challenges associated with hydrokinetic systems and developing appropriate techniques to address those.

3.4 Summary of applied research review

The literature review presented in this chapter, albeit non-exhaustive, provides important directions toward further activities. Subtle observations in this regard are

- Only a handful of publications discuss the power tracking control issues as appropriate for hydrokinetic systems.
- Vast amount of information is available in the wind energy industry and there exists significant synergy in controller synthesis between WECS and HECS technologies.
- To date, power tracking control challenges that are unique to hydrokinetic systems, have not been explicitly identified and this step should precede any further controller design initiative.

In latter sections, further review is conducted in the context of the topic being discussed. Also, citations to reference materials are given throughout the dissertation such that avenues for independent research can be found.

Part II

Development and Validation of Simulation Models

Development and Validation of Simulation Models

In order to carry out systematic studies on power tracking control issues, it is critical to develop and validate a set of numerical models that is reliable and sufficient in details. This part of the thesis outlines these activities. The first chapter (Chapter 4) in this part outlines generic methods of representing tidal or river flow variations as observed by a turbine system. This, and the previous discussions (Part I) are further refined and subsequent focus is given on a vertical axis hydrokinetic system. Given the breadth and diversity of various turbine systems and their fields of applications, it becomes indispensable to carry out targeted research on a system that can be built, tested, and modeled. Therefore, this research focuses on a vertical axis straight bladed Darrieus rotor based HECS. The rotor is coupled to a multi-pole outer rotor permanent magnet generator and is interfaced to the single phase electric grid through an ac-dc-ac conversion system. In Chapter 5, a method of steady state performance prediction for a vertical axis Darrieus rotor is presented. This performance information is embedded in dynamic modeling of the complete hydrokinetic system as described in Chapter 6. This chapter also contains component-level model validation. In Chapter 7, description of laboratory and tow tank test apparatus is given. This chapter also includes verification of the numerical models developed in the preceding section. Subsequent control analysis in Part III and Part IV rely heavily on these models.

Chapter 4

Flow Field Representation

The flow field consists of a set of factors that are external to the hydrokinetic device's control boundaries but affect the incident energy flux on the system and determine the overall power capture.

The objective of this chapter is to consider hydrokinetic systems a class of conversion solutions (horizontal/vertical, ducted/un-ducted, river/tidal, floating/bottom-mounted/surface-mounted, or small/large device) and to

- Identify various flow field components affecting a hydrokinetic system and assess their possible impacts on the overall power extraction.
- Analyze the time scale of variation reflecting the dynamics of relevant flow field components.
- Establish the magnitude and range of various flow field parameters that are of interest to the power tracking control problem.

The incident water velocity is the most perceivable factor that determines the power capture of a hydrokinetic turbine. Unlike wind turbines and unique to this class of conversion principle, there are other elements that deserve due attention. Eq. 4.1 expresses this relationship and identifies the contributions of various flow-field elements.

$$P_{rot} = \frac{1}{2} C_p \rho_w A_r v_p^3 k_{dp} \quad (4.1)$$

$$k_{dp} = k_{avg} \times k_{prof} \times k_{skew} \times k_{yaw} \quad (4.2)$$

Here, P_{rot} is captured rotor power, C_p is rotor performance coefficient, ρ_w is density of water, A_r is effective rotor area, v_p is point velocity observed near the rotor, and k_{dp} denotes a set of design and placement related factors. Further breakdown of these factors are illustrated in Fig. 4.1.

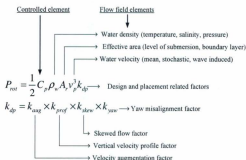


Figure 4.1: Flow-field elements

While the separation of the design and placement related factors from the performance coefficient is a novel proposition of this research (which can be argued), any relevant research may also consider consolidating these factors under one coefficient staying within the present norms of the relevant literature.

4.1 Velocity of water

Velocity of water is the single most dominant element amongst the flow field elements. Variation in water velocity has strong dependence on the field of application (such as, river, tidal, tidal-rivers, artificial channels, dam tailrace, etc). This dependence arises from numerous factors such as, channel cross-section (river channel profile, tidal channel bathymetry, etc) or climatic factors (such as, precipitation, snow melting, etc.).

In wind energy studies, wind resource is estimated over a large geographical location (in the range of square kilometers). Also, readily available wind data is used in conjunction with standard methods of analysis [118]. In hydrokinetic applications, resource levels may appear significantly different within several meters along the same stream. Also, there is no standard method of classifying and quantifying the resource characteristics.

Traditionally river velocity measurements are conducted with objectives such as, determining volumetric flow rate and assessing sediment transport, erosion levels, etc. Tidal stream measurements are conducted with a view to assessing the impact on navigation, coastal protection, etc. Very rarely river or tidal stream velocity is documented and made available for hydrokinetic technology purposes. Even though river velocity measurement is the first step in determining volumetric discharge, most databases only report the latter. This is primarily so because, velocity is a highly localized parameter, as against volumetric flow, which is interpretable throughout a channel.

In order to evaluate subtleties of velocity variation, a set of time series plots pertaining to river and tidal streams on diverse time-horizons will be useful. As seen in Fig. 4.2 (Yukon River, measurement at Pilot Station (GRDC-ID 4103200, 162.5 °N 61.5 °E, Drainage area 831390 km²) for year 1987 – 88 [119]), river velocity typically exhibits peak seasonal characteristics, owing to environmental factors such as, elevated rainfall or temperature increase (resulting in snow melting).

Further examination on a time-series dataset that span throughout several months,

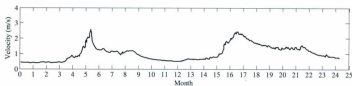


Figure 4.2: Example of annual (year to year) variations of river velocity

indicate that it is quite possible to have near-constant velocity for a number of days as shown in Fig. 4.3 (time series of water surface velocity measured by RiverSonde for the Cowlitz River at Castle Rock, Washington [120]).

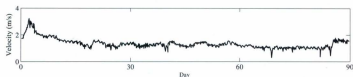


Figure 4.3: Example of monthly (month to month) variation of river velocity

Even though a mean velocity prevailing over a number of days is common for river streams, it does not imply that stochastic variations from minutes to hours could be insignificant. Fig. 4.4 (five hour measurement in White River, Indianapolis, USA [121]) shows an example of such hourly variations.

Typically, river velocity and discharge levels are predicted using various numerical estimation methods such as, correlating historical climate data to forecast streamflow conditions or least square fitting. Tidal velocity and height prediction, on the other hand, can be done using various readily available classical algorithms. As seen in Fig. 4.5 (predicted tidal velocity (absolute value) at Grand Manan Channel (Bay of Fundy entrance), New Brunswick Current; Jan. 01, 2009, to Dec. 31, 2009 [122]), tidal velocity variation

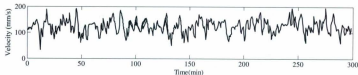


Figure 4.4: Example of hourly river velocity variation

is highly periodic and dominant fluctuations can be observed between spring and neap tides (fortnightly cycle). These dominant variations can be clearly seen in the case of Fig. 4.5.

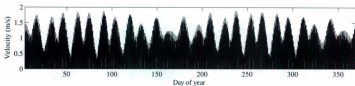


Figure 4.5: Example of year round tidal current velocity

Within hourly/daily time-scales, most tidal sites exhibit strong semidiurnal (two high waters and two low waters each day) variations as shown in Fig. 4.6 (time series of north-south velocity at Scripps Pier in La Jolla, California [123]).

A closer look at part of one tidal cycle (3 hours) indicates subtle stochastic velocity components residing with the mean velocity as shown in Fig. 4.7 (Measurements at Parker River Estuary, Plum Island Sound, Massachusetts over one-half of a tidal cycle [124]).

In order to synthesize and analyze water velocity variations through numerical approaches, variations in the forms of seasonal/mean conditions, turbulence contributions as well as wave-current interactions need to be studied in greater details.

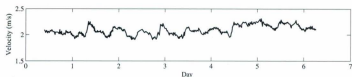


Figure 4.6: Example of daily (day to day) tidal velocity variation

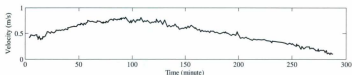


Figure 4.7: Example of hourly (hour to hour) tidal velocity variation

4.1.1 Seasonal variation component

Seasonal water velocity variations may take place on a long term basis spanning from hours to days. In most cases (especially for the purposes of controller synthesis), such variations can be considered having a mean/constant value, which is further superimposed by a faster turbulence component.

In classical open channel hydrological studies, mean river velocity is empirically cross-correlated to friction losses, channel slope, and hydraulic radius through Manning equation [125], which states

$$v_R = \frac{1}{n_m} R_m^{2/3} S_m^{1/2} \quad (4.3)$$

where n_m is Manning resistance constant (m/s), R_m is hydraulic radius (m^{-3}/s) and S_m is channel slope (m/m). In Table 4.1 a set of typical examples of Manning

resistance constant is given.

Table 4.1: Manning resistance constant [125]

Channel condition (s)	n_{ms}
Glass	0.010
Painted Steel	0.014
Unfinished concrete	0.014
Corrugated Metal	0.016
Masonry Rubble	0.025
River valley	0.025
Natural clean and straight	0.030
Major rivers	0.035
Sluggish reaches and deep weedy pools	0.065

A field measurement of the velocity spectrum indicates that low-frequency variations are primary energy carriers and there is no specific high-frequency component of interest. Fig 4.8(a) shows an example of river velocity spectrum (White River, Indianapolis, USA, during 23 May-7 June 1999 [121]), whereas (b) shows frequency spectrum of tidal velocity variations (horizontal tidal current velocity at Stn. T, in the Mizushima Sound (Mizushima-Nada), Seto Inland Sea, Japan, measured during Sept. 22 - Oct. 7, 1977 [126]).

Tidal velocity can be estimated a-priori through classical tidal harmonic synthesis [127, 128] using expressions of the form

$$v_T = f_t (C_t \sin(\omega_t t)) \quad (4.4)$$

where ω_t and C_t are frequency and amplitude of various harmonic elements (M2, S2, N2, K2, K1, O1, P1, Q1, Mf, Mm, Sm), which are in essence summed through the function f_t . Further details of these elements are given in Table. 4.2.

As seen in Fig. 4.8, in sharp contrast to river velocity spectrum, tidal variations exhibit dominant semidiurnal and other components.

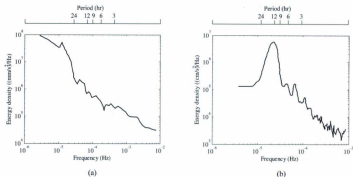


Figure 4.8: Examples of (a) river current velocity spectrum (b) tidal current frequency spectrum

4.1.2 Turbulence component

In the previous section subtle aspects of river and tidal velocity variations, which fall in the range of minutes to hours, have been discussed. In the higher end of the velocity spectrum there resides high frequency variations, typically termed as turbulence component. In hydrokinetic applications, these high frequency variations may occur due to two broad reasons. Various site-specific factors such as, channel profile, bed roughness, wind-wave interactions etc. may contribute to the overall turbulence conditions. Also, the hydrokinetic turbine system itself as well as various multi-body interactions (mounting arrangement, augmentation channel, or additional nearby rotors) will cause the incoming water jet to form eddies in its field of operation.

A series of tests conducted as part of this work reinforces this notion (albeit qualitatively) as shown in Fig. 7.27. Bow waves formed at the upstream of the hydrokinetic system, disperses into turbulent wakes at the downstream. Also, the mounting structure,

Table 4.2: Tidal harmonic components [128]

Tidal harmonics name	Harmonic elements	Equilibrium Amplitude(m)	Period(hr)
Semidiurnal			
Principal lunar	M2	0.242334	12.4206
Principal solar	S2	0.112841	12.0000
Lunar elliptic	N2	0.046398	12.6584
Lunisolar	K2	0.030704	11.9673
Diurnal			
unisolar	K1	0.141565	23.9344
Principal lunar	O1	0.100514	25.8194
Principal solar	P1	0.046843	24.0659
Elliptic lunar	>Q1	0.019256	26.8684
Long Period			
Fortnightly	Mf	0.041742	327.85
Monthly	Mm	0.022026	661.31
Semiannual	Sm	0.019446	4383.05

turbine's rotation, and reflected waves constitute a complex and turbulent flow field.

With a view to demonstrating such fast water current variations, a set of time series measurement at Upper Mississippi River, Brownsville, MN [129] is shown in Fig. 4.9. In addition, tidal river velocity time series measurements at Ota River estuary, Hiroshima Bay, Japan [130] is presented in Fig. 4.10, with this regard.

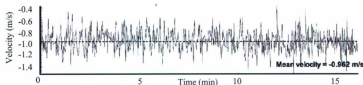


Figure 4.9: River velocity time series measurement (variations in short time scale)

Such turbulence is typically correlated to its velocity spectrum through the Kolmogorov's $-5/3$ law [131]. This empirical formulation is given as

$$S_v(\omega_v) = \alpha_k (\sigma_u \varepsilon)^{\frac{2}{3}} \omega_v^{-\frac{5}{3}} \quad (4.5)$$

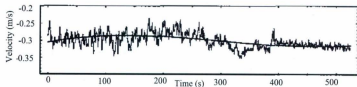


Figure 4.10: Tidal river velocity time series measurement (variations in short time scale)

Here, α_k is Kolmogorov's empirical constant (≈ 0.48), ε is turbulent kinetic energy dissipation rate (cm^2/s^3), σ_u is longitudinal mean velocity (cm/s), and ω_e is the frequency of velocity variation (rad/s).

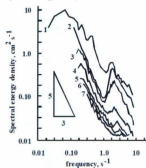


Figure 4.11: Kolmogorov's law and river velocity spectrum [131]

Fig. 4.11 (curve 1 is fit to Kolmogorov's law with $\varepsilon = 12.5 cm^2/s^3$, $\sigma_u = 15 cm/s$). This velocity spectrum is for measurements at Jordan River at the mouth region (at 7 different cross-sections) into Lake Kinneret, Israel [131].

4.1.3 Wave-current interactions

Hydrokinetic turbines placed in tidal environment are subject to ocean current as well as wave induced velocity. The magnitude and frequency of this velocity component, which will be discussed momentarily, can be of significance to power tracking control purposes [88, 132]. The prevailing sea-state (characterized by significant wave height and wave period [132]), water depth, and rotor hub-height - all play important roles in determining this effect. These two-dimensional small-amplitude (i.e. small with respect to the depth of the water and have small water surface angles) waves are called short or Stokes waves. Analysis of wave-current interaction is a complex, nonlinear, and dynamic problem. However, a set of classical yet simpler formulations deemed useful in this regard is given in the following discussion.

The Stokes transport phenomena occur between crests and troughs of a wave and these orbital velocities diminish with an increase in water depth as shown in in Fig. 4.12 [133].

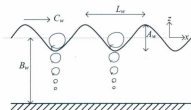


Figure 4.12: Stokes transport phenomena

A regular swell traveling with a velocity C_w over an area with constant water depth B_w is typically characterized by its amplitude A_w (height between crest and trough) and period T_w .

Solving classical Navier-Stokes equations under the assumptions of incompressible, inviscid and irrotational flow, the velocity potential ϕ_w for the small-two dimensional waves can be found as

$$\phi_w(x, z, t) = \frac{gA_w \cosh k_w(z + B_w)}{2\omega_w \cosh k_w B_w} \sin \frac{2\pi}{L_w}(k_w x - \omega_w t) \quad (4.6)$$

Small signal perturbation above the mean surface is given as

$$\xi_{ss}(x, t) = \frac{A_w}{2} \sin \frac{2\pi}{L_w}(k_w x - \omega_w t) \quad (4.7)$$

For the class of waves in discussion, the wave number is defined as $k_w = \frac{2\pi}{L_w}$ where L_w is the wavelength. The wave velocity has the form

$$C_w^2 = \frac{gL_w}{2\pi} \tanh \frac{2\pi A_w}{L_w} \quad (4.8)$$

and using the definition of wave velocity $C_w = \frac{\omega_w}{k_w}$, the wave radian frequency ω_w is found as

$$\omega_w^2 = gk_w \tanh k_w A_w \quad (4.9)$$

The above relationships can be simplified further for shallow, deep, or intermediate water depths. For deep-water conditions ($\frac{B_w}{L_w} > 0.5$, $L_w = \frac{gT_w^2}{2\pi}$) with $x \rightarrow \infty$, $\tanh x \rightarrow 1$, the wave velocity equation above simplifies to $C_w = \sqrt{\frac{g}{k_w}}$, whereas the wave frequency becomes $\omega_w = \sqrt{gk_w}$.

For shallow water conditions with $x \rightarrow 0$, $\tanh x \rightarrow x$, the wavelength and waver velocity becomes $L_w = T_w \sqrt{gB_w}$ and $C_w = \sqrt{gB_w}$, respectively. For intermediate depths ($0.25 > \frac{B_w}{L_w} > 0.05$), the wave velocity equation is solved iteratively and is approximated as $L_w = L_w \sqrt{\tanh \frac{2\pi B_w}{L_w}}$.

In deep water, the orbital motion is exhausted at the bottom and exponential distribution of the tangential velocity component is given as

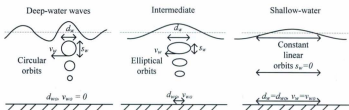


Figure 4.13: Water depth versus wave-current interactions

$$v_w = \frac{\pi A_w}{T_w} \exp(k_w z) \cos(k_w x - \omega_w t) \quad (4.10)$$

For shallow water depths, the orbital motion is diminished to mere linear motion and the corresponding velocity component becomes

$$v_w = \frac{A_w}{2} \sqrt{\frac{g}{B_w}} \cos(k_w x - \omega_w t) \quad (4.11)$$

In intermediate depths, the orbital motion is elliptical and the approximates of the velocity vector is

$$v_w = \frac{\pi A_w}{T_w} \frac{\cosh k_w (B_w + z)}{\sinh k_w B_w} \cos(k_w x - \omega_w t) \quad (4.12)$$

At $z = 0$ this equation represents identical surface velocity as found in the deep-water velocity equation. Also, at the bed ($z = -B_w$) this equation agrees with formulations as given in [133].

Placement of tidal hydrokinetic turbines in shallow channels is not attractive due to weaker tidal regimes. Similarly, far-offshore installations are also not feasible for lesser

energy potential and installation challenges. Most attractive tidal resources are in rather constrained channels and it is reasonable to expect intermediate depth scenarios are of interest.

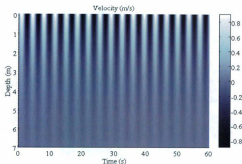


Figure 4.14: Velocity distribution at various water depths due to wave-current action

Using standard PM (Pierson - Moskowitz [134]) Sea Spectrum the spatial (channel depth 7.5m) and temporal (60 second observation) velocity distribution for sea state 2.5 ($A_w = 1$ m, $T_w = 3.5$ s, $L = 12$ m, moderate) is plotted in Fig. 4.14 for a hypothetical rotor placed at the wave-crest ($\frac{x}{L} = 0.25$).

4.2 Density of water

Salinity is defined as the total amount of solid material dissolved in water. The power produced by a hydrokinetic turbine is directly proportional to the density of water. Similar to wind energy studies, most hydrokinetic systems research considers water density to be constant (1000 kg/m^3). Often ignored is the fact that water density is highly site-dependent, susceptible to climatic conditions, and may exhibit variations within hours.

From freshwater to seawater, density may vary from $< 1000 \text{ kg/m}^3$ to $> 1030 \text{ kg/m}^3$. Therefore, inaccurate assessment of density may result in as much as 3% error in power estimates.

Water density is a function of dissolved solids (salinity), temperature, and pressure (depth) as shown in Eq. 4.13.

$$\rho_w = \rho_w(S, T, p_f) \quad (4.13)$$

Pure water has a maximum density (at 4°C , atmospheric pressure) of

$$\rho_w = \rho_w(0, 4^\circ\text{C}, 1\text{bar}) = 1000 \text{ kg/m}^3 \quad (4.14)$$

Typically the salinity of fresh water (rivers, lakes, and streams) is significantly less than that of seawater (0.1%, compared to 3.5% in typical open oceans) and therefore density variations is minimal. On the contrary, seawater salinity varies greatly as shown in a typical nonlinear relationship chart below [135]. For hydrokinetic turbines placed in the tidal channels, the near-surface salinity relationship given in Fig. 4.15 is readily usable.

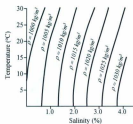


Figure 4.15: Water density as a function of salinity and temperature

Various standard coherence studies amongst tidal velocity, temperature, and salinity indicate that variations in water density (albeit small in magnitude) may occur in

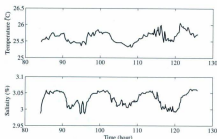


Figure 4.16: Measurement of salinity and temperature variations

the range of several hours [126, 136]. Fig. 4.16 shows temperature and salinity measurements at Stn. T, in the Mizushima Sound (Mizushima-Nada), Seto Inland Sea, Japan, measured during Sept. 22 - Oct. 7, 1977 [126].

4.3 Design and placement related factors

The velocity observed at the vicinity of a turbine rotor can be significantly different from the effective velocity accounted for ultimate power capture. Any subtle difference between assumed and actual velocity will have an effect proportional to the cube of this difference.

For a hydrokinetic turbine system, the relevant design and placement factors are related to: use of duct augmentation, vertical velocity profile, velocity skew effect, and yaw misalignment. Taking, $k_{eq} = \frac{1}{2}C_p\rho_w A_r$, the relationship between captured power and effective velocity v_{eff} and point velocity v_p is given through

$$P_{rot} = k_{eq}v_{eff}^3 \quad (4.15)$$

$$P_{rot} = k_{eq}v_p^3 k_{dp} \quad (4.16)$$

This yields the design and placement factors as

$$k_{dp} = \left[\frac{v_{eff}}{v_p} \right]^3 \quad (4.17)$$

In the following discussion these factors along with their simple mathematical interpretations are presented.

4.3.1 Velocity augmentation factor

Use of a duct allows the incident velocity to increase linearly until the augmentation effect is saturated. This linear relationship is reflected in the augmentation factor through a constant k_{aug}^0 , while the non-linear/saturation effect is accommodated using higher order terms as

$$k_{aug} = \left[\frac{v_{eff}}{v_p} \right]_{aug}^3 = k_{aug}^0 + k_{aug}^1 v_p + k_{aug}^2 v_p^2 \dots \quad (4.18)$$

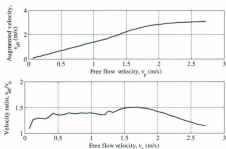


Figure 4.17: Measurement of salinity and temperature variations

A thoroughly studied system reported in [78,79] exhibits linear velocity increase up to $v_p \approx 1.5$ (m/s). This relationship is presented in terms of the ratio of effective to point velocity in Fig. 4.17. Corresponding augmentation factor coefficients are: $k_{aug}^o = 1.8$, $k_{aug}^1 = 1$, $k_{aug}^2 = 0.3$.

To date, there has been no agreed way of representing the duct augmentation effect into the velocity-power relationship (Eq. 4.1). Also, this factor is highly design-specific and the technology is not proven through extensive field trials. For a basic augmentation system, only the constant term in Eq. 4.18 (i.e., linear velocity augmentation) can be used. For systems where ducts are not used, $k_{aug} = 1$ is to be used.

4.3.2 Vertical velocity profile factor

Depending on the placement method of a hydrokinetic turbine (bottom mounted, floating, or surface-structure mounted) and characteristics of the river/ocean bed, the effective velocity at the rotor hub-height will be different from the velocity measured at any other depth. The vertical velocity distribution in such conditions is typically represented in two ways: (a) logarithmic profile method, and (b) empirical power law.

The logarithmic profile relates the mean flow velocity to the distance above the channel bottom. This method relies on the roughness characteristics of the bed and applies only within the boundary layer (part of the water column in which the velocity is significantly influenced by the bottom layer) [137].

Under this formulation, the effective velocity at a height z from the bottom is given as,

$$v_{eff}(z) = \frac{u_*}{\kappa} \ln \frac{z}{z_o} \quad (4.19)$$

where u_* is the shear velocity (cm/s), κ is the von Karman constant (≈ 0.41), and z_o is the hydraulic roughness length (cm) [137, 138]. Bottom roughness parameters for selected terrains are given in Table 4.3.

Table 4.3: Bottom roughness parameters [128]

Characteristics	Roughness length, z_0 (cm)	Shear velocity, u_* (cm/s)
Silt	0.02	0.3
Irregularities of organic origin	0.01-6.3	0.66-0.57
Dunes of gravel and sand	0.08-0.14	4.2-8.7
Gravel	0.13	1.3
Silty sand	0.16	2.3
Small trenches with even bottom and sloped walls covered with sand ripples	0.49	0.66
Fine grained sedimentary deposit	2	0.05-0.35

The logarithmic profile law is applicable within the boundary layers and therefore is suitable for shallow water channels and rivers. The empirical power law, on the contrary, is applicable for scaling the velocity measurements throughout the vertical distribution.

Under steady uniform turbulent flow of a fluid in an open channel, the power-law relates the velocity v_{ref} measured at a reference elevation z_{ref} to the velocity v_z at elevation through:

$$\frac{v_z(z)}{v_{ref}(z_{ref})} = \left(\frac{z}{z_{ref}} \right)^{\alpha_z} \quad (4.20)$$

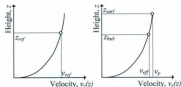


Figure 4.18: Vertical velocity profile

Extending this concept to a hydrokinetic turbine placed near the surface of a river/tidal channel, the hub-height velocity is related to the surface velocity through

$$\frac{v_{eff}(z_{hub})}{v_p(z_{surf})} = \left(\frac{z_{hub}}{z_{surf}} \right)^{\alpha_z}; \quad z_{hub} < z_{surf} \quad (4.21)$$

The exponent α_z usually ranges between 1/4 and 1/2 and depends on the turbulence intensity of the water flow. However, $\alpha_z = 1/7$ is widely accepted amongst the hydrologists [138].

The velocity profile factor to be incorporated in the hydrokinetic system's flow field relationship is therefore:

$$k_{prof} = \left[\frac{v_{eff}}{v_p} \right]_{prof}^3 = \left(\frac{z_{hub}}{z_{surf}} \right)^{\alpha_z} ; z_{hub} < z_{surf} \quad (4.22)$$

4.3.3 Skewed flow factor

Horizontal and vertical axis turbines may operate under skewed flow conditions resulting from nearby obstacles. These obstacles include, mounting structures near the surface or dunes at the bottom of the channel. The velocity of the deflected water and the incident angle need to be considered in identifying the effective velocity that contribute to the turbine's operation and power production.

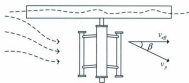


Figure 4.19: Velocity skew in relation to the rotor

According to [139], the point velocity v_p measured under a flow skewed at angle β , can be converted to effective velocity through

$$v_{eff} = v_p \cos \beta \quad (4.23)$$

Therefore, the skewed flow factor to be incorporated in the power capture Eq. 4.17

becomes

$$k_{skew} = \left[\frac{v_{eff}}{v_p} \right]_{skew}^3 = \cos^3 \beta \quad (4.24)$$

4.3.4 Yaw misalignment factor

To date, most horizontal axis turbines are not equipped with yaw alignment mechanisms. This will cause the measured velocity to be different from effective velocity seen by the rotor (Eq. 4.20). The observed point velocity v_p with an angle of incidence δ should therefore be used to determine the effective velocity using

$$v_{eff} = v_p \cos \delta \quad (4.25)$$

The corresponding correction factor is

$$k_{yaw} = \left[\frac{v_{eff}}{v_p} \right]_{yaw}^3 = \cos^3 \delta \quad (4.26)$$

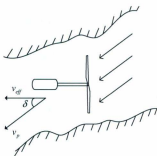


Figure 4.20: Yaw misalignment in relation to the rotor

It should be mentioned that vertical axis turbines are not subject this yaw alignment factor as these devices are suitable for operation under omni-directional flow. Wind

turbines equipped with yaw alignment capabilities may operate 1-2% below their rated capacity [118]. Hydrokinetic systems devoid of such mechanisms may perform significantly below their ratings.

4.4 Effective rotor area

A vertical axis turbine placed near the surface using a non-floating structure will be subject to variations in water depth. Under such circumstances, in addition to affecting the level of submersion, contributions from the boundary layer near the surface will determine the effective height of the turbine that is used for power extraction. Also, horizontal axis turbines placed in a shallow channel will face free-surface proximity related boundary layer effects as reported in [140].

For a vertical turbine, an ideal relationship between level of submersion h_{sub} and effective height h_{eff} would have been equality. The rotor area is therefore direct product of effective height and rotor diameter D as shown below and in Fig.

$$A_r = h_{eff} \times D \quad (4.27)$$

$$h_{eff} = h_{sub}; \quad h_{sub} \leq H \quad (4.28)$$

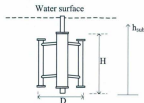


Figure 4.21: Effects of rotor submersion

Test results collected as part of this work indicate that this relationship is barely linear [141] subtle observations with this regard are summarized in Table 7.4:

4.5 Simulation of flow field

In the previous sections, various characteristics of river and tidal resource variations have been discussed and analyzed. For power tracking control study purposes, it is equally important to synthesize the flow field time-series, especially in the range of several seconds to minutes. With this regard, various elements of the flow field need to be incorporated judiciously. A summary of usability of these components is given below (Table 4.4) where variability of these factors is established (far right column).

Table 4.4: Short simulation of hydrokinetic flow-field

Flow field elements		Field of application	Turbine type	Nominal variability	Variability in simulation
Velocity of water	Seasonal variation component	River, tidal, and others	Horizontal and vertical	Hours to days	Constant
	Turbulence component	River, tidal, and others	Horizontal and vertical	Seconds to minutes	Variable
	Wave-current interactions	Tidal	Horizontal and vertical	Seconds	Variable
Density of water		Tidal	Horizontal and vertical	Hours to days	Constant
Design and placement related factors	Velocity augmentation factor	River, tidal, and others	Horizontal and vertical	Not applicable	Constant
	Vertical velocity profile factor	River, tidal, and others	Horizontal and vertical	Hours to days	Constant
	Skewed flow factor	River, tidal, and others	Horizontal and vertical	Hours to days	Constant
	Yaw misalignment factor	River, tidal, and others	Horizontal	Hours to days	Constant
Effective area correction		River, tidal, and others	Vertical (near surface fixed mounting)	Hours to days	Constant

For short simulation scenarios (several minutes to hours), only time-varying parameters are the turbulence component and wave induced velocity (for tidal current applications). For longer simulations, other parameters need to be accommodated accordingly. Taking the long term velocity to be of a constant magnitude, Eq. 4.29 outlines

the interrelationship between various components.

$$v_p(t) = \bar{v}_s + v_i(t) + v_w(t)$$

$$\bar{v}_s = \begin{cases} v_R, & \text{River seasonal mean} \\ v_T, & \text{Tidal hourly mean} \end{cases} \quad (4.29)$$

As discussed in [118,142], the synthesis of turbulence component starts with a-priori selection of total number of discrete frequencies. For hydrokinetic systems this selection is done within the Kolmogorov's -5/3 Law spectrum. For the i^{th} instance, the corresponding frequency is given by $\omega_i = 2\pi f_i$ ($T_i = 1/f_i$) and a sampling time T_{si} is chosen such that ($T_{si} \ll T_i$ where $i = 1, 2, 3, \dots$ etc.

For each discrete frequency the time-dependence of velocity component is given by Eq. 4.30, whereas the corresponding amplitude can be determined by using Eq. 4.31 in conjunction with Eq. 4.5.

$$v_i(t) = \sum_{i=1}^{N_i} A_i \cos(\omega_i t + \varphi_i) \quad (4.30)$$

$$A_i = \frac{2}{\pi} \sqrt{\frac{1}{2} [S_v(\omega_i) + S_v(\omega_{i+1})] \cdot [\omega_{i+1} - \omega_i]} \quad (4.31)$$

Here, φ_i is uniformly distributed phase angle within $0 - 2\pi$ range. Defining the mean velocity during the interval as \bar{v}_i two intermediate steps, as outlined below, need to be followed:

- Standard deviation:
 - Empirical relationship between turbulence intensity and site roughness conditions:

$$I_t = \frac{1}{\ln(z/z_0)}$$
 - Standard deviation from the definition $I_t = \frac{\sigma}{\bar{v}_i}$.
- Shaping filter gain and time constant:

- Time constant is related to turbulence scale length $T_F = \frac{L}{v_i}$.
- Static gain is related through $K_F = \sqrt{\frac{2\pi}{6(1/2,1/3)} \frac{T_F}{T_m}}$.

The driving element within the flow simulation process is a random number generator that produces white noise $E_w(s)$ and is transformed to colored noise using a shaping filter realized by a transfer function such as in Eq. 4.32.

$$H_F(s) = K_F \frac{(m_1 T_F s + 1)}{(T_F s + 1)(m_2 T_F s + 1)} E_w(s); \quad m_1 = 0.4, m_2 = 0.25 \quad (4.32)$$

The colored noise signal is multiplied with standard deviation to generate the i^{th} component of turbulence velocity. Summation of all these components generates the complete turbulence spectrum.

$$\begin{aligned} v_{i1}(t) &= \sigma_t h_F(t) \\ v_i(t) &= \sum_{i=1}^N v_{i1}(t) \end{aligned} \quad (4.33)$$

Consolidating the numerical procedures discussed above, a block representations similar to Fig. 4.22, can be utilized toward developing a simulation model.

As part of this research, such a scheme has been implemented in the Matlab-Simulink™ (Fig. 6.13). In Fig. 4.23, an example of stochastic simulation (with $v_s = 2 \text{ m/s}$) is shown and this model has been used throughout the work toward studying the performance of various power tracking techniques under time-varying flow conditions.

These simulations results have been analyzed against other reports ([89, 143]) and have been found to be suitable for further use. Since variations in water velocity and elevation demonstrate strong co-dependence ([125, 143]), similar blocks have been used in simulating water elevation patterns.

4.6 Summary of flow field representation methods

With regard to variations in the resource field, the primary time range of interest for studying the power tracking control issues is in the range of several minutes. During

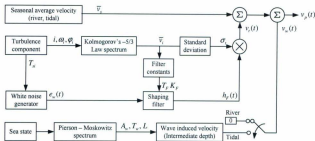


Figure 4.22: Water velocity simulation blocks

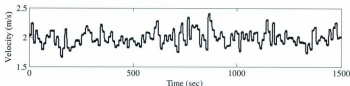


Figure 4.23: Simulation of water velocity variations

this interval, variations of water velocity are to be observed while other factors (density, submersion level, shear factor, etc) can mostly be considered constant. In addition to incident velocity changes, a hydrokinetic system operating in tidal environments will be subject to seasonal variations in water density. Factors such as augmentation, skew, shear, and yaw-misalignment need to be incorporated according to the turbine design, placement, and site characteristics in question. In this chapter, a simplified outline of flow field simulation has been presented, which can be used in studying power tracking control issues, under a number of user-induced conditions.

Chapter 5

Darrieus Rotor Operation and Performance Analysis

Among various types of vertical axis wind and hydrokinetic turbines, the Darrieus rotor configuration has gained significant attention owing to its unique performance, operational and design features. French inventor G. J. M Darrieus patented this concept in 1931 with the U.S. Patent Office, which employs a set of curved blades approximating the shape of a perfectly flexible cable, namely the Troposkien shape. Later, vertical axis designs comprising straight blades appeared under names such as, 'H-Darrieus' or 'Squirrel Cage Darrieus' turbines [77, 144].

5.1 General principle

Darrieus turbines employ airfoil shaped blades, which primarily utilize the lift force generated due to the blade's motion against the water flow. For a well-designed system the drag force generated during this process is typically smaller than the lift component. Also, for a given blade shape and Reynold's number, the lift and drag coefficient data is commonly available in chart or graphical forms as a function of angle of attack [77, 145].

The cumulative effect of these forces can be further separated along the normal and tangential axes of the blade, where the tangential component is responsible for rotating the rotor. With a given rotational speed ω_{rot} , and upstream velocity v_{up} , the rotor blades develop varying levels of attack angles α_b with changing azimuth angle θ_a (Fig. 5.1).

A typical turbine unit employed in electricity generation may consist of a rotor structure along with components such as, gearing, bearing, electrical generator, power

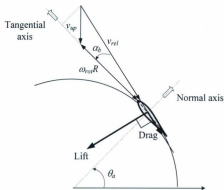


Figure 5.1: Blade-flow interaction

conditioning, and end load unit (Fig. 5.2). The primary objective of the system is to convert mechanical energy into electrical form. Therefore, investigation of the rotor's performance is of great importance and this aspect is emphasized here in this discussion.

In order to develop an insight into the working principle of a turbine, the pressure and velocity distribution around a rotor and their subsequent effects on the blades need to be studied using the principles of fluid-dynamics. As an approaching stream of fluid interacts with the rotor disk, the pressure right before and after the rotor becomes equal in magnitude but opposite in sign compared to the surrounding pressure. The boundary of the stream tube also diverges from the turbine in the wake of the rotating body. The upstream velocity v_{∞} reduces to v_{eff} at the rotor disk, which reduces further to downstream velocity v_{ds} as shown in Fig. 5.3.

For any two points a and b (along the rotor cross section, i.e. axis x in Fig. 5.3) if the corresponding fluid velocity (pressure) is v_a (p_a) and v_b (p_b), respectively, for a

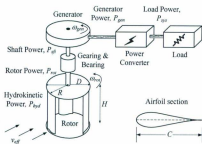


Figure 5.2: Turbine system components

stream of water with density ρ_w and effective/average velocity v , Bernoulli's equation states that

$$\rho_w v dv = dp_f \quad (5.1)$$

$$\rho_w \left(\frac{v_a + v_b}{2} \right) (v_a - v_b) = (p_a - p_b) \quad (5.2)$$

For the case of Darrieus type hydrokinetic rotor, it implies that for the upstream flow

$$\rho_w \left(\frac{v_{up} + v_{eff}}{2} \right) (v_{up} - v_{eff}) = (p_{up} - p_{rot}) \quad (5.3)$$

Similarly, for the flow downstream to the rotor, Bernoulli's equation takes the form of

$$\rho_w \left(\frac{v_{eff} + v_{dn}}{2} \right) (v_{eff} - v_{dn}) = (p_{rot} - p_{dn}) \quad (5.4)$$

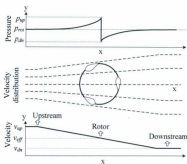


Figure 5.3: Pressure and velocity distribution around a turbine

In other words, the relationship between upstream and downstream flow can be found as

$$\rho_w \left(\frac{v_{up} + v_{dn}}{2} \right) (v_{up} - v_{dn}) = (p_{up} - p_{dn}) \quad (5.5)$$

Using moment equation of fluid flow at the rotor cross section, it can be written that

$$\rho_w v_{eff} (v_{up} - v_{dn}) = (p_{up} - p_{dn}) \quad (5.6)$$

Comparing Eq. 5.5 with Eq. 5.6 the effective/average water velocity at the rotor cross-section is found as

$$v_{eff} = \frac{v_{up} + v_{dn}}{2} \quad (5.7)$$

$$v_{up} - v_{eff} = v_{eff} - v_{dn} \quad (5.8)$$

$$v_{ap} - v_{dn} = 2(v_{ap} - v_{eff}) = 2(v_{eff} - v_{dn}) \quad (5.9)$$

If the energy lost by a body of water having a mass m_w is denote by E_w , the corresponding kinetic energy harnessed by a turbine is given by

$$E_w = \frac{1}{2}m_w(v_{ap}^2 - v_{dn}^2) \quad (5.10)$$

Since, mass flow rate at the rotor is expressed as $\dot{m}_w = \rho_w A_r v_{eff}$, Eq. 5.10 can be re-written to identify the power extracted by the rotor using

$$P_{rot} = \frac{1}{2}\rho_w A_r v_{eff}(v_{ap}^2 - v_{dn}^2) \quad (5.11)$$

$$P_{rot} = \frac{1}{2}\rho_w A_r v_{eff}(v_{ap} - v_{dn})(v_{ap} + v_{dn}) \quad (5.12)$$

$$P_{rot} = \frac{1}{2}\rho_w A_r v_{eff}(2(v_{ap} - v_{eff}))(2v_{eff}) \quad (5.13)$$

On the contrary the total hydraulic power incident on the rotor is defined as

$$P_{hyd} = \frac{1}{2}\rho_w A_r v_{ap}^3 \quad (5.14)$$

The hydrokinetic power input P_{hyd} can be related to the rotor's mechanical power capture P_{rot} by a term commonly know as power coefficient C_p^o , which is a measure of the turbine's hydrodynamic efficiency (excluding effects of cross arm, shaft, and walls).

$$P_{rot} = C_p^o P_{hyd} \quad (5.15)$$

Therefore, the rotor's theoretical hydraulic efficiency (i.e, the power coefficient) is expressed as

$$C_p^o = \frac{P_{rot}}{P_{hyd}} \quad (5.16)$$

$$C_p^o = \frac{\frac{1}{2}\rho_w A_r v_{eff} (2(v_{up} - v_{eff})) (2v_{eff})}{\frac{1}{2}\rho_w A_r v_{up}^3} \quad (5.17)$$

$$C_p^o = 4 \left(\frac{v_{eff}}{v_{up}} \right)^2 \left(1 - \frac{v_{eff}}{v_{up}} \right) \quad (5.18)$$

Under such circumstances, the term induction factor, a_{ind} can be defined as,

$$a_{ind} = 1 - \frac{v_{eff}}{v_{up}} \quad (5.19)$$

Using this definition, Eq. 5.18 can be rewritten as,

$$C_p^o = 4(1 - a_{ind})^2 (a_{ind}) \quad (5.20)$$

The maximum theoretical efficiency (i.e., the Betz limit) can be found by equating

$$\left. \frac{dC_p^o}{da_{ind}} \right|_{C_{pbetz}} = 0 \quad (5.21)$$

This results in $a_{ind} = \frac{1}{3}$ and $C_{pbetz}^o = \frac{16}{27} \approx 0.59$. The use of augmentation channels or ducts around a turbine may increase this theoretical limit by concentrating the incoming energy flux toward the rotor.

For a turbine with an effective swept area of A_r placed in a fluid body having velocity v_{eff} and density ρ_w , Eq. 5.15 can be re-written as

$$P_{rot} = C_p^o \frac{1}{2} \rho_w A_r v_{eff}^3 \quad (5.22)$$

In most literature, the two dimensionless quantities: power coefficient C_p^o and the tip speed ratio λ are used for illustrating the effectiveness of a turbine's power extraction at various rotational conditions. Here, tip speed ratio λ is an index of rotor's rotational speed ω_{rot} (rad/s) against the effective fluid velocity v_{eff} . This is defined as

$$\lambda = \frac{\omega_{rot} R}{v_{eff}} \quad (5.23)$$

where, R is the rotor's radius. Another term, torque coefficient C_T^o , is equally important toward indicating the performance of a turbine. This is defined as

$$C_T^o = \frac{C_p^o}{\lambda} \quad (5.24)$$

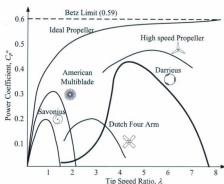


Figure 5.4: Performance of various rotors [47, 146]

A set of C_p^o vs. λ curves is shown in Fig. 5.4, which illustrates the superiority of horizontal axis propeller type and Darrieus turbines against other rotor options in terms of efficiency. However, drag type turbines (such as, Savonius and Multiblade types) have better starting capabilities. With regard to Fig. 5.4, it should be pointed out that even though the plotted performance curves are for wind turbines, similar observations can also be made for hydrokinetic turbines [47].

5.2 Performance analysis of Darrieus rotors

There exists a number of methods for performance analysis of Darrieus-type rotors. Many of these methods were developed as part of early stage vertical axis wind turbine design and demonstration activities [77,147]. At the present state of digital computer based numerical/computational capabilities and understanding of vertical axis turbines' characteristics, these methods can be considered as sufficiently mature approaches. However, in absence of commercially available tools that can be treated as industry standards, many research efforts (especially in the hydrokinetic technology domains) have thus far been directed toward rotor-specific computational tool developments [3,91].

5.2.1 Methods of analysis

As discussed in [3,77,91] and further classified in [148] the most common methods of fluid-dynamic performance assessment can be classified through Fig. 5.5. Each of these methods are characterized by various levels of complexity and accuracy. Certain approaches and their refinements may accommodate dynamic stall phenomena, unsteady dynamics, boundary layer effects, vortex shedding, skin effects, and cavitations. In hydrokinetic system analysis, a simple single-disk single-streamtube method is presented in [6]. In references [3,91] hydrokinetic rotors are analyzed for more comprehensive yet computationally demanding features.

The momentum theory or the actuator disc theory and have been studied extensively in multiple areas of fluid-dynamics (especially for aircraft [149] or ship propeller design [150]). For analyzing the vertical axis wind rotors, Templin introduced the single-streamtube approach [151]. This scheme considers the full rotor within one streamtube and the flow velocity is considered constant throughout the rotor. In order to achieving further accuracy using this theory, two separate approaches have evolved: (a) to divide the flow into multiple streams along the flow direction, and (b) to introduce multiple actuator disks perpendicular to the flow direction. Strickland [152] introduced refinements to the single streamtube method by considering multiple streamtubes that

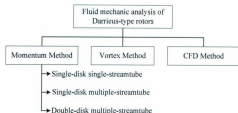


Figure 5.5: Methods of performance analysis of Darrieus rotor

accommodate differences between upstream and downstream flows. The works conducted by Paraschivoiu [77] resulted in further progression by successfully incorporating double or multiple disks along the rotor cross-section.

As a trade-off between acceptable accuracy and manageable computational requirements, the approach opted in this research falls into single-disk multiple-streamtube category. A similar tool has been presented in [144] or analyzing wind turbines. As the name implies, in single streamtube modeling, the performance of the complete rotor is determined on the basis of computations done on one single tube of streaming fluid. On the other hand, in multiple streamtube analysis, a series of equal streamtubes are assumed to pass through the rotor. For each tube, the momentum equations are computed and the effects of all the streamtubes are integrated in order to determine the forces acting on a rotor blade. Although, single streamtube modeling has proven to be sufficiently accurate for most applications, this method fails to explain the flow fields around the rotor. On the other extreme, methods such as vortex models and double-multiple streamtube models are more accurate only when proper assumptions and inputs are incorporated. Therefore, in this work, multiple streamtube modeling has been used in order to maintain reasonable accuracy and simplicity by utilizing the computing capabilities of modern day computers.

5.2.2 Single-disk multiple-streamtube analysis

The single-disk multiple-streamtube approach is in essence a two-dimensional analysis and can yield good results specially for low tip speed ratios and low solidity turbines. The accuracy of the results can be controlled by introducing higher number of streamtubes.

By taking a constant incremental azimuth angle $\Delta\theta_a$, the rotor cross section can be divided in $180/\Delta\theta_a$. Corresponding flow distribution and velocity variations are outlined in Fig. 5.6(a) and (b). According to this method [152] the tube cross section area remains the same along the path from upstream Fig. 5.6(c).

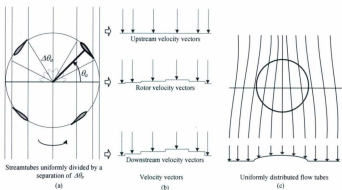


Figure 5.6: Flow distribution around a vertical axis turbine [144]

The flow within each streamtube is associated with two pulses of forces per revolution of a blade. Each of the streamtube experience continuous momentum loss (i.e., thrust) and can be calculated using

$$F_{thrust} = \rho_w A_t v_{eff} \times 2(v_{up} - v_{eff}) \quad (5.25)$$

Here $A_t = HR\Delta\theta_a \sin\theta_a$ is the cross sectional area of each streamtube. By normalizing Eq. 5.25 using $\frac{1}{2}\rho_w v_{up}^2 A_t$ as the base, the definition of thrust coefficient C_{thrust} can be established as

$$C_{thrust} = \frac{\rho_w A_t v_{eff} \times 2(v_{up} - v_{eff})}{\frac{1}{2}\rho_w v_{up}^2 A_t} \quad (5.26)$$

Utilizing the definition of induction factor (Eq. 5.19) this can be written as

$$C_{thrust} = 4 \frac{v_{eff}}{v_{up}} \left(1 - \frac{v_{eff}}{v_{up}}\right) = 4(1 - a_{ind})a_{ind} \quad (5.27)$$

Even though, Eq. 5.27 may appear sufficient to determine the torque quantities, the relationship between upstream and rotor velocity (i.e. the induction factor, a_{ind}) is indeterminate. This requires formulations of another set of equations representing the rotor characteristics.

An observation of the basic lift-drag functionality of a single blade (as shown in Fig. 5.1) traversing against a stream indicates that the relative flow velocity is

$$v_{rel} = \sqrt{(v_{eff} \sin\theta_a)^2 + (v_{eff} \cos\theta_a + \omega_{rot}R)^2} \quad (5.28)$$

This expression can be normalized as

$$\frac{v_{rel}}{v_{up}} = \sqrt{((1 - a_{ind}) \sin\theta_a)^2 + ((1 - a_{ind}) \cos\theta_a + \lambda)^2} \quad (5.29)$$

With reference to Fig. 5.1, Eq. 5.30 can be used to determine the angle of attack developed in the blade as it travels along the circular periphery of the rotating disk (Fig. 5.1). Such variation in angle of attack along the blade's traveling path is shown in Fig. 5.7.

$$\alpha_b = \tan^{-1} \left(\frac{-(1 - a_{ind}) \sin\theta_a}{(1 - a_{ind}) \cos\theta_a + \lambda} \right) \quad (5.30)$$

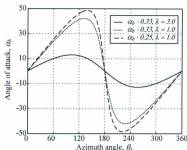


Figure 5.7: Blade-flow interaction

The tangential force component, which effectively determines the cumulative affect that causes the rotor to rotate, can be expressed in terms of an associated force coefficient C_{tang} , which implies

$$C_{tang} = C_L \sin \alpha_b - C_D \cos \alpha_b \quad (5.31)$$

where, C_L and C_D are lift and drag coefficients of the airfoil blade. Similarly, the normal force component is found as

$$C_{norm} = -C_L \cos \alpha_b - C_D \sin \alpha_b \quad (5.32)$$

For an angle of attack α_b the effective thrust force on the rotor blade (with a chord length C) is therefore expressed as $\frac{1}{2} \rho_w v_{rel}^2 (HC) (-C_{norm} \sin \theta_a - C_{tang} \cos \theta_a)$. The average thrust force (twice per revolution) acting on N_b number of blades is given as

$$F_{thrust} = N_b \frac{\Delta \theta_a}{\pi} 2 \left(\frac{1}{2} \rho_w v_{rel}^2 (HC) (-C_{norm} \sin \theta_a - C_{tang} \cos \theta_a) \right) \quad (5.33)$$

Normalizing this expression using $\frac{1}{2} \rho_w v_{tip}^2 A_t$ as the base, the second definition of thrust coefficient can be found as

$$C_{thrust} = \frac{N_b}{2R} \left(\frac{v_{rel}}{v_{eff}} \right)^2 \frac{2}{\pi} \left(-C_{norm} - \frac{C_{tang}}{\tan \theta_a} \right) \quad (5.34)$$

Eq. 5.34 and Eq. 5.27 can now be solved iteratively to identify the magnitude of a_{inf} . This also allows the determination of relative water velocity v_{rel} . Therefore, for each streamtube the instantaneous torque on a single blade at a given angle of attack α_s can be found using

$$T_{ast} = \frac{1}{2} \rho_w v_{rel}^2 (CH) C_{tang} R \quad (5.35)$$

The average torque on the rotor in presence of N_b number of blades, in one complete rotation is given by

$$T_{mst} = N_b \frac{\sum_{i=1}^{2m} \frac{1}{2} \rho_w v_{rel}^2 (CH) C_{tang} R}{2m} \quad (5.36)$$

Here m is the number of streamtubes. Considering the symmetry in the upper and lower halves of the rotor, the total rotor torque is given by

$$T_{mcc} = N_b \frac{\sum_{i=1}^m \frac{1}{2} \rho_w v_{rel}^2 (CH) C_{tang} R}{m} \quad (5.37)$$

A convenient measure of turbine mass, structure, and dimensions is given by the term 'rotor solidity'. This is determined by the ratio of total blade chord length (for all blades) to rotor diameter as given in Eq. 5.38

$$\sigma_r = \frac{N_b C}{D} \quad (5.38)$$

Using normalizing torque as $\frac{1}{2} \rho_w v_{c_{ff}}^2 D H R$, the torque coefficient of a straight bladed Darrieus turbine is given through Eq. 5.39 [144]. The power coefficient C_p^o can then be evaluated using Eq. 5.24.

$$C_T^o = \sigma_r \frac{\sum_{i=1}^m \left(\frac{v_{ast}}{v_{c_{ff}}} \right)^2 C_{tang}}{m} \quad (5.39)$$

Before embarking upon the analysis method stated above, a set of subtle issues need also be considered. Firstly, consideration for Gluert's empirical formula, and secondly, lift/drag data correction. Brief discussions on these issues are presented below:

- *Gluert's empirical formula:*

According to the classical momentum theory, the thrust force exerted on the rotor exhibits a decreasing characteristics as soon as the induction factor reaches a threshold. This is implied in Eq. 5.27 where the thrust coefficient decreases after $a_{ind} > 0.5$. Horizontal axis turbine may experience such conditions only in limited circumstances (especially for turbulent states during start-up or shut-down [153]). On the contrary, the blades of vertical axis turbines may operate well beyond such thresholds especially for high solidity turbines or for operation at high tip speed ratio conditions (during blade positions orthogonal to the incoming flow [144]).

Experimental data collected through tests on wind turbines, autogiros, and helicopters indicate that the parabolic relationship between induction factor and thrust coefficient (as in classical momentum theory) deviate greatly from physical applications. This is primarily due to a monotonic increase in thrust force with increasing induction factor in the turbulent wake state. Gluert [154] observed these anomalies and proposed an empirical relationship to overcome the limitations of the classical theory (Fig. 5.8).

According to this formulation, the classical theory is valid for $a_{ind} < 0.4$ and empirical relationships (Eq. 5.40) need to be considered beyond this threshold.

$$\begin{aligned} C_{thrust} &= 4(1 - a_{ind})a_{ind} & ; & \quad a_{ind} < 0.4 \\ C_{thrust} &= \frac{20}{13}a_{ind} + \frac{4}{13} & ; & \quad 0.4 < a_{ind} < 1.0 \end{aligned} \quad (5.40)$$

In conducting the streamtube analysis for predicting the performance of the Darrieus rotor, this aspect needs to be considered in revealing the system behavior with greater accuracy. Therefore, Eq. 5.27 need to be corrected for Eq. 5.40.

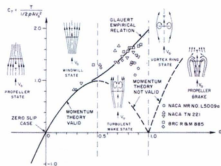


Figure 5.8: Gluert's empirical formula

- *Lift and drag data correction:*

These two parameters (C_L and C_D , lift and drag coefficients of the airfoil blade) primarily depend on the blade shape and Reynold's number under a given operating condition, and need to be accessed using proper set of tabulated data. Commonly available data sets such as in, [77, 145] are not readily usable for analysis of Darrius turbines that are used in hydro applications. These tables typically contain lift/drag information for high Reynolds number, low angle of attack and infinite blade aspect ratio. Suitable corrective measures need to be performed on available data sets in order to use them in further fluid-dynamic analysis. These three issues are briefly addressed in the discussions below:

- *Reynold's number modification:* Reynold's number is an index of turbulence created by a body placed in fluid [77, 155]. This can be expressed as

$$R_e = \frac{v_{eff} \cdot D}{\nu} \quad (5.41)$$

where, $\nu = 1.1 \times 10^{-6}$ is the kinematic viscosity of water [155]. For a given rotor diameter D and water velocity v_{eff} , an estimate of R_e can be found. For this

work, R_c is taken to be 1.5×10^6 , which is in line with similar reported works [96]. However, most airfoil data are not readily tabulated for this particular Reynolds number and corrective measures need to be undertaken before using such data [144].

- *Aspect ratio modification:* Aspect ratio of a blade is a measure of its length and slenderness. For a blade with chord length C and height H (Fig. 5.2), the aspect ratio is defined as

$$R_B = \frac{H}{C} \quad (5.42)$$

Typical airfoil data is given for infinite aspect ratio, whereas a true blade is of finite length. This calls for a modification of available data for a given application case.

- *Angle of attack modification:* Lift and drag data are normally available for low angle of attacks (typically, $10-20^\circ$), as shown in Fig. 5.9. However, for a Darrieus turbine, this angle may vary widely depending on a blade's position and speed (Fig. 5.7). Performance analysis of such a turbine will fail unless data modification for high angle of attack instances is incorporated.

A procedure detailed in [144] can be utilized to obtain corrected airfoil data. Employing these computations in Matlab [156], significantly divergent plots for the airfoil NACA 63-018 is found (Fig. 5.9, Fig. 5.10).

Following the aforementioned steps for multiple streamtube modeling, a set of performance curves for the straight bladed Darrieus (solidity 25%, NACA 63-018 blades) is obtained and is plotted in Fig. 5.12. As seen in this figure, the power and torque capabilities of the Darrieus rotor are poor in the low tip speed conditions. Although varying levels of rotor solidity may shift these curves right or left, the starting problem remains. The starting torque depends on the rotor's angular position as shown in Fig. 5.7. The turbine may self-start if a blade is held securely in the optimum position where the generated tangential force exceeds the starting requirements. This problem may also be approached by external mechanical, electrical or electromechanical means.

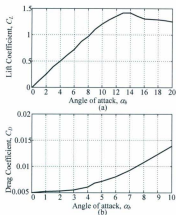


Figure 5.9: Typical airfoil data (NACA 63-018)

5.3 Design considerations

The design problem of straight bladed Darrieus rotor is essentially an optimization problem where decision on the rotor's structure, dimension and blade design is sought. For a given application (river or tidal energy), resource dependent parameters such as, water density and mean annual flow need to be incorporated. Apart from common knowledge of system designing, fluid-dynamic considerations are also brought in during the design process.

Amongst the two types of straight bladed Darrieus turbine, the H-Darrieus rotor is mostly used in larger turbines where mechanical strength is of great significance [73]. In smaller turbines, use of H-type structure may cause significant turbulence, reducing the turbine efficiency. Therefore, squirrel cage configuration is suited for low scale power generation as exemplified in [6, 43, 95, 157]. In the discussions to follow, this type of rotor

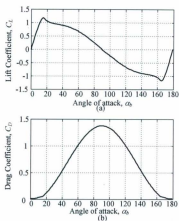


Figure 5.10: Modified airfoil data (NACA 63-018 with $R_B = 10$, $Re = 2 \times 10^6$)

will be considered, although the design of H-Darrieus rotors can also be approached using the same technique.

5.3.1 Basic dimensioning

For the cylindrical shape of the straight-bladed squirrel cage rotor, basic dimensioning implies a decision on the choice of rotor diameter and height. The design process can be initiated by modifying the power expression given in Eq. 5.22 for incorporating overall system efficiency as given in Eq. 5.43.

$$P_{sys} = \eta_{sys} \frac{1}{2} \rho_w A_r v_{eff}^3 \quad (5.43)$$

The overall system efficiency η_{sys} is defined in terms of efficiency contributions of

all the cascaded stages (Fig. 5.2) as given in the equation,

$$\eta_{sys} = \eta_{rot} \cdot \eta_{gen} \cdot \eta_{ele} \quad (5.44)$$

$$\eta_{rot} = C_p^o \cdot \eta_{flow} \cdot \eta_{drv} \quad (5.45)$$

$$C_p = C_p^o \cdot \eta_{drv} \quad (5.46)$$

Rule of thumb values for these efficiency terms are tabulated in Table 5.1. For small systems (as rigorously studied in this work, e.g, Fig. 9.6) these values will be significantly lower. This implies, the efficiency values given in the table below are akin to larger turbines.

Table 5.1: Typical efficiency values

Efficiency term	Typical value	Ref.
Hydrodynamic, C_p	0.45	[67, 70, 73]
Gearing-bearing, η_{drv}	0.90	[95]
Generator, η_{gen}	0.875	[95]
Power Converter, η_{ele}	0.875	[95]

The input value of water density may vary significantly for a given site (river and ocean), which may further relate to annual average temperature, precipitation, and geographical location.

A decision on water velocity, which may also be termed as rated velocity from a design point of view, is an unsolved problem by its own merits. This term may comprise several other factors as given in Eq. 5.47:

$$v_{eff} = \bar{v}_s \cdot k_{aug} \cdot k_{econ} \quad (5.47)$$

Here, \bar{v}_s stands for mean river water velocity. Deciding a value for this term requires study of water velocity patterns in various rivers on a global basis. Reasonable values can be selected and resource qualities can be tagged against each velocity level. In the absence of such a detailed study, a result of a micro scale investigation reported in [42] is opted in this exercise (Fig. 5.11).

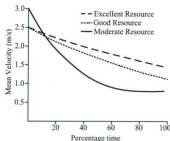


Figure 5.11: (a) Water density variations (b) Velocity duration curves and resource classification

The augmentation factor k_{aug} in Eq. 5.47 essentially incorporates the effects of adding a channel augmentation device. A moderate value of $k_{aug} = 1.5$ is considered in this work, whereas reports of even higher value is available in [42, 78]. The remaining term in the velocity expression, k_{econ} relates the economics of a turbine operating in varying velocities around the year. Discussions on optimal choice of rated velocity for variable speed wind turbines can be found in [158]. Use of this factor is common in wind turbine designs, where a typical rated wind velocity is around 10 – 12 m/s even if the site mean velocity is 7 – 8 m/s . In this work, a more conservative value $k_{econ} = 1.5$ is chosen.

Using the factual values of water density, rated velocity and efficiency terms in Eq. 5.43, the swept rotor area A_r can be determined for a given level of desired output power. The effective area encountered by the water is essentially a rectangle, given as:

$$A_r = H \cdot D \quad (5.48)$$

Even though, different height (H) and diameter (D) combinations may yield the same rotor area and therefore the same theoretical power, ultimate performance of the

system depends on several more subtle factors. A qualitative overview of these issues is given below:

- *Power capture and efficiency:* For a given power level and rotor area, an increase in diameter implies decrease in turbine height. Since, the airfoil shaped blades are present in the vertical spacing only, this measure eventually reduces the power output. In a rotor with higher diameter the blades can be separated far apart. This reduces the mutual effects due to turbulence eventually elevating the efficiency. Therefore, a trade off need to be reached between rotor efficiency and power output while deciding the height-diameter ratio [95].
- *Torque, speed and generator selection:* Selection of an electrical generator is heavily dependent on rotor speed and torque. With increased diameter and reduced height (for a given power level and rotor area), the rotor speed reduces and shaft torque increases. With regard to using a direct drive generator or low-conversion-ratio gearbox, this measure is not recommended. On the contrary, higher torque may reduce the problem of rotor starting for a vertical axis turbine [157].
- *Behavior in skewed flow:* Skewed fluid flow is significant in constrained flow channels such as, shallow river or built environment. Depending on the skew angle, rotors with varying height-diameter ratios perform differently. Such considerations need to be incorporated in the design process when flow patterns are not uniform for a channel [85].

A decision on height-diameter ratio H/D , (typical values may range from 0.5 to 1.5) would yield values of rotor height and diameter from Eq. 5.48.

5.3.2 Blade design

When basic dimensioning is complete, the subsequent problem is to select a set of blades with certain shape and solidity. The blades of a lift type device are of airfoil shape and

the tangential forces induced in the blades are the prime movers of the rotor. Therefore, fluid-dynamic factors dictate its performance and the process of blade designing requires performance predictive modeling and delicate decision making.

Probably the foremost and clichéd problem in the rotor design process inquires what number of blades would optimize the performance of a turbine. Although a good number of theoretical and experimental studies that attempt this problem is available [6, 67, 69, 71, 73, 95, 96, 144], there is no agreed solution. With increasing number of blades, the solidity of the turbine increases and induced torque is higher. This reduces the starting problem of Darrieus turbines. On the contrary, lower number of blades reduces turbulence of fluid flow and increases the hydrodynamic efficiency. A turbine with lesser blades usually runs on higher rpm, which eases the generator selection problem. Although, incorporating 2 to 6 blades is possible, examples of 4 or 5 bladed Darrieus turbines are more common for hydro applications [6, 73].

The subsequent problem, which is also an open problem, is to decide on the shape of airfoil to be used. Since water turbines experience large torque variations as a blade rotates along the rotor circumference, symmetric blades are generally preferred [6, 67, 69, 71, 73, 95, 96]. The most common blade profiles used in Darrieus turbines are: NACA 0012, NACA 0015, NACA 0018, and NACA 63-018. Availability of lift/drag data may become difficult for some shapes (e.g. NACA 63-018) especially for low Reynolds number as discussed earlier.

The dimension of a rotor, number of blades and blade chord length are interrelated through the solidity parameter σ_r . Water turbines are of higher solidity than wind turbines and solidity values may range from 0.15 to 1.6 [6, 96, 144]. Lower solidity implies better hydrodynamic performance and higher values generally allow stronger mechanical structure and increased induced torque [6, 67, 69, 71, 73, 95, 96]. For a given blade shape, decision on blade number and blade chord length can be approached through fluid-dynamic performance analysis. The modeling methods discussed in the earlier section can

be used in this regard. Multiple streamtube analysis carried out on a turbine consisting of NACA 63-018 blades is plotted in Fig. 5.12.

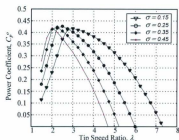


Figure 5.12: Performance of Darrieus rotor at various solidity

As seen in the plot, solidity values around 0.30 seems more suitable for the given blade shape (NACA 63-018) and application (hydro). However, practical considerations such as, model inaccuracy, structural strength, and increased torque induction may require even higher solidity. When a certain value is decided based on these observations, for a rotor with specific number of blades, blade chord length can be determined using the definition of solidity. Additionally, rotor speed can be calculated from tip speed ratio data obtained from Fig. 5.12 and Eq. 5.23. Information on the rotor's rotational speed is vital in selecting proper gearing/transmission mechanism and electrical generator.

5.3.3 Design example

As discussed in the foregoing sections, the design of a Darrieus rotor involves performance modeling and decision making based on practical observations. The process of designing can be described with a flow chart given in Fig. 5.13. The major components of this process is to analyze the turbine performance and based on the outputs, decide on the design parameters.

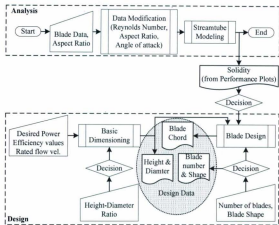


Figure 5.13: Rotor design process

In this work, an exercise on rotor designing with NACA 63-018 blades is carried out. Raw blade data (Fig. 5.9) has been modified for $Re = 1.5 \times 10^6$, $A_r = 10$ and $\alpha_b = 0 - 180^\circ$ (Fig. 5.10). Multiple streamtube modeling was done in Matlab and performance plots are given in Fig. 5.12. From these plots, a solidity value $\sigma = 0.25$ appears more reasonable.

For a desired output power $P_{\text{req}} = 1000 \text{ W}$, rated water velocity $v_{\text{eff}} = 2.25 \text{ m/s}$ (from Eq. 5.47), taking $\bar{v}_s = 1.0 \text{ m/s}$ and $\eta_{\text{req}} = 31\%$ (from Eq. 5.44 and Table 5.1), the rotor swept area is found to be, $A_r = 0.566 \text{ m}^2$. Deciding height-diameter ratio $H/D = 1/1.5$, the values of rotor height and diameter are: $H \approx 0.60 \text{ m}$ and $D \approx 0.90 \text{ m}$.

With the performance data and basic dimensions available at hand, the blade design procedure can be initiated. Deciding the turbine to be of 5 blades ($N_b = 5$), the

chord length of each blade is found by (Eq. 5.38). For a solidity $\sigma_r = 0.35$, the chord length is found to be, $c \approx 6.25$ cm. Additionally, from Fig. 5.12, optimum tip speed ratio for this turbine is $\lambda = 2.25$. Using this value in Eq. 5.23, the expected rotor speed is found to be around 100 rpm. To summarize, the design outputs for this high-level example system is given in Table 5.2.

Table 5.2: Turbine design example

Design parameter	Symbol	Value
Rotor diameter	D	0.9 m
Rotor height	H	0.6 m
Number of blades	N_b	5
Blade profile	–	NACA 63-018
Blade chord	C	6.25 cm

Since these design steps involve many cause-effect decisions and approximations, the final performance of a turbine might deviate greatly from the desired results. Structural considerations will undoubtedly alter the design of the rotor. A more acceptable method would be to design-test-redesign, even though this may cost significant time and resource.

5.4 Summary of rotor performance analysis

In this chapter, a method for predicting the performance of a vertical axis turbine rotor has been presented where the underlying numerical technique is based on the principles of single-disk multiple-streamtube analysis. Also, design considerations for hydrokinetic turbines have been discussed with emphasis on a broad range of physical and operational conditions that may impact the operational conditions of the turbine. This numerical method has been replicated toward understanding the performance characteristics of a 4-bladed test rotor (employing NACA 0015 blades, chord 10.1 cm, height 0.4 m, diameter 1 m, solidity 40%) in conjunction with various test and modeling activities presented in Chapter 7 (e.g, Fig. 7.26) and in Chapter 9 (e.g, Fig. 9.10) .

Chapter 6

Dynamic Modeling of Hydrokinetic System Components

Vertical axis hydrokinetic turbines bear unique advantages of operating under bi-directional water flow and having the power take-off unit (gearing/transmission/generator) mounted above the water surface [2, 5]. The drawbacks of vertical turbines include: weaker start-up behavior and torque ripple propagation [2, 6]. While the use of a permanent magnet alternator (PMA) may eliminate the need for gear-coupling [159], the issue of cogging torque, common in such machines [160, 161], may deteriorate the self-starting capabilities. This is even more dominant in fixed bladed vertical turbines [6]. The issue of oscillating torque, on the other hand, can be addressed by use of suitable power electronic interfaces and filtering arrangements. It is therefore important to understand the operational characteristics of vertical axis hydrokinetic devices both through field-trials and numerical analysis.

At present, many small-scale hydrokinetic systems are being designed, developed, and tested throughout the world [2, 10, 14]. Use of off-the-shelf components and sub-optimal part selection is common in such initiatives. However, recent activities on optimum system design [5, 159] and real-world demonstrations [10, 45] have provided significant insight into the underlying challenges and possible solutions.

Recent publications on horizontal axis turbines, particularly focusing on rotor fluid-dynamic characteristics, have underlined various subtle aspects of device operation and design [93, 162]. Discussions on system inertia [163] and device trials [164] have also

been presented. To date, most research on vertical hydrokinetic technologies has focused on rotor design and fluid-mechanic analysis [70, 165]. Important dynamic/time-series performance information that has been generated through these pioneering works [69, 165] were not studied for system-level dynamic modeling. Results presented in [3, 4, 79, 94, 159] also provide information on part-system device characteristics. If fluid dynamics (associated with unsteady flows, multi-body interactions, etc.) and electrical dynamics (pertaining to power electronics, protection, etc.) are considered as two separate fields of interest, this work focuses on electromechanical dynamics that couple these two areas.

This research takes the existing knowledge-base further ahead by analyzing the system behavior in terms of electrical power quantities and completing a time-domain large-signal modeling. In light of a number of design and testing activities associated with this work, principle electro-mechanical dynamics are represented in these numerical formulations. Three areas, as indicated above (start-up, torque ripple, and nonlinear efficiency), have been given due emphasis and the model is validated against actual test data.

While real-world deployments provide critical information on system performance and reliability, tests in controlled environment allow detailed investigation on device characteristics that are of high significance toward successful device design. Tow-tank tests and modeling exercise presented in this work aim at generating useful information in this regard. Given the operational and architectural analogy between wind turbines and hydrokinetic devices, wind modeling exercises (such as, [98, 111, 156]) are of high relevance. However, considering the nascent status of the hydrokinetic technologies, it is important to capture subtle operational aspects (such as, start-up, cogging, ripple, flow interactions, efficiency, etc.) through detailed analysis. As the technology matures and more validation exercises are conducted, it is expected that such initiatives will converge to similar models as found within the area of wind power.

6.1 System description

A complete hydrokinetic energy conversion system (HECS) essentially consists of three stages of power transformation: primary (fluid-mechanical), secondary (electro-mechanical), and tertiary (electrical interface to the load/grid) (Fig. 6.1). In the front-end, the rotor captures mechanical power through interactions with the incoming water stream. This mechanical power is transferred to the electrical machine through a suitable drive-train that augments the rotational speed. The tertiary stage supplies the electrical load (such as, isolated load or electrical network) after necessary frequency/voltage conversions.

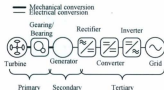


Figure 6.1: General structure of a hydrokinetic energy conversion system (HECS)

True system representation of a complete hydrokinetic turbine unit will require detailed modeling of all the subsystems as outlined previously (Fig. 6.1). Caveats for allowing system losses/efficiency information need also be provided in order to realize correct steady-state outputs. This is particularly true for small systems where losses can be significant compared to the total overhead.

In this work, dynamic behavior in the time frame of electro-mechanical transients (as against electro-magnetic transients) is of attention. Therefore, torque contributions of each of the subsystems will be linked to formulate a complete system model. More traditional swing-equation type formulations [98, 111, 163] have not been pursued here primarily for to two reasons. Firstly, issues such as cogging and oscillations need to

Table 6.1: Major subsystems of the hydrokinetic turbine setup

Subsystem	Manufacturer/Model	Brief Description
Rotor	NECE: 4 bladed	1m width, 0.4m height, fixed pitch, 4 radial arms and a center shaft
Transmission	Custom	Rotor steel shaft 1m, Chain sprocket gearing with ration 1:3.43
Generator	Crystalyte: X-lyte 505	Outer rotor permanent magnet alternator (350 rpm and 700 watt)
Rectifier	Vishay:26MT40	Three phase diode rectifier (400V 25A)
Filter	Panasonic	Parallel combination (3x1500 μ F)
Converter	Vicor: VI-NN3-EM	Two modular units in series/parallel configuration
Inverter	SWEA: UWT-I-250	Grid tie inverter with variable dc input
Load (for tank testing)	Custom	Series-parallel combination of 12 individual resistors (5 Ω , 225 watt)
DAQ	Custom	Four channels (rotor rpm, bus voltage, load current, and water/carriage speed) with USB 1208LS DAQ card

be treated through separate torque terms, which are typically not used in wind turbine modeling. Secondly, in order to represent the system behavior more realistically, large signal non-linear modeling is indispensable [166]. This is particularly important for smaller systems where system losses can be highly nonlinear and may exhibit large deviations on different operating conditions. Various subsystems being studied in detail in the preceding sections are highlighted in Table 6.1. The torque contributions of each of the subsystems will be linked to formulate a complete system model. These torque components have the breakdown as shown in Fig. 6.2 and will be detailed in the following discussions.

6.2 Vertical axis rotor

The total hydrodynamic torque fed into the rotary system (turbine, transmission, and generator) consists of two parts: (i) average torque, and (ii) dynamic torque. The latter component can be further broken down into: (a) ripple torque and its harmonics, and (b) stochastic torque (arising from system vibration and water turbulence). Since the stochastic component is mostly filtered out by the conversion system, only the predom-

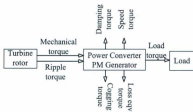


Figure 6.2: Torque components of the hydrokinetic turbine system

inant ripple torque will be considered here. The total rotor torque is therefore the sum of average mechanical torque and oscillating torque as given by Eq. 6.1.

$$T_{rot} = T_{mec} + T_{osc} \quad (6.1)$$

This average mechanical torque arising from the rotor-fluid interaction is given through Eq. 6.2.

$$T_{mec} = \frac{1}{2} \rho_w A_r C_T v_{eff}^2 R \quad (6.2)$$

Here the torque coefficient C_T depends on power coefficient (a measure of rotor efficiency) C_p and tip speed ratio λ , whereas rotor area $A_r = 2RH$. Also, it should be noted that the power coefficient considered here incorporates rotor stray losses (radial arms, center shaft, turbine walls etc.) represented by η_{aux} , and determined from the theoretical/ideal power coefficient C_p^o .

$$C_T = \frac{C_p}{\lambda} \quad (6.3)$$

$$\lambda = \frac{\omega_{rot} R}{v_{eff}} \quad (6.4)$$

$$C_p = \eta_{aux} C_p^o \quad (6.5)$$

The theoretical estimate of power coefficient C_p^o is a highly nonlinear property of the rotor [167] and is dependent on tip speed ratio λ (Eq. 6.6, Eq. 9.20).

$$C_p^o = f_r(\lambda) \quad (6.6)$$

This function, along with other major non-linear efficiency properties of subsequent subsystems is provided in the Appendix B. For consistency and comparability, these efficiency terms are plotted against per-unit/normalized quantities in Fig. 9.6.

In a horizontal axis turbine, each blade contributes uniformly to the total induced torque. The only major oscillatory effect is related to the issue of tower shadow. In a vertical axis turbine, however, each blade induces varying magnitude of torque depending on its azimuth position. When a blade passes through its high-lift zone, upstream of the rotor, a torque pulse is transferred to the shaft. In the downstream, another pulse of smaller magnitude (harmonics) is generated. These characteristics are discussed further in latter sections and are shown in Fig. 7.30.

The frequency of this oscillation can be determined with a straightforward multiplication of rotor speed with number of blades. The magnitude of the ripple, however, will require detailed fluid-dynamic analysis for an accurate estimate [165, 168]. In this work, an empirical approach is taken and is derived from experiments. Two major observations are:

- from electrical output point-of-view, torque ripples are reflected in output current and is effectively visible only when the system is loaded.
- the effects of the ripple torque is dominant in low tip speed ratio conditions and is gradually diminished with higher tip speeds.

Based on these heuristics, the following expression is used:

$$T_{osc} = \hat{T}_{osc} \sin \theta_b \times f_h(I_{gr}) \quad (6.7)$$

Here the Heaviside step function, f_h acts as a logical operator that nullifies the expression when the system is unloaded. Also, azimuth position is calculated by

$$\theta_h = \int N_{\theta} \omega_{rot} dt \quad (6.8)$$

The peak ripple torque, which is defined as function of average torque and tip speed ratio, also depends on an empirical constant k_{osc} .

$$\hat{T}_{osc} = \frac{T_{mec}}{k_{osc} \lambda} \quad (6.9)$$

While this formulation simplifies the problem of determining ripple components, exact instant of each torque pulse cannot be identified. This arises from the fact that azimuth angle is not referenced to any specific axis, whereas actual pulsations take place only at specific angular positions along the blade trajectory. Therefore, the simulated ripple behavior will be time-shifted compared to a true scenario.

6.3 Transmission

The total rotor torque is transferred to the generator shaft by a transmission system consisting of a rotor shaft, a gear-box, and several bearings.

With a gear ratio N_{gr} and drive-train efficiency η_{drv} , the generator input torque T_{gen} can be related to rotor torque T_{rot} and low-speed shaft torque T_{lss} , as given in the following set of equations (Eq. 6.10 - Eq. 6.12, [168]):

$$T_{rot} = J_{rot} \frac{d\omega_{rot}}{dt} + T_{lss} + B_{rot} \omega_{rot} \quad (6.10)$$

$$T_{gen} = \eta_{tran} \frac{T_{lss}}{N_{gen}}, N_{gr} = \frac{\omega_{gen}}{\omega_{rot}} (N_{gr} > 1) \quad (6.11)$$

$$T_{lss} = k_{spr} \int (\omega_{rot} - \frac{\omega_{gen}}{N_{gen}}) dt \quad (6.12)$$

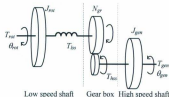


Figure 6.3: Two-mass representation of the drive-train

This two-mass model can be reduced to a single-mass expression by determining the equivalent system inertia. This will increase the computational speed at the expense of losing some information on torsional modes of oscillation.

6.4 Permanent magnet alternator

In wind/hydro applications permanent magnet generators are attractive options, because of advantageous features such as, direct-drive coupling, higher energy density, low speed-high torque operation, and higher efficiency. In the literature, these generators are commonly termed as permanent magnet alternator (PMA), permanent magnet synchronous generator (PMSG), or brushless dc generator (BLDC). Axial flux and radial flux multi-pole machines are particularly common in small wind turbines (Fig. 6.4). Even though, the fundamental operational characteristics of all these machines are the same, there are certain subtle differences. With regard to wind/hydro applications, the term 'brushless dc (BLDC)' generator has also been used extensively, reflecting the associated machine structures and characteristics [169].

Permanent magnet alternators are multiphase synchronous machines where the magnetic field and rotor rotate in synchronism. However, its operational characteristics are more akin to dc machines. Instead of running only at a synchronous speed, it oper-

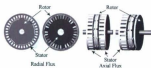


Figure 6.4: Radial flux (inner & outer rotor) and axial flux (double & single stator) PM generators

ates in variable speed variable frequency mode. Also, the torque-speed characteristics are similar to dc machines. Construction-wise, it has hybrid features: brushless power flow (as in synchronous machines) coupled with outer field-inner armature (as in dc machines) arrangement. BLDC motors used in servo/HVDC applications are commonly called permanent magnet synchronous motors (PMSM) and they have typical synchronous machine structure. However, BLDC generators (i.e. PMAs) found in wind/hydro turbines usually have an inside-out structure, where the outer field rotates allowing electrical power flow through inner stationary armature coils without requiring brushes [169].

For permanent magnet alternators, a closer realization of dc machine is possible when a rectifier-coupled system is considered. In other words, this would behave as a true dc system (dc quantities at the output and dc machine characteristics during operation) even with the use of an synchronous machine. Such arrangements are common in small wind turbines and hydro applications, automotive power regeneration and synchronous generator field excitation system.

Details and model parameters of a PMA/PMSM/BLDC generator can be found through finite element modeling and subsequent investigation of design features. A traditional model involves coupled d-q axis representation. Extracting such model parameters and implementing them in computational simulation tools is very laborious. Moreover, in the literature, there is a high level of model ambiguity, inappropriateness and apparently unnecessary use of such complicated models [98]. Intuitively it appears that a PMA

model that captures the essence of its dc machine like behaviors would be the simplest solution. However, since the PMA machine is, in principle, an ac machine, the transition for ac to dc analogy must be based on relevant theories and range of model validity need to be clearly spelled out.

In this work, such modeling is approached through classical ac machine theories and a simplified dc machine analogy is established based on the observations. The machine considered here is an outer rotor, radial flux, permanent magnet, three-phase star-connected PMA. In order to realize a true dc machine-like behavior, an uncontrolled rectifier at the generator output is considered. Such arrangements are very common in small wind energy conversion systems.

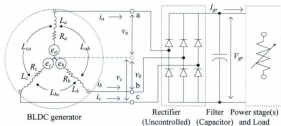


Figure 6.5: Rectifier-coupled permanent magnet alternator

6.4.1 Simplified modeling

Equivalent circuit model of a rectifier-coupled PMA and its associated loads are outlined in Fig.1. For any arbitrary waveform, the per-phase time-varying terminal voltage equations of the PMA generator in machine variables are:

$$[v_{abc}] = -[R_{abc}][i_{abc}] + p[\lambda_{abc}] \quad (6.13)$$

where $[v_{abc}] = [v_a \ v_b \ v_c]^T$ is terminal voltage, $[R_{abc}] = \text{diag} [R_a \ R_b \ R_c]$

is the resistance, p is operator d/dt , and $[i_{abc}] = [i_a \ i_b \ i_c]^T$ is armature current matrix. Considering a linear system, the flux linkage per-phase is given by:

$$[\lambda_{abc}] = -[L_s][i_{abc}] + [e_{abc}] \quad (6.14)$$

Here, $[e_{abc}] = [e_a \ e_b \ e_c]^T$ is per-phase time-varying open circuit voltage induced by the permanent magnets and is directly proportional to the rotational speed. Considering a balanced system ($i_a + i_b + i_c = 0$) and all the self and mutual inductances to be equal, (i.e, $L_a = L_b = L_c = L$ and $L_{ab} = L_{bc} = L_{ca} = M$, respectively) the synchronous reactance inductance L_s is defined as, $[L_s] = \text{diag} [L_g \ L_g \ L_g]$, given $L_g = L - M$.

Classically, ac machines are studied through direct and quadrature axis ($dq0$) theory. According to this theory, synchronous machine 3-phase armature quantities can be converted into two rotating components (aligned to the field and rotor, respectively) especially for salient pole machines. Stator quantities see time varying inductance due to the saliency. But in $dq0$ mode, the transformed quantities see constant magnetic path (i.e, constant inductance) as they rotate along the rotor.

When such transformation is conducted on a balanced set of three-phase time varying quantities, the 0 axis component is always zero. Therefore, the equivalent d and q axis quantities of the three terminal voltages in (Eq. 6.13) becomes

$$[v_{dq}^g] = -R_g [i_{dq}^g] + p_{dq}^g [\lambda_{dq}^g] \quad (6.15)$$

where $[v_{dq}^g] = [v_d^g \ v_q^g]^T$ are the orthogonal voltage terms. Also, on the right hand side, first term incorporates per-phase armature resistance $R_g = R_a = R_b = R_c$ and currents in each axis $[i_{dq}^g] = [i_d^g \ i_q^g]^T$, whereas the second term includes, an operator $p_{dq} = \begin{bmatrix} p & -\omega_{sre} \\ \omega_{sre} & -p \end{bmatrix}$, and flux linkage $[\lambda_{dq}^g] = \begin{bmatrix} \lambda_d^g \\ \lambda_q^g \end{bmatrix} = \begin{bmatrix} -L_d i_d + \lambda_m \\ -L_q i_q \end{bmatrix}$. Simplifying further, the matrix equations above yield

$$v_d^g = -R_g i_d^g - p L_d^g \dot{i}_d^g + \omega_{re} L_q^g i_q^g \quad (6.16)$$

$$v_q^g = -R_g i_q^g - p L_q^g \dot{i}_q^g - \omega_{re} L_d^g \dot{i}_d^g + \omega_{gre} \lambda_m \quad (6.17)$$

where ω_{gre} is electrical angular velocity, λ_m is machine constant/flux linkage, and L_d^g, L_q^g represent direct and quadrature axis inductances. The generator output power expression becomes

$$P_{gen} = \frac{3}{2} (v_d^g i_d^g + v_q^g i_q^g) \quad (6.18)$$

Subsequently, for a machine with N_p poles, the electrical load torque is:

$$T_{load} = \frac{3 N_p}{2} (\lambda_d^g i_d^g - \lambda_q^g i_q^g) = \frac{3 N_p}{2} (\lambda_m i_q^g + (L_q^g - L_d^g) i_d^g) \quad (6.19)$$

The aforementioned observations are applicable to a set of time varying quantities having any waveform. Extending this to a set of balanced sinusoidally varying quantities, one can consider the direct axis voltage to be zero and quadrature axis voltage to be equal to the peak of the time-varying quantity [170, 171]. Therefore, expressing the terminal voltages $[v_{abc}] = V_g [\cos \theta_{gre} \quad \cos(\theta_{gre} - 2\pi/3) \quad \cos(\theta_{gre} + 2\pi/3)]^T$, the corresponding outcome is, $v_d^g = V_g, v_q^g = 0$.

Another key assumption, which makes the transition to dc machine analogy very easy, is related to direct and quadrature axis inductances (L_d^g, L_q^g). Typically these quantities are in the range of mH and mutual difference is almost always within an order of magnitude [172]. Depending on machine design these can differ significantly. However, with a view to achieving simplifications, it can be reasonably assumed that $L_q^g = L_d^g = L_g$ for most machines. With these simplifications ($v_d^g = 0, v_q^g = V_g, L_q^g = L_d^g = L_g$), replacing i_d^g in Eq. 6.17 from Eq. 6.16 gives

$$V_g = -(R_g + pL_g)i_q^g - \frac{(\omega_{gpc}L_g)^2}{R_g + pL_g}i_q^g + \omega_{gpc}\lambda_m \quad (6.20)$$

The second term can be neglected compared to the other terms, because of the typical small inductance values. Denoting the quadrature axis current, which is the only effective current under discussion, as $i_q^g = I_g$, this expression may be re-written as

$$V_g = -(R_g + pL_g)I_g + \omega_{gpc}\lambda_m \quad (6.21)$$

It can be immediately noticed that, this equation is typical to dc machines and indicates why a PMA, even with a multiphase ac construction/operation, works more like a dc (permanent magnet) machine. Not surprisingly, this equation also accommodates synchronous machines. Fig. 6.6 reinforces this notion, where the non-linear resistance signifies the no-load losses, to be discussed later.

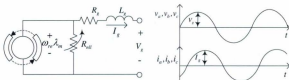


Figure 6.6: Per-phase circuit model and waveforms

The implication of this equation is that the per-phase peak voltage at the terminal is directly proportional to the rotational speed minus the drops in armature impedance. A rectifier-coupled system allows even closer realization of a dc machine. The key assumptions that allow the ac machine theories to transit toward dc machine analogy for a rectifier-coupled PMA are:

- The generator loading is balanced.
- Generator waveforms are sinusoidal.

- Direct and quadrature axis inductances are equal.
- The system is magnetically linear (inductance is the ratio of flux linked).
- All the self and mutual inductances among the phases are equal.

The permanent magnet alternator has outer rotor multi-pole structure and when coupled to a rectifier block, exhibits operational characteristics of a dc machine. Owing to this particular characteristics, these machines are often referred to as brushless dc machines (BLDC) and more information on modeling, simulation, and analysis can be found in [173–175].

Taking generator open circuit voltage $E_g = \omega_{gr}\lambda_m$ in Eq. 6.21 and denoting the peak value of generator stator voltage and current by V_g and I_g (Fig. 6.5), respectively, the stator expression is:

$$V_g = -(R_g + pL_g)I_g + E_g \quad (6.22)$$

Ignoring the stator electromagnetic transients, this equation becomes

$$V_g = -R_g I_g + E_g \quad (6.23)$$

Here the various speed terms are converted using

$$\omega_{gr} = \frac{N_p}{2}\omega_{gen}; \omega_{gen} = \frac{N_{gen}}{60}2\pi \quad (6.24)$$

Total generator power output is given by

$$P_{gen} = \frac{3}{2}V_g I_g = V_{gr} I_{gr} + 2V_f I_{gr} \quad (6.25)$$

whereas the electrical torque is expressed as

$$T_{load} = \frac{3}{2} \frac{N_p}{2} \lambda_m I_g \quad (6.26)$$

The loss torque term introduced in Fig. 6.2 and expressed through Eq. 6.32 is somewhat non-conventional. This can be used to reflect the nonlinear electrical losses, which depend on machine's speed, loading, and design [166]. For the PMG machine, this torque is expressed as

$$T_{loss} = \frac{P_{nll} + P_{ll}}{\omega_{gen}} - B_{gen}\omega_{gen} \quad (6.27)$$

Here the damping torque component is subtracted from the first term in order to avoid its multiple usage, which is already embedded in the friction & windage loss component (no-load losses, Fig. 6.7). A complete breakdown of the generator-rectifier losses is given in Fig. 6.7.



Figure 6.7: Power losses in the generator-rectifier system

Defining a no-load resistance attributed to the no-load losses as $R_{nll} = k_a + k_b F_{gen} + k_c F_{gen}^2$, (where the coefficients k_a , k_b , and k_c can be found empirically), the loss equations are:

$$P_{nll} = 3 \left(\frac{E_g}{\sqrt{2}} \right)^2 \frac{1}{R_{nll}} \quad (6.28)$$

$$P_{ll} = P_{cl} + P_{rl} = 3 \left(\frac{I_g}{\sqrt{2}} \right)^2 R_g + 2V_f I_{gr} \quad (6.29)$$

Further description on these formulations are available in [173, 174]. Also, alternate representation of these losses (i.e. generator and rectifier efficiency) is given in the appendix in normalized form. The voltage output at the diode-bridge is given as

$$V_{gr}^o = \frac{3\sqrt{3}}{\pi} V_g - 2V_f \quad (6.30)$$

At any given instant two phases of the generator and the filter capacitor bank at the rectifier terminal constitute an LC filter. The filtered dc voltage is therefore given by

$$\frac{V_{gr}}{V_{gr}^o} = \frac{1}{L_{fg}C_{fg}s^2 + R_{fg}C_{fg}s + 1} \quad (6.31)$$

where $L_{fg} = 2L_g$ and $R_{fg} = 2R_g$.

The generator input torque, as transferred through the transmission mechanism, can be divided into various components as shown in Fig. 6.2 and expressed through Eq. 6.32.

$$T_{gen} = J_{gen}p\omega_{gen} + B_{gen}\omega_{gen} + T_{cog} + T_{load} + T_{loss} \quad (6.32)$$

The cogging torque T_{cog} is an important characteristic of a PMA and could be dominant during the start-up phase of a hydrokinetic turbine. Presence of this torque term is essentially reflected as an additional load to the rotor, which depends on rotor position (i.e., alignment of magnet poles with stator windings) and specific machine design [160]. Given that a turbine is generally kept unloaded until it passes the cut-in conditions and attains full speed, this torque component can be represented as

$$T_{cog} = \hat{T}_{cog} \sin \theta_g \times f_A(-I_{gr}) \quad (6.33)$$

where \hat{T}_{cog} is the peak cogging torque (to be determined from design parameters or tests), θ_g represents angular positions (magnetic poles where cogging takes place, $\theta_g = \int N_p \omega_{gen} dt$), and f_A acts as a logical operator that considers this equation only in unloaded conditions. In addition to the reasoning presented above, this operator is necessary to increase the simulation speed.

6.4.2 Parameter Estimation

The parameters required for the model discussed above can be determined from a set of simple tests. For a permanent magnet three-phase star-connected PMA the following tests are sufficient to estimate the parameters.

Resistance Test

For phase resistance measurement, a dc source (preferably a controllable current source not to exceed the safe limits) can be placed across one phase of the machine. The resultant current and voltage information would reveal the resistance of that phase (for Star connected system):

$$Rg' = \frac{V_{dc}}{2I_{dc}} \quad (6.34)$$

The increase in resistance due to temperature elevation for continuous operations need to be incorporated. As a rule of thumb, the equivalent resistance from room temperature (t_{rm} , $25^{\circ}C$) to machine temperature (t_{mc} , $90^{\circ}C$) is generally considered using the empirical relationship below [176]:

$$Rg'' = \frac{Rg'(234.5 + t_{mc})}{(234.5 + t_{rm})} \quad (6.35)$$

The effective resistance may include the skin effect factor (typically 1.25) applicable to ac machines, as follows:

$$Rg = 1.25Rg'' \quad (6.36)$$

Open Circuit Test

The machine constant λ_m and equivalent no-load loss resistance R_{nl} can be determined from the open-circuit test. This test requires, a set of tabulated data containing open-loop phase voltage V_g , no-load power input/dissipation (P_{ll}), and corresponding electrical

angular velocity ω_{gpc} for a sufficiently wide range of rotor speed (up to 150%) of rated speed. The slope of the linear $V_g - \omega_{gpc}$ curve yields the parameter λ_m . The range of values for R_{nl} can be calculated using Eq. 6.28. These values can be curve fitted against electrical frequency for use in the system model. Here, the effect of magnetic saturation is ignored.

Inductive Load Test

In order to determine the synchronous inductance L_g , a three-phase balanced inductive load test (using high-Q/high-magnitude inductors) can be carried out at rated speed (Fig. 6.8). This test assumes that at or near the rated rotational speed, the armature resistance is negligible compared to the synchronous reactance [172]. At this condition, the difference between the generated e.m.f ($E_g = \omega_{gpc} \lambda_m$) and load voltage (V_{gt}) appears across the armature inductance. Measuring the phase current (I_{gt}), the inductance can be determined as

$$L_g = \frac{E_g - V_{gt}}{2\pi F_{gen} I_{gt}} \quad (6.37)$$

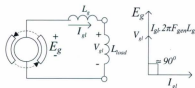


Figure 6.8: Inductive load test

For a given rotational speed N_{gen} and corresponding PMA output voltage frequency F_{gen} , the number of poles can be easily found by using the synchronous machine frequency-speed relationship given as, $N_p = 120F_{gen}/N_g$.

Inertia and Friction Test

Use of conventional methods toward identifying the generator moment of inertia (as in [176]) is mostly infeasible for the alternator being considered in this work. The primary reason being, the outer-rotor structure poses difficulty in conducting a belt-friction test. Such tests could potentially establish only the friction torque for use in overall torque equation (such as, Eq. 6.32), whereas other torque terms (cogging and losses) would require additional tests. Under such constraints, a theoretical estimation approach can be followed [177].

The permanent magnet alternator contains a number of rotating masses with different shapes. These parts are shown in Fig. 6.9. The combined inertia can be calculated by doing an algebraic summation of each of these parts' individual inertia using Eq. 6.38

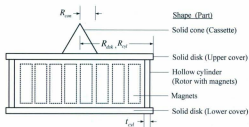


Figure 6.9: Generator dimensions for inertia estimation

$$J_{gen} = J_{con} + 2J_{dsk} + J_{cyl} \quad (6.38)$$

Here J_{con} , J_{dsk} , and J_{cyl} correspond to cone/cassette, disk/cover, and cylinder/rotor inertia, respectively. These parameters can be found by utilizing the standard methods for calculating polar moment of inertia of non-point masses as discussed in [177].

$$J_{con} = \frac{3}{10} M_{con} R_{con}^2 \quad (6.39)$$

$$J_{dsk} = \frac{1}{2} M_{dsk} R_{dsk}^2 \quad (6.40)$$

$$J_{cvt} = M_{cvt} R_{cvt}^2 (1 - t_{cvt} + \frac{1}{2} t_{cvt}) \quad (6.41)$$

Here M , R , and t stand for mass, radius, and thickness for components indicated by corresponding suffix. In Fig. 6.9, generator dimensions are indicated for use in the equations above.

6.5 Power electronic converters

Among various possible power electronic conversion schemes that can be used in hydrokinetic systems [178, 179], this work considers an ac-dc-ac topology as shown in Fig. 6.1. This scheme is realized through cascaded use of a rectifier bridge, paralleled dc-dc converters, and a grid-tie inverter (Table 6.1). Even though such an approach is not indispensable for hydrokinetic systems (especially for larger units where back-to-back inverters can be more suitable for grid-interfacing permanent magnet machines), the scope and objective of this research necessitates its use. In addition, instead of designing and building an application tailored optimized power conversion units, various off-the-shelf components have been used. Drawback of using an ac-dc-ac scheme (especially with an intermediate dc-dc stage) includes higher cost and increased power loss. None-the-less, the primary reasons behind opting for such topology are:

- *Modularity:* Most off-the-shelf power converters for use in small-scale alternative energy applications (mostly solar photovoltaic, fuel-cell or wind turbines) are highly modular and scalable. This allows matching the baseline design requirements with greater ease (such as, power ratings, input voltage ranges, controllability, etc.) during implementation in hydrokinetic systems.

- *Reliability:* While conducting laboratory tests with limited resources, off-the-shelf components prove to be more robust and reliable, as these devices typically contain features such as, EMI filter, grounding, and over-current/over-voltage protection. Custom-built systems, especially at the prototype level, generally do not contain these features and thereby operate under restrictive conditions.
- *Practical scenarios:* Considering the fact that hydrokinetic technologies are still in a nascent phase, it is expected that most small-scale applications will have to rely on industry-standard power electronic systems. Therefore, use of such devices allows one to study a more realistic scenario. In addition, this work aims at exploring a number of subtle control and operational characteristics, such as, efficiency non-linearity and advanced power tracking. The power converters used in this work are suitable for investigating these issues as well as other the practical challenges associated with their usage in practical hydrokinetic applications.

In Section 6.4, the rectifier bridge and associated filter capacitors have been modeled alongside the permanent magnet alternator (PMA). In the following sections, system description and modeling formulations pertaining to the dc-dc converter and dc-ac inverter are presented.

6.5.1 Zero-current-switching dc-dc converter

A dc-dc converter transforms a range of dc input voltages into a desired level at its output. High-frequency transformer coupled converters may also provide galvanic isolation. In this work, however, the primary purpose of using a dc-dc converter is to introduce enough flexibility such that the operating point of the overall hydrokinetic system can be controlled.

At the input side, the rectifier-coupled permanent magnet alternator provides an uncontrolled variable dc. On the other hand, a grid-tie inverter is connected to the output

of this converter. The dc-dc converter, with its ability to control the output dc voltage, regulates the bus voltage at the input of the inverter (Fig. 6.1).

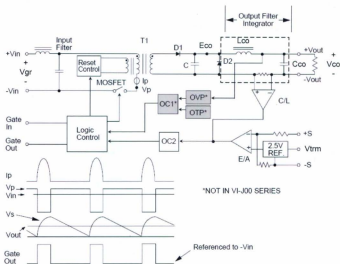


Figure 6.10: Zero-current-switching operation [180]

In order to achieve this objective, a commercially available dc-dc converter block (Vicor MegaMod™ VI-NN3-EM; input: 36 – 75 V, nominal output: 24 V, rated power 600 watt) is used. This power electronic component employs a zero-current-switching (ZCS) architecture and is galvanically isolated (Fig. 6.10). The output voltage can be trimmed (controlled) around 50% - 110% of the nominal value. It has built-in over-current, over-voltage, and thermal protections [180].

According to the manufacturer's specifications, the steady-state output voltage $E_{co} = V_{co}$ can be controlled by a trimming signal V_{trim} (Fig. 6.10). In ideal conditions, this output is given by

$$E_{co}^o = \frac{V_{trim}}{2.5} V_{cnom} \quad (6.42)$$

However, this relationship is valid only around the nominal operating point. Effects of voltage regulation and control limitations become dominant when the output current is high or the input voltage is low (with regard to the converter ratings). Denoting the converter voltage regulation by R_{cvr} , the voltage drop at off-nominal operating conditions is given by $\Delta E_{co} = E_{co}^o R_{cvr}$. This in-turns defines the output voltage as

$$E_{co} = E_{co}^o - \Delta E_{co} \quad (6.43)$$

The above relationships can also be expressed using the definition of voltage regulation

$$R_{cvr} = \frac{\Delta E_{co}}{E_{co}^o} = \frac{E_{co}^o - E_{co}}{E_{co}^o} \quad (6.44)$$

While the converter's controllability is given through Eq. 6.42, effects of voltage regulation is none-the-less implied. Therefore, this has to be characterized through empirical approaches. Since both the input voltage V_{gr} (fed by the rectifier-coupled generator) and output current I_c contribute significantly toward the system's voltage drop, a formulations such as Eq. 6.45 can be used.

$$R_{cvr} = f(V_{gr}, I_c) = q_0 + q_1 V_{gr} + q_2 I_c + q_3 V_{gr}^2 + q_4 I_c^2 + q_5 V_{gr} I_c \quad (6.45)$$

Here, converter voltage regulation is fitted two-dimensionally with input voltage and output current through a set of coefficients ($q_0 - q_5$). While the above formulations

allow a realistic characterization of the dc-dc converter in a large-scale steady-state domain, further modeling need to be conducted in order to represent the dominant system dynamics.

As discussed in [181] and shown in Fig. 6.10, the LC filter block between the internal voltage E_{co} and output V_{co} can be modeled using inductor voltage ($E_{co} - V_{co}$) and capacitor voltage ($I_{Lco} - I_c$) as given in Eq. 6.46 and Eq. 6.47.

$$I_{Lco} = \frac{1}{L_{co}} \int (E_{co} - V_{co}) dt \quad (6.46)$$

$$V_{co} = \frac{1}{C_{co}} \int (I_{Lco} - I_c) dt \quad (6.47)$$

The output current in Eq. 6.47 can be found by either $I_c = \frac{P_{con}}{R_{co}}$ or $I_c = \frac{P_{con}}{V_{con}}$, where P_{con} and R_{co} denote the converter's output power and load resistance, respectively.

6.5.2 Grid-connected dc-ac inverter

Hydrokinetic energy conversion systems have significant potential for contributing electric power in the form of distributed resources. Grid-connected inverters are critical components in that regard. These power electronic systems essentially interface an asynchronous or dc power source to the distribution network through single-phase connections. The primary objective of using a grid-connected inverter in this work, however, is to facilitate continuous power dissipation into the grid without requiring additional mechanisms to match the load with the harnessed power (such as in off-grid systems).

The grid-tie inverter used in this work is an off-the-shelf product (SWEA™ [182]; input 24 – 48 V dc, output power 0 – 250 watt). This unit is equipped with an over-voltage/over-speed dump load protection system (Fig. 6.11). The inverter contains a front-end converter that steps up the dc voltage and interfaces the grid through an H-bridge circuit.

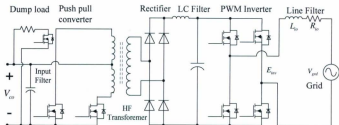


Figure 6.11: Grid connected inverter functional blocks

For the hydrokinetic test setup being considered (Fig. 6.1), the input of the inverter is connected to the dc-dc converter's output. The SWEATM inverter establishes an output power based on its dc input and is characterized by the following expression, as specified by the manufacturer:

$$P_{inv}^* = 10V_{co} - 250; \text{ for } 24 < V_{co} < 48 \quad (6.48)$$

Beyond the input voltage range the power output is zero (Eq. 6.49). The over-speed/over-voltage dump load circuit is activated around $V_{co} \approx 48$ and a system shut-down/power-cycling is needed to re-energize the inverters.

$$P_{inv}^* = 0; \text{ for } V_{co} < 24 \text{ and } V_{co} > 48 \quad (6.49)$$

Assuming the internal inverter voltage to be sinusoidal, the fundamental power transfer relationship between the inverter and the utility-grid is defined by the classical power angle equation [183,184]. Denoting the power angle by α_{ps} and the line filter reactance (assuming zero filter resistance) by X_{line} , this expression is given by Eq. 6.50.

$$P_{inv} = \frac{E_{inv} V_{gd}}{X_{to}} \sin \alpha_{ps} \quad (6.50)$$

The power transfer from the inverter to the utility-grid can be regulated by adjusting this power angle using a PI type controller. The difference between power demand P_{inv}^* (a function of input voltage V_{in} , Eq. 6.48) and actual output P_{out} can work as the error signal in this control scheme.

$$\alpha_{ps} = K_{pinc}(P_{inv}^* - P_{out}) + K_{invc} \int (P_{inv}^* - P_{out}) dt \quad (6.51)$$

The output power, for use in the equation above, is a function of grid voltage, inverter current, and power factor. The SWEATM inverter maintains a constant power factor of 0.97 lagging.

$$P_{out} = V_{gd} I_i \cos \theta_{pf} \quad (6.52)$$

While the formulations in Eq. 6.48-Eq. 6.52 define the power control mechanisms in the steady-state domain, the inverter model needs incorporation of dynamic features. These inverter dynamics are associated with input filter capacitance, rectifier LC filter, and output line filter (Fig. 6.11). Assuming the front-end conversion processes (the push-pull type converter with input and output filters) maintains a constant dc voltage throughout the range of inverter's operation, the only dominant dynamics may arise from the output line filter. Denoting the voltage drop across this filter by V_{df} , the inverter current can be expressed using the dynamic equation below [185]:

$$L_{to} \frac{dI_i}{dt} + R_{to} I_i = V_{df} \quad (6.53)$$

In order to identify the voltage drop across the inverter line filter, the basic circuit configuration in Fig. 6.12(a) and the phasor diagram in Fig. 6.12(b) can be consulted. It

should be pointed out that the phasor diagram demonstrates the inverter operation with lagging power factor conditions and the expressions below correspond to this condition only.

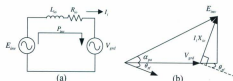


Figure 6.12: Inverter power control and phasor diagram

With a inverter current I_i (lagging the grid voltage V_{grd} by an angle θ_{pjf}) and line reactance X_{i0} , the voltage drop across this reactance can be approximated by Eq. 6.54 and Eq. 6.55.

$$\cos(90^\circ - \theta_{pjf}) = \sin \theta_{pjf} = \frac{E_{inv} \cos \alpha_{ps} - V_{grd}}{I_i X_{i0}} \quad (6.54)$$

$$V_{dij} \approx I_i X_{i0} = \frac{E_{inv} \cos \alpha_{ps} - V_{grd}}{\sin \theta_{pjf}} \quad (6.55)$$

The dynamic models of the dc-dc converter and dc-ac inverter essentially represents the large-signal nonlinear time domain characteristics. Being an off-the-shelf component, exact system architecture and control methods cannot be determined for these systems. Therefore, in this work, empirical models have been developed using available design information and validation is done through experimental tests.

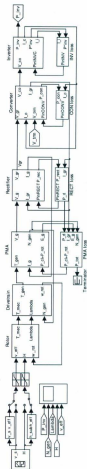


Figure 6.13: Matlab-Simulink™ implementation of the simulation model

6.6 System simulation and summary of dynamic modeling

Throughout this research, various design, development, and integration activities have been carried out in conjunction with numerical modeling and simulation in almost every step. The primary software tool used in this regard is Matlab-SimulinkTM [156]. This allowed greater flexibility in studying the subtleties associated with rotor, generator, power converters, and hydrokinetic system, in general.

This very model is used in subsequent power tracking control studies where the de-dc converter's trimming voltage acts as the primary control variable for the whole hydrokinetic system. For various control methods described in Chapter 10 and Chapter 13, only difference against the system represented in Fig. 6.13 is that each of the methods are run under separate control blocks (Fig. 10.4 and Fig. 13.7).

The modeling scheme presented in Fig. 6.13 contains unreduced large-signal description of each of the HECS subsystem (i.e. turbine-rotor, gear, generator, rectifier, converter, and inverter). As inputs to the system, variations in water velocity and elevation are incorporated with their stochastic variation models described in Section 4.5 and in Fig. 4.22. All the major subsystems are interlinked with corresponding loss models, which allow describing the system on a more realistic and non-linear domain.

Chapter 7

Test Apparatus and Model Validation

The numerical models developed in this thesis are one of the most critical contributions of this research. This task is both challenging and important for a multitude of reasons. The challenges associated with system modeling primarily arise from the fact that the research focus is on small-scale systems where adequate attention needs to be given on a number of minute details. Many of these factors (such as, losses, voltage regulation, etc.) can be effectively ignored in larger systems, which is not acceptable for smaller test systems. For instance, most commercial-grade large-scale electric machines or converters would have sufficient name-plate information and the relevant specifications can be followed throughout the operating range of the device. On the contrary, small-scale prototypes may not have such information and their underlying characteristics may deviate significantly from one point of operation to the next. The importance of the modeling activities lie within the fact that a detailed model provides sufficient flexibility, which can be further simplified as per requirements of a larger system. In this work, these models are also used as the test platform for comparison and synthesis of various power tracking control methods.

In order to convey sufficient confidence in these models, it is critical to establish the models' validity. In addition, the test setup, conditions, and apparatus need to be adequately described such that the underlying accuracy and limitations can be properly inferred. In this chapter, both the test scenarios and model validation results are provided. The test and measurement activities pertaining to the model validation and

general performance analysis task have been carried out under two scenarios (electrical laboratory and tow-tank). Most electrical and electromechanical subsystems of the HECS have been studied within the laboratory environment. The hydrokinetic turbine along with the generator and rectifier (coupled to a resistive load bank) have been tested in the tow-tank setup.

7.1 Laboratory test apparatus and electrical systems

The laboratory test rig primarily consists of a prime mover (universal dc motor) and the permanent magnet alternator. The generator is placed in a horizontal platform and is coupled to the dc motor through chain sprocket arrangement. The gear ratio on the generator side can be remotely changed. Using this feature the start-up and cogging characteristics have been studied. Also, the generator model validation is carried out using this arrangement. This test rig can potentially be used as a hydrokinetic system emulator platform as part of any further research.



Figure 7.1: Laboratory test rig setup

The prime mover is supplied using a customized power supply (single phase thyristor controlled ac-dc converter), which can be operated either manually (a variac controlling the firing angle) or by dc signal fed from a personal computer based data acquisition hardware (Fig. C.1). As part of this setup, a multi-purpose switchable resistor box has

also been built in order to study the generator, rectifier, converter, and turbine rotor characteristics (Fig. C.2).

7.1.1 Rectifier coupled permanent magnet alternator

The permanent magnet alternator (PMA) being used in his work is primarily designed for electric bicycles. Even though this machines was found to be suitable for use in a low-speed/high-torque applications such as in hydrokinetic systems, several critical challenges were observed in developing its models. With little available machine data, the need for parameter determination became apparent. Also, being a outer-rotor chain-coupled unit (Fig. 7.2), direct torque measurement was not possible.

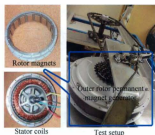


Figure 7.2: Outer rotor PMA coupled to turbine shaft

In light of these challenges, a set of test methods discussed in Section 6.4.2 has been utilized and the following parameters were determined (Table 7.1). The no-load loss equivalent resistance was estimated as $R_{null}(\Omega) = 5.5 + 0.041F_{gen}^2 + 0.01F_{gen}^3$, using a curve fitting approach. The generator inertia has been numerically calculated using Eq. 6.38. In this step, corresponding masses and dimensions are taken as, $M_{disk} = 0.17$ kg, $M_{con} = 2$ kg, $M_{cpl} = 1.5$ kg, $R_{con} = 0.0575$ m, $R_{disk} = R_{cpl} = 0.17$ m, and $l_{cpl} = 0.01$ m.

Table 7.1: Permanent magnet alternator model parameters

Parameter	Value	Unit
Per-phase armature resistance, R_a	0.23741	Ω
Per-phase armature inductance, L_a	0.4156	mH
Machine constant, λ_{ms}	0.06142	$V/(rad.s)$
Number of poles, N_p	24	-
Generator inertia, J_{gms}	0.055	$kg - m^2$
Generator Friction constant, B_{gms}	0.1565	$Nm/(rad.s)$
Diode forward voltage drop, V_f	0.70	V

The PMA unit has been tested using the emulator setup described in the previous section, where a dc series motor worked as a prime mover. The output of the generator, after converting into dc (through rectifier and filter), has been fed to a switchable resistive load.

This rectifier-coupled alternator was studied for voltage-current and power-speed relationships using a range of resistor values. As can be seen from Fig. 7.3, the expected loading characteristics match with the predicted curves with a high degree of accuracy. However, it was observed that the measured rotor speed had an error of 3% and was accommodated in the plots accordingly.

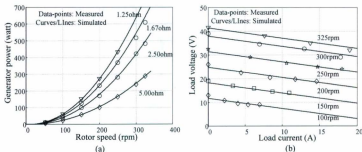


Figure 7.3: Generator performance in steady state (a) output current and voltage (b) output power and speed

While the performance of the generator as well as the model's accuracy is shown in steady state domain in the figures above, the dynamic performance is validated through a Matlab-Simulink™ based scheme shown in Fig. 7.4. Simulation results confirming a set of physical tests are given in Fig. 7.5.

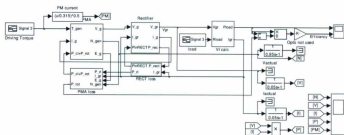


Figure 7.4: Matlab-Simulink™ model of the PMA

The generator speed is sensed using a mechanical sensor (tachogenerator), whereas the current and voltage signals are acquired through custom built circuitry. The generator is loaded sequentially with 5, 2.5, 1.67 Ω resistors around $t = 8, 13.5, 20 \text{ sec}$. At $t = 30, 38, 43 \text{ sec}$, the PMA is unloaded in the reverse order.

The initialization part ($t < 5 \text{ sec}$) of the simulation contains mismatches due to different start-up procedures applied during the physical tests and has been truncated. The relationship between prime-mover current and input torque to the generator has been established through separate tests on the prime-mover itself. This estimation contains subtle errors at the start-up and shut-down conditions, as shown in Fig. 7.5. Other than this limitations, the simulation runs agree almost entirely with the test measurements.

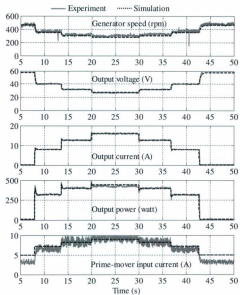


Figure 7.5: Generator model validation (dynamic simulation)

7.1.2 Zero-current-switching dc-dc converter

Apart from the rectifier block considered within the generator test and modeling task, the remaining power electronic components are: dc-dc converter and dc-ac inverter. The dc-dc converter, being an off-the-shelf hardware, lacks sufficient parametric information toward developing a detailed model. Therefore, various empirical approaches have been followed.

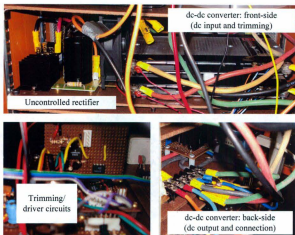


Figure 7.6: Converter (dc-dc) stage containing two bricks

The output of the rectifier is fed into the converter block, which contains two dc-dc bricks (input terminals in parallel, output terminals in series). The converters are driven by individual driving/trimming circuits, which take signals either from a DAQ/control system or from a separate dc power supply. These connections are shown in Fig.7.6.

While most of parameters for the dc-dc converter were collected from the manufacturer's specification sheet [180], the output inductance L_{co} and capacitance C_{co} are assumed staying in line with works done in [186]. The coefficients associated with voltage regulation calculation are done using a curve-fit program [187].

Table 7.2: Converter model parameters

Parameter	Value	Unit
Nominal output voltage, V_{cnom}	48	V
Converter output filter inductance, L_{co}	80	μH
Converter output filter capacitance, C_{co}	16	nF
Voltage regulation curve-fit coefficients, q_0	6.36	—
Voltage regulation curve-fit coefficients, q_1	-0.337	—
Voltage regulation curve-fit coefficients, q_2	1.51	—
Voltage regulation curve-fit coefficients, q_3	0.0042	—
Voltage regulation curve-fit coefficients, q_4	-0.0132	—
Voltage regulation curve-fit coefficients, q_5	-0.00776	—

For the purpose of testing the converters' steady-state and dynamic performance, the input terminals were supplied by a dc power supply (instead of the rectifier block). Representative performance plots for this setup are shown in Fig. 7.7, which confirms to the data specifications given in the original data-sheets [180].

The overall dynamic modeling scheme presented in Section 6.5.1 has been implemented in Simulink™ (Fig. 7.8). With a dc supply of $V_{gr} = 35$ V and trimming level set at $V_{trim} = 2.0$ V multiple step changes are applied in the output resistive load. As shown in Fig. 7.9, these step changes are imposed at $t = 1.15, 2.30, 3.15, 4.10$ sec, which correspond to an output resistance of 10, 5, 10, ∞ Ω , respectively.

The test and simulation results plotted in Fig. 7.9 indicate that the dominant system dynamics are within an order of milliseconds and have good match between theoretical and actual performances.

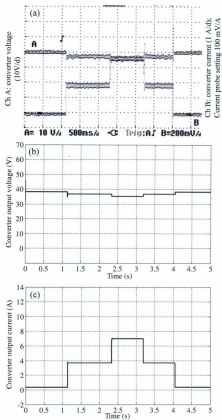


Figure 7.9: Converter model validation (a) test - output current and voltage (b) simulation - output voltage, and (c) simulation - output current

7.1.3 Grid-connected dc-ac inverter

The power electronic inverter for interfacing the dc output from the converter into a single-phase ac, has been tested in the laboratory environment using a regulated dc power supply and various measurement instruments. The inverter contains a dump-load over-voltage protection scheme (and associated control circuit) and an internal dc step-up and a subsequent H-bridge stage (Fig. 7.10). These inverters can also be used as modular/scalable manner as in the case of dc-dc converter. However, in this application, the power and voltage ratings can be met sufficiently by only one block.

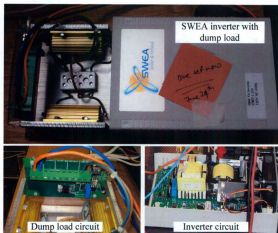


Figure 7.10: Inverter (dc-ac) stage containing dump-load circuit

Using the manufacturer's specification as well as consultation with the device developer, the following parameters have been used in modeling the inverter in both steady-state and dynamic domain (Table 7.3).

Table 7.3: Inverter model parameters

Parameter	Value	Unit
Utility-grid voltage, V_{grid}	118.5	V
Inverter internal voltage, E_{inv}	120	V
Inverter line filter inductance, L_{in}	30	mH
Inverter line filter resistance, R_{in}	0.37	Ω
Power factor angle, θ_{pf}	0.25	rad
Inverter power angle controller parameter (integral), K_{inv}	-0.0175	-
Inverter power angle controller parameter (proportional), K_{pinv}	-0.000125	-

With regard to steady-state inverter performance characteristics, specifications given through Eq. 6.48 and Eq. 6.49 are tested and validated as shown in Fig. 7.11. It can be seen that around $V_{co} = 49.5$ the over-voltage protection is activated, which requires a full power cycling in order to restart the system.

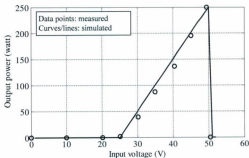


Figure 7.11: Inverter steady-state performance: input voltage and output power relationship

The inverter system model has been simulated using the descriptions presented in Section 6.5.2 as well as the parameters listed in Table 7.3 (Fig. 7.12). It should be pointed out that, being an empirical modeling exercise, various internal control loops are

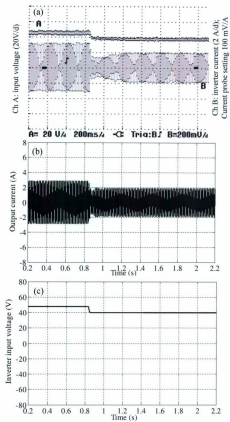


Figure 7.13: Inverter model validation (a) test - output current and voltage (b) simulation - output voltage, and (c) simulation - output current

7.2 Tow-tank test apparatus and turbine rotors

As part of this research, a series of turbine design, development, and tank trials were performed at Memorial University of Newfoundland (MUN). Each of these steps had certain objectives and valuable experience was gained through this exercise. In total, three turbine units were tested at the towing tank in the Faculty of Engineering & Applied Science's Ocean Engineering Research Center (OERC). The OERC towing tank has a physical dimension of $70\text{ m} \times 4\text{ m} \times 2.5\text{ m}$ (length, width, depth). However, only about 55 m of its length can be used for effective towing purposes (Fig. 7.14).

The towing carriage has a maximum speed capacity of 5 m/s . The water depth during the turbine tests was kept around 2 m and the turbine system was placed such that the generator stays above the surface, whereas the instrumentation electronics was placed on a deck. The mounting frame holding the turbine rotor has a dimension of $1.5\text{ m} \times 0.5\text{ m} \times 0.73\text{ m}$ (length, width, depth). The walls of the frame were filled with high-density styrofoam and the edges of the structure (except the top part) was given an oblique shape to reduce the drag (Fig. 7.15).

Two of these were designed and built in-house, whereas New Energy Corp Inc. [45]¹ contributed the third turbine rotor (Fig. 7.16, Fig. 7.17, Fig. 7.18, Fig. 7.19), which has been machined to fit the mounting frame and towing carriage.

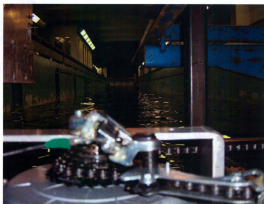
¹Lent by New Energy Corporation Inc. (NECI), Suite 473, 3553 31 st Street NW, Calgary, Alberta, T2L 2K7; <http://www.newenergycorp.ca>



Towing carriage



View of tow tank & beach



Tow tank (beach), as seen from the rotor

Figure 7.14: MUN-OERC tow-tank

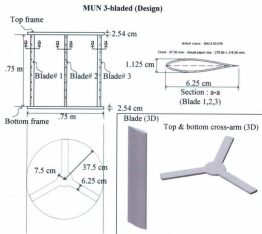


Figure 7.16: Three bladed turbine design and fabrication at MUN



Figure 7.17: Three bladed turbine test at MUN OERC tank

MUN 6-bladed (design, development and testing)

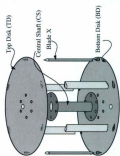
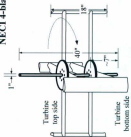


Figure 7.18: Six bladed turbine designed and tested at MUN

NECI 4-bladed (Mounting and testing)



Turbine dimensions

Turbine blade, cross arm, and flanges



Figure 7.19: Four bladed turbine provided by NECI

Rotor	Turbine description	Test objective	Observations	Test summary
MTN 3-bladed:	<ul style="list-style-type: none"> NACA 63-018 blades, chord 6.25 cm, height 0.75 m, diameter 0.75 m, solidity 25%. Two radial arms at the top and bottom hold the blades with no center shaft. The structure is of cantilever type. 	<ul style="list-style-type: none"> To identify towing tank/carriage suitability To observe basic structural, starting, and rotary/oscillatory behaviour 	Clearly the turbine was structurally weak and had high cut-in speed. However, the exercise indicated that the tank facility is suitable for short runs of tests and the rotor had self-starting issues. It would not start unless positioned in certain azimuth angles, and rotary motion was not smooth.	Rotors with higher solidity and support frame needed for structural purposes. Also, number of blades needed an increase to improve start-up performance. All these steps, however, risk reduction in operating efficiency.
MTN 6-bladed:	<ul style="list-style-type: none"> NACA 0012 blades, chord 6.75 cm, height 0.4 m and diameter 0.8 m, solidity 50%. A center shaft holds the rotor to a frame, which was mounted to the towing carriage. Two self-aligning water sealed bearings were used. Also, two solid disks provide radial support. 	<ul style="list-style-type: none"> To realize a better structure To observe power output, start-up, and oscillatory characteristics. 	High inertia, slow start-up and low run-time yielded the design to be unsuitable for testing in this tank facility. Also, apparently the skin friction resulting from the top and bottom disks reduced the performance drastically (i.e. the generated power equaled the system losses, - 200 watts).	A 4 or 5 bladed system with similar or less solidity would be more suitable as long as the radial arms/disks are well machined and optimally sized for reduced mass/inertia.
NECI 4-bladed:	<ul style="list-style-type: none"> NACA 0015 blades, chord 10.1 cm, height 0.4 m, diameter 1 m, solidity 40%. A set of four radial arms (piecewise tear-drop shaped) connects the blades to the shaft. The shaft, bearings, and mounting frame have been retrofitted from the previous setup. 	<ul style="list-style-type: none"> To observe electrical power output characteristics at the generator terminals. To identify subtle aspects of testing in a controlled environment. 	In general, the tests yielded important observations in relation to the intended objectives. Further discussion will be given in the following sections.	The tests were successful in establishing the basic behaviour of a vertical rotor. However, a number of limitations unique to this test arrangement were observed. These aspects along with some generic observations will be presented in the next sections.

Figure 7.20: Summary of turbine design and performance features

In order to collect the rotor performance data (as well as to conduct various laboratory testing), a simple and robust data acquisition (DAQ) system has been developed. This customized DAQ system consists of four channels. The dc voltage and current at the load (dc bus) is sensed and fed to a data acquisition card (USB 1208LS). The speed of the turbine is sensed at the generator using a custom-built optical (infrared signal based) sensor. While the intention was to avoid underwater instrumentation, the generator, however was subjected to frequent splashes of water. Therefore, the sensor was housed in a water sealing arrangement. Also, the length of the wire and noise introduced by ambient equipment (especially, drive system of the towing carriage) was noticeable. The flow/carriage speed is sensed using a setup embedded to the carriage. All these signals contained noise components and filtering/scaling circuits were built to interface these to the data acquisition (DAQ) card (Fig. 7.21, Fig. 7.22).

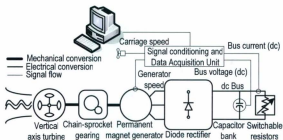


Figure 7.21: Data acquisition arrangement

The customized data acquisition unit contains first order RC filter at the interface of the DAQ board. While these filters are indispensable in truncating the high frequency noise, they also induce some dynamics. This issue is not critical for the system's operation in open-loop condition, as followed in this exercise. However, in order to match the

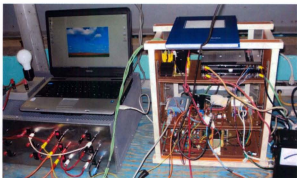


Figure 7.22: Data acquisition and power electronic hardware

test results with the simulations, effects of these filters need to be identified. The DAQ channels inadvertently make subtle contributions to the system modeling/representation. From a number of design and test procedures the sensor signal processing is represented using the following first order transfer function:

$$\frac{V_{sen}^k}{V_{act}^k} = \frac{1}{\tau_k s + 1} \quad (7.1)$$

Here $k = 1, 2, 3, 4$ for rotor speed, current, voltage, and water velocity signals, respectively. It should be pointed that the rotor speed sensor has a long electrical path from the generator to the DAQ board and also is susceptible to ambient machinery (motor drive at the tow tank carriage). In order to eliminate a low frequency noise component, this filter is designed with a higher time constant compared to the rest (current, voltage, and carriage speed).

7.2.1 Rotor performance evaluation

As part of this research, a series of tests were carried out on the vertical axis turbine systems with a view to developing insights into their design and operational aspects. The primary focus of these tests is on a set of subtle observations pertaining to the use of permanent magnet alternator (PMA) in small vertical turbine units. Such scale-model tests are essential first steps toward full-scale design and deployment. Therefore, these results will have important repercussions on large-scale systems when interpreted with sufficient reasoning.

To specify further, the objectives of the test arrangement are to observe the system performance in terms of efficiency, start-up, output oscillations, factors leading to performance degradation, and free-surface/submersion effects. A good level of research activities can be observed mostly on rotor's hydrodynamic characteristics with emphasis on design [6], tank/field trials [3, 4, 165], and theoretical investigation [96, 188]. However, it would be worthwhile to observe the system performance from an electrical power output perspectives, as pursued in this work.

Another motivation behind the test activities is to identify issues that are of interest to control analysis and synthesis. Issues such as, whether one normalized performance curve (efficiency vs. tip speed ratio) is sufficient to backtrack the speed-power relationships, whether a turbine can start on its own, whether the system damping is sufficient to provide stability or too high to cause for excessive losses, etc., are important questions that have bearing on the control aspects of the system. This section primarily investigates these questions through a series of tests conducted in a controlled environment.

Although a high level of research and development activities can be perceived in the field of vertical axis turbines, most of the information has apparently remained protected for commercial reasons. Two examples of extensive vertical axis turbine design, development, tank testing, and field trials can be found in references [6, 165]. While these initiatives have given valuable insight into turbine behavior, the published information

mostly deals with issues such as complexity of hydrodynamics, start-up problems, and efficiency characteristics. This work provides time-series performance data and complements the previous studies by considering the effects of power take-off system. Other relevant publications (horizontal axis marine current turbine [4, 93], small wind turbines with similar test setup [189]) were also studied to develop understanding of the tests carried out as part of this investigation.

It should be pointed out that the design and development activities were performed with very limited resources. Also, the aims of the studies were to develop greater understanding of a vertical axis turbine's behavior when coupled with a permanent magnet generator serving an electrical load (Fig. 7.20). Clearly, no significant attempts were given in visualization, fluid dynamics, and design optimization to realize commercial-grade turbines.

While the three and six bladed turbines designed and built at MUN were found to be unsuitable for detailed testing, the NECI four bladed rotor was used for a number of tests. The basic principle of testing the turbine-generator unit is to ramp-up the flow (i.e. carriage speed), allow rotor revolution to reach steady/high value after the carriage has reached its steady speed, impose electrical loads (from low to high in discrete steps), and gather all the four sensed parameters (rotor speed, flow velocity, bus voltage, and bus current) in a data file.

Prior to each run a carriage velocity was set manually. Since the total towing time is very small (15 – 25 sec) and the rotor may not achieve its steady state during the run, a manual push was given to assist the rotor to start up, thereby reducing the initialization period. The effect of such manual start is limited within the start-up period. All subsequent step changes (electrical load variations) have been introduced only after a steady state has been reached. Therefore, this action contributes minimally to the overall outcome of the tests.

In addition to calibrating the sensors for measuring rotor speed, generator voltage,

and load current, the carriage velocity was also adjusted for true values. The latter calibration involved measurement of time using a stopwatch and distance using a measuring tape. Linear calibration has been applied for all the sensors and overall error has been found to be $< 0.5\%$. Various general observation pertaining to the rotor's level of submersion, oscillating characteristics, start-up behavior, and overall efficiency are discussed in the following sections.

Level of submersion

With a general assumption that the depth of rotor submersion will linearly change the effective rotor area, the power output should ideally vary linearly with effective water level. However, it is understood that the free-surface proximity and subsequent boundary layer effects, and air suction due to funneling will play a critical role. The first set of tests, as outlined in the following section was carried out to gain further insight into this issue.

Figure 7.23 shows a typical set of time-series plots as collected, analyzed, and evaluated throughout this work. This particular plot, however, focuses on the issue of free surface proximity and depth of submersion. The term 'full submersion' implies the rotor is submerged in water and the top of the blade-plane is around 10 cm below the calm water level. On the other hand, 'partial submersion' indicates the rotor have around 10 cm of exposed blade-length in free air under calm water conditions.

As the carriage containing the rotor is towed in water, the turbine is manually started. After reaching a carriage speed of 2.35 m/s the rotor speed and voltages are observed to see if these parameters are 'high' enough. This is done because under unloaded conditions the rotor speed and generator output voltage will increase monotonically until the run time is nearing the end.

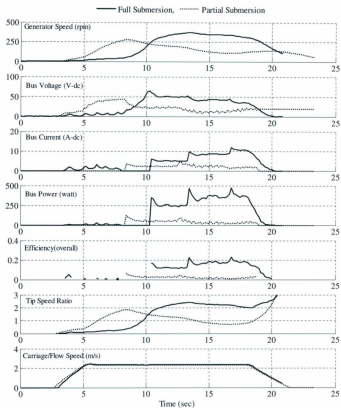


Figure 7.23: Effect of rotor submersion and free surface interactions

Table 7.4: Effects of vertical rotor submersion level on effective rotor height

Submersion	Implications (Rotor height = 0.4 m)	Overall efficiency	Effective height
Full	rotor is submerged in the water and the top of the blade-plane is around 10 cm below the calm water level	18%	100% of rotor height
Partial	rotor have around 10 cm of exposed blade-length in free air under calm water conditions	5%	27.8% of rotor height

As seen in Fig. 7.23, the 'partial submersion' case has a better start-up performance probably owing to a higher push during the manual start. Three discrete loads (10Ω , 5Ω , and 3.33Ω) were imposed in each case. The focus of attention in this plot should, however, be the efficiency values. The 'full submersion' case indicates an overall efficiency (dc output power to theoretical fluid power) between 12% to 19%. However, the 'partial submersion' case indicates significant reduction in efficiency (5% or less). These results are tabulated in Table 7.4. It can be argued that in the 'partial submersion' case the rotor was not allowed to reach a steady/higher speed (Fig. 7.23, rotor speed plots during $t = 5 - 10$ sec). But, in this test, repeated attempts showed the maximum unloaded rotor speed to be around 250 rpm. Therefore, this test has, to some extent, captured the peak performance under the given conditions. A further reduction in water level did not allow the rotor to sustain its rotation and such attempts were discarded.

Comparing the results with regard to the variations in water depth, it can be seen that water level plays a very significant role in rotor performance. The visible free-surface interaction (i.e. formation of bow-waves and air-suction during the rotation) can induce exponential reduction in overall performance. In contrast, the fully submerged rotor, in spite of being subject to high level of drag and turbulence from the frame edges (top part), indicates better efficiency. While the extent of these variations cannot be quantified through these tests, it can be said that the relationship between power output and water depth is expected to be nonlinear.

Oscillating behavior

It is widely known that vertical axis turbines, due to their unique principle of operation, are subject to torque ripples. This phenomenon has been studied extensively in wind energy domain for assessing blade fatigue and structural strength [147]. In this work, however, the reflected oscillatory characteristics at the load terminal (dc bus in Fig. 7.21) is observed and analyzed.

In Fig. 7.24 a set of time series observations are presented to shed further light on this issue. The tests were conducted with a steady carriage speed of 2.5m/s. The applied resistive loads are 5Ω , and 2.5Ω . The voltage output of the PMA depends dominantly on its rotational speed. The oscillations in this quantity as shown in Fig. 7.24 are due to the contributions from variations in generator current caused by the torque ripples. The output current, as expected, carries the oscillating behavior at the load terminals.

The application of the higher load at around $t = 7 \text{ sec}$ caused the rotor to migrate to a low tip speed ratio condition. While the system runs almost in a limping mode, the oscillatory behavior is quite dominant and visible in this condition. The ramp during the interval of $t = 7 - 10 \text{ sec}$ shows the gradual increase in the ripple characteristics. It should be pointed out that, the aggregated inertia of the rotor-generator unit and placement of a filter capacitor at the dc bus play important role in curtailing output ripples, especially at the higher tip speed ratio conditions. It can also be observed that the ripple frequency is directly related to the rotor's rotational speed.

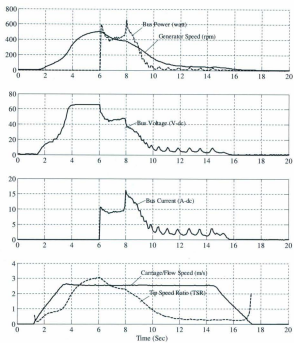


Figure 7.24: Torque ripple in the system output

Even though it is expected that a hydrokinetic turbine system will operate mostly at the near-optimal tip speed ratio (by means of power tracking control), and hence ripple effects will be minimal, there are other implications of this phenomena. Firstly, when a turbine enters the low tip speed zone (sub-optimal conditions), significant structural stress is imposed on the drive-train. Secondly, large-scale hydrokinetic systems injecting electric power to a weak grid may introduce flicker conditions as soon as optimum tip speed conditions are not met. The tests performed here bring insight into the characteristics, occurrence, and frequency of the torque ripple phenomena.

Start-up behavior

The term 'start-up' refers to the condition where a turbine initiates its rotation and sustains its motion following a stalled state. Horizontal axis turbines are inherently self-starting. However, vertical turbines, depending on the number of blades and their shapes, may not bear that feature. Also, starting requirements may become more stringent due to reflected torques from the generator and load side.

Unlike the previous case, as part of this test, the rotor is initially allowed to rotate without any assistance. Also, the generator terminal is unloaded throughout the run and the rotor is fully submerged. Initial tests were carried out with the generator decoupled from the rotor. It was observed that the rotor, by itself, started to rotate at around 0.65 m/s to 0.75 m/s of water velocity. Also, the rotor azimuth angle apparently did not play a great role in this regard.

As the generator is attached to the rotor, the start-up condition degrades greatly when compared to the previous case (rotor without the generator coupled to it). After conducting a number of runs at increasing water/carriage speeds, it became apparent that the turbine (with the PMA) self-started at speeds between 1.75 m/s and 1.85 m/s (Fig. 7.25). The rotor blades (*NACA0015*) have highest lift coefficients at $10 - 15$ degree angle-of-attack. Therefore, a favorable azimuth angle to the blades (around $10 - 15$ degrees) was allowed in certain instances. However, it was observed that even with such

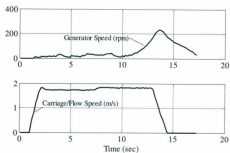


Figure 7.25: Start-up behavior

arrangement, any rotor movement is locked until the start-up velocity (between 1.75 m/s and 1.85 m/s) is attained. Clearly, the generator cogging torque and friction contributed to this problem.

System efficiency

While the system efficiency is an important figure of merit, it is almost impossible to realize an optimistic performance curve through small-scale tests done in controlled environments. In this particular setup the overall losses (radial arms, frame walls, frame edges, tank walls, gearing, bearing, generator, and rectifier) would undoubtedly be significant compared to the overall output.

In this investigation the turbine system is tested for a number of water/carriage velocities and loading conditions. The data accumulated in each of the runs is reviewed using plots similar to Fig. 7.23. Since efficiency is a steady-state parameter, the transient data points are manually truncated to reflect a more steady behavior. Finally, efficiency (electrical output to fluid power ratio) data is plotted against tip speed ratio. In Fig. 7.26,

these data sets are presented. It should be mentioned that some of the remotely scattered points are due to transient conditions that could not be eliminated from the time series data. The peak efficiency for this setup is above 20% and the optimum tip speed ratio is around 2.15.

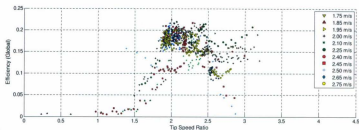


Figure 7.26: System efficiency at various carriage/water speeds

Even with various losses associated with the conversion process, the efficiency characteristics are encouraging. In fact, for this type of converter peak efficiencies around 20% are very common [3, 165, 189]. There also exists ample room to improve the power output with design modifications such as, hydrodynamic shaping of radial arms, higher efficiency generator fabrication, and elimination of gears.

One interesting phenomenon that was observed in this test is that at each operating velocity (i.e. operating conditions, in general) there exists a separate performance curve (Fig. 7.26). This arises from the fact that the fluid dynamic interactions at each operating conditions are highly non-linear and complex. Also, stability of the structure and initial conditions (start-up, level of loading etc.) contribute to this. As an established norm, these variations are averaged and fitted through a single curve [189]. This raises a question as to whether a single curve can be used in backtracking the various operating

conditions, which clearly take dispersed routes. Provided, performance curves are particularly important in describing the overall system, the issue of possible non-existence of a unique curve is particularly important in system modeling and control synthesis. This behavior, although mostly overlooked, is also seen in other works [6, 190].

General observation and limitations

In order to provide caveats for the test results presented in this work, as well as to encourage further research, a set of observations and limitations are presented here. For testing hydrokinetic systems under controlled environment, longer tow-tanks (with an effective length of 200 m) or high-speed flume tanks (> 2 m/s velocity capability) are desirable. As experienced in this test exercise, the effective length of the OERC tank was insufficient to carry out longer runs. It should also be pointed out that operations at higher speeds pose risks of damaging the rotor due to strong reflected waves hitting the structure. The flow regime within the rotor frame and in its wake appeared highly turbulent and non-stationary. A sequence of snapshots are given in Fig. 7.27 with this regard. Any further research should emphasize on quantifying the effects of rotor frame and flow characteristics on the rotors operation by means of more sophisticated visualization and data acquisition tools.

The permanent magnet alternator used in this experiment exhibited weak start-up performance, caused reduced efficiency, and required gear coupling arrangements. However, it should be stated that these issues are not typical for such generators and can be effectively eliminated through proper design as long as the requirements are known. The tests presented here indicate some of the design needs of PMAs for use in hydrokinetic turbines (i.e, low-speed, low-cogging, high-efficiency generators).



Figure 7.27: Turbulence in rotor's flow field

While the sensory and data acquisition system proved to be very useful in amassing the test results, the underwater speed sensor faced frequent failures due to water splashing and leaking. In light of this experience, it can be stated that a robust hydrokinetic turbine should avoid usage of underwater electronic equipment in order to reduce the system cost and increase overall reliability.

Typical to any other small sized system tested in controlled environments, several underlying limitations can be identified for this work. For instance, overhead power losses are quite significant compared to the overall system size. Use of rotor frame (which, in an ideal deployment, will be replaced by augmentation ducts) and absence of any flow profiling and visualization tools (needed for more realistic tests) introduced important measurement limitations. Being tested in underwater conditions for about 2 weeks, the NECI rotor structure went through visible degradation, fouling, and rusting. To date, most hydrokinetic turbines that have gone through field trials have faced significant degradation problems. Any further research should also quantify the extent of such degradation and possibly suggest solutions for system protection and longevity. To summarize the test results the following can be stated:

- In order to establish greater confidence in the derived results, especially in a tow-tank environment, due attention needs to be given on model size, wall-effects, steadiness of rotor wake, and cavitation.
- Variations in water elevation will induce linear change in power output only in an idealized situation. In reality this imposes a high degree of nonlinearity.
- While permanent magnet alternators are effective devices for power conversion, a better design should include features such as, direct coupling, lower cogging, and higher efficiency.
- The ripple behavior is dominant at lower tip speed ratio conditions with given system inertia and electrical filtering at the output.
- Rotor start up may not be an issue as long as sufficient design considerations are given (i.e, four or more blades, low cogging generator and/or automated startup sequence).

- Reducing effects of radial arms, transmission components, and electrical losses can improve system efficiency.
- The system performance curve ($C_p - \lambda$ curve) is enveloped with high degree of non-linearity and uncertainty. A single efficiency curve is probably not sufficient to accurately describe wide diversity of operating conditions (e.g. water velocities, loading and unsteady hydrodynamics).
- Over-time structural degradation may introduce deviations from expected performance.
- A hydrokinetic turbine devoid of underwater instrumentation is highly desirable.

While the tests and subsequent observations presented in the work give a good description of what can be achieved through testing in controlled environment [8], actual commercial development will undoubtedly identify and address these issues. Therefore, the results generated through this work should not be regarded as inherent bottlenecks. Rather these should be treated as steps toward realizing an optimum system.

7.2.2 Part-system model validation

In Chapter 6.1, Fig. 6.1, the outline of a grid-connected HECS has been presented. With the limitation of the tow-tank, it was evident that prolonged tests necessary for such a scheme (appropriate start-up, shut-down, grid-synchronization, etc.) cannot be performed. A simpler representation of such an architecture can be realized by considering an isolated electrical load, instead of interfacing it to the utility grid (Fig. 7.28). This setup is particularly suitable for carrying out tow-tank tests where the length of test run is limited by the physical size of the test facility. In absence of grid-interfacing components, time required to conduct synchronization and safe power-electronic interfacing can be more effectively used for sequentially switching the resistive loads.

This simplified structure, devoid of supervisory/dynamic control procedures for grid interfacing, allowed a range of successful testing. Details of the test runs and tow

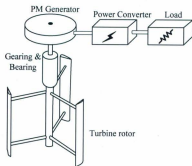


Figure 7.28: Simplified system structure with a dc end-load

tank arrangements are given in [8, 141, 191] and will be briefly outlined later.

The subsystems of the HECS described above have been individually modeled and validated. The complete system has been integrated in the Matlab-Simulink™ environment. Three specific areas pertaining to the three core issues (efficiency, start-up, and torque ripple) have been studied through the simulations and test results using the 4-bladed NECI rotor have been used in validating these models.

Unlike optimally designed augmentation ducts (such as, [79, 92]), the mounting frame used in these tests did not incorporate sufficient features to elevate the flow velocity. On the contrary, it has been observed that the boundary layers and turbulence introduced by this structure (especially the top railings) degraded the rotor performance. This has been assessed by various visualization procedures (video recordings/sequential snapshots) and power output calculations. Subsequently, rotor stray loss (arms, shaft, walls etc.) term η_{loss} has been incorporated in (Eq. 6.6). Unlike a duct, the magnitude of η_{loss} is taken to be < 1 and has been identified through multiple simulation of the overall system.

Start-up performance

Inherent start-up difficulty of a vertical axis turbine may become exacerbated in presence of a permanent magnet alternator. This is more dominant in presence of a gear-box where the reflected cogging torque as seen by the low-speed shaft is amplified further. This effect, as introduced in Eq. 6.32 and further elaborated in Eq. 6.33, is simulated to reproduce the experimental observations. In Fig. 7.29 the corresponding results are plotted. It has been observed during the tank tests that the turbine starts to rotate at speeds between 1.75 m/s and 1.85 m/s . At $t = 7.5\text{ sec}$ this velocity transition is introduced in the simulation, in accordance with the actual tests. It should be pointed out that the hydrokinetic turbine system is disconnected from external electrical loads throughout this procedure.

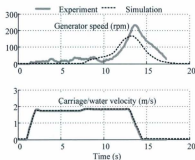


Figure 7.29: Start-up behavior of the hydrokinetic turbine

While the experimental plots show that the rotor develops very weak and unsteady patterns at $V < 1.8\text{ m/s}$, the simulations do not reflect this characteristics. Also, the magnitudes of the rotor speed do not entirely confirm. This is expected because of two fundamental reasons. Firstly, at very low speeds (i.e. at low tip speed ratio), the per-

formance curve as formulated through Eq. 6.3, Fig.9.6(a)), is incapable of describing the torque/power coefficient accurately. Secondly, and more importantly, start-up condition is surrounded by a number of complex fluid dynamic interactions, which are beyond the scope of this work. In spite of these apparent limitations, the modeling scheme presented here is fairly accurate in identifying the threshold at which the rotor will start to spin.

Torque ripple

In Fig. 7.30 a set of time series observations are presented to shed light on the turbine's torque oscillation behavior. The tests were conducted with a steady carriage speed of 2.5 m/s. The applied resistive loads are 5 Ω , and 2.5 Ω at $t = 6$ sec and $t = 8$ sec, respectively. The voltage output of the PMA depends dominantly on its rotational speed. However, the oscillations in generator voltage quantity as shown in Fig. 7.30 are due to the contributions from variations in generator current caused by the torque ripples.

The output current, as expected, greatly reflects this oscillating behavior at the load terminals. The application of a higher load at around $t = 8$ sec causes the rotor to migrate to a low tip speed ratio condition. While the system runs almost in a limping mode, the oscillatory behavior is quite dominant and visible in this condition. This has been formulated through Eq. 6.7 and the simulations successfully agree to the experiments. However, as identified before, the exact instance of the torque pulses cannot be matched without undertaking more rigorous fluid-mechanic study.

Overall performance

Throughout the modeling scheme, a number of efficiency terms and non-linearity issues were identified. Also, detailed description of the relevant subsystems has been developed. The simulation results superimposed on a set of test data are presented in fig.7.31. The steady state water velocity is 2.25 m/s for these tests and loading changes are introduced at $t = 5.3$ sec (15 Ω), $t = 7.7$ sec (7.5 Ω) and $t = 11.2$ sec (5 Ω).

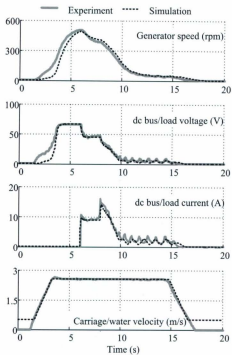


Figure 7.30: Torque ripple behavior of the hydrokinetic turbine

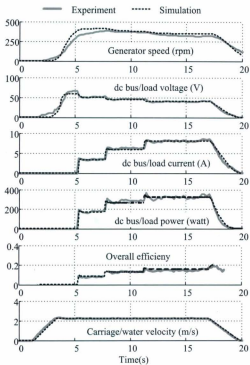


Figure 7.31: General performance of the hydrokinetic turbine

As seen from Fig. 7.31 the modeling is highly successful in representing the subtle dynamic states as well as the steady-state parameters. Particularly, the comprehensive set of efficiency formulations described earlier, has yielded results with high degree of accuracy. It should be pointed out that the input power is dependent on water velocity and is determined by $\frac{1}{2}\rho_w A_r v_{eff}^3$, whereas the output dc power is found by $V_{gr} I_{gr}$. Overall system efficiency is directly calculated using the ratio of output power to input power. Necessary parameter values are given in the Appendix.

While the models and their simulations have demonstrated faithful reproduction of the experimental scenarios, there are various areas where further attention can be given. A future work pertaining to this research may explore the following perceived limitations of this work:

- *Considerations for measurement limitations*

A total of four parameters (generator speed, flow velocity, dc current, and dc voltage) were measured as part of the tow-tank test and validation activities discussed in this work. While the associated sensor circuitry have been tested separately, various other parameters could not be established adequately. This includes, effective level of rotor submersion, length of boundary layers (due to walls and free surface), and density of tank water. Any future work should provide more attention toward determining these quantities with regard to hydrokinetic turbine's design and operation.

- *Improvement of the start-up behavior model*

The start-up characteristics as represented by the model, does not replicate the test results to the fullest extent (Fig. 7.29). This issue may need to be revisited as part of a future research.

- *Contribution of rotor structure on overall performance*

Contribution of the rotor frame as well as general understanding of ducts/walls need to be investigated further. Research activities such as, [7, 92] may bring further insight on these issues.

- *Addition of stochastic and unsteady hydrodynamics*

While this work only considers the test cases with stable wake conditions, further investigation need to carried out toward formulating more comprehensive system models that may explain various unsteady/stochastic hydrodynamic conditions.

- *Elimination of sensor dynamics*

In order to eliminate the measurement noise low pass filters have been used in the sensors within the DAQ system. As a result, a time-constant is introduced, which contributes to the overall dynamics of the systems. Any future work may opt for eliminating the filter-dynamics through more sophisticated design exercises.

- *Simplification of system models*

Depending on the intended purpose of model usage (e.g. system design or grid-integration studies), the formulations presented in this work can be simplified further by truncating various torque terms associated with cogging, oscillations, or losses.

The small scale HECS prototype studied here indicates that the use of permanent magnet alternators in vertical axis hydrokinetic turbines may pose certain challenges in their operation. However it should kept in mind that this test system was not optimally designed. The objective of this work was to develop numerical models that represent the behavior of such a system, and this has been achieved. Further modifications and refinements will allow more rigorous study in this domain.

7.3 Summary of testing and model validation

In this section, dynamic performance of a vertical axis hydrokinetic energy conversion system has been presented and its numerical model has been validated. This system includes a permanent magnet alternator and an uncontrolled rectifier, coupled to a dc switchable load. Simulation results are validated against actual test data. These tests were conducted in a controlled environment using tow-tank facilities. Three areas were

identified as issues of interest: (a) start-up, (b) torque ripple, and (c) overall efficiency. Mathematical formulations along with their implementation in Matlab-SimulinkTM has proven to be successful. These models can be refined, modified, and tuned to match diverse needs arising from turbine system synthesis and analysis.

Part III

Evaluation of Power Tracking Control Methods

Evaluation of Power Tracking Control Methods

In Part II, a set of design and test initiatives involving hydrokinetic turbine systems has been discussed. This experience, as well as the review of technological status presented in Part I have been extended within Chapter 8 - 10 (Part III) toward developing greater insight into the control challenges and possible solutions. The numerical model developed in the previous sections have been used toward evaluating these control techniques and directions for further refinements are put forward. As a parallel activity, the effects of nonlinear efficiency characteristics (within various cascaded subsystems of a HECS) has been investigated. These discussions provide the motivation and direction toward developing more suitable power tracking control techniques for possible implementation in hydrokinetic systems.

Chapter 8

Power Tracking Control Challenges in Hydrokinetic Systems

The generic objective of controlling a hydrokinetic turbine (or a wind turbine, for that matter) is to maximize the energy yield, reduce mechanical stress, and improve overall system performance staying within the limits of safety and operability. A subset of these goals consist of objectives such as to stabilize the system, to improve transient characteristics, and to achieve better steady-state (i.e., tracking) performance. Contrary to popular belief, tracking control is probably the most significant problem in the wind energy industry and has been the subject of detailed research [102, 146, 192, 193]. This, by itself, involves an array of adjudicating factors such as, system efficiency, energy capture, and underlying economics. With a view to achieving these goals variable speed operation (employing, fixed-pitch, stall regulated turbines) is becoming the norm, especially in the technology realms of small-scale vertical axis turbines based hydrokinetic systems [86, 194]. This chapter serves to present a high-level introductory discussion pertaining to the definitions and scope of hydrokinetic system's maximum power tracking (MPT) control problem.

8.1 Control regions

In the absence of sufficient literature and operational experience that may clearly outline the various regions of HECS system operation, knowledge gathered in the wind energy domain can be consulted. The operational regions of a wind energy conversion systems

(WECS) is rather well-defined, where cut-in, rated and cut-out wind speeds divide the full range into four parts (Fig. 8.1(a,c)). Such classification is perhaps more suitable for small-scale stall-regulated wind turbines where an asynchronous link (such as, permanent magnet generators with ac-dc-ac interface) provides the electric power for end use. While the start-up and shut down regions relate more to supervisory control, the below-rated and above-rated areas are of interest with regard to maximum power tracking and dynamic control [102, 146, 193, 195]. The latter is further broken into power tracking, speed limiting and power limiting regions. The power tracking region, also called 'Region 2' [196] is the focus of attention as the turbine mostly operates within this operating range.

Through this research, a proposition to characterize the operational zones of a fully submerged HECS is given through Fig. 8.1(b,d). As discussed in Section 4.3.1 and shown in Fig. 4.17, the free stream water velocity becomes saturated at a certain ceiling. Therefore, contrary to wind turbines, water velocity in a channel augmented system is contained within a short range. In hydrokinetic turbines where duct usage is not considered, the upper ceiling of the water velocity is mostly considered to be $2.5 - 3.0 \text{ m/s}$ [45, 60]. Unlike wind turbines, the definition of rated velocity pertaining to hydrokinetic turbines is also not well-defined. Directions for deciding this quantity is given in Section 5.3.1 where site resources, energy economics and effects of channel augmentation are included in a simplified form. If a hydrokinetic turbine is designed such that its rated velocity is in the vicinity of the maximum water velocity, it becomes evident that the MPT region (along with a short speed limiting region) occupy most of the spectrum. Subsequently, MPT problem becomes even more prevalent than that of wind turbines, making the supervisory control problems somewhat less constraining.

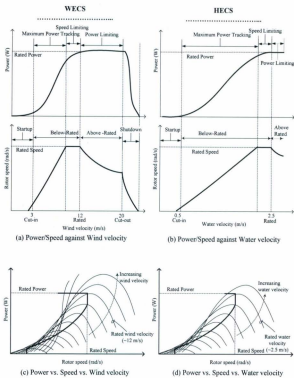


Figure 8.1: Control regions of wind and hydrokinetic turbines (fully submerged)

It has been shown that river surface velocity (for selected sites¹) may vary within the power-tracking range for 70 – 85% of the time [42]. Also, 65 – 80% of annual tidal energy yield (for selected sites) will occur with water velocities less than 2.5 m/s [197]. Therefore, undoubtedly, this region of operation deserves highest priority in ensuring maximum energy yield. This notion is reinforced by the test results obtained from Seaflow™ turbine pilot project (Fig. 8.2), where the entire range of operation is located within the power-tracking domain [198].

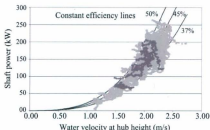


Figure 8.2: Seaflow™ turbine test data [198]

Unlike wind generators, there is no survival region or cut-out velocity for this class of turbines. Although, there is no industry threshold of cut-in and rated velocities, clearly there exists an agreement that these values are in the ranges of 0.5–0.85 m/s and 2.1 – 2.5 m/s, respectively [28, 199]. Further discussions on various regions of operation and their implications on overall control requirement are given in Section 9.1.

¹Sites/areas that have certain attractive features (such as, high peak velocity, channel bathymetry) for tidal/river turbine installation and have been studied for such purposes.

8.2 Power tracking control challenges

The challenges associated with hydrokinetic turbine's power tracking is surrounded with a multitude of factors: both technical and non-technical in nature. Some of these challenges arise from the operational conditions (hydro environment, river flow pattern, etc.), while others originate from the configuration of the system itself (placement, speed control, etc.). Highlights of various relevant issues are given below:

- *Technological diversity:*

Hydrokinetic energy conversion, in general, encompasses a wide variety of technological solutions. At present, research and development efforts are being put forward both toward horizontal and vertical axis turbines for a number of applications such as, rivers, tides, artificial channels, industrial outflows, etc. Also, use of ducts and floating platforms are currently being explored. Such structures and their effects on the overall performance of the turbine, compound the problem of mathematical modeling. This contributes significantly toward developing the control method through numerical approaches.

In addition to these factors, placement of hydrokinetic turbines may pose significant challenge toward the power tracking method being used. This is particularly true for turbines that are mounted near the surface with a fixed structure. For such turbines, as the velocity and elevation of incoming water varies, available power and its tracking trajectory varies considerably in a 2 dimensional manner (Fig. 8.3). As seen in this figure, for a given rotor depth, with increase in water velocity the peak power point is exhibited by a nonlinear trajectory in the rpm versus power/torque plane. However, for variations in rotor submersion, this locus is shifted along to water elevation axis. In order to maximize the energy capture, it is desirable that the tracker considers variations in both velocity and elevation, particularly for vertical turbines mounted on a fixed near-surface structure.

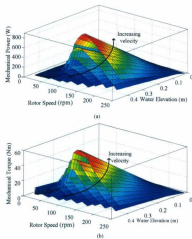


Figure 8.3: Example of small vertical axis turbine's (height 0.4 m, diameter 1 m) (a) power and (b) torque curves with water velocity variations from 0–2.5 m/s (at 0.25 m/s interval)

- *State of the technology:*

At the current state of the hydrokinetic energy industry, the requirements for system control (both supervisory and dynamic control) are not clear. However, it is expected that the wide number of demonstration and pre-commercial projects being pursued throughout the world, will produce significant knowledge that will aid understanding the control challenges better. In the interim, control methods that may serve both in the short-term and longer-term needs, can be deemed more valuable than that of device/project specific solutions.

- *Resource conditions:*

A controller tuned for a hydrokinetic turbine to be deployed in freshwater channels may not perform optimally in salt-water conditions, and vice versa. Variations in flow conditions, water density and channel stage pose different control requirements in various fields of application.

- *Turbine design and operation:*

Hydrokinetic turbines, albeit analogous to wind turbines, contain a number of unique design and operational characteristics. These factors affect the turbine's performance both in steady-state and dynamic conditions.

Perhaps, the greatest challenge in designing an optimum control methods is to establish the hydrokinetic turbine's performance curve (i.e. $C_p - \lambda$ curve). As discussed in Chapter 7.2.1, [141], this curve and the location of the optimum operating point becomes uncertain even under tests in controlled environment. Since the rotor is subject to a set of complex fluid-dynamic interactions, its expected behavior may never be realized in its entirety. For instance, findings in [68] (Fig. 8.4(a)) indicate that a Darrieus turbine may operate within an envelop of a $C_p - \lambda$ curves, instead of following only one curve, which, in ideal circumstances, could have served the purpose of power tracking control entirely.

It has also been observed within the scope of this research and other contemporary projects [200, 201] that the turbine structure may become subject to bio-fouling, icing, and accumulation of debris (Fig. 8.5). From the power tracking control's point of view, these factors may result in drifts in the the set-point (i.e. the optimum tip speed ratio), which may require further sophistication.

Discussions in Chapter 9 [202] establishes that nonlinear efficiency characteristics of various subsystems within a HECS, may result in unique situations where the theoretical/expected maxima on the performance curve may actually be shifted to an unknown point or even manifest in local extrema. For small-scale systems having

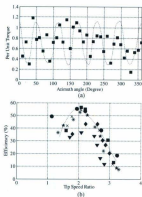


Figure 8.4: Test results on (a) torque ripple [6], and (b) performance curve [68]

multiple cascaded conversion stages, this effect may become a dominant factor toward the success of overall tracking method.

Compared to wind energy conversion systems (WECS), the performance characteristics of hydrokinetic turbines is exhibited through a narrower $C_p - \lambda$ curve. It can be seen from Fig. 8.6 that the same degree of inaccuracy in the set-point (i.e., deviations from the optimum tip speed ratio) may cause the HECS to operate under significantly reduced efficiency. This, in turns, implies that the hydrokinetic turbine's control set-point needs to be established a-priori and attained during operation, with a view to ensuring overall optimum operation.

The dynamic performance of a hydrokinetic turbine, especially when vertical rotors and permanent magnet alternators are employed, may require subtle attention in addressing start-up and cogging torque issues. It is also understood that vertical axis turbines may exhibit oscillatory power/torque output under certain conditions



Figure 8.5: Example of bio-fouling and accumulation of debris (tests on Kobold™ turbine [200])

(Fig. 8.4(a)). The power tracking control requirements may extend to minimizing the output oscillations toward achieving higher quality of electric power and lower component fatigue. Provided hydrokinetic turbines run on low-speed, high-torque conditions exhibiting high moment of inertia (compared to wind turbine), appropriate considerations need to be given in designing power tracking controllers.

- **Underwater instrumentation:**

Depending on the method of rotor placement and control technique employed, hydrokinetic turbines may require measurement of water velocity and water elevation. Such measurements are inherently subject to inaccuracies due to turbulence and skewed flow. For power tracking control purposes, the point of measurement needs to be appropriately selected. This aspect is dependent on the fact that the parameter being measured needs to be optimally spaced such that the measurement is related

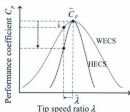


Figure 8.6: Effects of sub-optimal operation in wind and hydrokinetic turbine

to the turbine yet unaffected by it. In other words, water flow measurements need to be scaled and calibrated with considerations for appropriate interpretations.

Suspended particles and floating objects may cause reliability issues for various underwater sensors. Also, signal wires connecting the sensors to the data acquisition system, needs to be adequately protected from mechanical damage, weather conditions and noise contamination. Prolonged and accurate measurement of water flow conditions is an expensive proposition, often requiring labor intensive procedures for installation, maintenance, and crew safety [120]. A power tracking control system that does not depend on water velocity/elevation parameters, is therefore ideally suited for hydrokinetic applications.

8.3 Possible opportunities

While there exists a number of unique challenges toward developing appropriate control tools for use in hydrokinetic systems, various opportunities that may aid this process can also be identified. A brief overview of such factors is given below

- *Experience from wind energy technologies:*

Hydrokinetic technologies, in general, lack in comprehensive understanding of pertinent control needs and techniques to address those. On the other hand, the wind

energy industry, with several decades of design, tests and operational experience has gathered in-depth knowledge of such issues. Considering the synergy in the design and operational aspects of hydrokinetic and wind turbines, lessons from the latter class can be adopted to suit the underlying control requirements. It should, however, be pointed out that subtle control aspects surrounding vertical axis turbines (such as, start-up, pitch-control, efficiency improvement, etc.) will still require further research efforts.

- *Resource variability:*

Variations in wind speed, which may occur well within seconds to minutes, have been a key challenge toward developing suitable wind turbine controllers. The magnitudes of wind variations spanning the full-range of turbine operation (Fig. 8.1), requires the controller to be strictly capable of accommodating a broad spectrum of conditions. On the other hand, dominant water speed and level variations may take place within minutes to hours. This relaxes the bandwidth requirement of the hydrokinetic system controller allowing such mechanisms to operate under much slower rate. As shown in Fig. 8.1, the hydrokinetic systems' upper velocity threshold is perhaps encountered only in selected sites (where there exists an extremely high flow velocity) and may impose less constraints on the controller.

- *Slow rotational speed:*

Even though the structural issues require a hydrokinetic turbine to be of higher mass and inertia (compared to a similar-sized wind turbine), the rotational speed of this class of devices is far less than that of wind turbines. This aspect is reflected through a narrow performance curve as shown in Fig. 8.6. The combined effect of higher rotor inertia and lower rotational speed is expected to result in similar dynamic characteristics as wind turbines, if not better.

8.4 Summary of control requirements

Within the power tracking control literature, there exists a large number of alternative methods that have evolved in the wind, photovoltaic, and other areas of engineering. In particular, diverse methods of power point tracking have long been implemented in the photovoltaic systems. Methods such as, hill-climbing, perturbation & observe, parasitic capacitance, incremental conductance, fractional open-circuit voltage, fractional short-circuit current, fuzzy logic, neural network, ripple correction, current sweep dc-link capacitor droop control, load current/voltage maximization, current/voltage slope feedback, etc. have been studied extensively [86, 203, 204].

The fundamental differences between photovoltaic and turbine systems (wind or hydrokinetic) are that the latter class operates under highly time varying conditions and employ rotary machines. In addition, photovoltaic converters produce dc output requiring the use of dc-dc converters in almost all applications. Wind or hydrokinetic turbines produce ac output and may not require dc-dc converters as an interface/buffer. System inertia, fatigue loading, over-speed protection are unique requirements for these turbines, compared to photovoltaic converters.

In this chapter, a high-level subjective evaluation of hydrokinetic systems' control requirements has been presented. In a number of cases, differences and opportunities associated with the control issues have been referenced to that of wind energy conversion systems. A comparative assessment of various basic control techniques that have been implemented in wind technologies, deem valuable in this regard. Also, methods that are characterized as model independent, self-driving, adaptive, and sensorless, appear particularly suitable for hydrokinetic systems.

Chapter 9

Effects of Efficiency Nonlinearity on Power Tracking Control

For all alternative energy systems, the control objective pertaining to the primary conversion process is to attain maximum conversion efficiency over a range of input. Operation at maximum conversion efficiency leads to highest energy production in a year. But, energy conversion efficiency of wind or hydrokinetic turbines is highest at certain optimum tip speed ratios (TSR, a measure of rotor speed to fluid velocity). Similarly, photovoltaic and fuel cell systems possess peak conversion efficiencies at specific loading conditions. The problem of power tracking, commonly known as, maximum power point tracking (MPPT), essentially imposes control requirements on the operation of the system such that peak efficiency on the front-end/primary process is achieved.

In order to convert extracted mechanical energy into usable forms, a number of cascaded conversion stages, namely, secondary and/or tertiary power units may deem necessary. As the definition of 'usable form' varies from space heating to distributed generation, the overall power conversion scheme may also take diverse routes. For instance, a turbine rotor is typically coupled to electrical generator via a gearbox. In many cases, especially for the systems with permanent magnet alternators (PMA), the electrical power is processed using power-electronic devices. The latter stage may also contain additional sub-systems, such as, ac-dc rectifier (controlled/uncontrolled), dc-dc converter and dc-ac inverter.

In addition to the primary converter, these secondary and tertiary units are also

nonlinear. Each of these components has their own unique operational characteristics, and more importantly, an efficiency profile. While the power tracking control technique provides answer to convex efficiency characteristics at the primary stage, it however, does not incorporate efficiency nonlinearity in the latter stages. Here the term 'efficiency nonlinearity' is used to describe cases where the efficiency of a subsystem can not be clearly established through a linear function while migrating along various operating points of this device. In limited cases, such nonlinearity is not of concern (for example, space heating [205], water pumping [57], etc.). In some cases, additional control arrangements are deployed in one or more of the subsystems (such as, loss minimization in generator [97, 99], efficiency tracking in dc-dc converters [206, 207], etc.). In most cases, however, it is assumed that higher efficiency regions of secondary and tertiary systems reside in a relatively linear zone (with a short-initial nonlinear rise) [199, 208]. This unveils a set of questions such as, (a) how successful a power-tracking control method will be when the efficiency characteristics of cascaded stages themselves have convex shapes, instead of an assumed linear shape? (b) in case a efficiency optimization control is to be deployed, which secondary or tertiary subsystems are to be considered? (c) how does the optimum operating point shift with progressive addition of such nonlinearity?

In this work, a hydrokinetic energy conversion system (HECS) is taken as an example of multistage renewable power technology. Two figures of merit, namely, 'success of power tracking' (SOPT) and 'deviation from optimum point' (DFOP) are introduced. In answering the questions posed earlier, a recursive algorithm is developed that incorporates efficiency information of each of the successive subsystems and produces a set of output curves. These curves, namely, 'power curve' (resource vs. power output) and 'performance curve' (efficiency vs. TSR) sweep through the full range of the system operation. These figures of merit are determined through numerical/graphical processing as part of the solution. In addition, this approach allows one to develop more realistic power curves and provides a breakdown of nonlinearity contribution of each of the subsystems toward overall performance.

In the following section, hydrokinetic energy converters, power-tracking objectives for such systems, and the scope of the problem to be discussed in this article, are introduced. The method of system performance evaluation under efficiency nonlinearity conditions is detailed in Section 9.2. The description of a HECS to be studied through simulation and also using experimental data is given in Section 9.3.

9.1 Multi-parameter control requirements

Hydrokinetic turbine systems convert the energy contained in a flowing water stream through electromechanical processes that are analogous to wind devices. At present, this technology is mostly experiencing a wide range of R&D and pre-commercial deployments. Being an emerging energy technology, various turbine topologies (horizontal, vertical, and cross-flow) with free-flow or augmentation channel arrangements are being explored. Also, their fields of application are considered to be very diverse with potential use in river streams, tidal channel, and artificial waterways (irrigation channels, industrial spillways, etc.). Depending on the design features, turbine systems will be mounted to different types of structures, such as, fixed near the surface, floating independently, or placed at the bottom of a water channel. As an interface to the end-use, diverse types of electrical machines and power converters (singly/doubly fed induction generators and permanent magnet generators) are being tested. Also, the turbine operation may incorporate features such as variable pitch (full span, power tracking, or speed regulating) or simple fixed pitch mechanism.

Given the diversity of hydrokinetic turbines and the emerging nature of this technology, a so-called 'water-to-wire' system is considered in this work (Fig. 2.1). This implies the turbine system (horizontal or vertical) consists of hydrodynamic (rotor, radial arms, shaft), mechanical (transmission, gearing/bearing), electro-mechanical (generator), and electrical (power converters) subsystems. Also it is assumed that the rotor will be completely submerged in water and will be subject to variations of water velocity to such an extent that tracking control is necessary for its optimum operation.

The primary energy conversion in these systems follows the expression in Eq. 5.22. This equation along with Eq. 5.23 and Eq. 6.6 are rewritten here for the sake of ease of referencing.

$$P_{rot} = C_p^o \frac{1}{2} \rho_w A_r v_{eff}^3 \quad (9.1)$$

$$\lambda = \frac{\omega_{rot} R}{v_{eff}} \quad (9.2)$$

$$C_p^o = f_r(\lambda) \quad (9.3)$$

where the hydrodynamic power coefficient C_p^o is nonlinearly dependent on tip speed ratio given by. This relationship, commonly known as 'performance curve', also varies based on the turbine topology (Fig. 5.4) and blade pitching arrangement.

While Eq. 9.2 is a non dimensional formulation, 'power curve' of a turbine relates the fluid velocity to system power output and this depends on the device size/rating. For a HECS, this curve has three regions of operation: (I) below cut-in (II) power-tracking, and (III) above rated (Fig. 9.1, [199])(Fig. 9.1). Regions I and II are derived from Eq. 9.1, whereas region III is essentially a power-limiting mode of operation. In region II, the control objective is to maintain an optimum rotor speed compared to the water velocity (i.e. to sustain optimum TSR) such that the peak hydrodynamic efficiency (Fig. 5.4) can be achieved.

The shape of the power curve itself is also of paramount importance, provided this information directly affects the estimates of annual energy yield from a turbine. Traditionally, this curve is derived from the ideal fluid power curve by incorporating constant efficiency terms of various subsystems (Fig. 9.1). While this simplified method is a good starting point, more realistic power curves need to be developed using the analytical approaches.

In [112], a wind energy system supplying a dc load through a PMA and a dc-dc converter has been studied. It has been shown mathematically that only one control variable (duty ratio of the converter) can be adjusted in achieving optimum rotor speed and hence the maximum power point can be tracked. This formulation assumes constant efficiency for the conversion units downstream to the rotor. This is a widely accepted concept and is valid for systems that fall into such regime (i.e. flat efficiency profile [199, 208]).

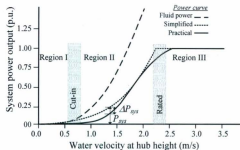


Figure 9.1: Typical HECS power curve

In order to decipher the control requirements of various conversion stages (primary, secondary, and tertiary) of a cascaded system, Fig. 9.2 can be used as a generic example. For the maxima on the performance curve, i.e. for $C_p^* = \hat{C}_p^*$, the required tip speed ratio is $\lambda = \hat{\lambda}$ as dictated by

$$\left. \frac{dC_p^*}{d\lambda} \right|_{\lambda=\hat{\lambda}} = 0 \quad (9.4)$$

For a constant water velocity, Eq. 9.1 and Eq. 9.2 require that at the optimum operating point, $P_{rot} = \hat{P}_{rot}$ and

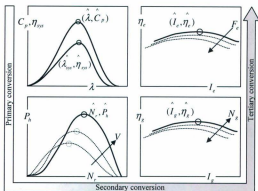


Figure 9.2: HECS system optimum operation

$$\left. \frac{dP_{rot}}{dN_{rot}} \right|_{N_{rot}=\hat{N}_{rot}} = 0 \quad (9.5)$$

Hence the control requirement for optimum power tracking of a rotor becomes:

$$N_{rot} = \hat{N}_{rot}; \text{ for given water velocity} \quad (9.6)$$

In the secondary conversion stage, the electromechanical power transfer through the generator is given by: $P_{gen} = \eta_{gen} P_{hss}$ where $\eta_{gen} = f_g(N_{gen}, I_g)$ and $N_{gen} = N_{rot} N_{gr}$ [173, 209]. The high speed shaft power P_{hss} is related to the rotor power P_{rot} through the drive-train efficiency η_{drv} as $P_{hss} = \eta_{drv} P_{rot}$. Assuming power-tracking objective in Eq. 9.6 is achieved (i.e. at constant/optimum rotor speed), generator efficiency becomes dependent on the output current only. For maximum power flow through the generator, i.e. at $\eta_{gen} = \hat{\eta}_{gen}$, the efficiency nonlinearity requires that

$$\left. \frac{d\eta_{gen}}{dI_g} \right|_{I_g = \hat{I}_g} = 0 \quad (9.7)$$

In other words, a new control requirement is imposed on the system given by

$$I_g = \hat{I}_g; \text{ for given rotor speed} \quad (9.8)$$

Similar formulations can be derived for the tertiary system, which mostly consists of power electronic converters where efficiency is a function of switching frequency and output current [210]. Power flow through a converter at steady state is given by $P_{dte} = \eta_{dte} P_{gen}$, provided, $\eta_{dte} = f_c(F_{dte}, I_c)$. At peak converter efficiency ($\eta_{dte} = \hat{\eta}_{dte}$), the maxima occurs following the expression:

$$\left. \frac{d\eta_{dte}}{dI_c} \right|_{I_c = \hat{I}_c} = 0 \quad (9.9)$$

This implies another control requirement:

$$I_c = \hat{I}_c; \text{ for given switching frequency} \quad (9.10)$$

As seen from Eq. 9.6, Eq. 9.8, and Eq. 9.10, each conversion stage will impose a set of control requirements toward achieving true maximum power tracking. These sets may constitute requirements from all the units with nonlinear efficiency characteristics. Efficiency maximization techniques in the latter stages can also be accommodated depending on the system topology and cost margin to allow further sophistication. For instance, generator losses can be minimized using dq axis current control applied on controlled rectifiers [97, 99] and power electronic efficiency can be improved by optimally adjusting the switching frequencies/deadband [206, 207]. Fortunately, the primary condition for power tracking Eq. 9.6 is the most significant aspect and most of the works to date encompass advancements in this area. In most systems, however, only the rotor speed tracking (condition Eq. 9.6) is realized leaving a question for whether or not to engage

in further efficiency improvements in the subsequent units. If no additional control is imposed, it is also not clear whether the nonlinearity in subsequent systems will translate into sufficient success at the terminating/load unit.

In light of the discussion presented thus far, this work focuses on the development of

- a method for establishing more realistic power curves for systems with nonlinear efficiency characteristics.
- a technique that shows breakdown of power transfer through cascaded subsystems and identifies contribution of each of the components toward overall nonlinearity.

In addition, a set of figure of merits that indicate (a) the success of conventional power tracking objective, and (b) deviation of the optimum TSR value from its theoretical/predicted value, are also formulated¹. These factors are defined as follows and can also be converted in percentage values:

Success of power tracking,

$$SOPT = 1 - \frac{\Delta P_{sys}(V)}{P_{sys}(V)} \quad (9.11)$$

Deviation from optimum point,

$$DFOP = 1 - \frac{\hat{\lambda}_{sys}}{\lambda} \quad (9.12)$$

The region II of a power curve is essentially a result of tracking control. However, such control applied at the rotor side, may not be totally successful in presence of variable efficiency of each of the subsequent component. The first factor (SOPT) implies the percentage of overall output as indicated through a realistic power curve, compared to a more conventional/simplified estimate (Fig. 9.1). Since this term essentially identifies the

¹These are unconventional indices and are mostly used for maintaining the brevity of this article.

accuracy of an estimated power curve, alternative methods focusing on determination of true power curves may replace this figure of merit. This work, however, discusses power tracking control issues in the context of these curves and therefore SOPT term is used hereinafter.

The rotor performance curve (i.e. the $C_p - \lambda$ curve), in a simplified case, can be translated into overall system efficiency by multiplying all the loss-factors introduced by the subsystems. This implies a linear reduction in system output and the optimum TSR remains fixed. However, when efficiencies of such systems are not constant throughout the full range of operation, the optimum TSR may diverge from the previous estimate. The second factor (DFOP) identifies the shift of the optimum operating point as shown in Fig. 9.2.

9.2 Determination of nonlinear efficiency effects

The overall output of a HECS can be determined by multiplying the efficiency of all the subsystems with the captured power at the rotor end. For systems with a dominant flat efficiency profile, constant/peak values representing each of these units are considered. However, in presence of nonlinearity in efficiency characteristics, which varies depending on operating conditions (such as, water velocity, generator speed, output current, etc.), subtle measures need to be taken. A simpler way is to relate the primary variable (i.e. resource variation) to the efficiency information of all the subsystems empirically. This method is not suitable when greater accuracy is sought. This is primarily because, efficiency of a given process is fundamentally related to variables within the subsystem and not to external parameters. In the following section, a repetitive process that overcomes this limitation (under given conditions) is presented.

9.2.1 Analytical power curve and efficiency curve

In this work, the overall power conversion scheme is considered as a set of subsystems that link the energy source to a sink/load (Fig. 6.1). The system is chosen to be a grid-connected HECS so that sufficient number of cascaded stages and their cumulative effects can be presented. With prior knowledge of efficiency characteristics of each of these units, a recursive algorithm presented here will essentially assess the overall shape of the power curve and performance curve as seen from the sink. The variables in the abscissa of these curves are water velocity, and TSR, respectively. These will be considered as sweeping variables and the algorithm starts at the primary conversion unit with initialization of these quantities (Fig. 9.3).

For developing a power curve, the front-end/rotor is considered to be controlled in power-tracking mode. This implies optimum efficiency in this stage. With sweeping values of water velocity, rotor power output and rotational speed can be determined. In order to generate a performance/efficiency curve, a constant water velocity and a sweeping TSR value is given. This step also produces a vector of rotor power and speed. These values are transferred into the secondary/tertiary stages for further processing.

For any given subsystem i , where $i = 0, 1, 2, 3, \dots$ etc. ($i = 0$ implies primary/rotor stage), the power input is equal to the power output of the previous stage.

$$P_{in}(i) = P_{out}(i - 1) \quad (9.13)$$

At this point, using the design specification (i.e. maximum/base input power rating, P_{inb}) of the unit under consideration, the value of an index variable² is generated Eq. 9.14, which identifies the unit's efficiency utilizing previously saved information Eq. 9.15.

$$P_{pa}(i) = \frac{P_{in}(i)}{P_{inb}(i)} \quad (9.14)$$

²implying per unitized subsystem variable(s) that directly determine the unit's efficiency

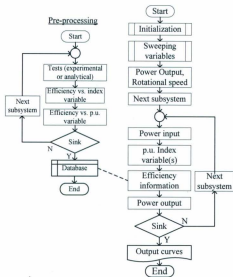


Figure 9.3: Algorithm flow-chart

$$\eta(i) = f_i(P_{pu}) \quad (9.15)$$

At this point, the power output at the given unit and overall efficiency up to the subsystem are determined using (Eq. 9.16).

$$P_{out}(i) = P_{in}(i)\eta(i) \quad (9.16)$$

$$\eta_{sys}(i) = \prod_{k=1}^i \eta(k) \quad (9.17)$$

This process is continued until the sink/load is reached and the results can be directly interpreted through graphical plots. As a precursor to initiating this approach, the efficiency characteristics of all the units need to be established through experimental/analytical tests (Fig. 9.3). Such tests will relate one or more system variables (such as, output current, machine speed, converter frequency, etc.) to the unit's efficiency. Since information of some of these variables will be carried forward from the primary subsystem (such as, rotor speed) or can be assumed constant for many cases (such as, variations of switching frequency of a power converter), the dominant index variable will consist of a set of output currents of each of these units. Converting these variables into their per unit values, efficiency of a subsystem indexed by i , is expressed as

$$\eta(i) = f_i(I_{pu}(i)) \quad (9.18)$$

The fundamental link that conjoins the a-priori efficiency data to the iterative process, is through the assumption

$$P_{pu}(i) = I_{pu}(i) \quad (9.19)$$

where $I_{pu} = \{I_g, I_c\}$ and $I_c = \{I_r, I_c, I_t\}$

This assumption essentially states that a system (electromechanical or electrical) operating at its rated voltage will have identical values for normalized power and current. Having per unit information and assuming the condition in Eq. 9.19 is critical in relating subsystem variables (such as, output current) to the parameters that dictate overall system performance (such as, water velocity or TSR).

9.2.2 Efficiency characterization

The method outlined above relies heavily on the accuracy of the efficiency information pertaining to each of the subsystems. Therefore, this step need to be carried out with due attention. For each conversion unit the efficiency data need to be generated through analytical/experimental tests. These datasets are first normalized and then fitted to curves that readily represent the expected trend. For highly nonlinear systems Gaussian curves are used. Systems that exhibit moderate nonlinearity or are almost linear, twin exponential curves are considered in this work (Fig. 9.4).

The primary conversion stage of a hydrokinetic turbine consists of rotor-blade assembly, transmission shaft, and gearing/bearing arrangements. The fluid mechanic interaction between the blades and water flow determines the energy conversion characteristics of the turbine rotor unit. The performance curve reflects this process and possesses almost a bell shape. Therefore, the function in Eq. 6.6 can be represented by a series of Gaussian curves as shown in Eq. 9.20.

$$C_p^w = \sum_{j=1}^n a_{tj} \exp \left(- \left(\frac{\lambda - b_{tj}}{c_{tj}} \right)^2 \right) \quad (9.20)$$

where $j = 1, 2, 3, \dots$ etc.

Typically $j = 2$ will be sufficient for most turbine rotors. In order to manage the complexity of this study, stray losses in the rotor (radial arms, central shaft, tip loss, etc.), friction losses in the transmission, and effects of channel walls/ducts are considered to be constant. Under this assumption, the overall turbine rotor efficiency becomes

$$\eta_{sys} = \eta_{rot} \cdot \eta_{gen} \cdot \eta_{ele} \quad (9.21)$$

$$\eta_{rot} = C_p^w \cdot \eta_{aero} \cdot \eta_{drv} \quad (9.22)$$

$$C_p = C_p^w \cdot \eta_{drv} \quad (9.23)$$

Establishing the rotor performance curve through experimental tests is an expensive and time-consuming proposition. An alternative to this problem is to undertake analytical steps. Although a combination of these two approaches is the best solution, the latter method when adequately modeled, can produce highly reliable results.

The secondary and tertiary stages of a hydrokinetic turbine consist of electro-mechanical and electrical components. Since the expected efficiency nonlinearity of these units is not very high (in comparison to the rotor) a set of two exponential curves can be used for each of their representation (Fig. 9.4). The coefficients of the exponential terms will readily determine the initial value of efficiency. The power terms in the first and second exponents identify the rate of rise and subsequent fall (if any) in efficiency, respectively.

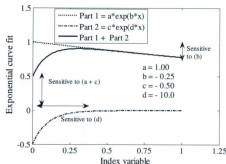


Figure 9.4: Exponential curve fitting

Efficiency of the power electronic components such as, rectifier, converter, and inverter is predominantly dependent of output current [210]. With this condition, the nonlinear efficiency characteristics for electrical subsystems can be expressed as

$$\eta_{ele} = a_{e1} \exp(b_{e1} I_e) + a_{e2} \exp(b_{e2} I_e) \quad (9.24)$$

$$\eta_{ele} = \{\eta_{rec}, \eta_{con}, \eta_{inv}\} \quad (9.25)$$

$$\eta_{rec} = f_{rec}(I_r) \quad (9.26)$$

$$\eta_{con} = f_{con}(I_c) \quad (9.27)$$

$$\eta_{inv} = f_{inv}(I_i) \quad (9.28)$$

The electromechanical unit, i.e, the generator performance can depend heavily on both the output current and rotating speed [209]. In cases where two index variables are of significance a variation of the exponential equation in Eq. 9.24 can be formulated and is given in Eq. 9.29. The expressions in each of the exponential terms can be determined empirically.

$$\eta_{gen} = a_{g1} \exp\left(\left(\frac{b_{g1}}{c_{g1} N_g + c_{g2}}\right) I_g\right) + a_{g2} \exp\left(\left(\frac{b_{g2}}{c_{g1} N_g + c_{g2}}\right) I_g\right) \quad (9.29)$$

In the following section, implementation of the efficiency characterization method detailed above, will be shown with a number of systems.

9.3 Case study of hydrokinetic systems

The hydrokinetic energy conversion system to be studied in this work consists of a number of cascaded stages and provides an ideal opportunity to investigate the efficiency nonlinearity issue. A set of simulation studies will be carried out on a complete grid-connected multistage system. Experimental results on part of the system will also be presented. In order to demonstrate a broader spectrum of results that can be generated through the assessment method presented in the previous section, the definition of the grid-connected system is formulated through three system. These are:

- *System A*: Test system that considers constant efficiency in the secondary and tertiary stages and represents a more conventional method where only dominant nonlinearity is in the primary/rotor stage.
- *System B*: Physical system with tested nonlinear efficiency information for all the subsystems and represents a practical case where moderate efficiency variations (within 15% of peak efficiency) are conceivable.
- *System C*: Fictive system that has significant efficiency nonlinearity in one or more of the subsystems (in addition to the rotor itself) and represents a system where extreme nonlinearity conditions (beyond 15% of peak efficiency) can be observed.

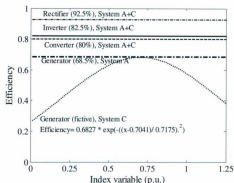


Figure 9.5: Efficiency information for 'System A' and 'System C'

Further elaboration on the process of efficiency characterization and its subtle advantages are discussed for the system B in the following section. With regard to system A, the constant efficiency values are assumed to be identical to the peak efficiencies as

found in the description of system B and are shown in Fig. 9.5. Information of system C is shown in the same figure where the generator efficiency is assumed to highly nonlinear and is represented using a Gaussian curve.

9.4 Efficiency characterization of a physical system

The physical hydrokinetic energy conversion system to be investigated here consists of a 4-bladed vertical axis turbine at the front-end and is coupled to an outer rotor PMA through chain-sprocket gearing. The variable ac output of the generator is interfaced to the utility grid using an ac-dc-ac power stage. Various off-the-shelf components have been integrated in realizing the complete system. The part information is given in Table. 6.1 and consists of rotor, generator, rectifier, converter, and inverter.

It is required to establish the efficiency profile of a system, in order to undertake an investigation on issues related to efficiency nonlinearity. The rotor performance curve can be developed using established concepts such as, computational fluid dynamics, momentum theory or vortex theory. These methods possess ascending degrees of complexity and accuracy [211]. To add further sophistication, each of these approaches may be modified to add various subtle features. For instance, the momentum theory can be formulated through either single, multiple, or double-multiple streamtube assessments.

As a good trade-off between computational complexity and desired accuracy, the performance curve, in this work, has been determined using momentum theory (multiple streamtube) as detailed in [167]. When this information (Fig. 9.6(a)) is translated into normalized rotor power output, as shown Fig. 9.6, it becomes apparent that for an optimum TSR, the rotor's rotational speed needs to make excursion over a wide range at various water velocities (Fig. 9.6(b,c)). Appendix B contains the curve fit parameters for the representation in Fig. 9.6. It should be pointed out that these subsystems have been individually tested/studied in determining their efficiency profiles.

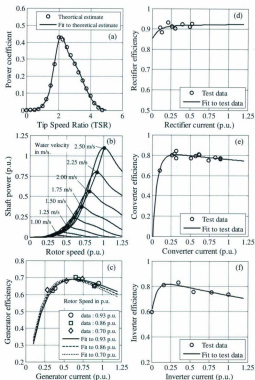


Figure 9.6: Efficiency characterization of a physical HECS

The generator efficiency is estimated analytically [173] and is fitted to the curve as functions of generator speed and output current. This represents a two-dimensional curve-fitting approach for systems where multiple variables may determine the overall efficiency. Equation Eq. 9.29 successfully fits to the general trend of such nonlinear profiles. Experimentally determined efficiency information of the rectifier, converter, and inverter and their representative curves are also shown in Fig. 9.6(d,e,f). The formulation in Eq. 9.24 deemed very successful in intuitively fitting these curves.

9.5 Simulation study

Designing, building, and testing a complete HECS is a very demanding and cost-intensive process. Undertaking such initiatives with a view to identifying the effects of efficiency nonlinearity for a complete grid-connected system is therefore beyond the scope of this work. While the following section describes a part-system experimental work, simulation based assessment is presented in this section. Such an exercise can be very useful in the design phase where the success of power-tracking and identification of the optimum TSR point can be realized.

The first set of simulation establishes the power curves for systems A, B, and C. As detailed in Section 9.2, the sweeping variable is given a range of values ($V = 0 - 2.5$ m/s) and power tracking control is imposed by taking $C_p = \hat{C}_p$; $\lambda = \hat{\lambda}$ (i.e. $\eta_e = 0.325$).

Fig. 9.7 shows the results of this simulation where power curves of these systems and the SOPT index can be observed. It can be readily seen that the physical system (system B) diverges from a more conventional/simplified power curve (system A), especially at the high water velocities. For the fictive system (system C) this is further deteriorated and a rather steep curve peaking at $V \approx 2.15$ m/s is observed. The SOPT curves, which essentially identifies the conformity to simple power curves (such as in system A), reveal a more diversified scenario. When a typical power-tracking control is applied (i.e., to track the rotor speed against water velocity variations), at velocities

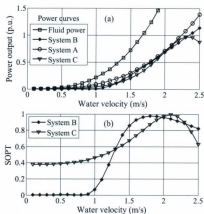


Figure 9.7: Simulation based determination of (a) realistic power curves (b) success of power tracking (SOPT) index

$V < 1.25 \text{ m/s}$ and $2.00 < V < 2.25 \text{ m/s}$, system C shows greater success than system B. It should be stated that in presence of a highly nonlinear subsystem in system C, it is intuitive to imagine that the power tracking may not be successful in its entirety. However, Fig. 9.7(b) shows the opposite. This reinforces the notion that success of power tracking cannot be established through conventional approaches and unique observations can be made through the formulations presented here.

Although power curves define the power output of the overall system, the same approach detailed above can be followed in identifying the power transfer through each of the subsystems. While the degree of efficiency nonlinearity, as characterized through tests, can predict the influence of each subsystem toward such power transfer, power curves plotted against resource variation can establish the extent of such variations. As seen in Fig. 9.8(a), the physical system (system B) conforms to the constant efficiency

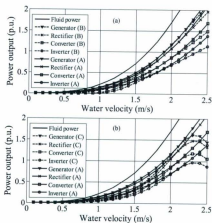


Figure 9.8: Power transfer and tracking success through each of the subsystems

model (system B) almost entirely up to the rectifier stage. The dc-dc converter and dc-ac inverter introduces further nonlinearity and overall power tracking capacity reduces after $V > 2.00$ m/s.

The highly convex efficiency curve of the generator considered for system C introduces greatest deviation from the constant efficiency model Fig. 9.8(b). Subsequent conversion stages essentially be dwarfed by this effect and overall output is highly reflective of the generator's characteristics. This clearly supports the decision to enforce efficiency optimization techniques for the generator in system C, compared to the other units.

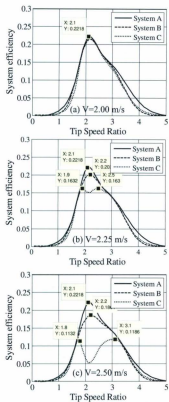


Figure 9.9: Simulation based evaluation of deviation from optimum point (DFOP) index (System A, B, C defined in Section 9.3)

While the preceding study focuses on overall power output with turbine system being controlled in power tracking mode, the following investigation focuses on identifying the system's overall efficiency at various TSR conditions. This approach allows one to determine the true optimum TSR point. The DFOP index becomes a useful tool in this regard. Following the methodology described in Section 9.2, a sweeping TSR value ($\lambda = 0 - 5$) is given for various water velocities ($V = 2.00, 2.25, \text{ and } 2.50 \text{ m/s}$ etc.). The results are plotted in fig.9.9.

It can be readily seen that for $V = 2.00 \text{ m/s}$ (and less) system nonlinearity has little impact on the optimum TSR ($\hat{\lambda} = 2.10, \text{ DFOP} \approx 0$). However, at higher velocities, the optimum point starts to shift and the value of DFOP takes non-zero values. At $V = 2.25$ and $V = 2.50 \text{ m/s}$ system B exhibits almost no change in the optimum TSR value with $\text{DFOP} = 4.7\%$ for both cases. In contrast, system C reveals the presence of twin peak points ($\text{DFOP} = +9.5\%, -19\%$ and $= +14\%, -47\%$ respectively). This clearly shows that assuming a optimum TSR value directly from the rotor performance curve may mislead the control objective. If nonlinearity is not acute (such as in system B), a newer but nearly constant optimum point can be found. For systems with very dominant nonlinearity components, optimum TSR control may only be applicable for reduced horizons.

9.6 Experimental study

The experimental hydrokinetic turbine setup considered here is essentially a partial implementation of the physical system described above (system B). This system incorporates the NECI 4-bladed rotor and is coupled to the permanent magnet alternator (PMA) using chain-sprocket arrangement. Relevant test arrangements and procedures have been discussed in Section 7.2.1.

The data accumulated in each of the runs is reviewed manually for apparent discrepancy or errors. The transient data points are truncated to reflect steady state

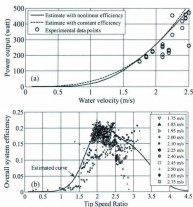


Figure 9.10: Experimental test results (a) power curve (b) efficiency curve

behavior. With a predicted optimum TSR (i.e., $\hat{\lambda} = 2.10$) steady state power is plotted against water velocities in fig.9.10(a). This essentially represents the power tracking mode of operation and can be observed further for nonlinearity issues. It can be seen that the estimated nonlinear power curve has a good match with the test data. The apparent mismatches are not unexpected and can be attributed to (a) unknown nonlinearity introduced by the rotor frame (wall effect), and (b) complex nonlinearity and unsteady hydro-dynamics. These issues are relatively well-known, very complex to solve and is beyond the scope of this work [3, 147, 165].

The estimated efficiency curve (electrical output to fluid power ratio) plotted in fig. 9.10(b) also shows a good match, especially for $\lambda_{opt} < 2.25$. The apparent mismatch at higher TSR conditions can be attributed to limitations in fluid mechanic modeling (momentum method/multiple streamtube approach [167]) and scattered data points are due to aforementioned complexities. For the observations within region II, the SOPT>

70%. Also, the deviation from the optimum point has been found to be minimal with $DFOP < 4.5\%$.

The turbine system was originally commissioned to test various design and dynamic performance (start up, torque ripple, etc.) issues [141]. However, results derived through this exercise appeared to be complementary to the studies presented in this work. Since the essence of this work is to outline a method for determining more realistic (a) power curves and (b) efficiency curves, the experimental data is studied for the match to these curves and have been found to be sufficiently in agreement.

9.7 Summary of nonlinear efficiency effects

Nonlinearity in efficiency profile of cascaded multistage energy conversion systems may greatly dictate the effectiveness of power tracking control imposed on them. In this work, hydrokinetic energy conversion systems are investigated in this regard. In addition to determining practical power curves and efficiency curves, this work introduces several figures of merit to assess the overall system performance under such nonlinearity issues. Simulation study encompassing three distinctive systems has been carried out to bring insight into the scope of the proposed methods. Also, experimental tests have verified the underlying principles. It has been established that the efficiency nonlinearities of the individual subsystems in the energy conversion system affect the overall maximum power transfer, and that the optimum maximum power tracking point is not determined only by the theoretical optimum TSR point of the hydrokinetic turbine. An alternative approach, in contrast to the methods detailed in this work, may be to use an optimization algorithm to determine the impact of the nonlinearities in each subsystem on the overall performance; i.e. to determine a global TSR that maximizes the overall output power. This global TSR may be very different from the optimum TSR of the hydrokinetic turbine. Further work may also include validation of this approach through extensive trials in real-world conditions and development of robust control algorithms that overcome the possible nonlinearity problem.

Chapter 10

Assessment of Generic Power Tracking Methods

Before initiating the development of sophisticated power tracking control schemes for use in hydrokinetic systems, it is a worthwhile venture to investigate relevant solutions that already exist in other similar areas, such as wind, tidal or solar energy. A review of various control methods [102, 194] indicate that the maximum power tracking (MPT) problem of wind turbines are typically addressed through three basic methods (and their variants). These techniques are: tip speed ratio (TSR) control, power signal feedback (PSF) control, and hill climbing search (HCS) control.

10.1 Tip speed ratio (TSR) control

The TSR control method is probably the most basic and the most direct method of power tracking that directly relies upon prior knowledge of the normalized performance curve ($C_p - \lambda$ curve). According to this method, the tip speed ratio is calculated continuously (using measured rotor speed and incoming water velocity) and the turbine is controlled around the optimum point, as found from the performance curve [212].

As shown in Fig. 5.23, in TSR control method, the turbine is operated around the optimum tip speed ratio, λ and exact knowledge of this optimum point is a precondition. While wind turbines operate at higher rotational speeds with $\lambda_{opt} \approx 7.0$, hydrokinetic turbines, owing to their higher solidity, typically exhibit λ within 2 – 3.

In addition to a-priori information on rotor's performance characteristics, the TSR method heavily relies on measurement rotor speed as well as flow velocity. The

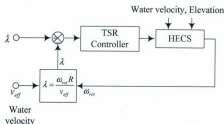


Figure 10.1: Outline of TSR control in hydrokinetic systems

latter parameter can be a challenging quantity to measure, especially under real-world conditions. Perhaps, owing to this reason, the TSR control method does not constitute the lion's share in the wind energy applications.

10.2 Power signal feedback (PSF) control

The PSF method is based on the dimensional performance curves (i.e. 'power vs. speed' or 'torque vs. speed' curve, e.g Fig. 8.1) and requires accurate and sufficient information on the system's behavior. According to this method a power signal feedback is acquired and is non-linearly mapped into an optimum rotor tracking speed [103, 213].

According to the PSF method the tracking reference (i.e. the reference rotor speed) is determined dynamically depending on the power output (Fig. 10.2). This is, in fact, a sensorless method for wind energy conversion systems. However, for hydrokinetic turbines, this method needs information of water elevation (i.e. level of rotor submersion).

When the turbine operates at a maximum power point, it is essentially working at optimum tip speed ratio, $\hat{\lambda}$. If the desired rotor speed is ω_{rot}^* , optimum tip speed ratio becomes

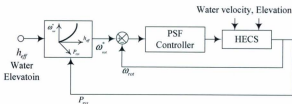


Figure 10.2: Outline of PSF control in hydrokinetic systems

$$\hat{\lambda} = \frac{\omega_{rot}^* R}{v_{eff}} \quad (10.1)$$

Denoting the power output at this optimum condition to be P_{opt}^* , Eq. 4.1 can be re-written as

$$\omega_{rot}^* = \left(\frac{P_{opt}^*}{k_{nec} h_{eff}} \right)^{\frac{1}{3}} \quad (10.2)$$

Here, k_{nec} is a non-linear curve constant through which Eq. 10.2 expresses the locus of all the maximum power points in Fig. 8.3(a).

$$k_{nec} = \rho_w R^4 \frac{\hat{C}_D}{\hat{\lambda}^3} k_{ef} \quad (10.3)$$

Apart from the requirement for water height determination, one of the greatest challenges of this method is to accurately determine the value of k_{nec} . It was reported in [196] that this constant needs to be lesser than its actual value and similar observation was made during this exercise. Therefore, a correction factor $k_{ef} = 0.5$ is brought in on trial and error basis. To date, methods of accurately determining this constant has not been reported.

10.3 Hill climbing search (HCS) control

The HCS solution, in theory, works without any system information and continuously adjusts itself to achieve an optimum operating point [103]. According to this method, in a turbine-generator system, typically the change in power and/or speed is measured periodically. If, for a given reference speed, an increase in power output is observed, the direction (i.e. sign) of the set-point signal remains unchanged and vice-versa (Fig. 10.3).

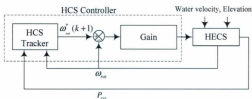


Figure 10.3: Outline of HCS control in hydrokinetic systems

The magnitude of the tracking reference may remain constant for each state, or may vary, depending on the proximity to the optimum point. These methods can be expressed through discrete time equations such as

$$\omega_{rot}^*(k+1) = \omega_{rot}^*(k) + \Delta\omega_{rot}^* \quad (10.4)$$

where $\omega_{rot}^*(k)$, $\omega_{rot}^*(k+1)$ and $\Delta\omega_{rot}^*$ represent the previous reference speed, new reference speed and step change demanded, respectively. The step change term comprises the sign and magnitude as shown in Eq. 10.5,

$$\Delta\omega_{rot}^* = \text{sign}(\Delta\omega_{rot}, \Delta P_{sys}) \times |\Delta\omega_{rot}^*| \quad (10.5)$$

Since in-depth investigations on extremum seeking control for wind turbines is not very abundant, a simple yet functional Steepest Ascent method presented in [111], is considered to be the benchmarking example. Toward determining the step sizes and their directions, this work considers that

$$|\Delta\omega_{rot}^*| = k_{phcs} |\Delta P_{sp}| \quad (10.6)$$

$$\text{sign}(\Delta\omega_{rot}, \Delta P_{sp}) = \text{sign}(\Delta\omega_{rot}) \times \text{sign}(\Delta P_{sp}) \quad (10.7)$$

Here, k_{phcs} is the HCS controller gain, $\Delta\omega_{rot}$ is the change in rotor speed, and ΔP_{sp} is the corresponding change in turbine system's power output.

10.4 Simulation based comparison

Simulating a wind turbine system and analyzing various control methods on it, is a well-established practice [194,212]. In this section, similar investigations are carried out for the hydrokinetic systems with a view to evaluating their success factors. In all cases, two disturbance inputs are considered for the hydrokinetic system (Fig. 10.4), which are: water velocity and height variation. For $t < 45$ sec only water velocity variation is considered, whereas for $t > 45$ sec variations in water elevation have been imposed. All simulation runs are of 90 sec duration and generate results in the forms of power output, generator speed, tip speed ratio, flow velocity, and water height.

For the HECS device being considered here, $\hat{\lambda} = 2.15$, as found through fluid-dynamic computations and experimental tests (Fig. 9.10(b)). As discussed in Section 6.5.1 and shown through Fig. 6.13, the controlled parameter for the system being studied, is the dc-dc converter trimming voltage.

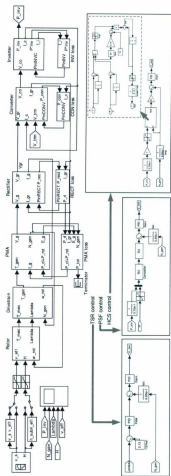


Figure 10.4: Matlab-Simulink™ implementation of the generic control methods

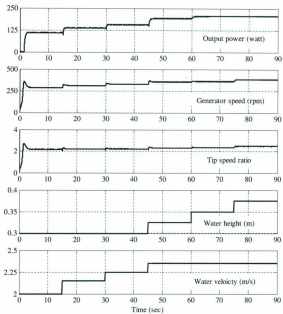


Figure 10.5: HECS performance with TSR control - step variations in flow condition

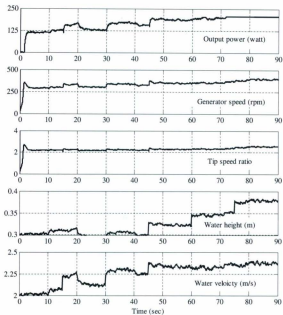


Figure 10.6: HECS performance with TSR control - stochastic variations in flow condition

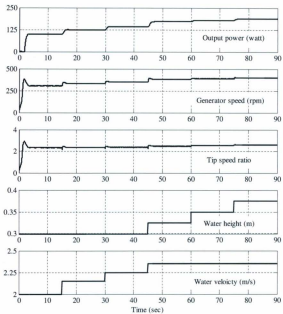


Figure 10.7: HECS performance with PSF control - step variations in flow condition

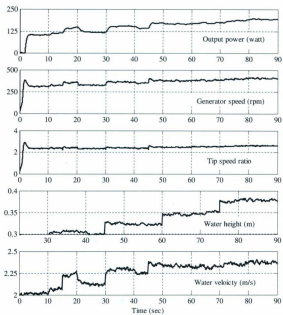


Figure 10.8: HECS performance with PSF control - stochastic variations in flow condition

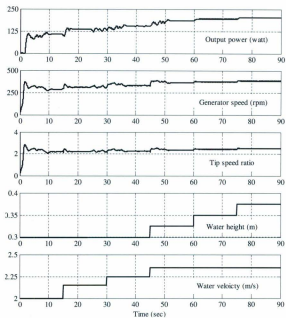


Figure 10.9: HECS performance with HCS control - step variations in flow condition

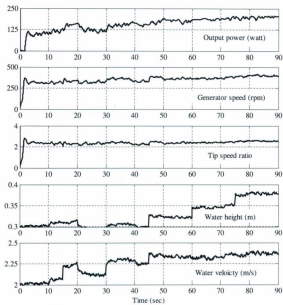


Figure 10.10: HECS performance with HCS control - stochastic variations in flow condition

In a TSR control scheme, a reference for this quantity is generated using the difference between present tip speed ratio and its optimum value.

$$V_{\text{ref}}^* = k_{\text{ptsr}}(\tilde{\lambda} - \lambda) \quad (10.8)$$

The control loop and the simulation results are given in Fig. 10.1 and Fig. 10.5, Fig. 10.6, respectively. The disturbance inputs are variations in water velocity and its elevation. For all the simulation tasks presented in this proposal, the pattern of these step changes are kept identical. While an ideal system would produce steady power output running around $C_p \approx 0.35$, a more realistic system indicates an oscillatory and sub-optimal performance.

Similar to the TSR control, a P-type controller generates the reference dc-dc converter trimming voltage through Eq. 10.9.

$$V_{\text{ref}}^* = k_{\text{pspf}}(\omega_{\text{rot}}^* - \omega_{\text{ref}}) \quad (10.9)$$

Since the PSF control method is essentially a derivative of the TSR method, the system behavior under similar inputs is almost the same as shown in Fig. 10.7, Fig. 10.8. However, it should be noted that, the value of the non-linear curve constant k_{pspf} has been determined optimally such that acceptable response can be achieved. This may not be possible in a physical system.

With regard to the HCS control method discussed earlier, a proportional controller (k_{phcs}) generates the converter trimming voltage reference depending on the error between the actual rotor speed and the set-point (Eq. 10.10).

$$V_{\text{ref}}^* = k_{\text{phcs}}(\omega_{\text{rot}}^*(k+1) - \omega_{\text{rot}}^*) \quad (10.10)$$

Taking $T_{\text{step}} = 5\text{ s}$ and $k_{\text{phcs}} = 0.15$, the simulation produced the results shown in Fig. 10.9, Fig. 10.10.

10.5 Summary of controller performance assessment

In this comparative evaluation, a set of three basic power tracking methods (TSR, PSF, HCS) have been studied and P-type controllers have been used in all cases. Also an identical hydrokinetic system model has been used throughout the evaluation. Subtle observation derived through this exercise are

- Tip speed ratio (TSR) control:
 - Superior steady-state and dynamic characteristics.
 - Conceptually simple.
 - Absolute reliance on a-priori knowledge of the optimum operating point.
 - Velocity measurement is required.
- Power signal feedback (PSF) control:
 - Moderate steady-state and dynamic characteristics.
 - Conceptually simple and less dependent on a-priori system knowledge.
 - High probability of sub-optimal operation.
 - Controller design process is often subject to device specific parameter tuning.
 - Water level measurement is required.
- Hill climbing search (HCS) control:
 - Model/device independent and exhibits adaptive performance.
 - Can be implemented without using underwater sensors.
 - System output can be oscillatory in nature.
 - Step size needs to be properly tuned considering the turbine's dynamics.

While the simulation results presented in this section may appear marginally different amongst various methods, it should be considered that significant effort has been given in tuning the control parameters and detailed information on the hydrokinetic system has been incorporated during the controller design phase. Nonetheless, the hill

climbing control method indicates good potential in the context of the control challenges identified in Section 8.4. However, further improvement in terms of dynamic performance, stability guarantee, and model independence need to be sought and applicability of a more suitable control method (such as, extremum seeking control, ESC) need to be explored.

Part IV

Synthesis of Extremum Seeking Controllers

Synthesis of Extremum Seeking Controllers

An evaluation of various candidate power tracking control method presented in the previous chapter provides the basis and directions for researching into more suitable tracking control techniques. A thorough literature survey in this regard has identified the potentials of using extremum seeking control (ESC) method in hydrokinetic systems. The ESC approach, having been researched vigorously in recent times, is uniquely suited for a class of control problems within diverse fields of applied and analytic research. In Chapter 11, a set of numerical formulations that outline the fundamental process of extremum seeking control, is discussed. Chapter 12 identifies the applicability of ESC method in hydrokinetic systems, whereas a process of ESC controller design is presented in Chapter 13.

Chapter 11

Extremum Seeking Control (ESC) Method

Extremum seeking control (ESC) is a special class of non-linear adaptive control method that is model-independent and self-regulating to an unknown set point. This technique is particularly suitable where a local maximum or minimum characterizes the non-linearity in the control problem. In essence, extremum seeking is an optimization method where the control objective is manifested as a cost function. Non-linearity in plant behavior can also be accommodated very effectively through this approach [214–217].

As defined in [218], *'adaptive control systems adapt the parameters or structure of one part of the system (the controller) to changes in the parameters or structure in another part of the system (the controlled system) in such a way that the entire system maintains optimal behavior according to the given criteria, independent of any changes that might have occurred'*. The fundamental difference between extremum seeking control (ESC) and mainstream adaptive control methods is that the latter techniques are applicable only for regulating the system operating conditions to a known reference. There exists a class of systems where the static relationship between the reference and the output has an extremum (maximum or minimum) and this relationship is either uncertain or unknown. ESC method can adaptively ride-through these discrepancies and drive the system output to the extremum by adhering to the optimum operating condition [214, 219].

Despite its recent resurgence as a promising area of research, ESC has a long and rich history. During the period of 1940 to 1970, extremum seeking control had seen

significant advancements, especially through Soviet era explorations. Even though the first reported investigation dates back to 1922 [220], this method of adaptive control did not flourish to its full potential primarily due to the lack of stability guarantees and absence of design guidelines [214, 217].

The ESC method has so far been used in applications where plants are open-loop stable with sufficiently damped poles. Since 1990's, a series of fundamental research by Krstić *et. al.* [214, 221, 222] has eliminated many of these bottlenecks and applied research is currently thriving. Areas of application of ESC includes: anti-skid braking, thermoacoustic coolers, automotive engine mapping, beam matching in particle accelerators, flight formation, bioreactors, PID controller tuning, internal combustion engine operation, radio telescope antenna adjustment, and autonomous vehicle tracking [214, 221, 222].

11.1 Classification of extremum seeking control methods

Several variants of ESC methods [223] in contrast to a set of more traditional adaptive control schemes [218] are shown in Fig. 11.1. As outlined in [110, 216, 223], extremum seeking control methods are typically categorized into three classes: perturbation systems, self-driving systems, and switching systems. A brief description of each of these methods is given below:

- *Perturbation systems:*

The most fundamental attribute of the perturbation system is the introduction of a small probing signal into the plant (Fig. 11.2). The component of this signal, as measured from the plant output, is multiplied directly by the probing signal itself, which generates an average/dc component once passed through a low-pass filter. Output of this filter/integrator is added to the probing signal and is fed to the plant as a driving signal.

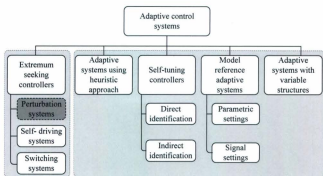


Figure 11.1: Classification of various adaptive control systems

The perturbation method effectively measures the slope of the plant characteristics. Under the assumption that there exists a maxima or minima in the plant's characteristics, the perturbation method drives the plant operating point near this point and establishes a stable limit cycle.

- *Self-driving systems:*

In a self-driving system the time derivative of the output is measured and is used to drive an integrator, which provides the necessary input to the plant. Unlike a perturbation or switching system, a self-driving system does not require any external signal or predetermined rate of input change. Such systems effectively operate on positive feedback principle and continuous assessment of available information is used to produce a control signal that drives the system toward an optimum (Fig. 11.2). Self-driving systems may not be self-starting, which would require initialization through a step input or ambient noise disturbance. In addition, such systems can potentially

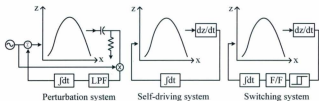


Figure 11.2: Extremum seeking control methods

deviate from the optimum operating point as a consequence of driving itself in the wrong direction.

- *Switching systems:*

The input to a switching system is supplied by an integrator, which is driven by a flip-flop type two-state device containing hysteresis. This switching element takes input from the time differential of the plant output and the flip-flop changes its state such that the switching action is associated with a negative value of the differential. The plant input is driven at a constant speed and in the same direction until an output reversal is observed. The switching scheme can be operated either continuously or with discrete steps.

With a resurgence of interest, primarily due to research conducted by Krstić *et. al.*, the perturbation based extremum seeking method is currently being seen as the method of choice against self-driving or switching systems. Most of the recent publications use the terms 'extremum seeking control' and 'perturbation method' synonymously [214, 224, 225]. Staying with the present norm, the focus of this research is on the extremum seeking method utilizing perturbation scheme. Therefore, the discussions throughout the work will use the terms 'extremum seeking control' and 'perturbation method' interchangeably.

11.2 Extremum seeking control in power tracking applications

Maximum power tracking, a native concept to many alternative energy schemes, is also currently benefiting from ESC methods. Reports of application in fuel cell stacks [224], photovoltaic systems [204, 226], and wind turbines [110, 225, 227] are also emerging. An example of wind turbine control by sinusoidally perturbed duty ratio control can be found in [104]. Also a limit cycle induced control approach is presented in [228].

Being a nascent field of application, there has been no reported research on use of ESC methods in hydrokinetic systems. In this chapter, this novel area will be explored to a great extent with a view to developing necessary insights and applied design procedures.

11.3 Principles of Extremum Seeking Control

In a perturbation-based extremum-seeking scheme, a probing signal is superimposed with the plant input and the gradient, as computed from the correlation between the input and output, is forced to zero. The system converges to a neighborhood of the extremum point and establishes a limit-cycle. The size of the neighborhood is dependent on the amplitude of the excitation signal.

In order to demonstrate the operating principle of the extremum-seeking controller in an intuitive manner, an elementary single-parameter maximization problem can be discussed. At first, the plant characteristic is considered to be of static nature. This discussion is then extended to plants with dynamic nonlinearity.

11.3.1 Extremum seeking control for plants with static nonlinearity

In this preliminary high-level study, the plant is taken to be a single-input-single-output (SISO) system with static nonlinearity. Even though both maximization and minimization problems can be addressed through this method, in keeping with the hydrokinetic systems' dominant nonlinear characteristics represented through its performance curve, a convex time-invariant function $f_x(\theta_x)$ is considered (implying a maximization problem).

Assuming the function has a maximum at $\theta_x = \theta_x^*$, this can be expanded using Taylor's series.

$$f_x(\theta_x) = f_x(\theta_x^*) + f'_x(\theta_x^*)(\theta_x - \theta_x^*) + \frac{1}{2}f''_x(\theta_x^*)(\theta_x - \theta_x^*)^2 + O[(\theta_x - \theta_x^*)^3] \quad (11.1)$$

At the maxima, the first derivative $f'_x(\theta_x^*) = 0$ and this value can be given as $f_x^* = f_x(\theta_x^*)$. In the above expression, the third and higher order terms can also be neglected. Denoting $f''_x = f''_x(\theta_x^*)$ the plant characteristics can be adequately given as

$$f_x(\theta_x) = f_x^* + \frac{1}{2}f''_x(\theta_x - \theta_x^*)^2 \quad (11.2)$$

Here $f''_x < 0$ and the objective of the control algorithm is to drive the operating point θ_x close to θ_x^* such that $(\theta_x - \theta_x^*) \rightarrow 0$ and $f_x(\theta_x) \rightarrow f_x^*$, under the assumption that both f_x^* and θ_x^* are unknown.

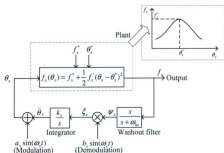


Figure 11.3: Extremum seeking control method for plants with static nonlinearity

In an ESC scheme (Fig. 11.3), a sinusoidal perturbation signal $a_x \sin(\omega_x t)$ modulates the estimate of θ_x^* (denoted by $\hat{\theta}_x$) and feeds the signal into the plant. A washout

(high-pass) filter identifies the higher frequency signals from the plant output that are representative of the modulating signal. A demodulating signal having similar characteristics to the perturbation signal (such as, $b_x \sin(\omega_x t)$) establishes a first-order derivative of the estimate of θ_x^* (i.e., $\dot{\hat{\theta}}_x$).

Denoting the estimation error as $\tilde{\theta}_x$, the corresponding expression is

$$\tilde{\theta}_x = \theta_x^* - \hat{\theta}_x \quad (11.3)$$

In order to demonstrate the success of the extremum-seeking algorithm, it will be sufficient to prove that this error diminishes (or approaches zero) as a result of the control action being imposed. In other words, the plant reaches the maximum operating point $\theta_x = \theta_x^*$ and provides an output $f_x = f_x^*$ when $\tilde{\theta}_x < 0$.

Since the control input $\theta_x = a_x \sin(\omega_x t) + \hat{\theta}_x$ and estimate of reference $\hat{\theta}_x = \theta_x^* - \tilde{\theta}_x$, the difference between current and maximum operating point becomes,

$$\theta_x - \theta_x^* = a_x \sin(\omega_x t) - \tilde{\theta}_x \quad (11.4)$$

Therefore, the plant output is given by

$$f_x(\theta_x) = f_x^* + \frac{1}{2} f_x'' (\theta_x - \theta_x^*)^2 \quad (11.5)$$

$$= f_x^* + \frac{1}{2} f_x'' (a_x \sin(\omega_x t) - \tilde{\theta}_x)^2 \quad (11.6)$$

$$= f_x^* + \frac{1}{2} f_x'' (a_x^2 \sin^2(\omega_x t) - 2a_x \tilde{\theta}_x \sin(\omega_x t) + \tilde{\theta}_x^2) \quad (11.7)$$

$$= f_x^* + \frac{1}{2} f_x'' a_x^2 \sin^2(\omega_x t) - f_x'' a_x \tilde{\theta}_x \sin(\omega_x t) + \frac{1}{2} f_x'' \tilde{\theta}_x^2 \quad (11.8)$$

$$= f_x^* + \frac{1}{4} f_x'' a_x^2 (1 - \cos(2\omega_x t)) - f_x'' a_x \tilde{\theta}_x \sin(\omega_x t) + \frac{1}{2} f_x'' \tilde{\theta}_x^2 \quad (11.9)$$

$$= f_x^* + \frac{1}{4} f_x'' a_x^2 - \frac{1}{4} f_x'' a_x^2 \cos(2\omega_x t) - f_x'' a_x \tilde{\theta}_x \sin(\omega_x t) + \frac{1}{2} f_x'' \tilde{\theta}_x^2 \quad (11.10)$$

$$= f_x^* + f_x'' \left(\frac{1}{4} a_x^2 + \frac{1}{2} \tilde{\theta}_x^2 \right) - \frac{1}{4} f_x'' a_x^2 \cos(2\omega_x t) - f_x'' a_x \tilde{\theta}_x \sin(\omega_x t) \quad (11.11)$$

The washout filter having a cut-off frequency of ω_{hx} (where $\omega_{hx} < \omega_x$) will eliminate all low-frequency terms. The output of this filter will therefore be

$$\psi_x \approx -\frac{1}{4} f_x'' a_x^2 \cos(2\omega_x t) - f_x'' a_x \bar{\theta}_x \sin(\omega_x t) \quad (11.12)$$

After a demodulation signal, namely, $b_x \sin(\omega_x t)$ is applied, the resultant signal can be given as

$$\xi_x = -\frac{1}{4} f_x'' a_x^2 b_x \sin(\omega_x t) \cos(2\omega_x t) - f_x'' a_x b_x \bar{\theta}_x \sin^2(\omega_x t) \quad (11.13)$$

$$= -\frac{1}{8} f_x'' a_x^2 b_x (\sin(3\omega_x t) - \sin(\omega_x t)) - \frac{1}{2} f_x'' a_x b_x \bar{\theta}_x (1 - \cos(2\omega_x t)) \quad (11.14)$$

$$= -\frac{1}{2} f_x'' a_x b_x \bar{\theta}_x + \frac{1}{2} f_x'' a_x b_x \bar{\theta}_x \cos(2\omega_x t) - \frac{1}{8} f_x'' a_x^2 b_x \sin(3\omega_x t) + \frac{1}{8} f_x'' a_x^2 b_x \sin(\omega_x t) \quad (11.15)$$

Presence of an integrator block with $k_x > 0$ determines that

$$\dot{\bar{\theta}}_x = \xi_x \quad (11.16)$$

Since $\bar{\theta}_x^*$ is constant, it is evident that

$$\dot{\bar{\theta}}_x = -\dot{\bar{\theta}}_x \quad (11.17)$$

Therefore, it can be shown that

$$\bar{\theta}_x \approx -\frac{k_x}{s} \xi_x \quad (11.18)$$

The integrator essentially attenuates the higher frequency/time varying terms and the output of this block becomes

$$\tilde{\theta}_x \approx -\frac{k_x}{s} \left[-\frac{1}{2} f_x'' a_x b_x \tilde{\theta}_x \right] \quad (11.19)$$

The first derivative of the estimation error is therefore

$$\dot{\tilde{\theta}}_x \approx \frac{1}{2} k_x a_x b_x f_x'' \tilde{\theta}_x \quad (11.20)$$

Since $f_x'' < 0$, $k_x a_x b_x > 0$, and $\text{sign}(\dot{\tilde{\theta}}_x) = \text{sign}(\tilde{\theta}_x)$, it can be guaranteed that $\dot{\tilde{\theta}}_x < 0$. This implies, the estimation error will always approach zero, allowing θ_x to converge toward θ_x^* . It can be shown that the plant output error achieves local exponential convergence to a neighborhood [214] following the relationship below:

$$(f_x - f_x^*) \rightarrow O\left(a_x b_x + \frac{1}{\omega_x^2}\right) \quad (11.21)$$

The convergence rate of the system is directly proportional to $k_x a_x b_x$. In many instances the perturbation and demodulation signals have same magnitude (i.e. $a_x = b_x$), which implies a quadratic relationship between convergence rate and probing signal magnitude. While large perturbations may aid reach faster convergence, it may induce unacceptable periodic variation in the plant output resulting in system fatigue and component failure. In addition, large values of k_x , a_x , and b_x increases the susceptibility to ambient and measurement noise [229]. Having a large gain k_x may make the plant unstable as the control bounds are more easily reached. Regarding the selection of perturbation frequency ω_x , typically three major time frames are of interest, which are

- Fastest: Plant dynamics, ω_{ps} .
- Medium: Perturbation signal frequency, ω_x .
- Slowest: Washout filter cut-off frequency, ω_{hx} .

While $\omega_{hx} < \omega_x < \omega_{ps}$ can be considered as a general rule, higher perturbation frequencies allow faster convergence and lesser settling error. On the contrary, with

increasing ω_x , the system becomes more susceptible to noise. As $\omega_x \rightarrow \omega_{ps}$, the algorithm may fail altogether as the plant dynamics become more dominant as compared to the perturbation signal [214, 230].

11.3.2 Extremum seeking control for plants with nonlinear dynamics

In the preceding section, the plant model was assumed to be static, or fast enough (quasi-static) such that its dynamic effects could be ignored. One way of addressing plant dynamics is to introduce a phase shift between the modulating and demodulating signals, which offsets the phase changes caused by the plant itself. In order to accommodate for the plant dynamics, improve system stability, and to augment overall performance more effectively, a dynamic compensator can be added in the extremum seeking feedback loop. In [229, 231, 232] this is achieved by introducing a compensator into the integrator block, which improves the overall relative degree and phase response.

With a view to facilitating the discussions in the following sections, the nonlinear plant dynamics is represented by the Hammerstein-Wiener scheme. Wiener or Hammerstein models are widely used in representing nonlinear dynamic systems by separating the nonlinearity and dynamic characteristics [110, 230].

The difference between Wiener and Hammerstein models lie in the order in which the linear and nonlinear blocks are cascaded. The Wiener model consists of a static nonlinearity followed by a linear dynamics block, whereas the Hammerstein model considers the linear dynamics prior to the nonlinear block (Fig. 11.4). For a system with dominant input/output nonlinearity a Wiener-Hammerstein representation is more suitable. On the contrary, hydrokinetic systems being considered in this research contain a dominant static nonlinearity in the form of $C_p - \lambda$ characteristics (in addition to the presence input and output dynamics), which necessitates the use of Hammerstein-Wiener type model.

This concept decouples the plant nonlinearity and dynamics using a cascade of three blocks: a static nonlinear map preceded and followed by two linear dynamic models:

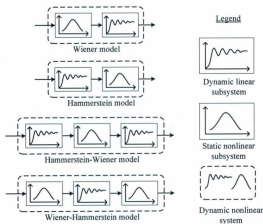


Figure 11.4: Decomposition of nonlinear dynamic systems

input dynamics and output dynamics, respectively [110, 231]. The system in Fig. 11.5 is therefore modeled using an equilibrium map $f_x(\theta_x)$ (having a maximum at $\theta_x = \theta_x^*$), linear input dynamics $F_{ix}(s)$, and linear output dynamics $F_{ox}(s)$. Under the extremum seeking control methodologies, it is allowed that all the plant characteristics are completely unknown.

In comparison to the ESC scheme shown in Fig. 11.3, the only major difference in Fig. 11.5 is that the latter system employs a compensator block. Addition of this compensator $C_x(s)$ within the integrator (along with a provision of the phase shift φ_x in the demodulation signal) improves the stability performance and relaxes the requirement of integrator gain k_x to be small. Also, judicious choice of controller parameters provides sufficient immunity from noise ϑ_x . In principle, the compensator $C_x(s)$ introduces derivative action and provides sufficient damping. This can, in turn, be considered

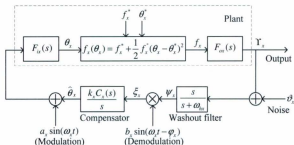


Figure 11.5: Extremum seeking controller with dynamic compensator

as a phase-lead compensator allowing greater phase margin in a loop containing higher relative degree.

In [232], a detailed analysis of extremum seeking system (in presence of a compensator) based on averaging method is provided. This fundamental research accommodates necessary lemmas, propositions, and proofs. A set of two linear models, one for tracking references changes and the other for sensitivity to noise has been developed. However, the derivation of these transfer functions is a non-trivial undertaking [232, 233] and beyond the scope of this work.

According to [229, 231, 232], for the system similar to Fig 11.5, the average linearized relationship between error in estimated operating point $\bar{\theta}_x$ and actual optimum point θ_x^* (which, may drift during prolonged operation or may be unknown due to modeling uncertainty) is defined through

$$\frac{\bar{\theta}_x}{\theta_x^*} = \frac{1}{1 + L_x(s)} \quad (11.22)$$

where

$$L_x(s) = q_x \frac{1}{s} F_{ix}(s) C_x(s) (e^{j\varphi_x} \frac{s + j\omega_x}{s + j\omega_x + h} F_{ox}(s + j\omega_x) F_{ix}(j\omega_x) C_x(j\omega_x) + e^{-j\varphi_x} \frac{s - j\omega_x}{s - j\omega_x + h} F_{ox}(s - j\omega_x) F_{ix}(-j\omega_x) C_x(-j\omega_x)) \quad (11.23)$$

Also, average linearized relationship between output error \tilde{Y}_x and system noise ϑ_x is characterized using the following transfer function [232]

$$\frac{\tilde{Y}_x}{F_{ox}(s)[f_x^*] + \vartheta_x} = -\frac{M_x(s)}{1 + M_x(s)} \quad (11.24)$$

where

$$M_x(s) = q_x \frac{s}{s + \omega_{hx}} F_{ox}(s) (e^{-j\varphi_x} F_{ix}(-j\omega_x) C_x(-j\omega_x) \frac{F_{ix}(s + j\omega_x) C_x(s + j\omega_x)}{s + j\omega_x} + e^{j\varphi_x} F_{ix}(j\omega_x) C_x(j\omega_x) \frac{F_{ix}(s - j\omega_x) C_x(s - j\omega_x)}{s - j\omega_x}) \quad (11.25)$$

In this analysis $q_x = \frac{1}{2} k_x a_x b_x$ is considered as the characteristic gain of the extremum seeking controller. It should be pointed out that the mixed use of symbols within $L_x(s)$ and $M_x(s)$ results from a unique convention used in [232]. For all practical systems, the presence of conjugate terms in these expressions will yield simpler transfer functions that can be readily analyzed.

11.4 Summary of ESC method attributes

With a resurgence in basic and applied research toward refining the extremum seeking control method for application in diverse fields of engineering, hydrokinetic systems may also benefit significantly from this approach. A high-level evaluation of ESC method's applicability in hydrokinetic devices may bring further insight, before embarking upon detailed controller design and analysis.

Chapter 12

Applicability of ESC in Hydrokinetic Systems

By virtue of the fundamental process of fluid-mechanic energy conversion, the performance characteristic of a hydrokinetic energy conversion system is established through $C_p - \lambda$ relationship. This characteristic is highly nonlinear and there exists a unique extremum point at which the power tracker drives the system to operate. Given the complexity of fluid-dynamic interactions, performance degradation, and overall system nonlinearity, it is almost impossible to identify and ensure a guaranteed operation at the optimum conditions by conventional means of power tracking. In addition, for the hydrokinetic systems, use of external underwater sensors (for measurement of water velocity/elevation, and rotor speed) is undesired. On the other hand, if only internal parameters are to be used for system operation, the control algorithm need also be immune to ambient and measurement noises. Under these constraints, an extremum seeking control approach appears ideally suited for hydrokinetic systems.

In the preceding sections, an outline of ESC using a general nonlinear system (steady state and dynamic) has been presented. It is important to assess the strengths and weaknesses of this method through hydrokinetic system models before initiating design initiatives for possible use in such systems. This section explores the applicability of ESC method in hydrokinetic energy conversion systems considering both steady state and dynamic plant models.

12.1 Hydrokinetic systems with static plant model

The most fundamental control requirement for a hydrokinetic energy conversion system, as far as power tracking is concerned, arises from its nonlinear performance curve (i.e., $C_p - \lambda$ characteristics). In this section, success of ESC method in tracking the optimum point on this curve is explored using static plant models. At first, the assessment focuses on the performance curve only, subsequently expanding into a more realistic hydrokinetic system.

12.1.1 Assessment of dominant nonlinear plant characteristics

The power tracking controller within a hydrokinetic system is required to regulate the system control variable (i.e., rotor speed) such that the optimum rotor operating point ($\hat{C}_p, \hat{\lambda}$) is achieved. For a number of reasons, exact determination of this point may not be possible. Firstly, the theoretical and experimental estimates of this characteristic tend to contain high level of mismatch, primarily owing to complexity of fluid-mechanic interactions. Secondly, rotor performance degradation for prolonged usage may cause the optimum point on the rotor performance curve to drift (i.e., reduced \hat{C}_p and/or shifted $\hat{\lambda}$). Finally, as discussed in Chapter 9 and in [202], for a smaller system with multiple cascaded conversion units each having their own nonlinearity, may require considerations of overall system characteristics (i.e., identification of $\hat{\eta}_{opt}, \hat{\lambda}_{opt}$ point).

Since the extremum-seeking control method does not require the plant characteristics to be exactly known a-priori, this approach can effectively overcome these challenges. As long as the optimization problem type (maximum or minimization) is known and existence of a suitable characteristics curve (convex or concave, respectively) is guaranteed, the ESC method is able to drive the system operating point to the maxima.

Assuming any sub-optimal initial operating condition (C_{pi}, λ_i) on the hydrokinetic system's $C_p - \lambda$ curve, the ESC scheme as given in Fig. 12.1 can be used to define the power coefficient characteristics as follows:

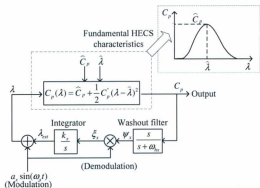


Figure 12.1: Extremum seeking control and performance curve

$$C_p(\lambda) = C_{p1} + C_p'[\lambda_i + a_x \sin(\omega_x t)] + \frac{1}{2} C_p''[\lambda_i + a_x \sin(\omega_x t)]^2 + \dots \quad (12.1)$$

Dropping the second and higher order terms this can be expressed as

$$C_p(\lambda) = C_{p1} + C_p' \lambda_i + C_p' a_x \sin(\omega_x t) \quad (12.2)$$

Designing the washout filter such that only the time-varying component of the plant output is passed it can be found that

$$\psi_x \approx C_p' a_x \sin(\omega_x t) \quad (12.3)$$

After demodulation of this signal by the perturbation signal itself (ie, considering

$a_x = b_x$ in Fig. 12.1) the demodulated signal becomes

$$\xi_x = C'_p a_x^2 \sin(\omega_x t) \quad (12.4)$$

$$= \frac{C'_p a_x^2}{2} - \frac{C'_p a_x^2}{2} \cos(2\omega_x t) \quad (12.5)$$

Since the initial value of the tip speed ratio was λ_i , in presence of the integration block with gain k_x , the estimate of optimum tip speed ratio is given by

$$\lambda_{est} = k_x \int \xi_x dt = \lambda_i + k_x \frac{C'_p a_x^2}{2} t - k_x \frac{C'_p a_x^2}{2} \int \cos(2\omega_x t) dt \quad (12.6)$$

With attenuation of the periodic component, the output of the integrator essential becomes

$$\lambda_{est} = \lambda_i + k_x \frac{C'_p a_x^2}{2} t \quad (12.7)$$

Eq. 12.7 describes the mechanism of system optimization where the second term assumes positive or negative sign depending on the location of the initial operating condition. As seen in Fig. 12.1, for $\lambda_i < \hat{\lambda}$ the slope of the curve $C'_p > 0$. In such conditions, the estimate of optimum point λ_{est} incrementally increases and approaches $\hat{\lambda}$. Similarly, for $\lambda_i > \hat{\lambda}$ the slope of the curve $C'_p < 0$ and λ_{est} incrementally decreases and establishes a limit cycle near the optimum point $\hat{\lambda}$.

In order to prove that the power tracker can stabilize the system with a small perturbation around the optimum point, the $C_p - \lambda$ characteristics as given in Eq. 6.3 can be expanded using Taylor's series.

$$C_p(\lambda) = \hat{C}_p + C'_p(\lambda - \hat{\lambda}) + \frac{1}{2} C''_p(\lambda - \hat{\lambda})^2 + O[(\lambda - \hat{\lambda})^3] \quad (12.8)$$

At the maxima of the curve, the second term in Eq. 12.8 becomes zero. The plant characteristics in steady state can now be given as

$$C_p(\lambda) = \hat{C}_p + \frac{1}{2}C_p''(\lambda - \hat{\lambda})^2 \quad (12.9)$$

Denoting the error in estimation of optimum tip speed ration by $\tilde{\lambda}$, it can be found that

$$\tilde{\lambda} = \hat{\lambda} - \lambda_{est} \quad (12.10)$$

$$\lambda = \lambda_{est} + a_x \sin(\omega_x t) \quad (12.11)$$

$$\lambda - \hat{\lambda} = a_x \sin(\omega_x t) - \tilde{\lambda} \quad (12.12)$$

Using the above expression, Eq. 12.9 becomes

$$C_p(\lambda) = \hat{C}_p + \frac{1}{2}C_p''[\lambda - \hat{\lambda}]^2 \quad (12.13)$$

$$= \hat{C}_p + \frac{1}{2}C_p''[a_x \sin(\omega_x t) - \tilde{\lambda}]^2 \quad (12.14)$$

$$= \hat{C}_p + \frac{1}{2}C_p''[a_x^2 \sin^2(\omega_x t) - 2a_x \tilde{\lambda} \sin(\omega_x t) + \tilde{\lambda}^2] \quad (12.15)$$

$$= \hat{C}_p + \frac{1}{2}C_p''a_x^2 \sin^2(\omega_x t) - C_p''a_x \tilde{\lambda} \sin(\omega_x t) + \frac{1}{2}C_p''\tilde{\lambda}^2 \quad (12.16)$$

$$= \hat{C}_p + \frac{1}{4}C_p''a_x^2(1 - \cos(2\omega_x t)) - C_p''a_x \tilde{\lambda} \sin(\omega_x t) + \frac{1}{2}C_p''\tilde{\lambda}^2 \quad (12.17)$$

$$= \hat{C}_p + \frac{1}{4}C_p''a_x^2 - \frac{1}{4}C_p''a_x^2 \cos(2\omega_x t) - C_p''a_x \tilde{\lambda} \sin(\omega_x t) + \frac{1}{2}C_p''\tilde{\lambda}^2 \quad (12.18)$$

$$= \hat{C}_p + C_p''\left(\frac{1}{4}a_x^2 + \frac{1}{2}\tilde{\lambda}^2\right) - \frac{1}{4}C_p''a_x^2 \cos(2\omega_x t) - C_p''a_x \tilde{\lambda} \sin(\omega_x t) \quad (12.19)$$

The output of this filter (after attenuation of the dc components) can be found as

$$\psi_x \approx -\frac{1}{4}C_p''a_x^2 \cos(2\omega_x t) - C_p''a_x \tilde{\lambda} \sin(\omega_x t) \quad (12.20)$$

After a demodulation by the probing signal itself, the resultant signal is given as

$$\xi_x = -\frac{1}{4}C_p''a_x^2 \sin(\omega_x t) \cos(2\omega_x t) - C_p''a_x^2 \tilde{\lambda} \sin^2(\omega_x t) \quad (12.21)$$

$$= -\frac{1}{2}C_p''a_x^2 \tilde{\lambda} + \frac{1}{2}C_p''a_x^2 \tilde{\lambda} \cos(2\omega_x t) - \frac{1}{8}C_p''a_x^3 \sin(3\omega_x t) + \frac{1}{8}C_p''a_x^3 \sin(\omega_x t) \quad (12.22)$$

Presence of an integrator block with $k_x > 0$ and elimination of the periodic terms due to integration action, determines that

$$\lambda_{est} = k_x \int \xi_x dt \quad (12.23)$$

$$= -\frac{1}{2} k_x C_p'' a_x^2 \int \tilde{\lambda} dt \quad (12.24)$$

Since $\tilde{\lambda}$ is a constant, from Eq. 12.10

$$\dot{\tilde{\lambda}} = -\frac{\tilde{\lambda}}{est} \quad (12.25)$$

Therefore it becomes

$$\dot{\tilde{\lambda}} \approx \frac{1}{2} k_x C_p'' a_x^2 \tilde{\lambda} \quad (12.26)$$

Since $C_p'' < 0$ and $k_x a_x^2 > 0$ it is evident that $\dot{\tilde{\lambda}} < 0$. This implies, the estimation error will always approach zero allowing λ_{est} to converge toward $\tilde{\lambda}$.

Simulation study with performance curve uncertainty

The extremum seeking control method can be used in systems where the plant characteristics are not adequately known. As a test of this feature in hydrokinetic systems, multiple performance curves can be examined in conjunction with the same ESC control schemes.

In Chapter 9 (Fig. 9.5) a set of hydrokinetic systems with diverse levels of system nonlinearity has been studied. In particular, System C, a hypothetical hydrokinetic system, has been shown to exhibit strong variations in its efficiency profile depending on the operating conditions (i.e. water velocity). In order to demonstrate the effectiveness of the ESC method this system is studied further under Matlab™ based simulation environment (Fig. 12.2).

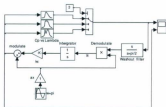


Figure 12.2: Matlab-SimulinkTM simulation blocks for studying performance curve uncertainty

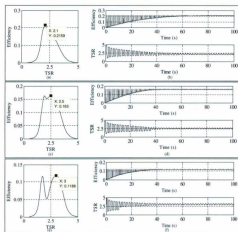


Figure 12.3: Simulation results for studying performance curve uncertainty

Using a control scheme as in Fig 12.1, with $k_x = 5.5, a_x = 1, \omega_x = \pi, \omega_{hx} = \frac{\pi}{2}$, (more systematic parameter tuning method is given in Chapter 13), three η_{sys} vs. λ_{sys} profiles have been simulated. Fig. 12.3 (a), (c), and (e) contain these system efficiency profiles whereas Fig. 12.3(b), (d), and (f) show the corresponding simulation results. In all these cases, the optimum tip speed condition is achieved around $t \approx 50$ seconds and the plant establishes a limit cycle near this point.

A set of subtle observations that can be made from this set of simulation study are:

- *Model independence:* Using the same controller parameters, the ESC scheme successfully drives the system toward the $\hat{\eta}_{opt}, \hat{\lambda}_{opt}$ point in all three cases. Unlike typical control methods where the set-point is established a-priori, the extremum seeking controller operates well even without detailed knowledge of the plant characteristics. However, the amplitude of the limit cycle may require further minimization in order to improve system performance.
- *Robustness against drift:* Even with detailed prior knowledge of the, under certain conditions the optimum operating point may drift to newer values. The ESC approach adapts the system to be operated in these newer optimum points.
- *Stabilization near maxima:* Even with the presence of a minima, the ESC method allows the system to settle only at a maxima. However, it has been observed that the initial flatness in the η_{opt} vs. λ_{opt} or $C_p - \lambda$ curve may cause difficulty in convergence, especially with very small perturbation signal amplitudes.

12.1.2 Assessment of controller parameter variations and disturbance inputs

A typical power tracker within a physical hydrokinetic system implicitly acts to achieve optimum tip speed ratio. However, on a more explicit level, such a tracking system measures various physical parameters such as rotor speed, flow velocity, shaft torque, or

output power and uses those to adjust the control variable accordingly. The scheme in Fig. 12.1 only serves the purpose of describing the fundamental control process, i.e., the implicit control method. In order to implement this control method in a real-life system, additional plant details and control loops need to be incorporated.

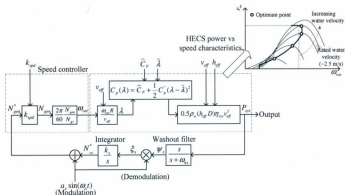


Figure 12.4: Extremum seeking control with additional system representation

As seen in Fig. 12.4, a physical hydrokinetic energy conversion system incorporates multiple modeling blocks beyond its core performance curve static map discussed in through Fig. 12.1. This representation (Fig. 12.4) is still a simplified model containing only steady state plant descriptions. Subtle features in this regard includes:

- Presence of an internal speed controller embedded within the plant that actuates necessary subsystems toward achieving overall optimum performance.
- Susceptibility to operate under varying water velocity, height, and poorly tuned internal speed controller (in addition to assuming the optimum point to be unknown or uncertain).

In this simulation study, the relevant ESC parameters are: $k_x = 2.5$, $a_x = 3$, $\omega_x = \pi$, $\omega_{Ax} = \frac{\pi}{2}$. A new variable k_{sp} is incorporated, which acts as a gain that varies the speed reference generated by the ESC loop. This, in effect, allows a mean for introducing controller inadequacies. This variable is in the path of speed reference and $k_{sp} = 1$ implies that there is zero error in generator speed. Any other value will imply either a higher or lower generator speed, compared to the actual speed reference.

The simulation is conducted with ramp increases in water velocity and height, as shown in Fig. 12.6. Also, $k_{sp} = 1$, 1.25, and 0.75 is used and the corresponding results are superimposed in the plot.

From Fig. 12.6, it can be seen that the ESC scheme successfully drives the hydrokinetic system to the optimum point of operation, regardless of parameter values in the internal speed controller or flow-field variations (water velocity and rotor submersion) external to the device. Only visible contribution of the speed controller is in the initialization period, where a smaller value indicates slower convergence.

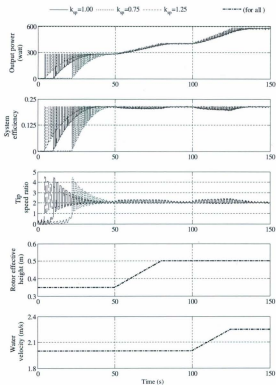


Figure 12.6: Simulation results for studying variations in disturbance input and control parameter

12.2 Hydrokinetic systems with dynamic plant model

Within a hydrokinetic energy conversion system the sources of dynamics include rotor-generator inertia, sensor time constants, and storage elements in power electronic converters. The investigations in the previous discussion consider these dynamics to be fast enough such that the perturbation method essentially undertakes control of a static plant.

In most circumstances, especially for hydrokinetic systems where the rotor-generator inertia could be high and system response is in terms of seconds, addition of a dynamic compensator becomes indispensable. This compensator, as shown in Fig. 11.5, works as a phase-lead compensator and improves the phase margin. In other words, in presence of this compensator a zero is placed following the expression

$$C_x(s) = 1 + d_x s \quad (12.27)$$

Since the tracking capability of an ESC is of utmost significance in hydrokinetic systems, influence of this compensator parameter as well as other quantities (controller gain k_x , signal frequency ω_x (rad/s), cut-out frequency ω_{hx} (rad/s), and phase shift φ_x (rad)) need to be understood in this context. Also, the performance of the system in presence of ambient and measurement noise may provide further insight.

Tracking capability of an extremum seeking controller and its sensitivity to noise can be very effectively identified through the transfer functions given in Eq. 11.22 and Eq. 11.24. In order to facilitate the tuning process of various parameters, a simple test system with identical input and output dynamics block has been considered (Eq. 12.28).

$$F_{ix}(s) = F_{ox}(s) = \frac{1}{0.5s + 1} \quad (12.28)$$

In addition, a total of five cases, each observing the effects of variation of one parameter (while leaving the other parameters constant), have also been set as shown in Table 12.1.

Table 12.1: Case descriptions for ESC dynamic analysis

Case	Study parameter	k_x	ω_x (rad/s)	ω_{hx} (rad/s)	d_x	φ_x (rad)
A	k_x	1 & 10	6	3	0.5	0
B	ω_x	5	1 & 10	3	0.5	0
C	ω_{hx}	5	6	1 & 10	0.5	0
D	d_x	5	6	3	0.1 & 1	0
E	φ_x	5	6	3	0.5	0.1 & 3

For each of these test cases, separate bode plot and step responses (both for tracking capability and noise sensitivity) are given in Fig. 12.7, 12.8, 12.9, 12.10, and 12.11.

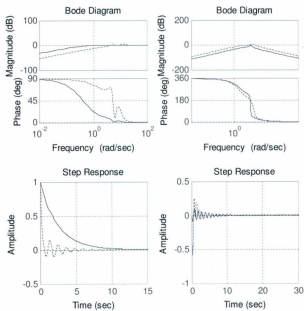


Figure 12.7: Variations in gain (solid: smallest and dash: largest) and corresponding influence on tracking capability (left) as well as noise sensitivity (right) for case A

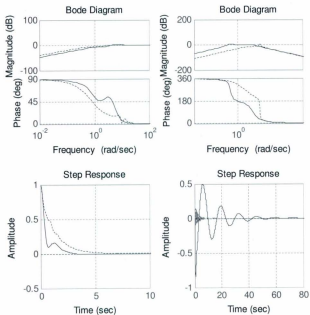


Figure 12.8: Variations in signal frequency (solid: smallest and dash: largest) and corresponding influence on tracking capability (left) as well as noise sensitivity (right) for case B

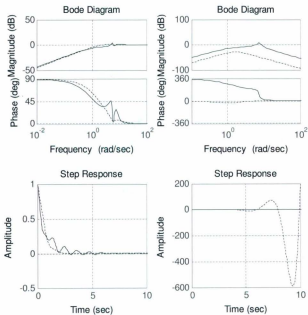


Figure 12.9: Variations in cut-off frequency (solid: smallest and dash: largest) and corresponding influence on tracking capability (left) as well as noise sensitivity (right) for case C

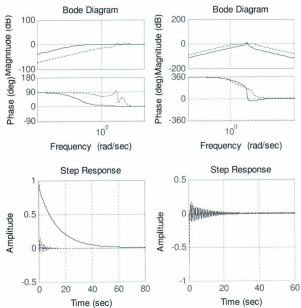


Figure 12.10: Variations in compensator coefficient (solid: smallest and dash: largest) and corresponding influence on tracking capability (left) as well as noise sensitivity (right) for case D

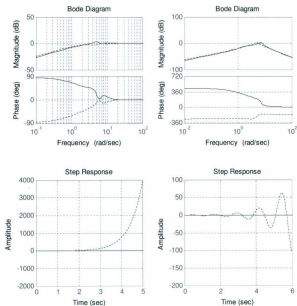


Figure 12.11: Variations in phase shift (solid: smallest and dash: largest) and corresponding influence on tracking capability (left) as well as noise sensitivity (right) for case E

12.3 Summary of ESC method's applicability in hydrokinetic systems

With reference to the case studies presented here, the following general observations can be made:

- An increase in controller gain ensures faster convergence to the optimum point at the expense of higher oscillations and ringing.
- The effect of modulation/demodulation frequency on tracking capability is minimal while the noise sensitivity is greatly affected by this quantity.
- A high cut-off frequency may drive the system unstable due to greater susceptibility to noise.
- An increase in compensator zero value improves both tracking capability (faster response) and noise sensitivity (less prone to noise pickup).
- An increase in phase shift may cause the ESC method to diverge from the optimum point as well as to cause instability due to noise.

While these observations are generic in nature and only serve to provide high-level understanding, judicious parameter selection is a vital step toward extremum seeking controller design. A systematic outline for parameter tuning is provided in the next section of this dissertation.

Chapter 13

ESC Synthesis and Implementation in Simulation Model

The power tracking control problem of hydrokinetic energy conversion systems can be broadly classified into two categories: (a) global technology-wide challenges, and (b) control-method specific challenges. As discussed in Section 8, the global challenges associated with hydrokinetic systems' power tracking control include technological nascency, lack of operational experience, diversity of system design (duct usage, mounting arrangements, field of applications), etc. From tracking control's point of view, turbine operation under variable flow conditions (water velocity and height) and use of underwater sensors (and associated cost/reliability implications) have also been identified as issues that may pose subtle challenges. A comparative study of various power tracking control options presented in Section 10 and pursuing discussions have indicated the need for devising an adaptive control method that may operate without using underwater sensors and may overcome many of these challenges. The extremum seeking control (ESC) principle outlined in the previous sections is an ideal candidate in this regard.

The ESC approach, none-the-less, requires a set of control-method specific issues to be resolved. On a hierarchical viewpoint, there are two levels of control within the ESC design exercise. These are

- Internal speed controller design (and development of input dynamics model).
- Extremum seeking controller parameter selection (and development of output dynamics model).

The process of designing the internal speed controller is common for most other power tracking methods (such as, tip speed ratio, hill climbing, or power signal feedback). For the purposes of completeness, this step is discussed here under the ESC design procedure. Also, this procedure will be utilized toward developing a simplified input dynamics model. Procedures for selecting various ESC parameters will rely upon aforementioned steady state and dynamic evaluations. The input and output dynamics models will be used toward assessing the dynamic performance of the ESC (utilizing the Hammerstein-Wiener model Fig. 11.4).

The hydrokinetic energy conversion system being studied in this work consists of a power electronic conversion stage that interfaces the rotor/generator to the utility grid. This stage, in turns, acts as an actuator that adjusts the overall power transfer to the grid. For a given water velocity, the rotor speed varies depending on the level of electrical loading. Therefore, power converters essentially act so as to allow the system to operate near the optimum tip speed ratio by adjusting the power flow into the electrical network.

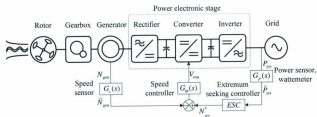


Figure 13.1: Hydrokinetic system power tracking control using extremum seeking method

The internal controller adjusts the set point of the power electronic stage such that the speed reference (as generated by the extremum-seeking controller) can be tracked. In this setup, the output voltage of the dc-dc converter is regulated by the internal control

loop. The extremum-seeking controller adaptively generates the speed reference using a sinusoidal perturbation method as described in Section 11. The control problems are approached through a set of reduced order linear models as shown in Fig. 13.1.

13.1 Internal speed controller design considerations

For controller design purposes, the internal speed control loop can be represented using a reduced order linear averaged model as shown in Fig. 13.2 [86, 102, 234]. Here the transfer functions $G_w(s)$, $G_s(s)$ and $G_{ps}(s)$ represent speed controller, speed sensor, and plant-actuator model, respectively. The parameters pertinent to the control block $G_w(s)$ is subject to design and selection. The sensor transfer function can be found using the design information of the instrumentation hardware. Identification of plant transfer function, on the other hand, is a non-trivial problem. This can be achieved by undertaking reduced order hydrokinetic system modeling.

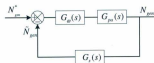


Figure 13.2: Internal speed control loop

The primary contributing factor within the plant-actuator system is the rotor-generator equivalent moment of inertia. In Fig. 13.1, the plant block incorporates the power electronics systems in addition to the electromechanical and mechanical systems. Since the time constants associated with power electronic systems are in the order of several milliseconds, and the rotor-generator system predominantly defines the system dynamics, it is therefore agreeable to use the reduced order representations of the latter class only.

Assuming, sufficient plant-actuator details are unavailable, in [102] a simplified

scheme has been used. According to [102] the plant-actuator transfer function can be represented as

$$G_{pa}(s) = \frac{k_{pa}}{\tau_{pa}s + 1} \quad (13.1)$$

Here the plant-actuator gain k_{pa} can be found by using the empirical relationship in [102].

$$k_{pa} = \frac{N_{gr}}{k_{tsc}} \quad (13.2)$$

The torque-speed constant k_{tsc} can be found by deriving the first order derivative of the rotor torque against rotor speed at the neighborhood of the optimum tip speed ratio. This can be identified using [102, 110]:

$$k_{tsc} = -\left. \frac{\partial T_{mcc}}{\partial \omega_r} \right|_{\tilde{\lambda}_{opt}} \quad (13.3)$$

$$= -\left. \frac{\partial}{\partial \omega_r} \left(\frac{1}{2} \rho_w A_r C_T(\lambda) v_{eff}^2 R \right) \right|_{\tilde{\lambda}_{opt}} \quad (13.4)$$

$$= -\frac{1}{2} \rho_w A_r v_{eff}^2 R \left(\left. \frac{\partial C_T(\lambda)}{\partial \omega_r} \right) \right|_{\tilde{\lambda}_{opt}} \quad (13.5)$$

$$= -\frac{1}{2} \rho_w A_r v_{eff}^2 R \left(\left. \frac{\partial C_T(\lambda)}{\partial \lambda} \right) \right|_{\tilde{\lambda}_{opt}} \frac{\partial \lambda}{\partial \omega_r} \quad (13.6)$$

$$= \frac{1}{2} \rho_w A_r v_{eff}^2 R \left(\left. \frac{\partial C_T(\lambda)}{\partial \lambda} \right) \right|_{\tilde{\lambda}_{opt}} \frac{R}{v_{eff}} \quad (13.7)$$

$$= -\frac{1}{2} \rho_w A_r v_{eff} R^2 C_{TO}^* \quad (13.8)$$

Here the first derivate of torque coefficient with respect to the tips speed ratio (around the optimum point) is given as

$$C_{TO}^* = \left. \frac{\partial C_T(\lambda)}{\partial \lambda} \right|_{\tilde{\lambda}_{opt}} \quad (13.9)$$

This constant can be determined through the definitions of torque coefficient Eq. 6.3) and curve-fit for power coefficient function (Eq. 9.20).

The plant-actuator equivalent time constant τ_{pa} can be estimated using the empirical formulation below [102].

$$\tau_{pa} = \frac{N_{gr} J_{erg}}{k_{tac}} \quad (13.10)$$

The equivalent rotor-generator system inertia J_{erg} (as reflected to the high speed shaft) is found by

$$J_{erg} = J_{gen} + \frac{1}{N_{gr}^2} J_{rot} \quad (13.11)$$

With determination of time constant τ_{pa} and gain k_{pa} , the reduced order plant-actuator equivalent model of can be found by Eq. 13.1.

13.1.1 Controller parameter tuning

The internal speed controller receives a speed reference from the external controller (ESC) and adjusts the turbine power output by actuating the power electronic systems (the trimming voltage of the dc-dc converter in this application) accordingly. As shown in Fig. 13.2, the speed signal feedback path requires considerations for the sensor dynamics and is given by Eq. 13.12.

$$G_s(s) = \frac{\hat{N}_{gen}}{N_{gr}} = \frac{1}{\tau_1 s + 1} \quad (13.12)$$

For the purposes of simplicity and to reflect the existing norms, a simple PI type regulator is considered as the speed controller. This controller can therefore be given as

$$G_w(s) = k_{pw} + \frac{k_{iw}}{s} \quad (13.13)$$

Here $k_{p\omega}$ and $k_{i\omega}$ are proportional and integral constants for the speed controller. Determination of these two parameters is dictated by two major factors, especially in the context of ESC design. These are:

- *Desirability of an over-damped system response:*

Given that there is no stringent requirement for the overall hydrokinetic system to act fast (compared to the flow variations, where the dominant components may vary within minutes to hours), system structural requirement (stress, fatigue, etc.) and component ratings (transient over-current, over-voltage, etc.) can be relaxed if transient overshoots can be eliminated. This in turn implies the desirability of an over-damped system response.

- *Need for lower order system model:*

The Hammerstein-Wiener model used in the process of dynamic compensator design for extremum seeking controllers (as discussed in Section 11.3.2), relies greatly on first order input and output dynamic models. Since, the speed control loop constitutes the input dynamics block, a reduced order model (preferably, first order) can simplify the design tasks significantly.

Considering the above factors, the PI controller parameters need to be tuned such that the output overshoot is minimal (such as, < 1%) and the system is sufficiently damped. However, the settling time should not be too high and a typical time range of interest for such applications (electromechanical system) is in the order of several seconds. Such controller design exercises are commonplace procedures ([235]) and readily available tools such as Matlab-SISOTool ([156]) can be used in this regard.

13.1.2 Input dynamics model

The input dynamics model for use in conjunction with the Hammerstein-Wiener approach, essentially consists of the rotor speed control loop, which relies on the controller,

feedback dynamics, as well as the reduced order plant-actuator model. The overall input system transfer function consisting of the blocks shown in Fig. 13.2 can be given as

$$F_{ix}(s) = \frac{k_{po}(k_{pw}\tau_1 s^2 + (k_{pw}\tau_1 + k_{pw})s + k_{iw})}{\tau_{po}\tau_1 s^3 + (\tau_{po} + \tau_1)s^2 + k_{po}k_{pw}s + k_{po}k_{iw}} \quad (13.14)$$

By tuning the controller parameters appropriately (as discussed above), this higher order system can be approximated through a first-order transfer function. This can be realized through a graphical approach where the plant response (in presence of a speed controller and speed sensor) for unit step input is plotted and the time required to reach the 63.7% mark of the steady-state output is identified.

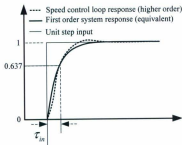


Figure 13.3: Determination of simplified input dynamics model

Denoting this time by τ_{in} (Fig. 13.3), the first order approximation of this system can be given as

$$F_{ix}(s) = \frac{1}{\tau_{in}s + 1} \quad (13.15)$$

This input dynamics transfer function, effectively represents a simpler Hammerstein model (Fig. 11.4) for use in dynamic compensator design procedures.

13.2 ESC parameter selection considerations

Apparent challenges in designing the extremum seeking controller, which generates the necessary rotor speed reference for the internal controller, largely resides within a large set of parameters that needs to be tuned appropriately. In order to guarantee the stability of the control method, proof of system stability need also be established at the design phase. A precondition for this step is to identify the output system dynamics (i.e. the Wiener model). Therefore, the associated subtleties include: (a) parameter selection, and (b) determination of output dynamics model and evaluation of system stability.

13.2.1 Parameter sensitivities

The parameters within the extremum seeking control loop, albeit large in number, can be selected through heuristics and general observations. Based on the fundamental principles of extremum seeking control method, as well as the steady-state and dynamic evaluation conducted in Chapter 12, a set of parameter sensitivity information is highlighted in Table 13.1. It should be pointed out that this information, in spite of being qualitative in nature, aids the process of judicious controller tuning and acts against any possible errors (while selecting the parameters using methods such as in 13.2) by general inspections.

As seen in the above table, for almost all practical purposes the amplitude of the modulating and demodulating signal can have identical values. A typical choice [204, 224, 225] in this regard is to consider the magnitudes of these signals to be less than 1% of the control variable's rated value (generator speed in the case of a hydrokinetic system outlined in Fig. 13.1) . This implies,

$$a_x = b_x < 1\% \text{ of } N_{gen}^{\delta} \quad (13.16)$$

The controller gain should, in principle, remain within the same order of magnitude as the modulating signal. Since, this quantity maps the system output (electric power) to the control variable (generator speed), a heuristic value can be

Table 13.1: Parameter sensitivity on ESC performance

Parameter	Symbol	Effects on performance
Controller gain	k_x	- Increase in these parameters result in faster convergence, higher overshoot, larger limit cycle, higher sensitivity to noise, and better capability to override local maxima.
Modulating (probing) signal amplitude	a_x	- For a given q_x , an increase in k_x is more effective in reducing the magnitude of limit cycle (compared to a_x or b_x). For a given q_x , an increase in a_x or b_x is more effective in increasing the convergence rate (compared to k_x).
Demodulating signal amplitude	b_x	- Monotonic increase in k_x may cause to reach one or more control bounds within the system, thereby making the overall control method insensitive to subsequent changes.
Characteristics controller gain	q_x	- Increase in a_x or b_x introduces cyclic oscillation in the system output and may cause additional structural stress.
Phase difference between modulating and demodulating signals	φ_x	- This parameter is highly sensitive to system stability and inappropriate values may cause overall instability.
Signal frequency	ω_x	- An increase in this parameter may result in faster convergence, higher sensitivity to noise, lesser structural stress, and smaller limit cycle. Increases beyond the frequency of plant dynamics may cause instability.
High pass filter cut-out frequency	ω_{hx}	- An increase in this parameter may result in faster convergence, higher sensitivity to noise, lesser structural stress, and smaller limit cycle. Increases beyond the frequency of plant dynamics may cause instability. Increase in this parameter generally results in faster convergence and lesser sensitivity to noise. Cut-off frequency larger than the perturbation signal frequency will cause the ESC method to fail.
Dynamic compensator zero placement	d_x	- An increase in this parameter results in faster convergence and higher overshoot and ringing. This parameter is an effective mean for designing ESC with higher plant dynamics.

$$k_x \approx \frac{P_{me}^b}{N_{gen}^b} \quad (13.17)$$

The introduction of a phase angle between the modulating and demodulating signal, albeit capable of improving system stability for higher order systems (by canceling out the associated phase lag), can be prone to inappropriate selection. In presence of a dynamic compensator, this parameter may deem redundant and can be eliminated. For the ESC design exercise here, this term is taken as zero.

$$\varphi_x = 0 \quad (13.18)$$

For a hydrokinetic system, the resource field variations are much slower than the plant dynamics. The modulating signal frequency and the washout filter cut-off frequency must reside between these two extremes. In this case, the representative frequency of plant dynamics for the hydrokinetic system can be given as

$$\omega_{ps} = 2\pi \frac{1}{\tau_{in}} \quad (13.19)$$

The underlying requirement toward selection of modulating/demodulating signal frequency becomes

$$\omega_{ps} \geq \omega_x \geq \omega_{hx} > \omega_v \quad (13.20)$$

Through relevant studies [204, 224, 225]) it has been observed that the modulating signal frequency and the washout filter cut-off frequency should remain within a closer bound (within a order of magnitude of each other and the plant). While the speed of the control scheme is primarily dependent on the selection of various parameters (as listed in Table. 13.1), Eq. 13.20 imperatively indicates that the controller speed would be in coordination with the dominant frequency of water speed variations as identified by ω_v .

The objective of the dynamic compensator within the ESC loop is to reduce the plant order and thereby improve the performance of the overall system. This in turn implies placement of a zero determined by the parameter d_x . Since, presence of the speed control loop is inevitable for a hydrokinetic energy conversion system, this quantity can be chosen to account for the corresponding pole (approximated by the input dynamics time constant) as

$$d_x \approx \tau_{in} \quad (13.21)$$

With judicious choice of each of these parameters the extremum seeking controller can be tuned such that the overall performance of a hydrokinetic energy conversion system is within the expected limits.

13.2.2 Output dynamics model and evaluation of system stability

Unlike the input dynamics model, the requirements for determining the output dynamics for use in stability analysis through the Hammerstein-Wiener scheme, is less substantial. This is primarily due to the fact that most of the significant dynamic elements (such as rotor-generator inertia, speed controller and speed sensors, etc.) are already considered in the input dynamics blocks (i.e. the Hammerstein model).

With reference to the extremum seeking scheme shown in Fig. 13.1 and its implementation procedures in Fig 11.5, it can be seen that the power measurement block and appears as a source of output dynamics, with respect to the extremum seeking control loop.

Therefore, for the hydrokinetic energy conversion system, the Wiener model can be represented as

$$F_{out}(s) = \frac{1}{\tau_{out}s + 1} \quad (13.22)$$

where τ_{out} is the time constant associated with the wattmeter/power measurement circuit. With determination of input and output dynamic blocks (Eq. 13.15 and Eq. 13.22, respectively), as well as selection of ESC parameters following the aforementioned procedure, the stability assessment steps can be initiated. Relevant transfer functions for drift/convergence evaluation and noise sensitivity analysis are given through Eq. 11.22 and Eq. 11.24, which can be determined through a computation tool such as Maple™.

13.3 ESC design procedures for hydrokinetic systems

The ESC design considerations discussed in the previous section provide the bases for embarking upon a design exercise for a physical hydrokinetic energy conversion system.

However, further streamlining of the discussed procedure is needed. In this section, the extremum controller design process is further simplified by separating these tasks on a sequential manner.

The overall design exercise can be separated, as discussed in the previous section, into two tasks: (a) internal speed controller, and (b) extremum seeking controller. A total of 20 steps are highlighted (each task containing 10 steps) in Table 13.2. Relevant logic and analysis are given in Section 13.1 and Section 13.3, respectively. In the rightmost column the design inputs for the small HECS system (being researched in this work) are given, while associated design outputs are shown in the column next to it.

For each step an equation for conducting necessary calculations and its reference to the original discussion is given. Also, for the physical test system discussed in the Chapter 6, the input data and output results are tabulated. While calculations for a given step largely depends on its preceding step, a-priori information needed for these tasks are also outlined.

Table 13.2: ESC design steps for hydrokinetic systems

Step	Equation	Ref.	Design output (test system)	Design input (test system)
1	$C_{TO}^* = \frac{\partial \mathcal{L}(\lambda)}{\partial \lambda} \Big _{k_{iso}}$	13.9	$C_{TO}^* = -0.0787$	$\lambda_{iso} = 2.15, C_p - \lambda$ curve
2	$k_{iso} = -\frac{1}{\lambda} \frac{\partial \mathcal{L}(\lambda)}{\partial \lambda} \Big _{k_{iso}}$	13.8	$k_{iso} = 8.856$	General data
3	$k_{ps} = \frac{N_{gen}}{N_{crit}}$	13.2	$k_{ps} = 0.387$	$N_{gr} = 3.43$
4	$J_{avg} = J_{gen} + N_{gr}^2 J_{rot}$	13.11	$J_{avg} = 0.1317$	$J_{gen} = 0.085, J_{rot} = 0.9025$
5	$\tau_{ps} = \frac{N_{gr}^2 k_{ps}}{k_{iso}}$	13.10	$\tau_{ps} = 0.051$	-
6	$G_{ps}(s) = \frac{N_{gr}}{s + \tau_{ps}}$	13.1	$G_{ps}(s) = \frac{0.887}{s + 0.051}$	-
7	$G_s(s) = \frac{N_{gen}}{s + \tau_{ps}}$	13.12	$G_s(s) = \frac{1}{s + 0.051}$	$\tau_s = 0.95$
8	$G_e(s) = k_{ps} + \frac{N_{gr}}{s}$	13.13	$G_e(s) = 0.85 + \frac{1.03}{s}$	$k_{ps} = 0.85, k_{iso} = 1.65$
9	$F_{in}(s) = \frac{N_{gr} [k_{ps} \tau_{ps}^2 + (k_{ps} \tau_{ps} + k_{ps} \tau_{ps} + k_{ps} \tau_{ps})]}{\tau_{ps} \tau_{ps}^2 + (k_{ps} \tau_{ps} + k_{ps} \tau_{ps} + k_{ps} \tau_{ps})}$	13.14	$F_{in}(s) = \frac{0.317s^2 + 0.944s + 0.64}{s^2 + 0.1s + 1.35 + 0.941}$	-
10	$F_{in}(s) = \frac{N_{gen}}{s + \tau_{ps}}$	13.15	$F_{in}(s) = \frac{0.887}{s + 0.051}$	$\tau_{ps} = 0.8$
11	$a_x = b_x < 1\%$ of N_{gen}	13.16	$a_x = b_x = 1.05$	0.3% of $N_{gen} = 350$
12	$k_x \approx \frac{N_{gen}}{N_{crit}}$ Equation	13.17	$k_x = 1.15$	$F_{des} = 400$
13	$\psi_x = 0$	13.18	$\psi_x = 0$	-
14	$\omega_{ps} = 2\pi \frac{1}{\tau_{ps}}$	13.19	$\omega_{ps} = 7.854$	-
15	$\omega_{ps} \geq \omega_x \geq \omega_{kr} > \omega_1$	13.20	$\omega_x = 2\pi, \omega_{kr} = \pi$	$\omega_1 \approx 0.5$
16	$d_x \approx \tau_{ps}$	13.21	$d_x = 0.8$	-
17	$C_x(s) = 1 + d_x s$	13.22	$C_x(s) = 1 + 0.8s$	-
18	$F_{out}(s) = \frac{1}{s + \tau_{ps}}$	13.22	$F_{out}(s) = \frac{0.787}{s + 1}$	$\tau_{out} = 0.75$
19	$\frac{d_x}{\tau_{ps}} = \frac{1 + \tau_{ps} \omega_1}{s + \tau_{ps}}$	11.22	$\frac{d_x}{\tau_{ps}} = \frac{0.857s + 1.4488s + 1.3535s^2 + 193.260s^3 + 0.6233s^4}{0.857s^4 + 1.3535s^3 + 1.4488s^2 + 1.0535s + 1.0}$	-
20	$F_{in}(s)F_{out}(s) = -\frac{M_{in}(s)}{1 + M(s)}$	11.24	$F_{in}(s)F_{out}(s) = -0.75s^2 + 3.20s + 3.13s^2 + 1.17s + 1.08$	-

The design process can be initiated by evaluating the performance curve of a hydrokinetic energy conversion system. This can be done through numerical fluid-mechanic analysis as exemplified in Chapter 5 or through field testing procedures discussed in Chapter 7. General information on the turbine system (inertia, gear ratio, physical dimension), relevant flow conditions (water velocity, frequency of velocity variation), and sensor time constants (generator tachometer and wattmeter) is sufficient to initiate the subsequent steps.

In Step # 8, the tuning of speed controller parameters need to be carried out either numerically or through graphical tools such as Matlab-SISOTool™. Using the latter approach, a root-locus plot and imposed criteria ($< 1\%$ overshoot and < 5 sec settling time) are shown in Fig. 13.4(a). After conducting the necessary tuning, the step response of the physical system is plotted in Fig. 13.4(b) and relevant parameters are tabulated.

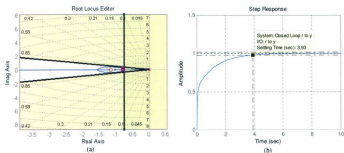


Figure 13.4: Speed controller tuning (a) root locus (b) step response

Determination of equivalent first order model for the input dynamics block is conducted through Step # 9 and 10. The higher-order system response as well as its equivalent reduced order representation is plotted in Fig. 13.5. Relevant discussions are given in Section 13.1.2.

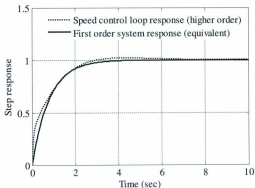


Figure 13.5: Internal speed control loop response (higher order and first order)

Step # 17 - 20 essentially allows an evaluation of the parameter selected in the preceding steps. For the physical hydrokinetic system being researched, the transfer functions for tracking capability (Eq. 11.22) and noise sensitivity (Eq. 11.24) assessment are found using Maple™ numerical tool.

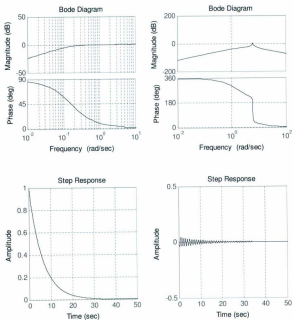


Figure 13.6: Hydrokinetic system tracking capability (left) as well as noise sensitivity (right) with selected controller parameters

In Fig. 13.6 the step response and bode plot for the hydrokinetic system's (with its reduced order model and selected controller parameters) tracking performance and noise sensitivity are given. In presence of the necessary information highlighted in the far-right column of Table 13.2, the control parameters found in Step # 8, 11-16. These quantities can then be readily implemented in the hydrokinetic system. It should be pointed out that this tracking performance information presented in Fig. 13.6 is not against time or resource variation, rather against a unit step change in the tracking set point.

13.4 Simulation based test of ESC method

The small-scale hydrokinetic energy conversion system and its associated peripherals being studied in this work, has been tested, modeled, and validated thoroughly. The test procedures included both steady-state and dynamic performance assessment. Individual subsystems models (electromechanical conversion, power electronic converters, and instrumentation hardware) as well as system-level numerical models (rotor-generator system with switched load bank) have been developed with a view to bringing insight into a realistic hydrokinetic system.

The extremum seeking controller design procedure discussed in the previous section relied on a set of reduced order system descriptions as well as averaging analysis. In this section, these control parameters are implemented on the full-order nonlinear hydrokinetic system model. The HECS simulation model is identical to that of presented in the comparative analysis in Chapter 10. Only difference in implementation is in the control blocks, which consist of an external extremum seeking control loop as shown in Fig. 13.7 (inset). This controller takes two inputs from the plant (generator speed and output power) and produces one control signal (trimming voltage for dc-dc converter). Within the ESC controller loop, the perturbation signal is added to the estimation error using the modulation/summation block and the internal speed control loop contains a negative feedback/subtraction block.

The simulation schemes presented in this chapter incorporate both deterministic (step and ramp-type input) as well as stochastic flow variations. In Fig. 13.11, the performance of the HECS is demonstrated in terms of output power, generator speed, and tip speed ratio, against a step variation of water velocity (from 2 m/s to 2.25 m/s at $t = 15$ sec) with a constant water elevation (0.3 m).

The dynamic behavior for $t < 5$ sec in Fig. 13.11 is associated with simulation initialization and should be ignored. Due to a step variation in water velocity at $t = 15$ sec, the rotor speed and output power reaches a steady state within 5 seconds. The limit cycle at the inverter output is around 1 watt and generator speed is 2.5 rpm. The resultant tip speed ratio, before and after the step variation is around 2.2, indicating a successful implementation of the ESC method.

The performance of the HECS against a ramp-type input (water velocity increase during $t = 0 - 5$ sec and decrease during $t = 25 - 30$ sec) is shown in Fig. 13.9. Similar to the previous case, the water elevation is taken to be constant at 0.3 m. The rotor starts to rotate at $t = 3.5$ sec and the corresponding water velocity is 1.85 m/s. The transient conditions settle within 5 seconds and establishes a steady limit-cycle throughout $t = 9 - 25$ sec. Data points showing high tip speed ration for $t > 26$ sec is due to high generator speed as a result of inverter shut-down (low input voltage) and should be ignored.

While Fig. 13.8 and Fig. 13.9 show the HECS behavior against deterministic-type flow variations, a more realistic scenario is given in Fig. 13.10. In this case, the flow conditions are generated using the flow simulator described in Section 4.5, where a turbulent velocity and height component is superimposed on average values (2.25 m/s and 0.3 m, respectively).

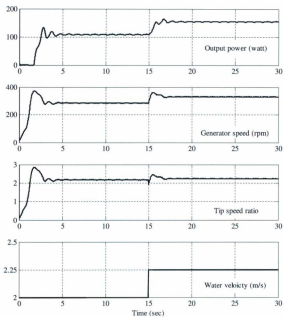


Figure 13.8: HECS performance with ESC control - step flow velocity variation

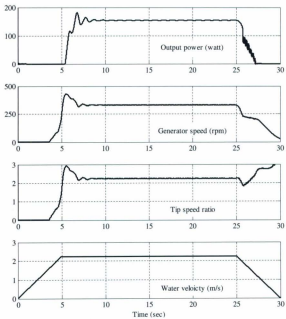


Figure 13.9: HECS performance with ESC control - ramp type flow velocity variation

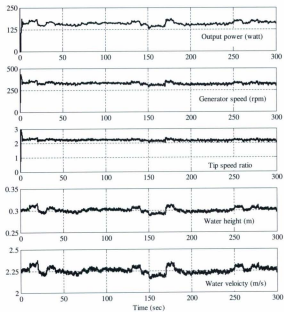


Figure 13.10: HECS performance with ESC control - stochastic flow conditions, without step variations

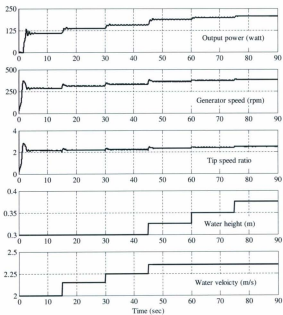


Figure 13.11: HECS performance with ESC control - step variations in flow condition

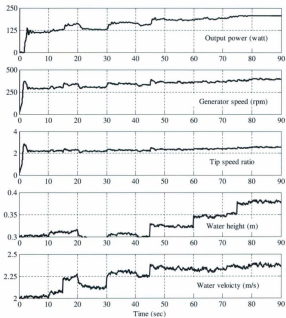


Figure 13.12: HECS performance with ESC control - stochastic variations in flow condition

With a view to facilitating a comparative evaluation of extremum seeking control approach, as against other control methods presented in Chapter 10, simulation runs with similar input flow conditions are presented in Fig. 13.11 and Fig. 13.12. As seen in these plots, for $t < 45$ sec the resultant tip speed ratio is around 2.2, whereas this ratio is increased accordingly with variations in water elevation.

13.5 Summary of ESC controller synthesis

A comparative summary of the extremum seeking control method, in conjunction with other generic methods studied in Section 10.4 is given in Table 13.3.

Table 13.3: Comparative performance review

Method	Design Issues		Implementation			Performance Attributes	
	Model dependence	Tuning	Required sensors	Sensors	Sensor Usage	Tracking capability	Transient Performance
TSR	Highly dependent	Simple	(Water velocity), generator speed		(Underwater), Above surface	Good	Good
PSF	Highly dependent	Complicated	(Water height), output power		(Underwater), Above surface	Poor	Good
HCC	Partially Independent	Moderately complicated	Output power, generator speed		Above surface	Moderate	Poor
ESC	Independent	Complicated	Output power, generator speed		Above surface	Good	Good

The extremum seeking control method possesses almost all the desired attributes for possible implementation in a hydrokinetic system. This includes, model independence, above surface instrumentation, good transient performance and good tracking capability. In addition, the ESC method can be tuned to guarantee overall system stability and this method operates adaptively, overriding the uncertainties associated with hydrokinetic system's operational conditions. In this research, strides are made toward developing a systematic procedure for controller parameter tuning, and the simulations results (exercised on a set of validated numerical models) indicate general success of this method.

Chapter 14

Conclusion

Through this research and the concurrent near-exhaustive review of hydrokinetic energy conversion systems (HECS), it has been established that this class of renewable power devices bears immense potential for electricity generation from rivers, tides and other resources. While the current industry initiatives mostly encircle device design, development, and testing, it is expected that greater pre-commercial and commercial deployments will take place in near future. A number of technological breakthroughs need to be achieved toward realizing this goal and turbine control (both supervisory and power tracking) is one of the most critical factors toward its success.

14.1 Research summary

In the absence of sufficient operational experience and publicly available scientific research results, this work has undertaken a set of turbine design, testing, and performance evaluation activities that has exposed a number of subtle, yet critical features of interest. A vertical axis small-scale hydrokinetic turbine has been taken as a HECS of choice. The electromechanical and electrical systems consist of permanent magnet alternator (PMA) and power electronic converters (ac-dc-ac topology), respectively. In addition, dynamic numerical models have been developed for each of these subsystems and validated against experimental data.

The rotor performance model (steady-state performance curve characteristics) has been developed through two-dimensional multiple streamtube analysis. Various elements

of resource field have been identified and a generic simulation model has been developed to represent the stochastic tidal/river flow conditions. The large-signal nonlinear full-order HECS model has been used toward evaluating various candidate power tracking control techniques (tip speed ratio, power signal feedback, and hill-climbing control). Pursuant discussions highlighted the need for an advanced algorithm that can adapt to internal/external parametric variations, operate with unknown set-points, and require no underwater instrumentation.

Considering the challenges of power tracking control, as appropriate for the diverse types of hydrokinetic systems, the extremum seeking control (ESC) method has been identified as the most suitable solution. However, it was identified that a large set of ESC parameters need to be tuned and there exists no systematic methods to address this problem. This research conducts a thorough evaluation of ESC method, identifies its applicability in HECS, and develops a method of ESC parameter tuning. Successful implementation of the ESC method has been demonstrated through simulation environment and further research needs to be conducted toward implementing this method in real-world scenarios.

14.2 Contributions

Throughout this research, a significant amount of effort has been given toward understanding the true requirements and challenges associated with maximum power tracking of hydrokinetic systems. In addition, due attention has been paid in addressing these challenges. The tangible outcomes of this research are

- Identification of the current state of the art and determination of the unique needs within power tracking control of hydrokinetic systems.
- Development of numerical models incorporating generic flow-field variations, rotor performance characteristics, and grid-tied turbine system.

- Evaluation of multiple candidate power tracking control methods and identification of subsequent control needs.
- Development of a systematic parameter tuning method for application of extremum seeking control technique in hydrokinetic systems.

Many of these contributions have been published through peer-reviewed journals and conference proceedings. Given the nascent nature of this field of engineering, this publications and contributions need to be treated in the appropriate context.

14.3 Further work

This research is as an open-ended initiative where further design and development activities are indispensable, especially toward validating the ESC control methodology being considered. Also, considering the current state of the overall hydrokinetic energy industry and absence of relevant knowledge-base, this work can be treated as an embryonic initiative.

Any future work along this topic needs to be directly linked to real-world trials. This is particularly important given that fundamental understanding of a hydrokinetic system's interaction with flow conditions, placement arrangements, and various other uncertainties (such as, rotor performance degradation, bio-fouling, and multi-body interactions) need to be developed. Also, device sizes (physical dimensions as well as power ratings) need to be large enough such that subsequent performance data and controller performance can be faithfully scaled to commercial/pre-commercial systems. Considerations for economic aspects, environmental impacts, and sustainability factors need also be given due importance from a global system-engineering perspective.

As a leverage to this research a number of test and development activities are currently being explored, which will see a mix of laboratory, open-channel and open-sea trials. In addition to advancement of the theories of extremum seeking control, various

applied methods of parameter tuning and implementation need to be achieved. Contemporary industrial initiatives that may complement the understanding of hydrokinetic system's performance, controller requirements, and may develop relevant solutions include:

- Continuation of laboratory scale tests using MUN laboratory test rig [174].
- Turbine performance evaluation through open sea trials of a 100 kW horizontal axis turbine [236].
- Turbine control and performance assessment through testing of a set of two 250 kW vertical axis turbines [237].

With increasing interest in the hydrokinetic energy technologies significant research and development efforts are currently being made throughout the world. It is expected that this research will aid this process, and in particular, instigate relevant discussions in the fields of power tracking controller development.

References

- [1] U.S. Department of Energy. (2009, Apr.) Marine and Hydrokinetic Technology Database. [Online]. Available: <http://www1.eere.energy.gov/windandhydro/hydrokinetic/default.aspx>
- [2] M.J. Khan, G. Bhuyan, M.T. Iqbal, J.E. Quaicoe, "Hydrokinetic energy conversion systems and assessment of horizontal and vertical axis turbines for river and tidal applications: A technology status review," *Applied Energy*, vol. 86, no. 10, pp. 1823-1835, 2009.
- [3] Calcagno, G., Salvatore, F., Greco, L., Moroso, A., Eriksson, H., "Experimental and Numerical investigation of an Innovative Technology for Marine Current Exploitation: the Kobold Turbine," in *International Offshore and Polar Engineering Conference*, 2006, pp. 323-330.
- [4] V.R. Klapcoz, G.W. Rawlings, Y. Nabavi, M. Alidsi, Y. Li, and S.M. Calisal, "Numerical and Experimental Investigation of a Ducted Vertical Axis Tidal Current Turbine," in *EWTEC 2007*, Porto, Portugal.
- [5] K. Nilsson, M. Grabbe, K. Yuen and M. Leijon, "A direct drive generator for marine current energy conversion - first experimental results," in *EWTEC 2007*, Porto, Portugal.
- [6] Mitsuhiro Shiono, Katsuyuki Suzuki, and Seiji Kiho, "An Experimental Study of the Characteristics of a Darrieus Turbine for Tidal Power Generation," *Electrical Engineering in Japan*, vol. 132, no. 3, pp. 38-47, 2000.
- [7] Alidadi M., Calisal S., "Effects of towing tank walls on the performance of a Vertical Axis Turbine," in *Oceans 2007*, Sept. 2007.
- [8] J. Khan, M.T. Iqbal, and J.E. Quaicoe, "Tow Tank Testing and Performance Evaluation of a Permanent Magnet Generator Based Small Vertical Axis Hydrokinetic Turbine," *Journal of Ocean Technology*, vol. 4, no. 1, pp. 66-82, 2009.
- [9] H Eriksson, A Moroso, Prof A Fiorentino, "The vertical axis Kobold turbine in the Strait of Messina - a case study of a full scale marine current prototype," in *World Maritime Technology Conference, London*, March 2006.
- [10] International Energy Agency: Ocean Energy Systems Implementing Agreement. (2007-08, Jan.) Annual Report. [Online]. Available: http://www.iea-oceans.org/_fich/6/IEA-OES_Annual_Report_2007.pdf
- [11] Energy Water: Hydrokinetic Fronts. (2008, Oct.). [Online]. Available: <http://www.energywatertm.com/en/about/index.html>

- [12] Ben Elghali, S.E.; Benbouzid, M.E.H.; Charpentier, J.F., "Marine Tidal Current Electric Power Generation Technology: State of the Art and Current Status," in *IEEE Electric Machines & Drives Conference, Turkey, Vol. 2, pp 1407-1412, May 2007.*
- [13] Hammons, T.J., "Tidal power," *Proceedings of the IEEE*, vol. 81 (3), pp. 419 - 433, Mar. 1993.
- [14] Roger Bedard, "Survey and Characterization: Tidal In Stream Energy Conversion Devices (TISEC)," Electric Power Research Institute (EPRI), Tech. Rep. EPRI TP 004 NA, Nov. 2005.
- [15] Triton Consultants Ltd., "Green Energy Study for British Columbia: Phase 2; Mainland Tidal Current Energy," Prepared for BC Hydro, Tech. Rep., Oct. 2002.
- [16] Canadian Hydraulics Centre, National Research Council Canada. (2008, Oct) Inventory of Canadas Marine Renewable Energy Resources; Tech. Report: CHC-TR-041. [Online]. Available: <http://www.oreg.ca/docs/Atlas/>
- [17] Ocean Renewable Energy Group, Bay of Fundy tidal-power turbines clear first hurdle. (2008, June). [Online]. Available: <http://www.oreg.ca/bi-weekly.html?subaction=showfull&id=1212619925&arch%ive=&start.from=&ucat=1&>
- [18] Puget Sound Tidal Energy Web Site, Proposed Tidal Energy Projects Located in Puget Sound. (2008, Oct.). [Online]. Available: <http://www.ptidalenergy.org/projects.htm>
- [19] Idaho National Laboratory, "Feasibility Assessment of the Water Energy Resources of the United States for New Low Power and Small Hydro Classes of Hydroelectric Plants," U.S. Department of Energy, Tech. Rep. DOE-ID-11263, Jan. 2006.
- [20] D. Dixon, "Assessment of Waterpower Potential and Development Needs," Electric Power Research Institute (EPRI), Tech. Rep. 1014762, March 2007.
- [21] US DoE, Hydropower: Hydrokinetic & Wave Technologies Workshop, 26-28 October 2005, Washington, DC. [Online]. Available: http://hydropower.id.doe.gov/hydrokinetic_wave/
- [22] Linda Church Ciocci, John Suloway, Stephen R. Brown, "Hydropower Research and Development Recommendations," *J. ENERGY ENGINEERING, ASCE*, vol. 129, no. 2, pp. 33-41, 2003.
- [23] FERC. (2008, Oct.) FERC News Release. [Online]. Available: <http://www.ferc.gov/industries/hydropower/indus-act/hydrokinetics.asp#s%kipnavsub>
- [24] Stoel Rives LLP. (2008, Oct) Ocean Law Alert: Congress Provides Boost to Emerging Marine and Hydrokinetic Renewable Energy Technologies. [Online]. Available: <http://www.stoel.com/showalert.aspx?Show=2809>
- [25] Hydro Green Energy, LLC . News Release : First-Ever Water Energy Projects In Mississippi Given Initial Approval, June 11, 2007. [Online]. Available: <http://www.hgenergy.com/FERC%20Approves%20MS2.pdf>

- [26] Electric Energy Online; September/October, 2007. "Alaska Power & Telephone: Energy Looking Forward". [Online]. Available:
URL:<http://electricenergyonline.com/article.asp?m=5&mag=45&article=339>
- [27] Detroit River Hydrokinetic Energy Project;. (2008, Oct.). [Online]. Available:
http://www.portdetroit.com/econdev/grantsmgmt/grantsmgmt_dte.htm
- [28] Verdant Power Canada ULC., "Technology Evaluation of Existing and Emerging Technologies-
Water Current Turbines for River Applications," Natural Resources Canada, Tech. Rep.
NRCan-06-01071, Jun.2006.
- [29] M.J.Khan, G. Bhuyan, A. Moshref, K. Morison, "An Assessment of Variable Characteristics of
the Pacific Northwest Regions Wave and Tidal Current Power Resources, and their Interaction
with Electricity Demand & Implications for Large Scale Development Scenarios for the Region,"
Powertech Labs Inc., Tech. Rep. 17485-21-00 (Rep 3), Jan. 2008. [Online]. Available:
<http://www.powertechlabs.com/cfm/index.cfm?It=106&Id=58>
- [30] M.J. Khan, M.T. Iqbal, J.E. Quicoe, "River current energy conversion systems: Progress,
prospects and challenges," *Renewable and Sustainable Energy Reviews*, vol. 12, no. 8, pp.
2013-2264, 2008.
- [31] Verdant Power, LLC, 4640 13th Street, North, Arlington, VA 22207, USA. (2008, Oct.). [Online].
Available: <http://www.verdantpower.com/category/newsroom/>
- [32] Atlantistrom. (2008, Oct.). [Online]. Available: <http://www.atlantistrom.de/description.html>
- [33] HydroVenturi Ltd. (2008, Oct.) HydroVenturi. [Online]. Available:
<http://www.hydroventuri.com/news.php>
- [34] Neo-Aerodynamic Ltd Company; TX, USA., (2008, Oct.). [Online]. Available:
<http://www.neo-aerodynamic.com/>
- [35] Arnold Energy System. (2008, Oct.). [Online]. Available:
<http://www.arnoldenergysystems.com/>
- [36] George W. Taylor, Joseph R. Burns, Sean M. Kammann, William B. Powers, and Thomas R.
Welsh, "The Energy Harvesting Eel: A Small Subsurface Ocean/River Power Generator," *IEEE
Journal of Oceanic Engineering*, vol. 26, no. 4, pp. 539 - 547, 2001.
- [37] Vortex Hydro Energy, Ann Arbor, MI (2008, Oct.). [Online]. Available:
<http://www.vortexhydroenergy.com/html/about.html>
- [38] Seasnail. (2008, Oct.). [Online]. Available:
<http://www.rgu.ac.uk/cree/general/page.cfm?page=10769>

- [39] BioPower Systems Pty. Ltd. (2008, Oct.) BioPower Systems - Biologically Inspired Ocean Power Systems. [Online]. Available: <http://www.biopowersystems.com/>
- [40] Tidal Sails AS. (2008, Oct.). [Online]. Available: <https://www.fondsinans.no/ff/public/SOL/TidalSails.pdf>
- [41] P. Garman, *Water Current Turbines: A Fieldworker's Guide*. Intermediate Technology Publishing, UK, 1986, ISBN: 0946688273.
- [42] R. L. Radkey and B. D. Hibbs, "Definition of Cost Effective River Turbine Designs," Report for U.S. Department of Energy, Aerovironment Inc., Pasadena, California, Tech. Rep. AV-FR-81/595 (DES2010972), Dec. 1981.
- [43] Geraldo L. and Tiago Fo, "The state of art of Hydrokinetic power in Brazil," International Small Hydro Technologies, Buffalo, NY, USA, July 2003, pre-conference Workshop.
- [44] A. M. Gorlov, "Harnessing Power From Ocean Currents And Tides," *Sea Technology*, vol. 45, no. 7, pp. 40-43, 2004.
- [45] New Energy Corporation Inc. (NECI), Suite 473, 3553 31 st Street NW, Calgary, Alberta, T2L 2K7. (2008, Oct.). [Online]. Available: <http://www.newenergycorp.ca>
- [46] Khan, J.; Bhayan, G.; Moshref, A.; Morison, K.; Pease, J.H.; Gurney, J., "Ocean wave and tidal current conversion technologies and their interaction with electrical networks," in *IEEE PES General Meeting, Pittsburgh, PA*, July 2008.
- [47] Jaro J. Vocadlo, Brian Richards, Michael King, "Hydraulic Kinetic Energy Conversion (HKEC) Systems," *J. Energy Engrg.*, vol. 116, no. 1, pp. 17-38, 1990.
- [48] Alternating Current Peru. (2008, Oct.). [Online]. Available: <http://www.ave.org/bo/doc.cfm?aid=656&lang=English>
- [49] Marlec Engineering Co Ltd., Rutland House, Trevithick Rd, Corby Northants, NN17 5XY. (2008, Oct.). [Online]. Available: <http://www.marlec.co.uk/>
- [50] CADDET Centre for Renewable Energy, ETSU, Harwell, Oxfordshire OX11 0RA, UK. (2008, Oct.). [Online]. Available: <http://www.caddet-re.org>
- [51] Thropton Energy Services, Physic Lane, Thropton, Northumberland NE65 7HU, United Kingdom. (2008, Oct.). [Online]. Available: <http://ourworld.compuserve.com/homepages/throptonenergy/homepage.htm>
- [52] David Alnsworth, Jeremy Thake, [Marine Current Turbines Ltd, for DTI (UK)], "Final Report on Preliminary Works Associated with 1MW Tidal Turbine Project," U.S. Department of Energy, Tech. Rep. T/06/00233/00/00, URN 06/2046, Aug. 2006. [Online]. Available: www.berr.gov.uk/files/file35033.pdf

- [53] Hydro Tasmania (Govt. of Australia). (2008, Oct.) Study of tidal energy technologies for derby; report no: Wa 107384 - cr-01. [Online]. Available: www.sedo.energy.wa.gov.au
- [54] The Engineering Business Limited, Broomhaugh House, Riding Mill, Northumberland, NE44 6EG, UK. (2008, Oct.). [Online]. Available: http://www.engb.com/services_09a.php
- [55] N. H. Al-Mamun, "Utilization of River Current for Small Scale Electricity Generation in Bangladesh," Master's thesis, Department of Mechanical Engineering, BUET, Dhaka, July 2001.
- [56] A.K.M. Sadrul Islam, N. H. Al-Mamun, M. Q. Islam, and D. G. Infield, "Energy from River Current for Small Scale Electricity Generation in Bangladesh," in *Proc. Renewable Energy in Maritime Island Climates*. Solar Energy Society, UK, Sep. 2001.
- [57] P. Garman, "Water Current Turbines: Providing Pumping, Power in Remote Areas," *Hydro Review Worldwide*, vol. 6, no. 5, pp. 24-28, 1998.
- [58] UEK Corporation, Abacus Controls, P.O. Box 3124, Annapolis, MD, 21403, USA. (2008, Oct.). [Online]. Available: <http://uekus.com/index.html>
- [59] Chris Lang, "Harnessing Tidal Energy Takes New Turn: Could the application of the windmill principle produce a sea change?" *IEEE Spectrum*, Sep, 2003.
- [60] Marine Current Turbines Ltd, The Court, The Green Stoke Gifford, Bristol, BS34 8PD, UK. (2008, Oct.). [Online]. Available: <http://www.marineturbines.com/>
- [61] Hammerfest STRM AS, Norway. (2008, Oct.). [Online]. Available: <http://www.hammerfeststrom.com/>
- [62] Tuckey, A.M., Patterson, D.J., and Swenson, J., "A kinetic energy tidal generator in the Northern Territory-results," in *Proc. IECON*, vol. 2. IEEE, Nov. 1997, pp. 937-942.
- [63] SMD Hydrovision, Wincomblee Road, Newcastle upon Tyne NE6 3QS, UK. (2008, Oct.). [Online]. Available: <http://www.smd.co.uk/>
- [64] J A Consult, 76 Dukes Avenue, London W4 2AF, UK. (2008, Oct.). [Online]. Available: <http://www.jaconsulting.co.uk>
- [65] Levy D., "Power from natural flow at zero static head," *International Power Generation*, 1995.
- [66] Rutten L., "Au fil de l'eau, une roue a aubes," *Systemes Solaires*, vol. 100, pp. 103-105, 1994.
- [67] Brian Kirke. (2008, Oct.) Developments in ducted water current turbines. Tidal paper 16-08-03 1. [Online]. Available: <http://www.cyberiad.net/tide.htm>
- [68] S. Kiho, M. Shiono, and K. Suzuki, "The Power Generation from Tidal Currents by Darrieus Turbines," in *Proc. World Renewable Energy Congress*, vol. 2, no. ., Denver, Colorado, USA, 1996, pp. 1242-1245.

- [69] Seiji Kihou and Mitsuhiro Shiono, "Electric Power Generations from Tidal currents by Darrieus Turbine at Kurushima Straits," *Transactions of IEE Japan*, vol. 112-D, no. 6, pp. 530-538, 1992.
- [70] S. Kihou, K. Suzuki, and M. Shiono, "Study on the power generation from tidal currents by Darrieus turbine," in *Proc. International Offshore and Polar Engineering Conference*, vol. 1, 1996, pp. 97-102.
- [71] Mitsuhiro Shiono, Katsuyuki Suzuki, and Seiji Kihou, "Output Characteristics of Darrieus Water Turbine with Helical Blades for Tidal Current Generations," in *Proc. International Offshore and Polar Engineering Conference*, vol. 12, 2002, pp. 859-864.
- [72] Blue Energy Canada Inc., Box 29068, 1950 West Broadway, Vancouver, BC, V6J 1Z0. (2008, Oct.). [Online]. Available: <http://www.blueenergy.com/index.html>
- [73] B. Davis, "Low head tidal power: a major source of energy from the worlds oceans," in *Proc. 32nd Intersociety Energy Conversion Engineering Conference, IECEC-97*, vol. 3, Aug. 1997, pp. 1982-1989.
- [74] B. V. Davis, "Water Turbine Model Trials to Demonstrate the Feasibility of Extracting Kinetic Energy from River and Tidal Currents," Nova Energy Limited Report for National Research Council of Canada, Tech. Rep. NEL-002, 1980.
- [75] Alexander N. Gorban, Alexander M. Gorlov and Valentin M. Silantyev, "Limits of the Turbine Efficiency for Free Fluid Flow," *Journal of Energy Resources Technology, ASME*, vol. 123, pp. 311-317, Dec. 2001.
- [76] G. G. Portnov and I. Z. Palley, "Application of the Theory of Naturally Curved and Twisted Bars to Designing Gorlov's Helical Turbine," *Mechanics of Composite Materials*, vol. 34, no. 4, pp. 343-354, 1998.
- [77] I. Paraschivou, *Wind Turbine Design: with Emphasis on Darrieus Concept*. Canada: Polytechnic International Press, 2002, ISBN 2-553-00931-3.
- [78] F. Ponta and G. Shankar Dutt, "An improved vertical-axis water-current turbine incorporating a channelling device," *Renewable Energy*, vol. 20, no. 2, pp. 223-242, 2000, ISSN 0960-1481.
- [79] F.L. Ponta, P.M. Jacovkis, "Marine-current power generation by diffuser-augmented floating hydro-turbines," *Renewable Energy*, vol. 33, no. 4, pp. 665-673, 2008.
- [80] Toshiaki Setoguchi, Norimasa Shiomi, Kenji Kaneko, "Development of two-way diffuser for fluid energy conversion system," *Renewable Energy*, vol. 29, pp. 1757-1771, 2004.
- [81] Ohya Y, Karasudani T, Sakurai A, Inoue M, "Development of high-performance wind turbine system by wind-lens effect (locally concentrated wind energy)," in *25th Symposium for Techniques utilizing Wind Energy*. JSFM [in Japanese], 2001, pp. 76-79.

- [82] David Gaden, Eric Bibeau, "Increasing the Power Density of Kinetic Turbines for Cost-Effective Distributed Power Generation," in *Power-gen, April 10-12, 2006*, Mandalay Bay, Las Vegas, NV.
- [83] D G Phillips, R G J Flay, T A Nash, "Aerodynamic analysis and monitoring of the Vortec 7 diffuse-augmented wind turbine," *IPENZ Transactions*, vol. 26, no. 1/EMCh, pp. 13-19, 1999.
- [84] Hannes Riegler, "HAWT versus VAWT," *REFOCUS*, 2003.
- [85] Sander Mertens, Gijs van Kuik, and Gerard van Bussel, "Performance of an H-Darrieus wind turbine in the skewed flow on a roof," *Journal of Solar Energy Engineering, ASME*, vol. 125, pp. 433-440, Nov. 2003.
- [86] Vincent Ginter, "Robust gain scheduled control of a hydrokinetic turbine," Master's thesis, Department of Mechanical and Manufacturing Engineering, University of Calgary, Calgary, Alberta, 2009.
- [87] Clayton Bear. (2008, Nov.) Transition to a Device Supplier, OREG Fall Symposium, Whistler, BC. [Online]. Available: http://www.oreg.ca/docs/2008_Fall_Symposium/Bear.pdf
- [88] S.E. Ben Elghali, Benbouzid Mohammed, J.F. Charpentier, "Modeling And Control of a Marine Current Turbine using a Doubly-Fed Induction Generator," in *2nd International Conference on Ocean Energy (ICOE), Brest, France, Oct. 2008*.
- [89] G. Mattarolo, J. Bard, P. Caselitz, J. Giebardt, "Control and Operation of Variable Speed Marine Current Turbines: Results from a Project funded by the German Ministry for the Environment," in *Oxemes, Citavecchia, Italy, April 2006*.
- [90] Marine Current Turbines Ltd. (2008, Nov.) SenGen Enters Final Stage of Commissioning, Press Release: (2008, 17 Nov.). [Online]. Available: <http://www.marineturbines.com/3/news/>
- [91] Ye Li, "Development of a procedure for predicting power generated from a tidal current turbine farm," Ph.D. dissertation, The University of British Columbia, BC, Canada, Oct. 2008.
- [92] C. J. Lawn, "Optimization of the power output from ducted turbines," *Journal Proceedings of the Institution of Mechanical Engineers, Part A: Journal of Power and Energy*, vol. 217, no. 1, pp. 107-117, 2003.
- [93] A.S. Bajah, W.M.J. Batten, G. McCann, "Experimental verifications of numerical predictions for the hydrodynamic performance of horizontal axis marine current turbines," *Renewable Energy*, no. 32, p. 24792490, 2007.
- [94] Alessandro Schönborn, Matthew Chantzidakis, "Development of a Hydraulic Control Mechanism for a Cyclic Pitch Marine Current Turbine," *Renewable Energy*, vol. (In Press), 2006.
- [95] Qinetiq Ltd., "Cycloidal Tidal Power Generation - Phase 1," Report for DTI Technology Program, Qinetiq Ltd., UK, Tech. Rep. T/06/00229/REP/1, 2004.

- [96] Sergio M. Camporeale and Vinicio Magi, "Streamtube Model for Analysis of Vertical Axis Variable Pitch Turbine for Marine Currents Energy Conversion," *Energy Conversion & Management*, vol. 41, pp. 1811-1827, 2000.
- [97] Morimoto, S.; Nakayama, H.; Sanada, M.; Takeda, Y., "Sensorless output maximization control for variable-speed wind generation system using IPMSG," *IEEE Trans. on Ind. Appl.*, vol. 41, no. 1, pp. 60 - 67, Jan.-Feb. 2005.
- [98] K. Tan, S. Islam, "Optimum control strategies in energy conversion of pmag wind turbine system without mechanical sensor," *IEEE Trans. on Energy Conv.*, vol. 19, no. 2, June 2004.
- [99] Senjyu, T.; Tamaki, S.; Urasaki, N.; Uezato, K.; Higa, H.; Funabashi, T.; Fujita, H.; Sekine, H., "Wind velocity and rotor position sensorless maximum power point tracking control for wind generation system," in *PESC 04*, vol. 3, 20-25 June 2004, pp. 2023 - 2028.
- [100] Wei Li; Abbey, C.; Joos, G., "Control and performance of wind turbine generators based on permanent magnet synchronous machines feeding a diode rectifier," in *PESC 06*, 18-22 June 2006, pp. 1 - 6.
- [101] T. Tatficht, K. Agboussou, A. Cheriti, M. L. Doumbia, "Output power maximization of a permanent magnet synchronous generator based stand-alone wind turbine," in *ISIE-2006*, Jul. 2006, pp. 2412-2416.
- [102] Iulian Munteanu, Antoneta Iuliana Bratu, Nicolae-Antonio Cutululis, Emil Ceanga, *Optimal Control of Wind Energy Systems: Towards a Global Approach*. Springer, Mar 31 2008, ISBN-10: 1848000790.
- [103] Quincy Wang; Liuchen Chang, "An intelligent maximum power extraction algorithm for inverter-based variable speed wind turbine systems," *IEEE Trans. Power Elect.*, vol. 19, no. 5, pp. 1242 - 1249, Sept. 2004.
- [104] Higuchi, Y.; Yamamura, N.; Ishida, M.; Hori, T., "An improvement of performance for small-scaled wind power generating system with permanent magnet type synchronous generator," in *IECON 2000*, vol. 2, 22-28 Oct, pp. 1037 - 1043.
- [105] Tsoumas, I.; Safacas, A.; Tsimploteftanakis, E.; Tatakis, E., "An optimal control strategy of a variable speed wind energy conversion system," in *ICEMS 2003*, vol. 1, 9-11 Nov. 2003 2003., pp. 274 - 277.
- [106] Farret, F.A.; Pfitscher, L.L.; Bernardon, D.P., "An heuristic algorithm for sensorless power maximization applied to small asynchronous wind turbogeneratoes," in *ISIE 2000*, vol. 1, 4-8 Dec 2000, pp. 179 - 184.
- [107] Moor, G.D.; Beukes, H.J., "Maximum power point trackers for wind turbines," in *PESC 04*, vol. 3, 20-25 June 2004, pp. 2044 - 2049.

- [108] Wang, Q.; Chang, L., "An independent maximum power extraction strategy for wind energy conversion systems," in *CCECE-1999*, vol. 2, 9-12 May, pp. 1142 – 1147.
- [109] Mutoh, N.; Nagasawa, A., "A maximum power point tracking control method suitable for compact wind power generators," in *PESC '06*, 18-22 June, pp. 1 – 7.
- [110] Xin Ma, "Adaptive extremum control and wind turbine control," PhD Thesis, Technical University of Denmark, May 1997.
- [111] Datta, R.; Ranganathan, V.T., "A method of tracking the peak power points for a variable speed wind energy conversion system," *IEEE Trans. on Energy Conv.*, vol. 18, no. 1, pp. 163 – 168, March 2003.
- [112] Koutroulis, E.; Kalaitzakis, K., "Design of a maximum power tracking system for wind-energy-conversion applications," *IEEE Trans. on Ind. Elect.*, vol. 53, no. 2, pp. 486 – 494, April 2006.
- [113] M. Simoes, B. Bose, and R. Spiegel, "Fuzzy logic based intelligent control of a variable speed cage machine wind generation system," *IEEE Trans. Power Elect.*, vol. 12, no. 1, p. 8795, 1997.
- [114] Abo-Khalil, A.G.; Dong-Choon Lee; Jul-Ki Seok; "Variable speed wind power generation system based on fuzzy logic control for maximum output power tracking," in *PESC 04*, vol. 3, 20-25 June 2004, pp. 2039 – 2043.
- [115] Chen, Z.; Gomez, S.A.; McCormick, M., "A fuzzy logic controlled power electronic system for variable speed wind energy conversion systems," in *Eighth Int. Conf. on Power Elect. & Variable Speed Drives, 2000.*, 18-19 Sept. 2000, pp. 114 – 119.
- [116] Jia Yaoqin; Yang Zhongqing; Cao Binggang, "A new maximum power point tracking control scheme for wind generation," in *PowerCon 2002*, vol. 1, 13-17 Oct. 2002, pp. 144 – 148.
- [117] Tanaka T.; Toumiya T.; Suzuki T., "Output control by hill-climbing method for a small scale wind power generating system," *Renewable Energy*, vol. 12, no. 4, pp. 387–400, Dec. 1997.
- [118] Endusa Billy Mubandos, Tomonobu Senjyu, Naomitsu Urasakia, Atsushi Yonaa, Hiroshi Kinjob and Toshihisa Funabashic, "Gain scheduling control of variable speed WTG under widely varying turbulence loading," *Renewable Energy*, vol. 32, no. 14, pp. 2407–2423, 2007.
- [119] T. Ngo-Duc, T. Oki, and S. Kanse, "A variable streamflow velocity method for global river routing model: model description and preliminary results," *Hydrol. Earth Syst. Sci. Discuss.*, no. 4, p. 43894414, 2007. [Online]. Available: www.hydrol-earth-syst-sci-discuss.net/4/4389/2007/
- [120] J. E. Costa, R. T. Cheng, F. P. Haeni, N. Melcher, K. R. Spicer, E. Hayes, W. Plant, K. Hayes, C. Teague, and D. Barrick, "Use of radars to monitor stream discharge by noncontact methods," *WATER RESOURCES RESEARCH*, vol. W07422, no. doi:10.1029/2005WR004430, 2006.

- [121] Lee Gordon, Sven Nylund, "EZQ Stage and Velocity Sensor: Test Results from The White River1," Tech. Rep., June 1999. [Online]. Available: <http://currentmeter.com/PDF/EZQ-Report.pdf>
- [122] WWW Tide and Current Predictor. (2009, March.) WWW Tide and Current Predictor. [Online]. Available: <http://tbone.biol.sc.edu/tide/index.html>
- [123] Aquadopp Current Profiler. (2009, March.) Aquadopp Current Profiler. [Online]. Available: <http://www.alec-electronics.co.jp/html/aquapro.htm>
- [124] Christopher J. Zappa, Peter A. Raymond, Eugene A. Terray, And Wade R. Megillis , "Variation in Surface Turbulence and the Gas Transfer Velocity over a Tidal Cycle in a Macro-tidal Estuary," *Estuaries*, vol. 26, no. 6, p. 14011415, 2003.
- [125] Ven Te Chow, *Open-channel hydraulics*. McGraw-Hill, 1959.
- [126] Hideo Nakajima, Norio Hayakawa, "A Cross-Correlation Analysis of Tidal Current, Water Temperature, and Salinity Records," *Journal of the Oceanographical Society of Japan*, vol. 38, pp. 52-56, 1982.
- [127] Dr. Russell L. Herman, Harmonic Analysis and the Prediction of Tides. [Online]. Available: {<http://www.russherman.com/Talks/Tidal%20Analysis.ppt>}
- [128] K. Gi. I. Marchuk, B. A., *Dynamics of Ocean Tides*. Kluwer Academic Publishers, 1989, ISBN 90-277-2552-7.
- [129] M. Muste , K. Yu , T. Pratt , D. Abraham, "Practical aspects of ADCP data use for quantification of mean river flow characteristics; Part II: fixed-vessel measurements," *Flow Measurement and Instrumentation*, no. 15, pp. 17-28, 2004.
- [130] K. Kawanisi and S. Yokosi, "Mean and Turbulence Characteristics in a Tidal River," *Estuarine, Coastal and Shelf Science*, vol. 38, pp. 447-469, 1994.
- [131] oris ShteinmanIand Yury Kamenir, "Energetics of Turbulent Jet Flow (An Example of Jordan River Mouth)," in *Fourth International Conference on Hydro-Science and -Engineering (ICHE2000)*, Seoul, Korea, Sept. 2000.
- [132] G. N. McCann, "Tidal current turbine fatigue loading sensitivity to waves and turbulence a parametric study," in *7th European Wave and Tidal Energy Conference, Porto, Portugal*, Sept. 2007.
- [133] University of Washington, Lecture notes, School of Oceanography, University of Washington. [Online]. Available: {<http://www.ocean.washington.edu/people/faculty/parsons/OCEAN549B/lwt-!%ect.pdf>}

- [134] US Military. (2009, March) Pierson - Moskowitz Sea Spectrum. [Online]. Available: http://www.eustis.army.mil/WEATHER/Weather_Products/sosstate.htm
- [135] J. S. Carlton, *Marine propellers and propulsion*. Oxford, Toronto: Butterworth-Heinemann Ltd., 1994, ISBN 0750601143 X.
- [136] USGS. (2009, March) Temperature, Salinity and Density, Woods Hole Science Center,. [Online]. Available: <http://woodshole.er.usgs.gov/operations/modeling/mbayopen/node23.html>
- [137] Stephen M. Wiestenbroek, "Estimates of Shear Stress and Measurements of Water Levels in the Lower Fox River near Green Bay, Wisconsin," U.S. Geological Survey, Reston, Virginia, Tech. Rep. Scientific Investigations Report 20065226, 2006.
- [138] Mahmoud F. Maghrebi, "Application of the single point measurement in discharge estimation," *Advances in Water Resources*, vol. 29, p. 15041514, 2006.
- [139] Sander Mertens, Gijs van Kuik, Gerard van Bussel, "Performance of an H-Darrieus in the Skewed Flow on a Roof," *Journal of Solar Energy Engineering, ASME*, vol. 125, 2003.
- [140] J. Whelan, M. Thomson, J. M. R. Graham and J. Peir , "Modelling of free surface proximity and wave induced velocities around a horizontal axis tidal stream turbine," in *7th European Wave and Tidal Energy Conference, Porto, Portugal, Sept. 2007*.
- [141] M.J. Khan, M.T. Iqbal, J.E. Quisicoe, "Tow Tank Testing and Performance Evaluation of a Permanent Magnet Generator Based Small Vertical Axis Hydrokinetic Turbine," in *North American Power Symposium (NAPS), Calgary, Canada, Sept. 2008*.
- [142] Cristian Nichita, Dragos Luca, Brayima Dakyo, And Emil Ceanga, "Cristian Nichita, Dragos Luca, Brayima Dakyo, And Emil Ceanga," *IEEE Transactions on Energy Conversion*, vol. 17, no. 4, 2002.
- [143] E. Lalander, M. Leijon, "Numerical modeling of a river site for in-stream energy converters," in *8th European Wave and Tidal Energy Conference, Uppsala, Sweden, 2009*.
- [144] (2005, Sept.) Darrieus wind turbine analysis. [Online]. Available: <http://windturbine-analysis.com/index.htm>
- [145] Ira H. Abbott and Albert E. von Doenhoff, *Theory of wing sections, including a summary of airfoil data*. New York: Dover Publications, 1959, ISBN: 4860605868 .
- [146] Harri Vihriala, "Control of variable speed wind turbines," PhD thesis, Tampere University of Technology, Tampere, Finland, Oct 2002.
- [147] Gregory F. Homicz, "Numerical Simulation of VAWT Stochastic Aerodynamic Loads Produced by Atmospheric Turbulence: VAWT-SAL Code," SANDIA LAB REPORT, Tech. Rep. SAND911124 I UC261.

- [148] M. Claessens, "The Design and Testing of Airfoils for Application in Small Vertical Axis Wind Turbines," Master's thesis, Faculty of Aerospace Engineering, Delft University of Technology, Netherlands, Nov. 2006.
- [149] Wieslaw Zenon Stepniewski, C. N. Keys, *Rotary-wing aerodynamics*. Dover Books on Engineering, 1984.
- [150] Neil Bose, "Rotary foil propellers," *Papers of the Ship Research Institute, Tokyo, Japan*, vol. 24, no. 5, pp. 45-67, 1987.
- [151] Tempelin, R., "Aerodynamic performance theory for the NRC vertical axis wind turbine," National Research Council (NRC), Canada, Tech. Rep. LTR-LA-160, 1974.
- [152] Strickland, J. H., "The Darrieus turbine: a performance prediction model using multiple streamtubes," Sandia National Laboratory Report, Albuquerque, NM, USA, Tech. Rep. SAND74-0431 UC-261, 1976.
- [153] Marshall L. Buhl, Jr., "A New Empirical Relationship between Thrust Coefficient and Induction Factor for the Turbulent Windmill State," National Renewable Energy Laboratory, Golden, Colorado, USA, Tech. Rep. NREL/TP-500-36834, 2005.
- [154] Glauert, H., "The Analysis of Experimental Results in the Windmill Brake and Vortex Ring States of an Airscrew," Aeronautical Research Committee Reports and Memoranda, London: Her Majesty's Stationery Office, Tech. Rep. Rept. 1026, 1926.
- [155] J. P. Breslin and P. Andersen, *Hydrodynamics of ship propellers*. New York: Cambridge University Press, 1994, ISBN 0521413605 .
- [156] Matlab-Simulink is a product of The Mathworks Inc, Natick, MA 017-2098, USA. (2009, Mar.). [Online]. Available: <http://www.mathworks.com>
- [157] K. Nilsson, E. Segergren, and M. Leijon, "Simulation of Direct Drive Generators Designed for Underwater Vertical Axis Turbines," in *Proc. Fifth European Wave Energy Conference*, Cork, Ireland, Sep. 2003.
- [158] Robert Harrison, Erich Hau, and Herman Snel, *Large Wind Turbines: Design and Economics*. John Wiley & Sons, Feb. 2001, ISBN: 0471494569.
- [159] Katarina Yuen, Karin Thomas, Mrten Grabbe, Paul Deglaire, Mathias Boasquerel, David sterberg, Mats Leijon, "Matching a Permanent Magnet Synchronous Generator to a Fixed Pitch Vertical Axis Turbine for Marine Current Energy Conversion," *IEEE Journal of Oceanic Engineering*, vol. 34, no. 1, 2009.
- [160] Stader, C.; Keyhani, A.; Sebastian, T.; Murthy, S.K., "Study of cogging torque in permanent magnet machines," in *IAS Annual Meeting, Page(s):42 - 49 vol.1*, Oct. 1997.

- [161] E. Muljadi, J. Green, "Cogging Torque Reduction in a Permanent Magnet Wind Turbine Generator, Tech. Rep. NREL/CP-500-30768, Jan. 2002.
- [162] Ben Elghali, S.E. Balme, R. Le Saux, K. El Hachemi Benbouzid, M. Charpentier, J.F. Hauville, F., "A Simulation Model for the Evaluation of the Electrical Power Potential Harnessed by a Marine Current Turbine," *IEEE Journal of Oceanic Engineering*, no. 32, pp. 786-797, 2007.
- [163] Mullane, A.; Bryans, G.; O'Malley, M., "Kinetic energy and frequency response comparison for renewable generation systems," in *Future Power Systems, 2005 International Conference on*, Nov. 2005.
- [164] David Ainsworth, Jeremy Thake, "Preliminary works associated with 1mw tidal turbine, Tech. Rep. Contract Number: T/06/00233/00/00; URN Number: 06/2046 (DTI, Sea Generation Ltd, Marine Current Turbines Ltd), Jan.
- [165] D. P. Coiro, F. Nicolosi, A. De Marco, S. Melone, F. Montells, "Dynamic behavior of novel vertical axis tidal current turbine: Numerical and experimental investigations," in *International Offshore and Polar Engineering Conference, 2005, 2006*, pp. 469-476.
- [166] C L Bottasso, A Croce, B Savini, "Performance comparison of control schemes for variable-speed wind turbines," *Journal of Physics: Conference Series*, vol. 75, 2007.
- [167] M. J. Khan, M. T. Iqbal, and J. E. Quasicoe, "Design Considerations of a Straight Bladed Darrieus Rotor for River Current Turbines," in *IEEE ISIE*, July 9-13 2006.
- [168] Lopes, L.A.; Lhuillier, J.; Khokar, M.F.; Mukherjee, A., "A Wind Turbine Emulator that Represents the Dynamics of the Wind Turbine Rotor and Drive Train," in *PESC*, Sept. 2005.
- [169] Y. Chen, P. Pillay, and A. Khan, "PM wind generator topologies," *IEEE Trans. on Ind. Appl.*, vol. 41, no. 6, Nov/Dec 2005.
- [170] P. C. Krause, O. Wasynczuk, and S. D. Sudhoff, *Analysis of Electric Machinery*. IEEE Press, 1986, ISBN 0-7803-1101-9.
- [171] B. S. Borowy, Z. M. Salameh, "Dynamic response of a stand-alone wind energy conversion systems with battery energy storage to a wind gust," *IEEE Trans. on Energy Conv.*, vol. 12, no. 1, March 1997.
- [172] J.Y. Chen, C.V. Nayar, D. Baker, "Determination of Parameters and Evaluation of Performance of an Outer-Rotor Permanent Magnet Generator for Wind Energy Applications," in *Power Electronic Drives and Energy Systems for Industrial Growth*, vol. 1, Dec 1998, pp. 353 - 358.
- [173] M. J. Khan, M. T. Iqbal, "Simplified modeling of rectifier-coupled brushless DC generators," in *ICECE*, Dhaka, Bangladesh, Dec. 2006.

- [174] M. J. Khan, M. T. Iqbal, and J. E. Quasico, "Simplified parameter estimation technique of brushless dc generators," in *NECEC 2006*, St. John's, NL, Nov. 2006.
- [175] J. Chen, C. V. Nayar, and L. Xu, "Design and finite-element analysis of an outer-rotor permanent-magnet generator for directly coupled wind turbines," *IEEE Trans. on Magnetics*, vol. 36, no. 5, Sept 2000.
- [176] E. Fitzgerald, Charles Kingsley, Jr., Stephen D. Uman, *Electric Machinery*. McGraw Hill, 2003, ISBN 0-07-366009-4.
- [177] Wikipedia. (2009, Apr.) Moment of inertia. [Online]. Available: http://en.wikipedia.org/wiki/Moment_of_inertia
- [178] Jahangir Khan, Ali Moshref, Gouri Bhuyan, "A Generic Outline for Dynamic Modeling of Ocean Wave and Tidal Current Energy Conversion Systems," in *IEEE PES General Meeting 2009*, Calgary, Alberta, Canada, July 2009.
- [179] Jahangir Khan, Gouri Bhuyan, Kal Abdolali, Ali Moshref, "Evaluation of Electrical Technology Solutions in Marine Energy," Natural Resources Canada (NRCan), Tech. Rep. Prepared by Powertech Labs Inc. (Report No: 18857-21-00 Rep-1), 2009.
- [180] Vicor Power. (2009, Aug.) MegaMod / MegaMod Jr. Chassis-Mount DC-DC Converters; Applications Manual: First Generation Converters and Accessory Modules. [Online]. Available: <http://www.vicr.com/products/configurable/megamod/>
- [181] Artoche, F ; Allongue, B ; Szoncs, F ; Rivetta, C, "EMI Filter Design and Stability Assessment of DC Voltage Distribution based on Switching Converters," in *7th Workshop on Electronics for LHC Experiments, Stockholm, Sweden*, Sept. 2001.
- [182] SWEA. (2009, Aug.) SWEA- Grid Tie Inverter: UWT-I-250 ST-Kit. [Online]. Available: <http://www.swes.nl>
- [183] El-Tamaly, A.M. El-Tamaly, H.H. Cengcelci, E. Enjeti, P.N. Muljadi, E., "Low cost PWM converter for utility interface of variable speed windturbine generators," in *Applied Power Electronics Conference and Exposition, 1999, Dallas, TX, USA*, Mar. 1999.
- [184] Huang, H., Clang, L, "Energy flow principles of IGBT inverters in wind energy conversion system," in *CCECE 2000*, vol. 1, 7-10 March, pp. 545 - 549.
- [185] J. Svensson, "Voltage angle control of a voltage source inverter. application to a grid-connected wind turbine," in *EPE '95*, pp. 539-544.
- [186] Louis A. Bufano, "Gain and Frequency Compensation Optimize Performance of ZCS DC-DC Forward Converter," *PCIM*, June 1998.

- [187] Zun Zun. (2009, Aug.) ZunZun.com Online Curve Fitting and Surface Fitting Web Site. [Online]. Available: <http://zunzun.com/>
- [188] Liang Zhang, Lu-Bing Wang, Feng-Lai Li, and Gui-Xiang Zhang, "Streamtube models for performance prediction of vertical-axis variable-pitch turbine for tidal current energy conversion," *Journal of Harbin Eng. Univ.*, vol. 25, no. 3, pp. 261-266, Jun. 2004.
- [189] Scott Larwood, Jim Senoebaugh, Brian Acker, "Controlled Velocity Testing of an 8-kW Wind Turbine," in *American Wind Energy Association's; WindPower 2001 Conference, Washington, D.C., June 4-7, 2001*, NREL/CP-500-30299.
- [190] Verdant Power LLC, and GCK Technology Inc., "Integration of Gorlov Helical Turbine into an Optimized Hardware/Software System Platform," Amesbury Tidal Energy Project (ATEP), Tech. Rep. ATEP Final Report (Rev 07.26.2005), April 30, 2005.
- [191] M. J. Khan, M. T. Iqbal and J. E. Quince, "Dynamics of a Vertical Axis Hydrokinetic Energy Conversion System with a Rectifier Coupled Multi-pole Permanent Magnet Generator," *IET Journal on Renewable Power Generation (accepted for publication)*, 2010.
- [192] Leithead, W.E., "Dependence of performance of variable speed wind turbines on the turbulence, dynamics and control," *IEE Proceedings-Generation, Transmission and Distribution, IEE Proceedings C*, vol. 137, no. 6, pp. 403 - 413, Nov 1990.
- [193] Leithead, W.E.; de la Salle, S.; Reardon, D., "Role and objectives of control for wind turbines," *IEE Proceedings-Generation, Transmission and Distribution, IEE Proceedings C*, vol. 138, no. 2, pp. 135-148, Mar 1991.
- [194] J. Marques, H. Pinheiro, H.A. Gradling, J.R. Pinheiro and H.L. Hey, "A survey on variable-speed wind turbine system," in *COBEP'03, Cortaleza, Brazil, 2003*, pp. 732-738.
- [195] Miller, A.; Muljadi, E.; Zinger, D.S., "A variable speed wind turbine power control," *IEEE Trans. on Energy Conv.*, vol. 12, no. 2, pp. 181 - 186, June 1997.
- [196] Kathryn E. Johnson, Lee J. Fingersh, Mark J. Balas, Lucy Y. Pao, "Methods for increasing region 2 power capture on a variable speed wind turbine," *Transactions of the ASME*, vol. 126, pp. 1092-1100, Nov. 2004.
- [197] The Carbon Trust. (2005, July) Variability of UK marine resources. [Online]. Available: <http://www.carbontrust.co.uk>
- [198] Peter Fraenkel. (2007, March) Marine Current Turbines: Exploiting Tidal Currents for Large-Scale Power Generation. [Online]. Available: <http://www.ion3.org/events/pdf/Peter%20Fraenkel%20MCT.pdf>

- [199] Hagerman, G., Polsgye, B., Bedard, R., and Previsic, M., "Methodology for Estimating Tidal Current Energy Resources and Power Production by Tidal In-Stream Energy Conversion (TISEC) Devices," Electric Power Research Institute (EPRI), Tech. Rep. EPRI-TP-001-NA Rev 2, June 2006.
- [200] Ponte di Archimede International S.p.A., "The Kobold Turbine (Multimedia Material)," tel: +39 090 37183202; Fax: +39 090 41049; info@pontediarchimede.it.
- [201] Clean Current Power Systems Incorporated; 405 - 750 West Pender Street; Vancouver, British Columbia; Canada V6C 2T7. (2008, Dec.). [Online]. Available: <http://www.cleancurrent.com/>
- [202] Jahangir Khan, Tariq Iqbal, John Quaicoe, "Effects of Nonlinear Efficiency Characteristics on the Power-Tracking Control: A Case Study of Hydrokinetic Energy Conversion System," in *IEEE Energy Conversion Congress and Exposition (ECCE) San Jose, California, USA, 2009*.
- [203] T Esram, PL Chapman, "Comparison of Photovoltaic Array Maximum Power Point Tracking Techniques," *IEEE Transactions on Energy Conversion*, vol. 22, no. 2, 2007.
- [204] Antoneta Iuliana Bratcu, Iulian Munteanu, Seddik Bacha, Bertrand Raison, "Maximum Power Point Tracking of Grid-connected Photovoltaic Arrays by Using Extremum Seeking Control," *Journal of Control Engineering and Applied Informatics*, vol. 10, no. 4, 2008.
- [205] L. Latkovskis, K. Rashevits, L. Rutmanis, J. Stabulnieks, "Maximum Power Transfer in Small Wind Energy Converter with Permanent Magnet Generator for Heating Purposes," in *EPE '99*.
- [206] Abu-qahouq, J.A.; Mao, H.; Al-atrashi, H.J.; Batarseh, I., "Maximum Efficiency Point Tracking (MEPT) Method and Digital Dead Time Control Implementation," *IEEE Transactions on*, vol. 21, no. 5, pp. 1273 - 1281, Sept. 2006.
- [207] Amei, K.; Takayasu, Y.; Ohji, T.; Sakui, M., "A maximum power control of wind generator system using a permanent magnet synchronous generator and a boost chopper circuit," in *PCC Osaka 2002*, vol. 3, pp. 1447 - 1452.
- [208] Grauers, A., "Efficiency of three wind energy generator systems," *IEEE Transaction on Energy Conversion*, vol. 11, no. 3, pp. 650 - 657, Sept. 1996.
- [209] Whaley, D.M.; Soong, W.L.; Ertugrul, N., "Investigation of switched-mode rectifier for control of small-scale wind turbines," in *Fourtieth IAS Annual Meeting*, ser. 2849 - 2856, vol. 4, Oct. 2005.
- [210] Polinder, H.; van der Pijl, F.F.A.; de Vilder, G.-J.; Tavner, P.J., "Comparison of direct-drive and geared generator concepts for wind turbines," *IEEE Transaction on Energy Conversion*, vol. 21, no. 3, pp. 725 - 733, Sept. 2006.
- [211] M.C. Claessens, "The Design and Testing of Airfoils for Application in Small Vertical Axis Wind Turbines," Master's thesis, Delft University of Technology, November 2006.

- [212] Mirecki, A.; Roboam, X.; Richardeau, F., "Comparative study of maximum power strategy in wind turbines," in *ISIE-2004*, vol. 2, 4-7 May, pp. 993 - 998.
- [213] Haniotis A.; Papathanassiou S.; Kladas A.; Papadopoulos M., "Control issues of a permanent-magnet generator, variable-speed, wind turbine," *Wind Engineering*, vol. 26, no. 6, pp. 371-381, Nov. 2002.
- [214] Kartik B. Ariyur, Miroslav Krstić, *Real-Time Optimization by Extremum-Seeking Control*. Wiley InterScience, September 2003, ISBN: 978-0-471-46859-2.
- [215] Sternby, J., "Extremum control systems An area for adaptive control," in *In Preprints Joint American Control Conference, Vol. WA2-A*, 1980.
- [216] J. Sternby, "A review of extremum control," Department of Automatic Control, Lund Institute of Technology, Tech. Rep. -, April 1979.
- [217] K.J. Astron, B. Wittenmark, *Adaptive Control*. Second ed., Addison Wesley, Reading, MA, 1995.
- [218] Bobl, V., Bhm, J., Fessl, J., Machcek, J., *Digital Self-tuning Controllers Algorithms: Implementation and Applications*. Wiley InterScience, 2005, ISBN: 978-1-85233-980-7.
- [219] Miroslav Krstić and Hsin-Hsiung Wang, "Extremum seeking feedback: Stability proof and application to an aeroengine compressor model," 1998.
- [220] M. Leblanc, *Sur l'électrification des chemins de fer au moyen de courants alternatifs de fréquence fixe*. Revue Générale de l'électricité, 1922.
- [221] Krstić, M. and H.H. Wang, "Design and stability analysis of extremum seeking feedback for general nonlinear systems," in *In Proceedings of the 36th IEEE Conference on Decision and Control, San Diego, vol. 2*, 1997.
- [222] —, "Stability of extremum seeking feedback for general nonlinear dynamic systems," *Automatica*, vol. 36, 2000.
- [223] P. F. Blackman, *An Exposition of Adaptive Control*. J. H. Westcott, Ed. New York: Macmillan, 1962.
- [224] Zhong Zhi-Dan; Huo Hai-Bo; Zhu Xin-Jian ; Cao Guang-Yi; Ren Yuan, "Adaptive maximum power point tracking control of fuel cell power plants," *Journal of power sources*, vol. 176, no. 1, pp. 259-269, 2008.
- [225] Iulian Munteanu, Antoneta Iuliana Bratcu, Emil Ceangă, "Wind turbulence used as searching signal for MPPT in variable-speed wind energy conversion systems," *Renewable Energy*, vol. 34, no. 1, pp. 322-327, 2009.

- [226] Leyva, R.; Alonso, C.; Queinnec, I.; Cid-Pastor, A.; Lagrange, D.; Martínez-Salamero, L., "MPPT of photovoltaic systems using extremum - seeking control," *IEEE Transactions on Aerospace and Electronic Systems*, vol. 42, no. 1, p. 249-258, 2006.
- [227] Komatsu, M.; Miyamoto, H.; Ohmori, H.; Sano, A., "Output maximization control of wind turbine based on extremum control strategy," in *American Control Conference*, 2001, pp. 1739-1740.
- [228] Matsui, M.; Dehong Xu; Longyun Kang; Yang, Z., "Limit cycle based simple MPPT control scheme for a small sized wind turbine generator system-principle and experimental verification," in *IPEMC 2004*, vol. 3, 14-16 Aug., pp. 1746 - 1750.
- [229] Krstić, M., "Towards faster adaptation in extremum seeking control," in *IEEE Conference on Decision and Control*, 1999, pp. 4766-4771.
- [230] Moncef Chloua, Bala Srinivasan, Michel Perrier, Martin Gussy, "Effect of Excitation Frequency in Perturbation-Based Extremum Seeking Methods," in *8th International IFAC Symposium on Dynamics and Control of Process Systems, Cancun, Mexico*, vol. 1, 2007.
- [231] Elong, E. Krstić, M. Ariyur, K.B., "A case study of performance improvement in extremum seeking control," in *American Control Conference*, vol. 1, 2000, pp. 428-432.
- [232] Miroslav Krstić, "Performance Improvement and Limitations in Extremum Seeking Control," *Systems and Control Letters*, vol. 39, pp. 313-326, 2000.
- [233] —, "Email correspondance: Derivation of $M(s)$ and $L(s)$ transfer functions," March 2009.
- [234] Hao, S.; Hunter, G.; Ramsden, V.; Patterson, D., "Control system design for a 20 kW wind turbine generator with a boost converter and battery bank load," in *Power Electronics Specialists Conference, Vancouver, BC, Canada*, vol. 4, 2001, pp. 2203-2206.
- [235] Katsuhiko Ogata, *Modern Control Engineering*. Prentice Hall, Nov 23 2001, ISBN-10: 0130609072.
- [236] Gouri Bhuyan, "Scope of the Canadian APP Project on Marine Energy in Collaboration with Korean Organizations," in *International Forum on Ocean Energy Exploitation Technology, Korea*, Jan. 2010.
- [237] Clayton Bear. (2009, Oct.) OREG Fall Symposium, Ottawa, ON. [Online]. Available: http://www.oreg.ca/docs/2009_FallEvents/Bear.pdf

Appendices

Appendix B

Subsystem data

Rotor

Design rating:

$$H = 0.4 \text{ m}; R = 0.5 \text{ m}; D = 1 \text{ m}; \rho_w = 1000 \text{ kg} - \text{m}^3; P_{hyd}^b = 1000 \text{ watt}$$

$$\text{Efficiency: } \eta_{base} = 0.8$$

Curve-fit data for Fig. 9.6(a) and Eq. 9.20:

$$a_{c1} = 0.2056; b_{c1} = 2.053; c_{c1} = 0.4296$$

$$a_{c2} = -1.799; b_{c2} = 2.592; c_{c2} = 1.328$$

$$a_{c3} = 2.099; b_{c3} = 2.606; c_{c3} = 1.297$$

The rotor dimensions are measured directly. The $C_p - \lambda$ relationship (Fig. 9.6(a) and Eq. 9.20) is derived through two-dimensional multiple streamtube analysis (Chapter 5.2, [167]). Curve-fitting is done using Matlab-CFT™ Toolbox. The efficiency term η_{base} is determined through comparative analysis with a similar rotor configuration as reported in [3].

Transmission

Drivetrain parameters: $N_{gr} = 3.43$, $k_{sgr} = 54226 \text{ Nm/rad}$, $J_{rot} = 0.9025 \text{ kg} - \text{m}^2$, $B_{rot} = 0.5 \text{ Nm.s/rad}$, $\eta_{drv} = 0.95$

Transmission parameters k_{sgr} , J_{rot} , B_{rot} are calculated numerically using the relevant dimensions, mass, and configuration. These were validated separately through simulation (not presented in this work). Transmission system efficiency η_{drv} is calculated using suppliers' data-sheet (for chain-sprocket gearing).

Generator

Generator parameters: $N_P = 24$, $R_g = 0.23741 \Omega$, $L_g = 0.4156 \text{ mH}$, $\lambda_m = 0.06142 \text{ V.s/rad}$, $J_{gen} = 0.055 \text{ Kg} - \text{m}^2$, $B_{gen} = 0.1565 \text{ Nm.s/rad}$, $R_{nd} = 5.5 + 0.041F_{gen} + 0.01F_{gen}^2 \Omega$,

$$\hat{T}_{\text{cog}} = 2.350 \text{ Nm}$$

$$\text{Design rating: } I_g^b = 20 \text{ A; } N_{\text{gen}}^b = 350 \text{ rpm; } P_{\text{gen}}^b = 700 \text{ watt}$$

Curve-fit data for Eq. 9.29:

$$a_{g1} = 0.8981; b_{g1} = -0.2954$$

$$c_{g1} = 0.875; c_{g2} = 0.15;$$

$$a_{g2} = -0.8981; b_{g2} = -4.452$$

$$\text{Conversion (p.u.): } N_{\text{ggu}} = \frac{N_{\text{gen}}^b}{N_{\text{gen}}^{\text{nom}}}; I_{\text{ggu}} = \frac{I_g^b}{I_g^{\text{nom}}}$$

Generator parameters $N_P, R_g, L_g, \lambda_m, R_{\text{all}}, \hat{T}_{\text{cog}}$ are determined experimentally within the laboratory settings. Similar testing and steady-state analysis are carried out in identifying generator efficiency η_{gen} . Curve-fitting is done using Matlab-CFT™ Toolbox. Generator inertia J_{gen} and damping constant B_{gen} are calculated analytically. Generator model is validated through separate modeling exercises.

Rectifier

$$\text{Rectifier and filter parameters: } V_f = 0.583 \text{ V, } C_{fg} = 4500 \mu\text{F}$$

$$\text{Design rating: } I_r^b = 10 \text{ A; } P_{\text{rec}}^b = 650 \text{ watt}$$

Curve-fit data for Eq. 9.24:

$$a_{e1} = 0.9159; b_{e1} = 0.007138; a_{e2} = -0.07075; b_{e2} = -11.92$$

$$\text{Conversion (p.u.): } I_{\text{rpu}} = \frac{I_r^b}{I_r^{\text{nom}}}$$

The rectifier parameters are primarily taken from manufacturer's specifications. Additional efficiency characteristics are identified through laboratory testing. Curve-fitting is done using Matlab-CFT™ Toolbox.

Converter

$$\text{Design rating: } I_c^b = 10 \text{ A; } P_{\text{con}}^b = 500 \text{ watt}$$

Curve-fit data for Eq. 9.24:

$$a_{e1} = 0.8336; b_{e1} = -0.09328; a_{e2} = -1.021; b_{e2} = -17.58$$

$$\text{Conversion (p.u.): } I_{\text{cpu}} = \frac{I_c^b}{I_c^{\text{nom}}}$$

The dc-dc converter parameters are identified through laboratory testing. Curve-fitting is done using Matlab-CFT™ Toolbox.

Inverter

Design rating: $I_1^b = 2.15 A$; $P_{inv}^b = 400 \text{ watt}$

Curve-fit data for Eq. 9.24):

$a_{e1} = 0.8545$; $b_{e1} = -0.1599$; $a_{e2} = -0.2733$; $b_{e2} = -16.26$

Conversion (p.u.): $I_{pu} = \frac{I}{I_1^b}$

The power inverter parameters are identified through laboratory testing. Curve-fitting is done using Matlab-CFT™ Toolbox.

DAQ

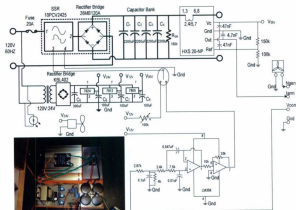
$\tau_1 = 0.95 \text{ s}$, $\tau_2 = 0.05 \text{ s}$, $\tau_3 = 0.05 \text{ s}$, $\tau_4 = 0.015 \text{ s}$, $\tau_{out} = 0.75 \text{ s}$

The DAQ unit is custom-built and the parameters are established using design information and laboratory testing.

Appendix C

Test apparatus

Laboratory test apparatus



Fabricated thyristor controlled power supply

Figure C.1: Thyristor controlled dc power supply for the emulator prime mover

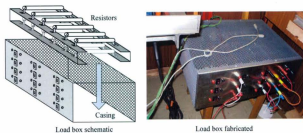


Figure C.2: Customized switchable load back for generator, converter, and turbine testing

Sensor systems

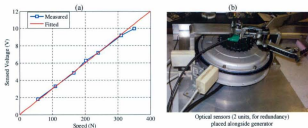
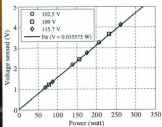


Figure C.3: Optical speed sensor mounted near the PMA



(a)



(b)

Figure C.5: Customized wattmeter for ac power measurement



